

Photoinduced oxidative addition at Rh and Ru centres

Barbara Procacci

A thesis submitted for the degree of Doctor of
Philosophy in Chemistry

The University of York

Department of Chemistry

September 2012

To my family

Abstract

Ultraviolet irradiation of $\text{CpRh}(\text{PMe}_3)(\text{C}_2\text{H}_4)$ in the presence of pentafluoropyridine $\text{C}_5\text{F}_5\text{N}$ yields an isolable $\eta^2\text{-C,C}$ -coordinated pentafluoropyridine complex. This is the first crystallographically characterised example of η^2 -coordination of pentafluoropyridine to a metal centre. Photolysis of $\text{CpRh}(\text{PMe}_3)(\text{C}_2\text{H}_4)$ in the presence of $\text{C}_5\text{F}_4\text{HN}$ affords cleanly the C-H activated product.

In contrast, photochemical reaction of $\text{CpRh}(\text{PMe}_3)(\text{C}_2\text{H}_4)$ in hexane in the presence of OMe- or NMe_2 - substituted tetrafluoropyridine results in the formation of metallacycles $[\text{Cp}(\text{PMe}_3)\text{Rh}(\kappa^2\text{-C,C})\text{CH}_2\text{N}(\text{CH}_3)\text{C}_5\text{F}_3\text{N}]$ and $[\text{Cp}(\text{PMe}_3)\text{Rh}(\kappa^2\text{-C,C})\text{CH}_2\text{OC}_5\text{F}_3\text{N}]$, fully characterized by spectroscopic and spectrometric techniques and X-ray crystallography. NMR studies suggest the need of the heteroatom and a primary carbon as in NMe_2 and OMe for the ring closure. Elimination of HF provides the driving force for the formation of the cyclometallated species.

The ability of $\text{Tp}^*\text{Rh}(\text{PMe}_3)_2$ and $\text{Tp}^*\text{Rh}(\text{CNneopentyl})(\eta^2\text{-PhN=C=N-R})$ complexes to activate B-H, Si-H and C-F bonds in photochemical reactions at room temperature in neat substrate (HBpin, $\text{Et}_3\text{SiH}/\text{Et}_2\text{SiH}_2/\text{PhSiH}_3$, $\text{C}_5\text{F}_5\text{N}/\text{C}_5\text{F}_4\text{NH}$) is presented. The complexes exhibit a remarkable preference for activating these bonds over the aliphatic or aromatic C-H bonds present on the substrates. The thermal stabilities of the products have been tested by heating in C_6D_6 up to 140°C . Products $\text{Tp}^*\text{Rh}(\text{PMe}_3)\text{H}(\text{Bpin})$, $\text{Tp}^*\text{Rh}(\text{PMe}_3)\text{H}(\text{Et}_2\text{SiH})$ and $\text{Tp}^*\text{Rh}(\text{PMe}_3)(\text{pyridyl})(\text{FHF})$ have been isolated and their molecular structures determined crystallographically. All the structures show characteristic bond lengths for a complete oxidative addition reaction. Competition reactions are performed in the presence of substrates and benzene simultaneously.

The photoreactivity of $\text{CpRh}(\text{PR}_3)(\text{C}_2\text{H}_4)$ complexes ($\text{R} = \text{Me}, \text{Ph}, \text{Me}_2\text{Ph}$) is explored in reactions with $(i\text{Pr})_2\text{NBH}_2$. Oxidative addition of the B-H bond is established for all the reactions to form the $[\text{CpRh}(\text{PR}_3)\text{H}(\text{BHN}(i\text{Pr})_2)]$. These

complexes are the first examples of oxidative addition of a B-H bond of aminoboranes to a 16-electron rhodium fragment.

Laser flash photolysis of **Ru1**, *cis*-[Ru((*R,R*)-Me-BPE)₂(H)₂] and **Ru2**, *cis*-[Ru((*R,R*)-Me-DuPHOS)₂(H)₂] generates the square planar Ru(PP*)₂ transient and allows measurement of reaction rates with different substrates. The data indicate that rate constants are smaller than those of analogues with less hindered achiral bidentate phosphines. The regeneration of the dihydride occurs with a higher rate constant than formation of either the hydrido-silyl or hydrido-boryl complexes. Moreover, the reactions of **Ru2** are about ten times slower than those of **Ru1**.

List of contents

CHAPTER 1

1 Introduction	1
1.1 Photochemical reactivity	1
1.2 Ligand Field excited states (LF)	2
1.3 Photochemistry of half-sandwich Rh compounds: C-H, Si-H, B-H and C-F activation and their coordination modes	5
1.3.1 C-H activation	5
1.3.2 Si-H activation	6
1.3.3 B-H and B-B activation	7
1.3.4 C-F activation	9
1.4 Photochemistry of Ru(PP) ₂ dihydride complexes	10
1.5 Time resolved methods and detection of transients	11
1.6 Outline of the thesis	12
1.7 Aim of the project	13

CHAPTER 2

2. Photochemical cyclometallation via HF elimination: synthesis and mechanism	14
2.1. Introduction	14
2.2. Results	22
2.2.1 Irradiation of 1 with pentafluoropyridine	22
2.2.2 Irradiation of 1 with 2,3,5,6-tetrafluoropyridine.	26
2.2.3 Irradiation of 1 with 4-dimethylamino-2,3,5,6-tetrafluoropyridine	27
2.2.4 Irradiation of 1 with 4-methoxy- 2,3,5,6 tetrafluoropyridine	30
2.3. Mechanistic studies	33
2.3.1 Reaction of complex 1 with pentafluoropyridine and 2,3,5,6-tetrafluoropyridine	33
2.3.2 Reaction of complex 1 with 4-substituted tetrafluorofluoropyridines	33
2.3.3 Kinetic Isotopic Effect (KIE)	35
2.4. Discussion	36
2.5. Summary	41
2.6. Experimental section	42
2.6.1 General Procedures	42
2.6.2 Mass spectrometry	42
2.6.3 X-ray crystallography	43
2.6.4 IR experiment	43
2.6.5 Synthesis and NMR Experiments	43
2.6.6 Preparation of $[(\eta^5\text{-C}_5\text{H}_5)(\text{PMe}_3)\text{Rh}(\eta^2\text{-C}_5\text{F}_5\text{N})]$, 2	44
2.6.7 Preparation of $[(\eta^5\text{-C}_5\text{H}_5)(\text{PMe}_3)\text{Rh}(\text{C}_5\text{F}_4\text{N})\text{H}]$, 3	44
2.6.8 Preparation of $[(\eta^5\text{-C}_5\text{H}_5)(\text{PMe}_3)\text{Rh} - (\kappa^2 \text{C,C}) \text{CH}_2\text{N}(\text{CH}_3)\text{C}_5\text{F}_3\text{N}]$, 4	45
2.6.9 Preparation of $[(\eta^5\text{-C}_5\text{H}_5)(\text{PMe}_3)\text{Rh} - (\kappa^2 \text{C,C}) \text{CH}_2\text{NC}_5\text{F}_3]$, 5	45

2.6.10 Preparation of $C_5F_4N(OCD_3)$	46
--	----

CHAPTER 3

3 Photochemical oxidative addition of B-H bonds at Ru and Rh centers: solution photochemistry 47

3.1 Introduction	47
3.2 Results	59
3.2.1 Ruthenium dihydride complexes	59
3.2.2 $Ru(dppe)_2H_2$ in the presence of HBpin and HBCat	60
3.2.3 Analysis of $Ru(dppe)_2H_2$ complex	61
3.2.4 Solution photochemistry: $Ru(dppe)_2H_2$ complex with HBpin	62
3.2.5 $Ru(dppe)_2H_2$ complex with HBCat	66
3.3 Cyclopentadienyl Rh complexes in B-H and B-B activation	69
3.3.1 Analysis of the $CpRh(C_2H_4)_2$ complex starting material	70
3.3.2 Solution photochemistry: $CpRh(C_2H_4)_2$ complex with HBpin	71
3.3.3 Solution photochemistry: $CpRh(C_2H_4)_2$ complex with B_2pin_2	73
3.3.4 Catalytic activity of $CpRh(C_2H_4)_2$ in the presence of HBpin and heptane	74
3.4 Discussion	75
3.5 Summary	79
3.6 Experimental	80
3.6.1 General procedures	80
3.6.2 Mass spectra	80
3.6.3 NMR spectroscopy	80
3.6.4 Synthesis of $Ru(dppe)_2H_2$. ⁴⁷	81
3.6.5 Synthesis of trans- $Ru(dppe)_2H(Bpin)$	81
3.6.6 Synthesis of trans and cis- $Ru(dppe)_2H(Bcat)$	82
3.6.7 Synthesis of $CpRh(C_2H_4)_2$	83
3.6.8 Synthesis of $CpRh(C_2H_4)H(Bpin)$	83
3.6.9 Synthesis of $CpRh(C_2H_4)(Bpin)_2$	83

CHAPTER 4

4 Oxidative addition of $(iPr)_2N-BH_2$ at rhodium centres 84

4.1 Introduction	84
4.2 Results	90
4.2.1 Photochemical reaction of $CpRh(PMe_3)(C_2H_4)$ in the presence of $H_2B=N(iPr)_2$	90
4.2.2 Photochemical reaction of $CpRh(PPh_3)(C_2H_4)$ in the presence of $H_2B=N(iPr)_2$	91
4.2.3 Photochemical reaction of $CpRh(PMe_2Ph)(C_2H_4)$ in the presence of $H_2B=N(iPr)_2$	92
4.3 Discussion	94

4.4 Photochemical reaction of CpRh(C ₂ H ₄) ₂ in the presence of 2-pyridine-N-methyldimethylsilazane	96
4.4.1 Results	97
4.5 Summary	102
4.6 Experimental	103
4.6.1 General procedures	103
4.6.2 Mass spectra	103
4.6.3 X-ray crystallography	104
4.6.4 NMR spectroscopy	104
4.6.5 NMR experiments	104
4.6.6 CpRh(PMe ₃)H(BHN(<i>i</i> Pr) ₂)	104
4.6.7 CpRh(PPh ₃)H(BHN(<i>i</i> Pr) ₂)	105
4.6.8 CpRh(PMe ₂ Ph)H(BHN(<i>i</i> Pr) ₂)	105
4.6.9 CpRh((SiMe ₂)N(κN-C ₅ H ₄ N)) ₃	105
CHAPTER 5	
5 C-F, B-H, and Si-H activation at Tp`Rh complexes	107
5.1 Introduction	107
5.2 Results	115
5.2.1 Starting material Tp`Rh(PMe ₃)H ₂	115
5.2.2 Photochemical reaction of Tp`Rh(PMe ₃)H ₂ in the presence of C ₅ F ₅ N	116
5.2.3 Photochemical reaction of complex Tp`Rh(PMe ₃)H ₂ in the presence of 2,3,5,6 - tetrafluoropyridine	123
5.2.4 Photochemical reaction of Tp`Rh(PMe ₃)H ₂ in the presence of HBpin	125
5.2.5 Photochemical reaction of Tp`Rh(PMe ₃)H ₂ in the presence of silanes	128
5.2.6 Starting material Tp`Rh(CNneopentyl)(η ² -PhN=C=N-neopentyl)	133
5.2.7 Photochemical reaction of Tp`Rh(CNneopentyl)(η ² -PhN=C=N-neopentyl) in the presence of C ₅ F ₅ N	134
5.2.8 Photochemical reaction of Tp`Rh(CNneopentyl)(η ² -PhN=C=N-neopentyl) in the presence of HBpin	135
5.2.9 Photochemical reaction of Tp`Rh(CNneopentyl)(η ² -PhN=C=N-neopentyl) in the presence of silanes	137
5.2.10 Competition reactions	138
5.3 Discussion	142
5.4 Summary	144
5.5 Experimental	145
5.5.1 General procedures	145
5.5.2 Mass spectra.	145
5.5.3 X-ray crystallography	146
5.5.4 NMR spectroscopy	146
5.5.5 Syntheses and NMR Experiments	146

5.5.6 $\text{Tp}^{\text{R}}\text{Rh}(\text{C}_5\text{F}_4\text{N})(\text{PMe}_3)\text{F}$ – major rotamer	147
5.5.7 $\text{Tp}^{\text{R}}\text{Rh}(\text{C}_5\text{F}_4\text{N})(\text{PMe}_3)\text{F}$ – minor rotamer	147
5.5.8 $\text{Tp}^{\text{R}}\text{Rh}(\text{C}_5\text{F}_4\text{N})(\text{PMe}_3)(\text{FHF})$	147
5.5.9 $\text{Tp}^{\text{R}}\text{Rh}(\text{C}_5\text{F}_3\text{NH})(\text{PMe}_3)\text{F}$	148
5.5.10 $\text{Tp}^{\text{R}}\text{Rh}(\text{C}_5\text{F}_4\text{N})(\text{PMe}_3)\text{H}$	148
5.5.11 $\text{Tp}^{\text{R}}\text{RhH}(\text{Bpin})(\text{PMe}_3)$	148
5.5.12 $\text{Tp}^{\text{R}}\text{RhH}(\text{Et}_2\text{SiH})(\text{PMe}_3)$	149
5.5.13 $\text{Tp}^{\text{R}}\text{RhH}(\text{PhSiH}_2)(\text{PMe}_3)$	149
5.5.14 $\text{Tp}^{\text{R}}\text{RhH}(\text{Et}_3\text{Si})(\text{PMe}_3)$	150
5.5.15 $\text{Tp}^{\text{R}}\text{Rh}(\text{CNneopentyl})\text{F}(\text{C}_5\text{F}_4\text{N})$	150
5.5.16 $\text{Tp}^{\text{R}}\text{Rh}(\text{CNneopentyl})\text{H}(\text{Bpin})$	151
5.5.17 $\text{Tp}^{\text{R}}\text{Rh}(\text{CNneopentyl})\text{H}(\text{Et}_2\text{SiH})$	151
5.5.18 $\text{Tp}^{\text{R}}\text{Rh}(\text{CNneopentyl})\text{H}(\text{PhSiH}_2)$	151

CHAPTER 6

6. Laser flash studies of $\text{Ru}(\text{PP})_2\text{H}_2$ complexes	153
6.1. Introduction	153
6.2. Results	163
6.2.1. Λ -[cis-Ru((R,R)-Me-BPE) ₂ (H) ₂] and Δ -[cis-Ru((S,S)-Me-DuPHOS) ₂ (H) ₂]: laser flash studies	163
6.3. Λ -[cis-Ru((R,R)-iPr-BPE) ₂ (H) ₂], Ru ₃ H ₂ : preliminary laser flash study	171
6.3.1. Transient spectra	171
6.3.2. LFP in the presence of Hydrogen	172
6.4. Ru(dppe) ₂ H ₂ : Laser Flash studies in the presence of HBpin	173
6.5. Discussion	174
6.5.1. Kinetics	175
6.6. Summary	179
6.7. Experimental	180
6.7.1. General procedures	180
6.7.2. Laser Flash Photolysis.	180

CHAPTER 7

7 X-Ray Crystallography	182
7.1 Introduction	182
7.2 Crystal structure analysis	182
7.2.1 Ruthenium hydride complexes	182
7.2.2 Ruthenium hydride dihydrogen complexes	186
7.2.3 Rhenium Carbonyl compounds.	190

CHAPTER 8	
8 SUMMARY AND CONCLUSIONS	195
I. Appendix to chapter seven	199
I.II. Crystals and their internal structure	199
I.III. X-ray in crystallography and diffraction	201
I.IV. Purification and crystal growth.	206
I.V. Choose a suitable crystal	208
I.VI. Obtaining unit cell geometry and preliminary symmetry information	209
I.VII. Data acquisition	209
I.VIII. Data reduction, solving the structure and refinement	210
II. LIST OF ABBREVIATIONS	213
III. BIBLIOGRAPHY	216

Table of figures

CHAPTER ONE

- Figure 1. Simplified molecular orbital diagram for the interaction of a metal centre with n ligands showing a $d-d$ transition (LF). 3
- Figure 2. Overlap diagram showing σ_g^* molecular orbital populated in the excited state which is M-H antibonding and H-H bonding. 4
- Figure 3. Top: Classical Chatt-Dewar-Duncanson bonding model. Bottom: Bonding scheme for boranes σ -coordination where the p orbital on boron contribute to the classical model. 8
- Figure 4. Two possible coordination modes of a borane to a metal complex. 9

CHAPTER TWO

- Figure 1. $^{31}\text{P}\{^1\text{H}\}$ NMR spectrum for complex 2 in C_6D_6 showing a doublet of doublet due to coupling of ^{31}P to ^{103}Rh and two inequivalent fluorines. 23
- Figure 2. Enlargement of the five resonances from ^{19}F NMR spectrum in C_6D_6 belonging to the five inequivalent fluorines on the pyridyl ring. 24
- Figure 3. Left. Molecular structure of 2. Right. Plane 1 C_2F_2 , Plane 2 C_5N , Plane 1 - Plane 2 42.02° , Hydrogen atom are omitted for clarity. Ellipsoids for the anisotropic displacement parameters are shown at the 50% level. 25
- Figure 4. Bond lengths in Å for the η^2 -coordinated pyridyl moiety. 25
- Figure 5. $^{31}\text{P}\{^1\text{H}\}$ NMR spectrum in C_6D_6 for complex 3 showing a doublet arisen from coupling to ^{103}Rh . 26
- Figure 6. ^1H NMR spectrum in C_6D_6 of the hydride resonance for complex 3. The doublet of doublets is due to coupling to ^{31}P and ^{103}Rh . 27
- Figure 7. ^{19}F spectrum in C_6D_6 for complex 3. The two resonances belong to the two sets of inequivalent fluorines. 27
- Figure 8. ^1H NMR spectrum of complex 4 in C_6D_6 . 29
- Figure 9. Molecular structure of 4. Hydrogen atoms are omitted for clarity. Ellipsoids for the anisotropic displacement parameters are shown at the 50% level. 29
- Figure 10. Three ^{19}F resonances for complex 5 in C_6D_6 . 31
- Figure 11. Molecular structure of 5. Hydrogen atoms are omitted for clarity. Ellipsoids for the anisotropic displacement parameters are shown at the 50% level. 31

- Figure 12. (a) Hydride resonance in the ^1H NMR spectrum after reaction of 1 with b. (b) broad peak at low field in the ^1H NMR spectrum assigned to HF. 34
- Figure 13. Energy profile for the possible mechanisms. Blue: C-F/C-H; Red: C-H/C-F. 39
- Figure 14. DFT calculations for the possible reaction mechanism. Numbers are $\Delta E/(\Delta G)$ in Kcal/mol. 40

CHAPTER THREE

- Figure 1. ^1H NMR spectrum of hydride region for complexes *cis/trans* $\text{Ru}(\text{dppe})_2\text{H}_2$ in C_6D_6 (top), and $^1\text{H}\{^{31}\text{P}\}$ NMR spectrum of hydride region for complexes *cis/trans* $\text{Ru}(\text{dppe})_2\text{H}_2$ in C_6D_6 (bottom). 62
- Figure 2. $^{31}\text{P}\{^1\text{H}\}$ NMR spectrum of complexes *cis*- $\text{Ru}(\text{dppe})_2\text{H}_2$ and *trans*- $\text{Ru}(\text{dppe})_2\text{H}_2$ in C_6D_6 . 62
- Figure 3. $^{31}\text{P}\{^1\text{H}\}$ NMR spectrum of reaction of the complex $\text{Ru}(\text{dppe})_2\text{H}_2$ with HBpin in C_6D_6 after 12 hours of photolysis at 90% of conversion. The stars referred to starting material left. Top: Enlargement of the resonances for $\text{Ru}(\text{dppe})_2\text{H}(\text{Bpin})$. 64
- Figure 4. Hydride region of the ^1H NMR spectrum (bottom) and $^1\text{H}\{^{31}\text{P}\}$ NMR spectrum (top) of photochemical reaction of complex $\text{Ru}(\text{dppe})_2\text{H}_2$ with HBpin in C_6D_6 . The minor peak in the $^1\text{H}\{^{31}\text{P}\}$ NMR spectrum is the starting complex $\text{Ru}(\text{dppe})_2\text{H}_2$. 64
- Figure 5. $^1\text{H}\{^{31}\text{P}\}$ - ^{31}P NMR spectrum of photochemical reaction of complex $\text{Ru}(\text{dppe})_2\text{H}_2$ with HBpin in C_6D_6 . 65
- Figure 6. $^{31}\text{P}\{^1\text{H}\}$ NMR spectrum of photochemical reaction of complex $\text{Ru}(\text{dppe})_2\text{H}_2$ with HBcat in C_6D_6 showing the singlet for the *trans* isomer and the ABMQ system for the *cis* one. 67
- Figure 7. Hydride region of the ^1H NMR spectrum of photochemical reaction of complex $\text{Ru}(\text{dppe})_2\text{H}_2$ with HBcat in C_6D_6 to form the new species *cis*- $\text{Ru}(\text{dppe})_2\text{H}(\text{Bcat})$ and *trans*- $\text{Ru}(\text{dppe})_2\text{H}(\text{Bcat})$. 68
- Figure 8. ^1H - $^{31}\text{P}\{^1\text{H}\}$ NMR spectrum of photochemical reaction of complex $\text{Ru}(\text{dppe})_2\text{H}_2$ with HBcat in C_6D_6 showing the ABMQ system in the $^{31}\text{P}\{^1\text{H}\}$ correlated to the *cis* hydride and a cross peak between the singlet in the $^{31}\text{P}\{^1\text{H}\}$ and the quintet resonance in the ^1H spectrum for the *trans* hydride. 68
- Figure 9. ^1H NMR spectrum of complex $\text{CpRh}(\text{C}_2\text{H}_4)_2$ in C_6D_6 . 71
- Figure 10. ^1H NMR spectrum: hydride resonance for complex $\text{CpRh}(\text{C}_2\text{H}_4)\text{H}(\text{Bpin})/\text{CpRh}(\text{C}_2\text{H}_4)(\eta^2\text{-HBpin})$. The broad peak is due to coupling to ^{11}B . 72
- Figure 11. $\{^{11}\text{B}\}^1\text{H}$ NMR spectrum of the hydride region for complex $\text{CpRh}(\text{C}_2\text{H}_4)\text{H}(\text{Bpin})/\text{CpRh}(\text{C}_2\text{H}_4)(\eta^2\text{-HBpin})$ in C_6D_6 . 73
- Figure 12. ^{11}B NMR spectrum showing the broad resonance for the $\text{CpRh}(\text{C}_2\text{H}_4)(\text{Bpin})_2$ complex in C_6D_6 . 74

CHAPTER FOUR

- Figure 1. Structure of possible substituted amine-boranes. 84
- Figure 2. The bis-(σ -BH) coordination product formed by thermal reaction of complex $\text{RuH}_2(\eta^2\text{-H}_2)_2(\text{PCy}_3)_2$ in the presence of amine-borane. 86
- Figure 3. Structures for the Rh(I) and Rh(III) Shimoi-type complexes of amine-borane. 87
- Figure 4. Crystal structures for Ru, Rh, Ir σ -borane complexes of $\text{H}_2\text{B-N}i\text{Pr}_2$.¹⁸ 87
- Figure 5. 2: Product formed by oxidative addition of H_2BNR_2 at Ir centre, (a) $\text{Ir}(\text{PMe}_3)_3\text{Cl}(\text{coe})$, toluene. 3: Ir-borylene species formed by chlorine abstraction from complex 2, (b) $\text{Na}[\text{BAR}_4]$, $\text{C}_6\text{H}_5\text{F}$. 88
- Figure 6. Top: ^1H NMR spectrum in C_6D_6 of complex $\text{CpRh}(\text{PMe}_3)\text{H}(\text{BHN}(i\text{Pr})_2)$ showing the broad resonance for the B-H proton. Bottom: $^1\text{H}\{^{11}\text{B}\}$ NMR spectrum of the same complex showing how the resonance sharpened under ^{11}B decoupling. 91
- Figure 7. ^{11}B NMR spectrum showing the broad resonance for the $\text{CpRh}(\text{PMe}_3)\text{H}(\text{BHN}(i\text{Pr})_2)$ complex in C_6D_6 . 91
- Figure 8. $^{31}\text{P}\{^1\text{H}\}$ NMR spectrum for complex $\text{CpRh}(\text{PPh}_3)\text{H}(\text{HBN}(i\text{Pr})_2)$. 92
- Figure 9. ^{11}B spectrum showing the broad resonance for the $\text{CpRh}(\text{PMe}_2\text{Ph})\text{H}(\text{BHN}(i\text{Pr})_2)$ complex in C_6D_6 . 92
- Figure 10. ^1H NMR spectrum at 240 K showing the low field peak for the cationic rhodium complex. 95
- Figure 11. Products formed from photochemical reaction of $\text{CpRh}(\text{C}_2\text{H}_4)_2$ with $\text{HSiMe}_2\text{OSiMe}_2\text{H}$. 97
- Figure 12. Structure of the silazane used in this work. 97
- Figure 13. ^1H NMR spectrum in C_6D_6 showing the hydride region. The major doublet belongs to the silicon containing complex. 98
- Figure 14. $\{^1\text{H}-^{29}\text{Si}\}$ 2D NMR spectrum showing correlation between the hydride resonance and the ^{29}Si signal. The ^{29}Si signal is two resonances, confirming the presence of two inequivalent ^{29}Si environments. 98
- Figure 15. Crystal structure for the rhodium-tris-silazane complex; hydrogen atoms are omitted for clarity. Ellipsoids for the anisotropic displacement parameters are shown at the 50% level. 99
- Figure 16. ^1H NMR spectrum for the rhodium-tris silazane complex in C_6D_6 . 101

CHAPTER FIVE

- Figure 1. Partially fluoroarenes investigated in photochemical reactions of the complex $\text{Tp}^{\text{Rh}}(\text{PMe}_3)\text{H}_2$. 112
- Figure 2. $^{31}\text{P}\{^1\text{H}\}$ NMR spectrum in C_6D_6 for the $\text{Tp}^{\text{Rh}}(\text{PMe}_3)\text{H}_2$ starting material. 115
- Figure 3. ^1H NMR spectrum in C_6D_6 for the $\text{Tp}^{\text{Rh}}(\text{PMe}_3)\text{H}_2$ starting material. The inset shows the hydride resonance. 115
- Figure 4. $^{31}\text{P}\{^1\text{H}\}$ NMR spectrum of the complex $\text{Tp}^{\text{Rh}}(\text{C}_5\text{F}_4\text{N})(\text{PMe}_3)\text{F}$. 116
- Figure 5. Low temperature ^{19}F NMR spectrum showing the presence of the two ortho conformers. 117
- Figure 6. Crystal structure of the complex $\text{Tp}^{\text{Rh}}(\text{FHF})(\text{C}_5\text{NF}_4)(\text{PMe}_3)$, hydrogen atoms are omitted for clarity apart from the bifluoride. Ellipsoids for the anisotropic displacement parameters are shown at the 50% level. 118
- Figure 7. ^1H NMR spectrum in C_6D_6 showing the broad low field peak belonging to the bifluoride proton. 119
- Figure 8. ^1H NMR spectrum in C_7D_8 showing a doublet at low field belonging to the bifluoride proton. 119
- Figure 9. ^{19}F NMR spectrum of complex $\text{Tp}^{\text{Rh}}(\text{FHF})(\text{C}_5\text{NF}_4)(\text{PMe}_3)$ showing: top, broad resonance assigned to the proximal fluorine of the bifluoride; bottom: doublet assigned to the distal fluorine of the bifluoride. 122
- Figure 10. $^{31}\text{P}\{^1\text{H}\}$ NMR spectrum for reaction of $\text{Tp}^{\text{Rh}}(\text{PMe}_3)\text{H}_2$ in the presence of $\text{C}_5\text{F}_4\text{HN}$ after 5 hours of irradiation. 124
- Figure 11. Top: ^1H NMR spectrum, hydride resonance for the complex $\text{Tp}^{\text{Rh}}(\text{C}_5\text{F}_4\text{N})(\text{PMe}_3)\text{H}$ in C_6D_6 . Bottom: ^{19}F NMR spectrum, fluoride resonance for the complex $\text{Tp}^{\text{Rh}}(\text{C}_5\text{F}_3\text{NH})(\text{PMe}_3)\text{F}$ in C_6D_6 . 124
- Figure 12. $^{31}\text{P}\{^1\text{H}\}$ NMR spectrum for the complex $\text{Tp}^{\text{Rh}}\text{H}(\text{Bpin})(\text{PMe}_3)$ in C_6D_6 . 125
- Figure 13. ^{11}B NMR spectrum of the $\text{Tp}^{\text{Rh}}\text{H}(\text{Bpin})(\text{PMe}_3)$ complex in C_6D_6 showing the typical broad resonance for metal-boryl complexes. 126
- Figure 14. Crystal structure for complex $\text{Tp}^{\text{Rh}}\text{H}(\text{Bpin})(\text{PMe}_3)$, hydrogen atoms are omitted for clarity except of the hydride. Ellipsoids for the anisotropic displacement parameters are shown at the 50% level. 127
- Figure 15. $\{^1\text{H}-^{29}\text{Si}\}$ 2D NMR spectrum showing correlation between the hydride resonance for the complex $\text{Tp}^{\text{Rh}}\text{H}(\text{Et}_2\text{SiH})(\text{PMe}_3)$ and the ^{29}Si signal. The ethyl protons are also linked to the ^{29}Si resonance. The second hydride belongs to starting material left. 129

- Figure 16. Crystal structure for complex $\text{Tp}^{\text{R}}\text{RhH}(\text{Et}_2\text{SiH})(\text{PMe}_3)$, hydrogen atoms are omitted for clarity apart from the RhH and SiH. Ellipsoids for the anisotropic displacement parameters are shown at the 50% level. 130
- Figure 17. $^{31}\text{P}\{^1\text{H}\}$ NMR spectra for the reactions of complex $\text{Tp}^{\text{R}}\text{Rh}(\text{H}_2)(\text{PMe}_3)$ with the different silanes. 133
- Figure 18. ^1H NMR spectrum of complex $\text{Tp}^{\text{R}}\text{Rh}(\text{CNneopentyl})(\eta^2\text{-PhN}=\text{C}=\text{N-neopentyl})$ in C_6D_6 . The spectrum shows the presence of some impurities. 134
- Figure 19. Low temperature ^{19}F NMR spectrum after photochemical reaction of complex $\text{Tp}^{\text{R}}\text{Rh}(\text{CNneopentyl})(\eta^2\text{-PhN}=\text{C}=\text{N-neopentyl})$ in the presence of $\text{C}_5\text{F}_5\text{N}$. 135
- Figure 20. ^1H NMR spectrum in C_6D_6 for the photochemical reaction of complex $\text{Tp}^{\text{R}}\text{Rh}(\text{CNneopentyl})(\eta^2\text{-PhN}=\text{C}=\text{N-neopentyl})$ in neat HBpin showing the hydride resonance arising from it. 136
- Figure 21. ^{11}B NMR spectrum showing the broad resonance for the rhodium-boryl complex. 136
- Figure 22. $\{^1\text{H}-^{13}\text{C}\}$ 2D NMR spectrum in C_6D_6 showing correlation between the BOC quaternary carbon and the methyl groups on the borane ring. 137
- Figure 23. $^{31}\text{P}\{^1\text{H}\}$ NMR spectrum for competition reaction of $\text{Tp}^{\text{R}}\text{Rh}(\text{PMe}_3)_2$ in 50/50 volume of $\text{C}_6\text{H}_6/\text{C}_5\text{F}_5\text{N}$ at reaction completed. 139
- Figure 24. $^{31}\text{P}\{^1\text{H}\}$ NMR spectrum for competition reaction of $\text{Tp}^{\text{R}}\text{Rh}(\text{PMe}_3)_2$ in 50/50 volume of $\text{C}_6\text{H}_6/\text{HBpin}$ at completion of reaction. 140
- Figure 25. $^{31}\text{P}\{^1\text{H}\}$ NMR spectrum for competition reaction of $\text{Tp}^{\text{R}}\text{Rh}(\text{PMe}_3)_2$ in 50/50 volume of $\text{C}_6\text{H}_6/\text{PhSiH}$ at completion of reaction. 140

CHAPTER SIX

- Figure 1. Transient UV/Vis spectra measured after solution laser flash photolysis (a)(d) 400 ns after flash and (e) 300 ns after flash. (a) Spectrum of $\text{Ru}(\text{dmpe})_2$ in cyclohexane under argon, (b) spectrum of $\text{Ru}(\text{depe})_2$ in heptane under 11 torr of H_2 , (c) spectrum of $\text{Ru}(\text{dppe})_2$ in cyclohexane under 760 torr of H_2 , (d) spectrum of $\text{Ru}(\text{dfpe})_2$ under 760 torr of H_2 and (e) spectrum of $\text{Ru}(\text{dmpm})_2$ under 100 torr of H_2 .³ 154
- Figure 2. The molecular orbital energy diagram proposed for a square planar MP_4 complex with a $^1\text{A}_{1g}$ ground state assuming D_{4h} symmetry.¹² 155
- Figure 3. UV- vis spectra for complex $\text{Ru}(\text{dmpe})_2$, a, and $\text{Os}(\text{dmpe})_2$, b in low temperature matrix. 157
- Figure 4. Schematic diagram comparing the rate constants for the investigated complexes. 160

Figure 5. Calculated reaction profile and representation of changes for the η^1 and η^2 approaches of H_2 to $[Ru(PH_3)_4]$.¹¹ 161

Figure 6. Left: transient UV-Vis spectra measured point-by-point at 295 K in cyclohexane on laser flash photolysis under 1 atm H_2 (308 nm) of: (a) Λ -*R,R*-Ru1H₂ and (b) Λ -*R,R*-Ru2H₂. Right: transient decay after photolysis of (c) Λ -*R,R*-Ru1H₂ recorded at 500 nm and (d) Λ -*R,R*-Ru2H₂ followed at 560 nm. The red lines show the fit to first order kinetics. The difference between the observed and the fitted decays are shown under the transient decays. 165

Figure 7. Plots of pseudo-first-order rate constants for the decay of the transients obtained upon laser flash photolysis (308 nm) of complexes Λ -*R,R*-Ru1H₂ and Λ -*R,R*-Ru2H₂ in cyclohexane vs the pressure of quenching gas (H_2 and D_2). The lines through the points show the best fits and the colored lines show the 95% confidence limits. 166

Figure 8. Plot of the pseudo first order rate constants, k_{obs} vs the concentration of HBpin: Λ -*R,R*-Ru1H₂ – left, Λ -*R,R*-Ru2H₂ – right. 169

Figure 9. Plot of the pseudo first order rate constants, k_{obs} vs the concentration of PhSiH₃: Λ -*R,R*-Ru1H₂ – left, Λ -*R,R*-Ru2H₂ – right. 169

Figure 10. Plot of the pseudo first order rate constants, k_{obs} vs the concentration of C₆F₅H: Λ -*R,R*-Ru2H₂ – right. 169

Figure 11. Left: transient UV-Vis spectra measured point-by-point at 298 K in cyclohexane on laser flash photolysis under 1 atm H_2 (308 nm) of Λ -*R,R*-Ru3H₂. Right: transient decay after photolysis of Λ -*R,R*-Ru3H₂ recorded at 470 nm under 1 atm of H_2 at 298 K. 172

Figure 12. Plots of pseudo-first-order rate constants for the decay of the transient obtained upon laser flash photolysis (308 nm) of complexes Λ -*R,R*-Ru3H₂ in cyclohexane vs the pressure of hydrogen. The line through the points show the best fits and the colored lines show the 95% confidence limits. 172

Figure 13. Left: transient decay after photolysis of Ru(dppe)₂H(Bpin) recorded at 470 nm at 298 K. Right: plot of the pseudo first order rate constants, k_{obs} vs the concentration of HBpin. 173

Figure 14. From the left: molecular structures of *trans*-*R,R*-Ru1(Cl)₂; *trans*-*R,R*-Ru1(Br)(H) and *trans*-*R,R*-Ru2(C₆F₅)(H). 175

Figure 15. Plot of log₁₀ k_2 versus the different quencher for Λ -*R,R*-Ru1H₂ (stipple) and Λ -*R,R*-Ru2H₂ (hatched) where k_2 is the second order rate constant. 176

Figure 16. Molecular structures of Λ -*R,R*-Ru1H₂ (left) and Λ -*R,R*-Ru2H₂ (right) (50% thermal ellipsoids), all hydrogen atoms omitted for clarity except for H(1) and H(2). Note that one phospholane ring in Λ -*R,R*-Ru1H₂ is disordered; just one form is shown. 176

Figure 17. Plot of log₁₀ k_2 versus the different Ru(PP)₂H₂ complexes in the presence of HBpin (blue) and H₂ (orange) where k is the second order rate constant. 179

CHAPTER SEVEN

Figure 1. Molecular structure of Δ -R,R-Ru(PhSiH₂)(H), 1 (left, top-bottom), and trans-R,R-Ru(C₆F₅)(H), 2 (right, top-bottom). Hydrogen atoms are omitted for clarity apart than the hydrides and the hydrogens bounded to the silicon. Ellipsoids for the anisotropic displacement parameters are shown at the 50% level. 183

Figure 2. Molecular structure of [Ru(BPE)₂(H₂)(H)]⁺[Bcat₂]⁻, 3. Hydrogen atoms are omitted for clarity apart the hydride and dihydrogen. Ellipsoids for the anisotropic displacement parameters are shown at the 50% level. 186

Figure 3. Phospholane moiety of complex 3 showing the disorder. Hydrogen atoms are omitted for clarity. Ellipsoids for the anisotropic displacement parameters are shown at the 50% level. 188

Figure 4. [Ru(PP)₂(H₂)(H)] fragment for complex 3 showing the disorder of the metal centre Ru1 / Ru1A, hydrides H1AA / H1C and dihydrogen H1AB-H1AC / H1B-H1A ligands. 188

Figure 5. Molecular structure of [Ru(BPE)₂(H₂)(H)]⁺[BAR^F₄]⁻, 4. Hydrogen atoms are omitted for clarity apart than the hydride and dihydrogen. Ellipsoids for the anisotropic displacement parameters are shown at the 50% level. 189

Figure 6. Molecular structure of Re(CO)₃(5,5'-BMCbpy)(OPF₂O), 5 (top left); [Re(CO)₃(bpy)(Pic)][PF₆], 6 (top right); and [Re(CO)₃(5,5'-BMCbpy)(NCCH₃)]⁺[PF₆]⁻, 7 (bottom). Hydrogen atoms are omitted for clarity. Ellipsoids for the anisotropic displacement parameters are shown at the 50% level. 191

Figure 7. View of the crystal packing in P2₁/c for complex 5 along *b* with representation of the symmetry elements. Green: Two-fold screw axes; Pink: Glide planes perpendicular to *b*; Light orange: Inversion centers. 192

Figure 8. Overlay of Re, O1, O2 and O3 atoms of the carbonyl ligands of Re(CO)₃(4,4'-BMCbpy)(OPF₂O) 5, (red) and [Re(CO)₃(4,4'-BMCbpy)(NCCH₃)]⁺[PF₆]⁻ 7, (green), showing the different orientation of the two COOCH₃ ligands. 194

APPENDIX to chapter seven

Figure 1. (a) Representation of a unit cell where *a, b, c* are the unit cell lengths and α, β, γ the angles.¹ (b) Schematic representation of a crystal lattice where every point is a lattice point. 199

Figure 2. Electromagnetic spectrum of light. 201

Figure 3. (Left) Geometric representation of Bragg's law; (Right) Bragg's law. 202

Figure 4. Miller indices in cubic crystals. 203

Figure 5. Flowchart for the steps of a crystal structure determination. 206

Figure 6. Schematic diagram of a four circle diffractometer. 208

Table of schemes

CHAPTER ONE

Scheme 1. Preference in photo-dissociation of phosphine instead of dihydrogen.	2
Scheme 2. Photodissociation of a CO from a metal-carbonyl.	4
Scheme 3. C-H bond activation by a transition metal centre.	5
Scheme 4. Possible coordination modes in Si-H activation by a Rh centre.	6
Scheme 5. The photochemistry of metal hydride complexes.	10

CHAPTER TWO

Scheme 1. Formation of a cobaltacycle from C-F activation of an aldehyde.	16
Scheme 2. Carbonylation of the cobaltacycle to give the organic product.	16
Scheme 3. Five coordinate Os metallacycle formed by C-F activation of thiofluoroarenes.	17
Scheme 4. Top: Formation of the platinacycle after C-F activation of an imine-substituted fluoroarene. Bottom: Catalytic methylation of polyfluorinated imines by a Pt complex.	17
Scheme 5. Catalytic cycle for pyridinidyl directed alkenylation of alcohols. A five membered rhodacycle is intermediate in the cycle. $RhL_n = [Cp^*RhCl_2]_2$.	18
Scheme 6. Eight membered oxo-rhodacycle found to be an intermediate in cycloaddition reactions, $L_n = (IMes)(COD)$.	19
Scheme 7. Rh-catalysed cyclo-addition reaction. $RhL_n = [Cp^*RhCl_2]_2$	19
Scheme 8. Para C-F activation of C_5F_5N by a rhodium-hydride complex.	20
Scheme 9. Photo-dissociation of C_2H_4 from complex 1 to form the 16-electron complex.	20
Scheme 10. Reaction of complex 1 with different substrates to afford different coordination type products.	21
Scheme 11. Fluorinated hetero-aromatics investigated.	22
Scheme 12. Photochemical reaction between complex 1 and pentafluoropyridine to form complex 2.	24
Scheme 13. Photochemical reaction of complex 1 with 4-substituted tetrafluoropyridines to afford metallacycles 4 and 5.	29

Scheme 14. Electron transfer mechanism where HF is eliminated to form the products.	38
Scheme 15. Mechanism for nucleophilic aromatic substitution which produce HF as by-product.	38
CHAPTER THREE	
Scheme 1. Schematic representation of cross-coupling reactions between an organoboron reagent and an organohalide.	47
Scheme 2. Proposed catalytic cycle for Suzuki-Miyaura coupling reactions.	48
Scheme 3. General reaction scheme for borylations involving boranes and diboranes substrates.	49
Scheme 4. General proposed mechanism for borylation reaction of primary C-H bonds via oxidative addition.	49
Scheme 5. Mechanism of methane borylation with σ -CAM step.	50
Scheme 6. Oxidative addition of HBcat at a Ru centre, phosphine coordinated, N-heterocyclic carbene species.	51
Scheme 7. Structure of the unusual bulky dioxaborocine used in hydroboration reaction.	53
Scheme 8. Formation of the unsaturated intermediate 3 in the hydroboration reaction of $\text{RuH}_2(\text{H}_2)_2(\text{PCy}_3)_2$ in the presence of HBpin.	53
Scheme 9. Proposed catalytic cycle for the Fe mediated hydroboration reaction of diene in the presence of HBpin.	54
Scheme 10. Possible coordination modes of a secondary borane to a metal hydride fragment.	55
Scheme 11. Bis σ -borane complex of H_2BMes .	56
Scheme 12. Cationic Ru complex of mesitylborane.	56
Scheme 13. Photochemical reactions of CpRh-phosphine complexes in the presence of HBpin and B_2pin_2 affording the oxidative addition products.	57
Scheme 14. Two different isomers formed in oxidative addition reactions of HBpin to a chiral phosphine-rhodium centre. The σ -compound was postulated as transition state by DFT calculations.	58
Scheme 15. Photoelimination of dihydrogen from $(\text{PP})_2\text{RuH}_2$ complexes to form the square-planar 16-electron intermediate $\text{Ru}(0)(\text{PP})_2$.	59

Scheme 16. Photochemical reaction of $(PP)_2RuH_2$ complexes with HBpin to form <i>cis</i> and <i>trans</i> $(PP)_2RuH(Bpin)$.	60
Scheme 17. Structure of the Ru complex investigated.	60
Scheme 18. Boranes used in these studies.	61
Scheme 19. Scheme for a <i>cis</i> Ru boryl complex which shows four different phosphorus environments.	63
Scheme 20. Reaction scheme for oxidative addition of HBpin to $RuH_2(dppe)_2$ to form the <i>cis</i> isomer $Ru(dppe)_2H(Bpin)$.	66
Scheme 21. Cis and trans isomers formed for reaction of $Ru(dppe)_2H_2$ with HBcat.	67
Scheme 22. Structure for the rhodium complex investigated.	69
Scheme 23. Photoactivity of the $CpRh(C_2H_4)_2$ complex in the presence of different substrates.	70
Scheme 24. Photochemical reaction of complex $CpRh(C_2H_4)_2$ in the presence of HBpin.	72
Scheme 25. Photochemical reaction of $CpRh(C_2H_4)_2$ and B_2pin_2 .	74
Scheme 26. Possible scheme for the regeneration of the starting complex $Ru(dppe)_2H_2$ upon reaction with C_6D_6 or HBpin.	77

CHAPTER FOUR

Scheme 1. General scheme for the metal assisted dehydrogenation of amine-borane.	84
Scheme 2. Proposed mechanisms for amine-borane dehydrogenation.	85
Scheme 3. Photochemical reaction of $CpRh(PR_3)$ complexes in the presence of HBpin and B_2pin_2 to give the oxidative addition products.	89
Scheme 4. Top: Structure of the $CpRh(PR_3)(C_2H_4)$ complexes investigated; Bottom: Structure of the amino-borane used in these studies.	89
Scheme 5. Photochemical reaction of complexes $CpRh(PR_3)(C_2H_4)$ in the presence of amino-borane to form the oxidative addition products.	94
Scheme 6. Proposed decomposition mechanism of the silicon containing rhodium complex leading to the formation of the Rh tris-silazane complex.	101

CHAPTER FIVE

Scheme 1. Structures of the Tp^*Rh complexes investigated.	107
--	-----

Scheme 2. C-H activation achieved in photochemical reactions of complex $\text{Tp}^{\text{R}}\text{Rh}(\text{CNneopentyl})(\eta^2\text{-PhN}=\text{C}=\text{N-neopentyl})$ with different aromatic and aliphatic hydrocarbons.	108
Scheme 3. Trend for Rh-C bond strengths for the activation of aliphatic, aromatic vinylic and allylic C-H bonds.	109
Scheme 4. Photochemical reaction of complex $\text{Tp}^{\text{R}}\text{Rh}(\text{CNneopentyl})(\eta^2\text{-PhN}=\text{C}=\text{N-neopentyl})$ in the presence of chloroalkanes.	109
Scheme 5. Migration from a secondary σ -alkane complex to a primary one to favor the activation of primary C-H bonds in chloroalkanes.	110
Scheme 6. Top: Partially fluoroarenes investigated. Bottom: Reactions of complex $\text{Tp}^{\text{R}}\text{Rh}(\text{CNneopentyl})(\eta^2\text{-PhN}=\text{C}=\text{N-neopentyl})$ in the presence of partially fluorinated arenes.	111
Scheme 7. Trend for reductive elimination of C_6H_6 between different $\text{Tp}^{\text{R}}\text{Rh}$ complexes and comparison with the Cp^* previously observed.	112
Scheme 8. Photochemical reaction of complex $\text{Tp}^{\text{R}}\text{Rh}(\text{PMe}_3)_2\text{H}_2$ in neat fluoroarenes to form the $\text{Tp}^{\text{R}}\text{Rh}(\text{PMe}_3)(\text{Ar}^{\text{F}})(\text{H})$ products.	112
Scheme 9. Activation of C-H and C-CN bonds in reaction of complex $\text{Tp}^{\text{R}}\text{Rh}(\text{PMe}_3)\text{Ar}^{\text{F}}\text{H}$ with CH_3CN .	113
Scheme 10. Structures of the substrates investigated.	114
CHAPTER SIX	
Scheme 1. Reactions of $\text{Ru}(\text{drpe})_2$ complexes with different quenching ligands.	156
Scheme 2. Scheme for reaction of $\text{Fe}(\text{dmpe})_2\text{H}_2$ in the presence of different substrates. Inset: different geometries adopted by the Ru and Fe transients.	157
Scheme 3. Reaction scheme for RuH_2 complexes with tetradentate phosphines.	158
Scheme 4. Reaction scheme for laser flash photolysis of $\text{Os}(\text{PP}_3)_2\text{H}_2$ complexes in the presence of different ligands.	159
Scheme 5. Photochemistry of ruthenium carbonyl hydride.	160
Scheme 6. Different phosphines used for the $\text{Ru}(\text{PP})_2\text{H}_2$ complexes investigated.	163
Scheme 7. Scheme for reactions of Ru1H_2 and Ru2H_2 in the presence of different quenching ligands.	164
Scheme 8. Photodissociation of H_2 and regeneration of the starting material upon laser flash photolysis.	167

Scheme 9. Structure of the phosphine used for Ru ₃ H ₂ complex.	171
Scheme 10. Schematic representation of the LFP apparatus.	181

APPENDIX TO CHAPTER SEVEN

Scheme 1. Schematic representation of the use of the Fourier Transform in crystal structure determination. The two pictures are not related to each other.	204
--	-----

Table of tables

CHAPTER TWO

Table 1. Selected bond lengths and angles for complex 3.	25
Table 2. Selected bond lengths and angles for complex 4.	30
Table 3. Crystallographic data and refinement data for complex 2 and 4.	30
Table 4. NMR data in C ₆ D ₆ for Precursor and Photoproducts (δ (J/Hz)).	32

CHAPTER THREE

Table 1. Chemical shifts δ (ppm) and coupling constants J (Hz) for complexes Ru(BPE) ₂ H(Bpin), Ru(DuPhos) ₂ H(Bpin) and Ru(dppe) ₂ H(Bpin).	75
--	----

CHAPTER FOUR

Table 1. Selected NMR data in C ₆ D ₆ for Precursor and Photoproducts (δ (J/Hz)).	93
Table 2. Crystallographic data and refinement data for the rhodium tris-silazane complex.	99
Table 3. Selected bond lengths and angles.	100

CHAPTER FIVE

Table 1. Refinement data for complex Tp`Rh(FHF)(C ₅ NF ₄)(PMe ₃).	120
Table 2. Selected bond lengths and angles for complex Tp`Rh(FHF)(2-C ₅ NF ₄)(PMe ₃).	121
Table 3. Selected torsional angles.	122
Table 4. Refinement and crystallographic data for complex Tp`RhH(Bpin)(PMe ₃).	126
Table 5. Selected bond length and angles for complex Tp`RhH(Bpin)(PMe ₃).	127
Table 6. Selected bond lengths and angles for complex Tp`RhH(Et ₂ SiH)(PMe ₃).	129
Table 7. Refinement and crystallographic parameters for complex Tp`RhH(Et ₂ SiH)(PMe ₃).	131
Table 8. NMR Spectroscopic Data (solvent C ₆ D ₆ , δ , (J/Hz)) for Products of Photoreaction of Tp`Rh(PMe ₃)H ₂ with Silanes.	132
Table 9. NMR Spectroscopic Data (solvent C ₆ D ₆ , δ , (J/Hz)) for Products of Photoreaction of Tp`Rh(CNneopentyl)(η^2 -PhN=C=N-neopentyl) with Silanes.	138

Table 10. Results of competition Reactions, measured by integration of $^{31}\text{P}\{^1\text{H}\}$ resonance. All measurements after 120 min irradiation. 138

Table 11. Rate constants for reactions of complex $\text{Tp}^-\text{Rh}(\text{PMe}_3)\text{H}_2$ in the presence of C_6H_6 , PhSiH_3 , HBpin , $\text{C}_5\text{F}_5\text{N}$ deduced from competition reactions. 144

CHAPTER SIX

Table 1. Pseudo-first-order rate constants for reaction of transient species at 295 K in cyclohexane with different quenching ligands. 167

Table 2. Second-order rate constants and kinetic isotope effects for reaction of transient species at 295 K in cyclohexane 170

Table 3. Pseudo-first-order rate constants for reaction of transient species $\text{Ru}(\text{dppe})_2$ at 295 K in cyclohexane with HBpin . 173

Table 4. Second order rate constants, $k_2 \text{ dm}^3 \text{ mol}^{-1} \text{ s}^{-1}$, for reaction of RuH_2 complexes with HBpin and H_2 . 178

CHAPTER SEVEN

Table 1. Crystallographic data for complexes 1 and 2. 184

Table 2. Selected Bond Lengths (\AA) and Angles (deg) for complexes 1 and 2. 186

Table 3 Crystallographic data for complexes 3 and 4. 187

Table 4. Selected bond lengths (\AA) for complexes 3 and 4 and comparison with the $[\text{Ru}(\text{DuPHOS})_2(\text{H}_2)\text{H}]^+$ complex, X, previously reported. 190

Table 5. Crystallographic data for complexes 5, 6 and 7. 192

Table 6. Selected Bond Lengths (\AA) and Angles (deg) for complexes 5, 6 and 7. 193

APPENDIX to chapter seven

Table 1. Crystal systems with point group symmetry restrictions and cell-dimensions restrictions. 200

Acknowledgements

A very special GRAZIE goes to my supervisor Robin Perutz for sharing with me his vast scientific knowledge, providing guidance and advice, for being always available throughout my studies and giving me the opportunity to carry out a PhD. His support and that of Sue are greatly appreciated.

A “cheers mate” to my special mates Marius and Jake. To Marius, for teaching me all what I`m capable to do in the lab and for sharing his secrets of “crystal fingers”. To Jake for being always ready with advice and especially for showing me how important is to communicate the science we do. But overall, cheers mates to have been two special friends, before and now.

A major thanks to Naser who taught me the way through the lab and most importantly for continuous helpful and kind attitude in and out of work.

Thanks to all the RNP group members, previous and present ones, Chris, Ruqia, Torsten, Olga, Alvaro, Dan, Magnus, Vargini, Jessica and Sarah for making my time at work very enjoyable with unforgettable memories.

A particular thank goes to Dan for proof reading this thesis and dealing with Italian mistakes, and to Alvaro for his continuous help with format and computer issues during the writing. Thanks also to Sharifa who shared with me the “writing up time” with many weekends at work.

Thanks to Adrian, Rob and Sam for teaching and helping me with crystallography, to Laurence for his assistance with the LFP apparatus, to Heather for help with NMR, to Karl for help with mass spec and to the entire workshop staff (Ryan, Chris and Chris) for making real any abstract idea of glassware, mechanical and electrical equipment we had.

A huge thank you to all the people I've met out of work and I've spent my spare time with. Everyone contributed to make my time in York very special. Between them a particular thank goes to Brigid, Piero, Lorenzo, Alejandro and Ali for being indispensable friends.

Per concludere, il piu` grande grazie va alla mia famiglia. Ai miei genitori Giuliano ed Emma, per essere stati un grande esempio di vita ed avermi trasmesso l'importanza di sognare ed impegnarsi duramente per realizzare i propri sogni. A mia sorella Michela e mio fratello Marco per esserci sempre; i soli capaci di farmi tornare il sorriso in ogni situazione. Al mio unico e vero amico Fabio, per "volare qui" a farsi una chiacchierata ogni volta che ce n'è bisogno. Questa bellissima esperienza non sarebbe stata possibile senza di voi. Grazie!

Author's declaration

I hereby declare that this submission is my own work and that, to the best of my knowledge and belief, it contains no material previously published or written by another person nor material which to a substantial extent has been accepted for the award of any other degree or diploma of the university or other institute of higher learning, except where due acknowledgment has been made in the text.

1 Introduction

1.1 Photochemical reactivity

The photochemistry of rhodium and ruthenium complexes in the presence of substrates containing C-H, C-F, B-H, B-B and Si-H bonds is described in this thesis. In addition to steady state studies, time-resolved experiments were performed for a novel class of ruthenium phosphine complexes. The aim of this introduction is to explain the photochemical process for such transition metal complexes and give an overview on the photochemistry of cyclopentadienyl rhodium and ruthenium dihydride compounds. When a photochemical reaction takes place, an electron is promoted from the ground state to the excited state causing a rearrangement in electronic distribution and a change in the reactivity of the species.

Photochemistry in organometallic chemistry is used to activate a metal centre and gain reactivity creating an excited state with a vacant site. However, the greatest advantage of the use of light in catalytic reactions by comparison with those which proceed thermally arises from the possibility of monitoring the reaction at low temperature in order to observe intermediates and have a deeper understanding of the reaction dynamics. Furthermore the use of photochemistry can lead to chemical processes which are not observed under thermal conditions.

Excited states have a very short life-time (microseconds to femtoseconds) and they can be classified on the basis of the electronic properties, reactivity and orbital parentage. Different excited states can arise from a photoreaction of an organometallic compound such as ligand-field, charge-transfer (MLCT or LMCT) and intra-ligand excited states.¹ The unsaturated species formed under photochemical conditions will be strongly reactive and therefore prone to substitution reactions with substrates.

Common photoactive ligands encountered in organometallic photochemistry are CO,² H₂,³ and C₂H₄,⁴ but examples of uncommon photolabile ligands have also been reported. Reaction of LCr(CO)₅, for instance, where L = PR₃, NR₃ shows L to be extruded in preference of the CO ligand depending on the choice of

wavelength.^{5,6} The loss of phosphine in $\text{ReH}_5(\text{PR}_3)_3$ competes with H_2 reductive elimination upon changing the wavelength of irradiation (Scheme 1).⁷ Finally, competing loss of ligands was also observed for the $\text{Ru}(\text{PPh}_3)_2(\text{IEt}_2\text{Me}_2)(\text{CO})\text{H}_2$ complex which can extrude PPh_3 or H_2 through an isomerization process.⁸



Scheme 1. Preference in photo-dissociation of phosphine instead of dihydrogen.

The choice of the wavelength is therefore important, different σ^* orbitals can be populated depending on λ and cause the dissociation of different ligands. More importantly, when low-lying MLCT absorption is exhibited, equilibrated excited states are formed on irradiation into this transition; their population from higher level orbitals may prevent the expulsion of ligands as in $\text{Re}(\text{CO})_3(\text{bpy})\text{X}$. However commonly, the photochemical process takes place by *prompt* photodissociation, where no equilibrated excited states are formed. The labile ligand is therefore “kicked off” on a femtosecond timescale and therefore the excited state formed has no time to relax back.

The photochemistry carried on in this thesis involves mostly ligand field excited states arisen from photolabilization at Rh and Ru centres having C_2H_4 and H_2 as photoactive ligands respectively. Therefore a brief explanation of the photo-physics for ligand field excited states will be given.

It is also important to mention that the analysis of the UV-vis spectrum of these species is not very helpful showing few broad bands and no clear maxima at all, likewise the spectra of the photoproducts. As a consequence, the determination of a quantum yield of reaction is not straightforward.

1.2 Ligand Field excited states (LF)

Labilization of a ligand is achieved in LF excited states; this will cause an increase in metal-ligand repulsion and possibly will lead to ligand-dissociation. The electronic transition which generates LF excited states directly is a $d-d$ transition. The promotion of an electron into the M-L σ^* orbital (antibonding

character) from a π -bonding orbital will considerably weaken the M-L bond (Figure 1). Considering the antibonding nature of the e_g orbitals in octahedral complexes, an electron placed in a e_g orbital, which is directed from the metal towards the ligand, will increase metal-ligand repulsion leading to the ligand dissociation. At the same time, the free t_{2g} orbital (with bonding character for octahedral complexes), available for new bond formation at the metal centre will allow the entrance of a new reactive species. LF excited states may also be formed indirectly as recently demonstrated in metal-carbonyl chemistry.²

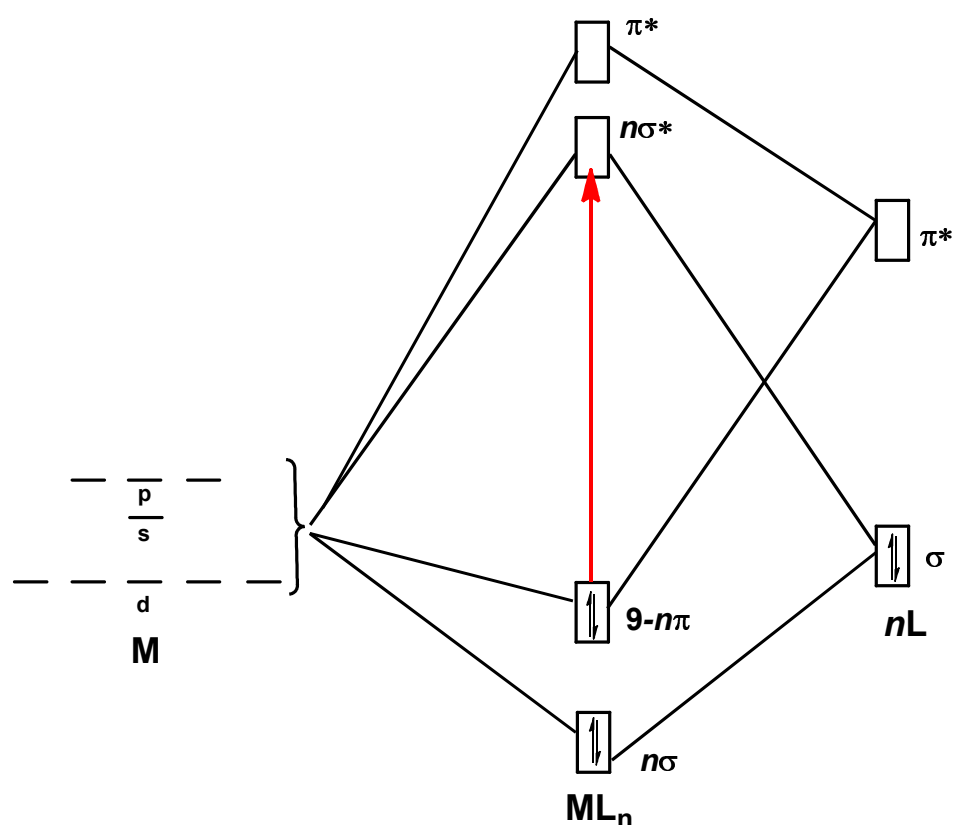
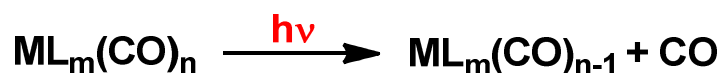


Figure 1. Simplified molecular orbital diagram for the interaction of a metal centre with n ligands showing a $d-d$ transition (LF).

The photochemistry of metal-carbonyls was the classic example given for ligand – field excited states (Scheme 2). The topic has been recently reviewed.² DFT calculations with Cr as the metal centre showed that metal to CO charge transfer (MLCT-CO) excited states can also play a role in the photo-dissociation

of a metal-CO bond.⁹ Extensive electron delocalization and state mixing make the choice of one excited state instead of the other not definitive in metal carbonyl chemistry. However, the initial population of the MLCT(CO) state and its smooth conversion to the dissociative $d \rightarrow d$ excited state has been proposed where the MLCT(CO) state acquires $d \rightarrow d$ character upon passing through the avoided crossing region and finally dissociate the M-CO bond through an indirectly formed LF excited state.



Scheme 2. Photodissociation of a CO from a metal-carbonyl.

Metal – dihydrides also photo-dissociate H_2 as a result of an electron promoted into the σ^* orbital of the MH_2 system.¹⁰ This will lead to an excited electronic state where the populated molecular orbital has H-H bonding character but is M-H antibonding (Figure 2).¹¹ The fragment generated is usually unstable and can undergo oxidative addition in the presence of substrates.

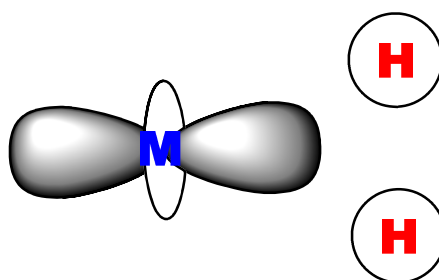


Figure 2. Overlap diagram showing σ_g^* molecular orbital populated in the excited state which is M-H antibonding and H-H bonding.

Ligand field excitation leads also to dissociation of π -coordinated species; the η^6 -arene ligand of the $[\text{CpFe}(\eta^6\text{-arene})^+]\text{X}^-$ complex was found to flip to an η^4 -coordination upon irradiation. One bond was labilized upon light absorption making a coordination site on the metal centre available. The presence of a

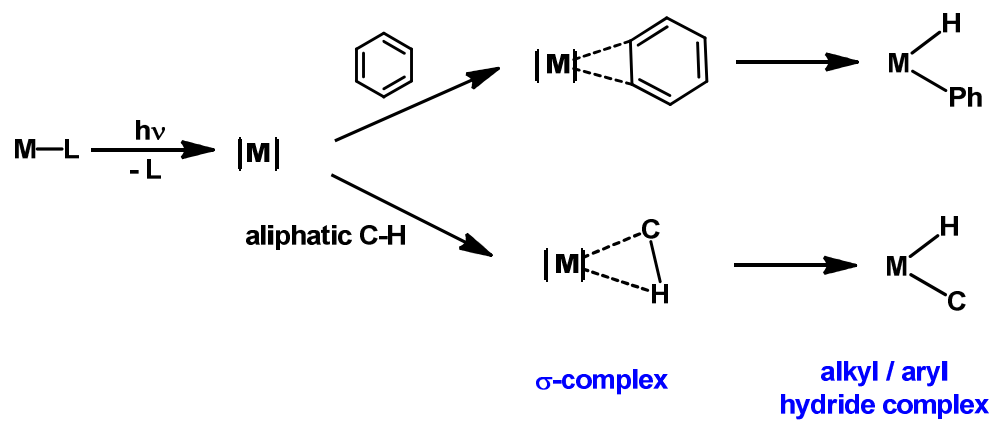
nucleophile in the reaction mixture led to the cleavage of the other arene and formation of the ligand-exchange product.¹²

1.3 Photochemistry of half-sandwich Rh compounds: C-H, Si-H, B-H and C-F activation and their coordination modes

Photochemical reactions of half sandwich compounds which implies loss of a strongly bound ligand and generation of a 16-electron fragment has been widely investigated by Bergman,^{13,14} Graham,^{15,16} Jones¹⁷⁻²¹ and Perutz²² groups using Rh and Ir centres.

1.3.1 C-H activation

The photo-activity of the complexes $(\eta^5\text{-C}_5\text{R}_5)\text{ML}_2$, $(\eta^5\text{-C}_5\text{R}_5)\text{M}(\text{H})(\text{C}_6\text{H}_5)$ and $(\eta^5\text{-C}_5\text{R}_5)\text{ML}(\text{H}_2)$ where $\text{M} = \text{Ir}, \text{Rh}$; $\text{L} = \text{CO}, \text{PR}_3, \text{C}_2\text{H}_4$ and $\text{R} = \text{H}, \text{Me}$, have been deeply explored in the presence of different C-H-containing substrates. The 16-electron species $(\eta^5\text{-C}_5\text{R}_5)\text{ML}$, generated *in situ*, has been shown to undergo oxidative addition of aliphatic, aromatic and fluoro-aromatic C-H bonds to afford the corresponding alkyl/aryl hydride complexes. Formation of the η^2 -adduct has also been detected. Different methods have been used for the understanding of the reaction mechanism such as low temperature matrix isolation,²³⁻²⁶ laser flash photolysis,^{27,28} photochemistry of complexes dissolved in liquefied or supercritical noble gases^{29,30} and isotopic labelling.³¹

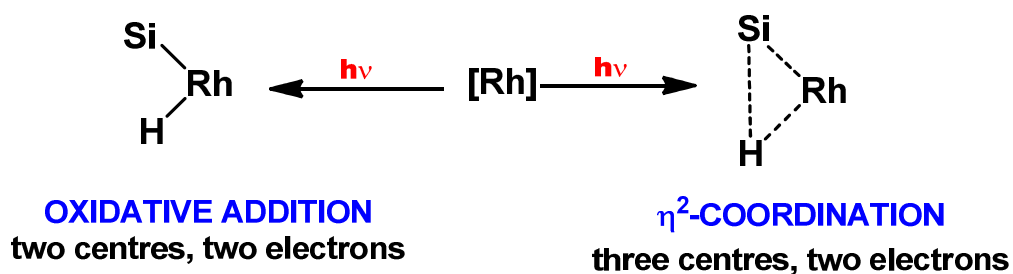


Scheme 3. C-H bond activation by a transition metal centre.

The relative stability of $M(\eta^2\text{-arene})$ and $M(\text{aryl})\text{H}$ depends on the metal and the other ligands; likewise for alkanes. While the observation of the metal-hydride complex is often easy, the detection of alkane/arene η^2 -species may be different because they show poor stability and require low temperature techniques to be detected. Nevertheless the participation of σ -complexes as intermediates in C-H oxidative addition reactions is nowadays well established (Scheme 3).^{19,32-39}

1.3.2 Si-H activation

The photochemistry of $(\eta^5\text{-C}_5\text{R}_5)\text{M}(\text{C}_2\text{H}_4)_2$ ($\text{M} = \text{Ir}, \text{Rh}; \text{R} = \text{H}, \text{Me}$) has also been investigated by Maitlis⁴⁰ and Perutz^{41,42} in the presence of silanes; silyl metal complexes are commonly used as reactants in the preparation of silicon containing compounds.^{43,44} $\text{CpRh}(\text{PR}_3)(\text{C}_2\text{H}_4)$ complexes ($\text{R} = \text{PPh}_3, \text{PMe}_3$) were found to be suitable precursors for Si-H bond activation too.⁴⁵ The mechanism has been found to proceed either through a direct oxidative addition to an unsaturated fragment or through a η^2 -intermediate.⁴⁶



Scheme 4. Possible coordination modes in Si-H activation by a Rh centre.

To distinguish the formation of a η^2 -complex from an oxidative addition product (Scheme 4) the analysis of coupling constants is very useful since they reflect the strength of the Si-H bond. The value of J_{SiH} is usually about 200 Hz for free silanes; a coupling between 20 and 100 Hz is expected when a σ -coordination takes place and a value of J_{SiH} smaller than 20 Hz for a complete oxidative addition. Crystal structure determination and bond length analysis also help to

discriminate one coordination mode from the other. More recently the field took advantage of the help of DFT calculations.⁴⁷ Nevertheless, the first example of a σ -silane complex goes back to the 1969; the authors describe the interaction between the silane and the metal in $\text{Ph}_2\text{SiH}_2\text{Re}(\text{CO})_8$ complex as a “three centre, two electron bond with the two electrons supplied by the original Si-H bond”.⁴⁸

1.3.3 B-H and B-B activation

The activation of B-H and B-B bonds has also been extensively investigated. The first report of photochemical reactions of metal complexes in the presence of boranes was published by Hartwig.^{49,50} He found that Cp_2WH_2 was able to activate B-B bonds in preference to C-H bonds of the C_6H_6 solvent. Following those results, the same group also succeeded in the photoactivation of B-H/B-B bonds using Fe^{51} and Re^{52} metal centres and discovered that borylation of alkanes was achieved by further photolysis of the metal-boryl complex.⁵³ Later, Rh was discovered as an excellent catalyst in alkane-borylation catalysed reactions, the complex $\text{CpRh}(\eta^4\text{-C}_6\text{Me}_6)$ reacted with HBpin to yield a mixture of two rhodium(V)boryl hydrides, $\text{CpRh}(\text{H})_2(\text{Bpin})_2$ and $\text{CpRh}(\text{H})(\text{Bpin})_3$. The catalytic product was the boryl functionalised alkane. DFT calculations suggested a partial B...H residual bond for those species suggesting formation a Rh(III) oxidation state instead of Rh(V).⁵⁴

The photochemical reaction of $\text{CpRh}(\text{PR}_3)(\text{C}_2\text{H}_4)$, ($\text{R} = \text{PPh}_3, \text{PMe}_3$) in the presence of HBpin and B_2pin_2 was reported by Perutz.⁴⁵ Products formed by oxidative addition reaction were characterised in solution, and a crystal structure of the $\text{CpRh}(\text{H})(\text{PPh}_3)(\text{HBpin})$ was obtained.

η^2 -Borane metal complexes have been experimentally isolated^{55,56} and proposed as intermediates in catalytic reactions by DFT calculations. The distinction between the two coordination modes is difficult just on the basis of NMR data, in this case even more difficult than silanes due to the quadrupolarity of boron which broadens the NMR resonances and make it impossible to measure coupling constants for σ -boranes complexes.

In order to understand the reactivity of boron-containing compounds it is fundamental to consider the presence of the empty p-orbital on the boron which contributes to the classical Chatt, Dewar and Duncanson bonding model (Figure 3). The empty p orbital allow back donation from the HOMO of the metal fragment to boron, whereas for other σ -complexes this occurs at the ligand σ^* orbital.

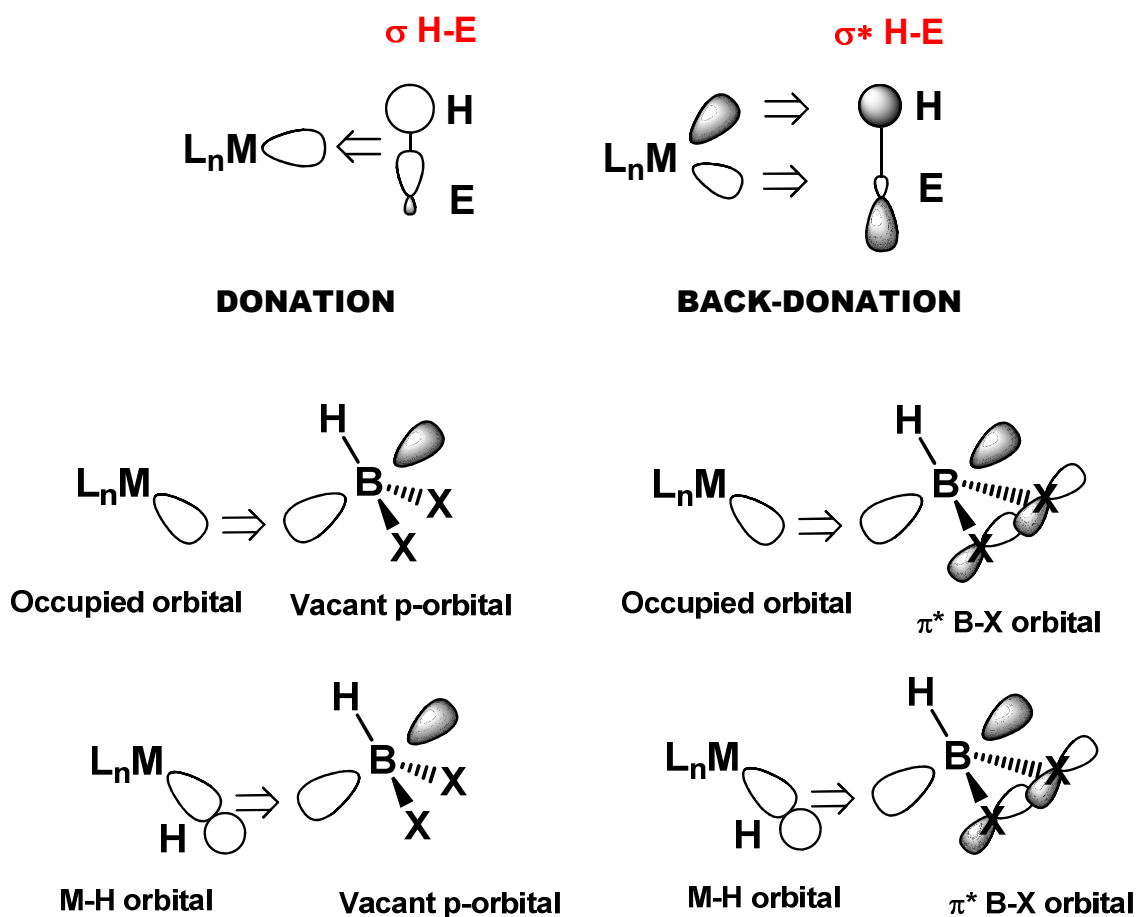


Figure 3. Top: Classical Chatt-Dewar-Duncanson bonding model. Bottom: Bonding scheme for boranes σ -coordination where the p orbital on boron contribute to the classical model. X = O, M = Ru, Rh.

The different substituents at the boron centre and the asymmetric character of the B-H bond compared to H-H can tune the binding mode. Distinction between σ -borane metal complexes with or without agostic interaction should also be

mentioned. In the first case the B-H moiety is coordinated in a three centre two electron fashion with no additional intramolecular binding. When an agostic interaction is present an additional contact arises intramolecularly between the metal and the coordinated ligand (Figure 4).⁵⁷ Finally, when back donation is predominant a complete oxidative addition is achieved and a metal-boryl hydride is formed.

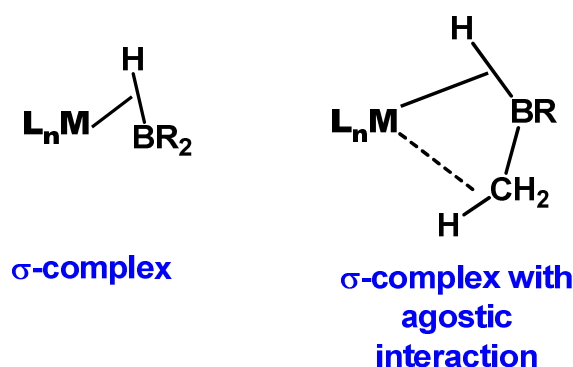


Figure 4. Two possible coordination modes of a borane to a metal complex.

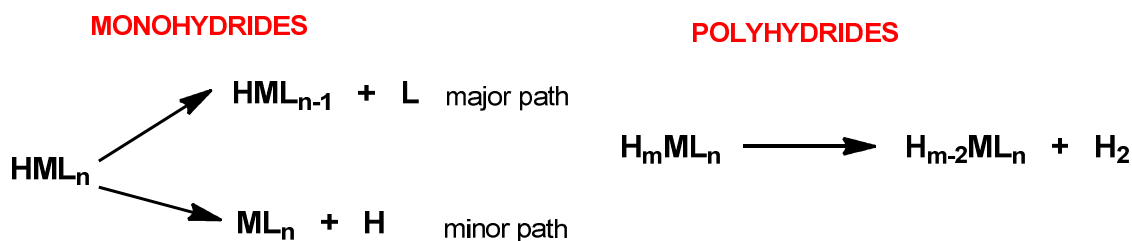
1.3.4 C-F activation

Cyclopentadienyl rhodium compounds have been employed for thermal and photochemical C–F bond cleavage reactions of aromatics in solution, and oxidative addition steps have also been investigated in matrix isolation studies at low temperature. Those types of complexes are good tools for C-F activation.⁵⁸ Perutz et al. found that photochemical reaction of $\text{CpRh}(\text{PMe}_3)(\text{C}_2\text{H}_4)$ complex in the presence of C_6F_6 led to the formation of the η^2 -complex $\text{CpRh}(\eta^2\text{-C}_6\text{F}_6)(\text{PMe}_3)$;³³ oxidative cleavage of the C-F bond was obtained replacing the Cp ligand with the Cp^* .^{59,60} The topic will be introduced more in details in Chapter two. Generally a preference for C-H activation is shown by these type of complexes.⁶¹ However if employed avoiding C-H sources they can act as excellent activators of a large variety of bonds.

1.4 Photochemistry of Ru(PP)₂ dihydride complexes

The photochemistry of metal hydrides is shown in Scheme 5. Complexes containing *cis* hydrides reductively eliminate molecular hydrogen leading to highly reactive 16 electron intermediates.¹¹ A reduction in oxidation state of two is achieved. While the photochemistry of *cis* dihydrides has been extensively explored, very few polyhydrides have been investigated photochemically.

Prompt photodissociation of dihydrogen was experimentally observed and proposed to take place for the formation of the coordinatively unsaturated fragment Ru(dmpe)₂ which was found to be completed within the instrumental rise time of *ca.* 16 ps by UV/Vis ultrafast (ps) spectroscopy of Ru(dmpe)₂H₂ under an atmosphere of H₂.⁶² Subsequent studies on Ru(depe)₂H₂ indicated that transient Ru(depe)₂ was formed within *ca.* 1 ps.⁶³



Scheme 5. The photochemistry of metal hydride complexes.

The photochemistry of group eight metal dihydrides of the type M(PP)₂H₂ (M = Ru, Os, Fe; PP = dmpe, depe, dppe) complexes has been extensively explored by Perutz.^{62,64-68} Their reactions in the presence of substrates such as silanes and H₂ led to the oxidative addition products to form the M(PP₂)H(SiR_mH_{n-m}) and to regenerate the starting material respectively. The photochemical activity of those complexes towards C-H activation was found to be poor due to the rapid recombination with H₂. An improvement in the reactivity for aromatic and aliphatic C-H bonds was achieved using a tridentate phosphine instead of a bidentate in reactions of the Os(PP₃)H₂ complex where PP₃ = P(CH₂CH₂PPh₂)₃.⁶⁹ Reactivity for CO, and C₂H₄ has been achieved by steady state photolysis and rate constants for these reactions established. B-H

activation has been achieved mainly for reactions of $\text{Ru}(\text{PP})_2\text{H}_2$ in the presence of HBpin.^{3,70} η^2 - Coordination species for this kind of complexes have not been observed. A more detailed explanation will follow in chapters three and six.

1.5 Time resolved methods and detection of transients

Time resolved methods are among the most used for experimental characterization of reaction intermediates. The rapid development in laser technology, digital electronics and fast detection systems gave access to methods of monitoring very short-lived reaction intermediates allowing their detection down to the nano, pico, femto second time domain. The spectral evolution followed at very short time intervals can be achieved by laser flash photolysis⁷¹ (LFP). In this way, a very short pulse of high intensity radiation (laser or flash lamp) initiates the reaction which is then followed by monitoring the changes in absorption or emission. The intermediate generated by the rapid photoexcitation is formed in acceptable yield to be detected by UV/vis or IR spectroscopy.

Spectral and kinetic information are obtained by the use of time resolved methods. A point-by-point spectrum can be built by looking at different frequencies at one moment in time while a transient decay can be obtained at one wavelength. Laser flash photolysis has been used in these studies to obtain information about reactive intermediates formed after flash photolysis of complexes *cis*- $[\text{Ru}((R,R)\text{-Me-BPE})_2(\text{H})_2]$ and *cis*- $[\text{Ru}((R,R)\text{-Me-DuPHOS})_2(\text{H})_2]$.³

1.6 Outline of the thesis

An outline of the thesis is provided below. A more detailed introduction is provided in each chapter.

Chapter two. The photochemical reactions of complex $\text{CpRh}(\text{PMe}_3)(\text{C}_2\text{H}_4)$ in the presence of pentafluoropyridine, 2,3,5,6 tetrafluoropyridine and 4-substituted analogues are explored. The mechanism for reactions with the 4-functionalised tetrafluoropyridines assessed by NMR spectroscopy, KIE and DFT calculations. Reaction products are fully characterised by multinuclear NMR spectroscopy, mass spectrometry and X-ray crystallography.

Chapter three. The photochemical reaction of the bidentate-phosphine ruthenium complex $\text{Ru}(\text{dppe})_2\text{H}_2$ in the presence of borolanes HBpin and HBcat is investigated by NMR spectroscopy. The nature of the products is discussed by comparison with previously isolated ruthenium-boryl complexes. On the same lines, the photoreactivity of $\text{CpRh}(\text{C}_2\text{H}_4)_2$ in the presence of HBpin and B_2pin_2 is tested in hexane as solvent in order to detect reaction intermediates. The catalytic ability towards borylation of heptane for the system is also determined by GC-MS method.

Chapter four. The photo-reactivity of $\text{CpRh}(\text{PR}_3)(\text{C}_2\text{H}_4)$ complexes ($\text{R} = \text{PMe}_3, \text{PPh}_3, \text{PMePh}_2$) towards the aminoborane $\text{H}_2\text{BN}(\text{iPr})_2$ is investigated by NMR spectroscopy and X-ray crystallography. The photochemical reaction of $[\text{CpRh}(\text{C}_2\text{H}_4)_2]$ in the presence of a silazane is also studied by NMR spectroscopy.

Chapter five. The photochemistry of $\text{Tp}^*\text{Rh}(\text{PMe}_3)\text{H}_2$ and $\text{Tp}^*\text{Rh}(\text{CNneopentyl})(\eta^2\text{-PhN=C=N-neopentyl})$ is investigated in the presence of $\text{C}_5\text{F}_5\text{N}$, HBpin, primary, secondary and tertiary silanes. The reactions are followed by NMR spectroscopy; photoproducts are isolated and fully characterized. Competition reactions are carried out and kinetic selectivity determined.

Chapter six. Laser flash photolysis of three ruthenium complexes with bidentate chiral phosphines is performed in the presence of different quenching ligands. The spectral information is analyzed as well as kinetic rate constants.

LFP is also performed on a ruthenium complex with a bidentate non chiral-phosphine. The results are discussed in comparison to data previously observed.

Chapter seven. Crystallographic analyses of different ruthenium and rhenium complexes are given.

1.7 Aim of the project

The project was designed to probe comparisons between different substrates in oxidative addition reaction and especially to discover more about B-H and B-B oxidative addition. The main strands of the project were:

- Competition between C-H and C-F activation.
- Target the selectivity for C-H bonds relative to B-B, B-H or Si-H bonds comparing different metals and ancillary ligands.
- Measure the rates of B-B and B-H oxidative addition reactions by laser flash photolysis.
- Search for reaction intermediates.
- Determine the rates and activation energies for their conversion to products.
- Investigate the reaction via theoretical calculations in collaboration with Prof. Eisenstein.
- Investigate precursors that are sensitive to visible light.

2. Photochemical cyclometallation via HF elimination: synthesis and mechanism

2.1. Introduction

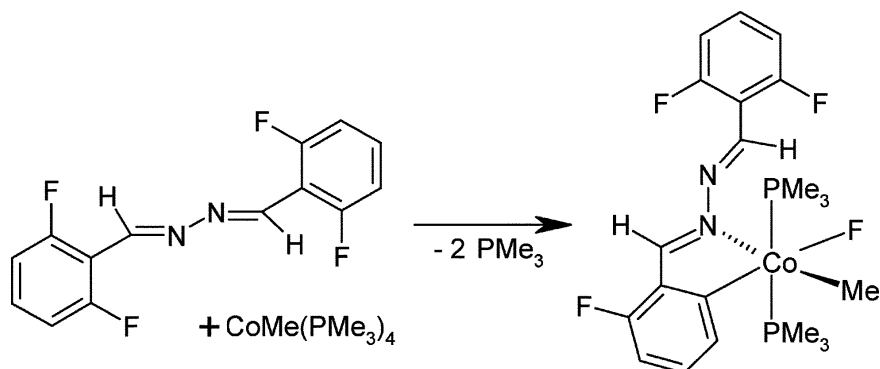
The activation of strong carbon-fluorine bonds is a great challenge in organometallic chemistry. Many reviews have been published looking at different aspects of the topic.¹⁻³ Nevertheless, not many examples of cyclometallation via C-F activation have been reported.

Albrecht reviewed cyclometallation reactions using d-block transition metals showing metallacycles have been successfully applied in organic transformations, catalysis and in various other domains of materials science.⁴ Since then, many other papers have been published presenting characterisations of new metallacycles,^{5,6} applications in hydrodefluorination catalysis,⁷ oxygen sensing⁸ and transfer hydrogenation.⁹

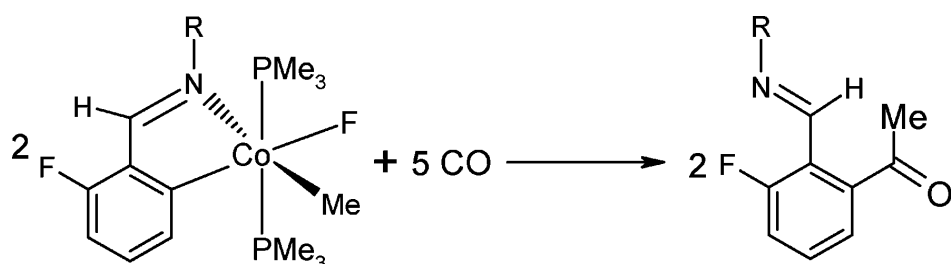
The reactivity of rhodacycles and iridacycles, for instance, has been described by the work of Jones and Li, where a wide range of metallacycles is involved in insertion reactions with different unsaturated ligands.¹⁰ Palladacycles have been investigated in reactions with phosphines to form new Pd complexes,¹¹ and cycloplatinated complexes have showed great photophysical properties opening themselves to a wide set of applications as light emitting devices or luminescent molecular sensors.¹²⁻¹⁴ A search into the literature highlighted few papers with metallacycles formed by C-F activation. Most of them proceed by intramolecular C-F oxidative addition favoured by the presence of a chelating ligand. The ligands coordinate firstly through the hetero atom (N or S) to the metal centre and the C-F bond is then oxidatively added. A metal fluoride is detected in all the following examples, either as final product or as intermediate in the catalytic cycle. No formation of HF has been detected or mentioned as side product in any of these publications.

C-F activations to form a metallacycle have been achieved thermally using a Co(I) centre with an aldazine-N atom as an anchoring group to afford an ortho-chelated cobalt(III) complex containing a [C-Co-F] fragment (Scheme 1). Intramolecular C-F activation precedes cyclometallation and it is favoured by the chelating effect of the imine ligand. No cyclometallation or C-F

activation were in fact observed using π -coordinated cobalt(0) compounds.¹⁵ Following their previous work, Li and coworkers looked at the reaction also from the catalytic side; they reported later that new organic fluorides are formed by carbonylation reactions of cobaltacycles (Scheme 2).¹⁶

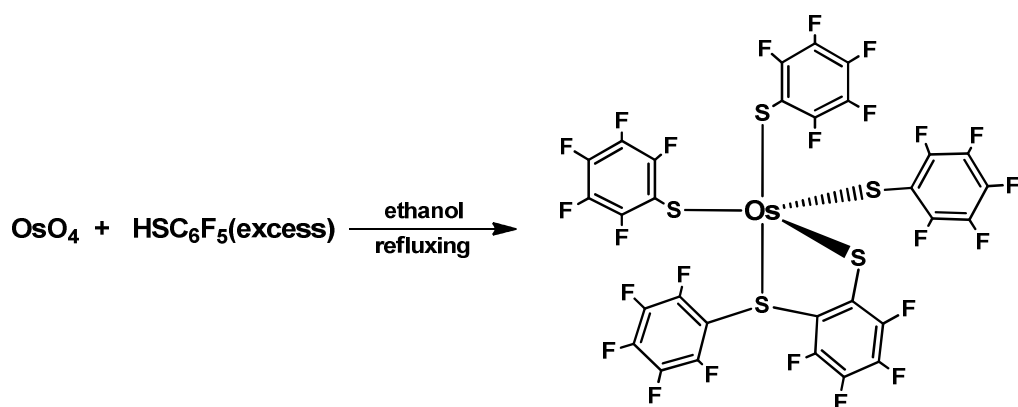


Scheme 1. Formation of a cobaltacycle from C-F activation of an aldazine.



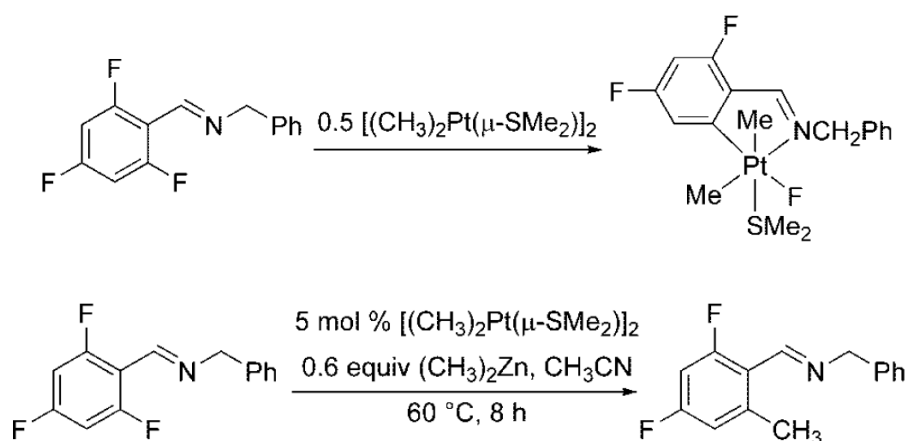
Scheme 2. Carbonylation of the cobaltacycle to give the organic product.

The second example presents the reaction of OsO_4 in the presence of HSR ($\text{R} = \text{C}_6\text{F}_5, \text{C}_6\text{F}_4\text{H}$) to afford different metallacycles through a process involving sulfur coordination in the first step and rupture of one or two ortho C-F bonds. Five coordinate Os complexes have been crystallographically characterised and shown to have trigonal-bipyramidal geometry (Scheme 3).¹⁷



Scheme 3. Five coordinate Os metallacycle formed by C-F activation of thiofluoroarenes.

Love *et al.* have also shown the activation of a C-F bond in ortho position to an imine substituent of polyfluorinated arenes catalyzed by Pt. The reaction proceeds through the formation of a cyclometalated Pt complex subsequent to ortho C-F activation. Reaction of the Pt-F complex with $\text{Zn}(\text{CH}_3)_2$ leads to the methylation of the polyfluorinated aryl imine ligand. The mechanism proposed involves transmetalation and reductive elimination steps to give the C-C coupling product (Scheme 4).¹⁸

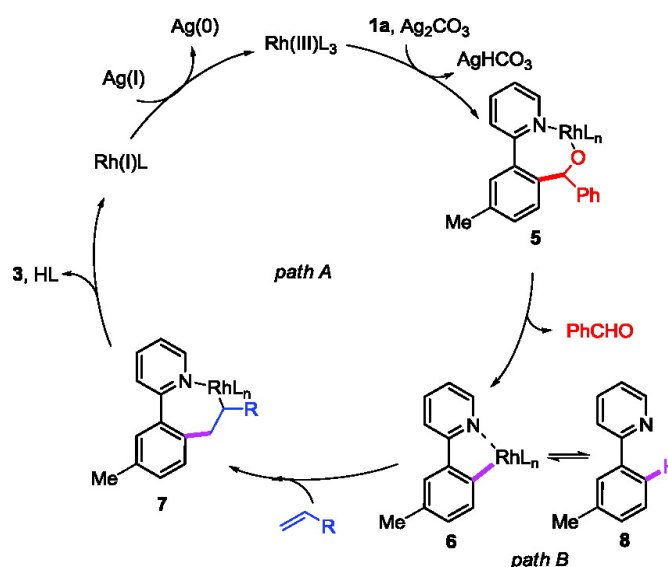


Scheme 4. Top: Formation of the platinacycle after C-F activation of an imine-substituted fluoroarene. Bottom: Catalytic methylation of polyfluorinated imines by a Pt complex.

The understanding of a cyclometallation mechanism is not always trivial. Despite this, many cyclometallation reactions involving C-H activation have been proved to undergo base-assisted mechanism, where the ligand plays

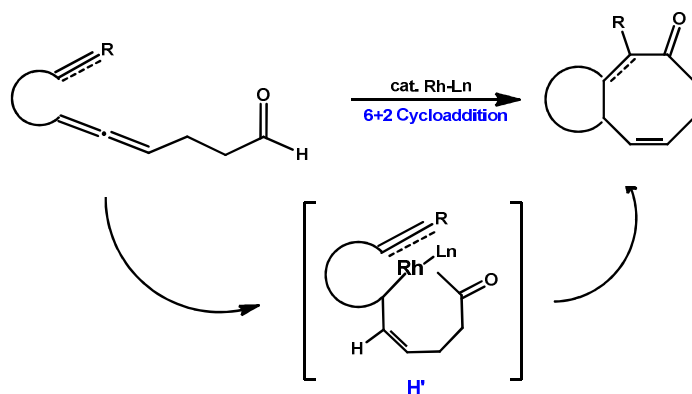
an important role.¹⁹⁻²¹ The solvent has been shown to play a part in the determination of the transition state.^{22,23}

Many examples of rhodacycles are found in the literature, mostly as intermediates in catalytic reactions to form functionalised organic compounds. C-H activation of heterocycles previously coordinated to the metal centre *via* the heteroatom seems to be the preferred route in order to achieve cyclometallation. A five-membered rhodacycle, for instance, has been recently reported and spectroscopically characterised, as intermediate in pyridinidyl directed alkenylation of secondary alcohols with olefins using a Rh(III) catalyst (Scheme 5).²⁴



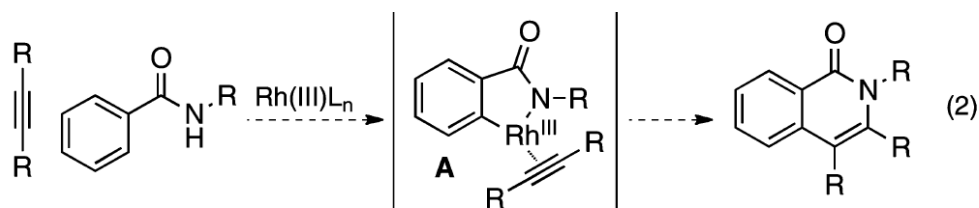
Scheme 5. Catalytic cycle for pyridinidyl directed alkenylation of alcohols. A five membered rhodacycle is intermediate in the cycle. $RhL_n = [Cp^*RhCl_2]_2$.

The first example of an eight-membered oxo-rhodacycle has been proposed as intermediate in cycloaddition reactions of $[Rh(IMes)(cod)]ClO_4$ and different allenal to obtain bicyclic ketones derivatives. The cyclometalation step to form the oxo-rhodacycle H^+ (Scheme 6) is followed by the insertion of the metal centre into the multiple bond. Reductive elimination of the organic bicyclic product regenerates the catalyst to start the loop over.²⁵



Scheme 6. Eight membered oxo-rhodacycle found to be an intermediate in cycloaddition reactions, $\text{L}_n = (\text{IMes})(\text{COD})$.

Finally, a five membered ring rhodacycle, formed by C-H/N-H activation has been proposed as intermediate in the Rh-catalysed oxidative cycloaddition of benzamides and alkynes to give isoquinolones (Scheme 7). The free coordination site at the metal is available for reaction with the unsaturated compound; the product is then formed by reductive elimination. The catalyst Rh(III)L_n is also regenerated.²⁶



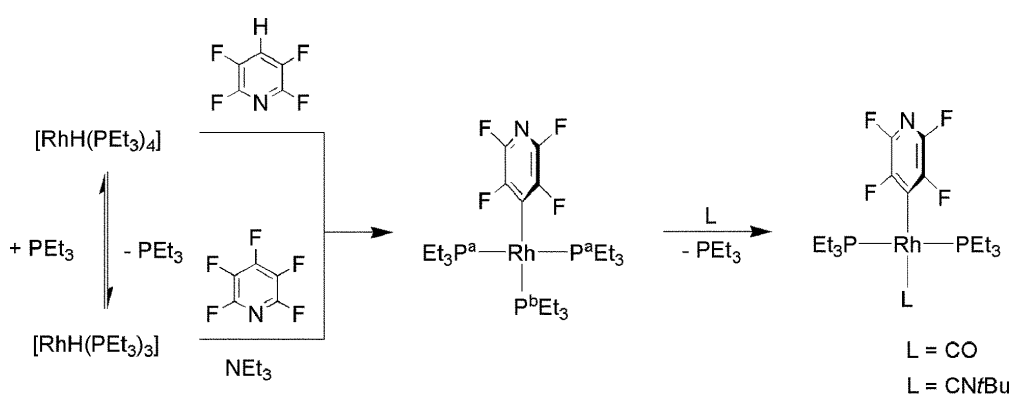
Scheme 7. Rh-catalysed cyclo-addition reaction. $\text{RhL}_n = [\text{Cp}^*\text{RhCl}_2]_2$

Rhodium is certainly a widely used metal for C-F activation reactions; the topic has been recently reviewed by Braun *et al.*²⁷ Particularly, phosphine-rhodium complexes show great capability in C-F activation; here some of the recent examples are cited.

Yamaguchi and co-workers published a cross-coupling reaction of polyfluoroarenes and disulfides catalysed by a $\text{RhH}(\text{PPh}_3)_4$ complex to obtain preferentially para-difluorobenzene with thiolate groups at the 2,3,5 and 6 positions.²⁸ Braun *et al.* found that $\text{RhH}(\text{PEt}_3)_3$ is capable of stoichiometric C-F activation by nucleophilic attack in 4-position of pentafluoropyridine to form a rhodium tetrafluoropyridyl complex. The latter

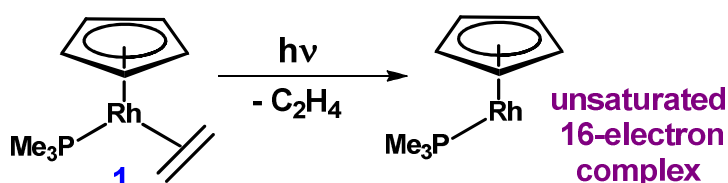
can then undergo oxidative addition with different oxidizing agents such as methyl iodide or carbon monoxide to form an unstable complex that further reacts thermally in solution either with CH_3I or CO , giving 4-functionalised tetrafluoropyridine (Scheme 8).²⁹

More recently, they also prepared the first 16-electron Rh(I)-boryl complex, which is capable of *ortho* C-F activation of pentafluoropyridine. DFT calculations on the same system suggested a boryl-assisted mechanism and showed that the regioselectivity derives from a nitrogen participation in the relevant transition state.³⁰



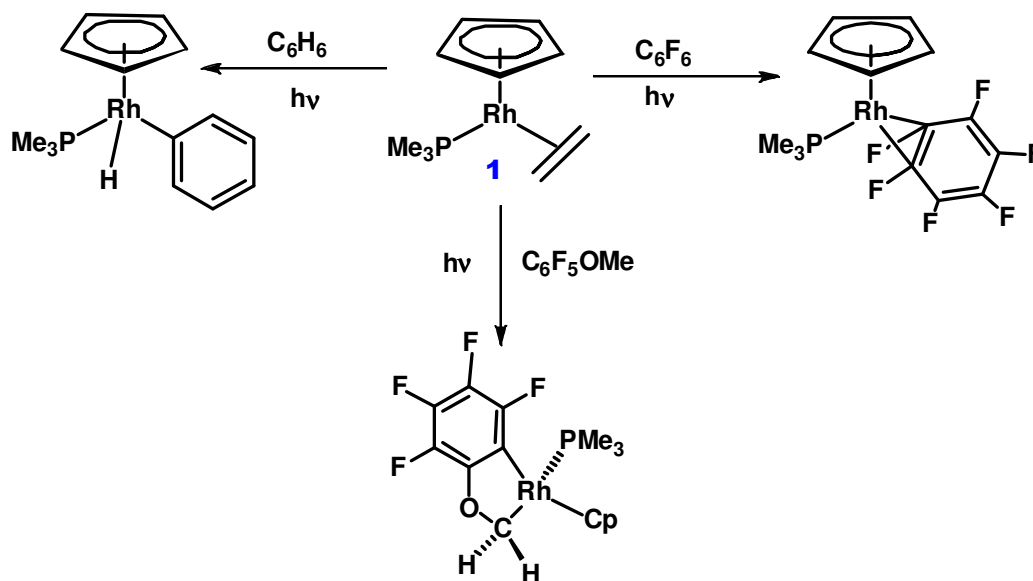
Scheme 8. Para C-F activation of $\text{C}_5\text{F}_5\text{N}$ by a rhodium-hydride complex.

The work carried out in our group in the past few years has also contributed to the field. The photochemistry of **1** was extensively explored at room temperature. Upon photolysis loss of ethene leads to the formation of an unsaturated $16e^-$ complex capable of activating a wide range of bonds (Scheme 9).



Scheme 9. Photo-dissociation of C_2H_4 from complex **1** to form the 16-electron complex.

The CpRh(PMe₃) fragment reacts with benzene to yield CpRh(PMe₃)(C₆H₅)H *via* a short-lived η^2 -arene complex; photolysis with C₆F₆ results in the isolation of a stable η^2 -hexafluorobenzene complex, CpRh(PMe₃)(C₆F₆)³¹ and reaction in pentafluoroanisole generates the metallacycle Cp(PMe₃)Rh(CH₂OC₆F₄) characterized by multinuclear NMR spectroscopy (Scheme 10).³²

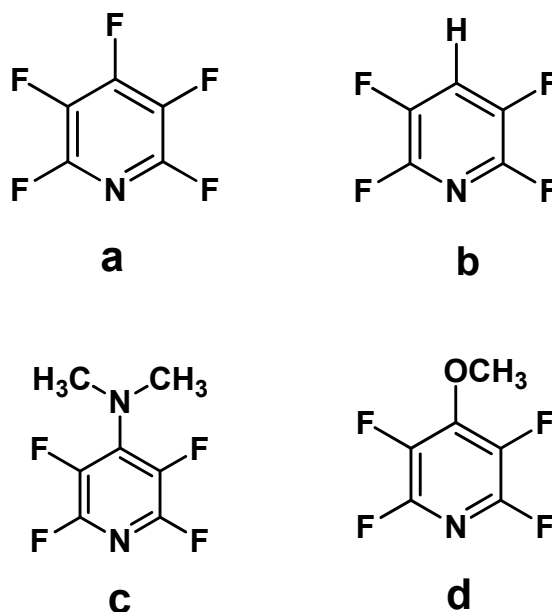


Scheme 10. Reaction of complex **1** with different substrates to afford different coordination type products.

C-F bond cleavage of hexafluorobenzene was achieved in reaction with (η^5 -C₅Me₅)Rh(PMe₃)(C₂H₄) where a more electron-donating ligand was employed (C₅Me₅ instead than C₅H₅). C-F activation took place upon further photolysis following η^2 -coordination of the perfluorobenzene.³³ Studies in Ar matrices at 12 K confirmed that while complex **1**, CpRh(PMe₃)(η^2 -C₆F₆), prefers to eliminate C₆F₆ to form the 16-electron fragment and a small quantity of C-F oxidative addition product, the more crowded (C₅Me₅)Rh(PMe₃)H₂ produces preferentially the C-F activated product with a small amount of unsaturated complex.³⁴ This explains the observation that no oxidative addition was observed for reaction of complex **1** with C₆F₆ in solution.

Considering the results above we thought it would be interesting to explore the behaviour of complex **1** in the presence of pentafluoropyridine,

tetrafluoropyridine and substituted analogues (Scheme 11. a-b-c-d) to obtain information about coordination modes, substituent effects and reaction mechanisms. Below we report the formation of two metallacycles **4** and **5** by intramolecular C-F activation of 4-substituted tetrafluoropyridines at the Rh centre. Reaction with 2,3,5,6 – tetrafluoropyridine formed selectively the C-H activated product whereas reaction with pentafluoropyridine allowed us to isolate the η^2 - complex.



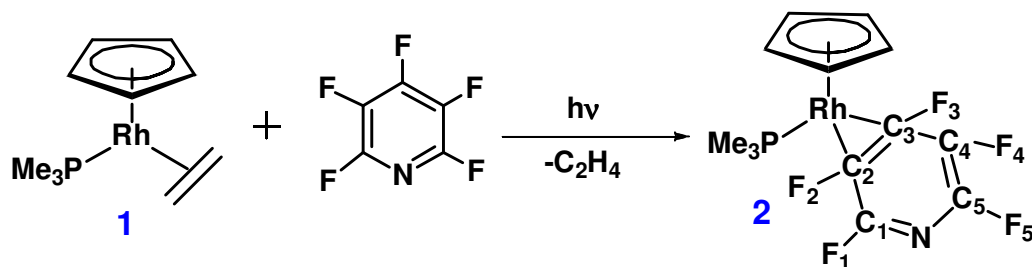
Scheme 11. Fluorinated hetero-aromatics investigated.

2.2. Results

2.2.1 Irradiation of **1** with pentafluoropyridine

The reaction of complex **1** in the presence of pentafluoropyridine was previously investigated in our group by a visiting student and a masters student. They found that the irradiation of **1** in hexane with excess pentafluoropyridine ($\lambda > 290$ nm, 8 h, room temperature) generates a large number of products with scarce selectivity for the formation of one particularly. They were able to identify and isolate some of the products.

On performing the reaction at low temperature (-20°C), the formation of one complex is preferred, leading to an NMR yield for complex **2** of $> 60\%$. This product was purified by sublimation followed by crystallization giving an orange product characterised by multinuclear NMR spectroscopy, EI mass spectrometry and X-ray crystallography. The $^{31}\text{P}\{^1\text{H}\}$ NMR spectrum shows a resonance at $\delta 4.28$, as a doublet of doublets of doublets ($J_{\text{RhP}} = 192$, $J_{\text{PF}} = 56$, 52 Hz) (Figure 1). The value of J_{RhP} indicates a Rh(I) oxidation state³¹ and the values of J_{PF} are similar to those for $\text{Rh}(\eta^2\text{-C}_6\text{F}_6)$ complexes.³¹ We therefore assign complex **2** as $\text{CpRh}(\text{PMe}_3)(\eta^2\text{-C}_4\text{F}_5\text{N})$ with the pentafluoropyridine bonded in an $\eta^2\text{-C,C}$ -mode. The distinction between coordination at C2-C3 and C1-C2 may be made through the ^{19}F NMR spectrum (Figure 2). The spectrum provides evidence of two fluorines close to the nitrogen $\delta - 55.5$ and $\delta - 119.8$. $^{19}\text{F}\{^{31}\text{P}\}$ NMR spectrum previously run by the masters student, allowed the exact assignments for the five inequivalent fluorine environments on the pyridine ring suggesting the two F close to N (F_1 , F_5) to be at $\delta - 55.5$ and $\delta - 119.8$, F_4 not involved in the η^2 coordination being at $\delta - 155.7$, and the two ones left at $\delta - 157.3$ (F_3 , on the side of the uncoordinated one) and F_2 at $\delta - 169.0$. Changes in coupling constants on decoupling from ^{31}P were observed just for these two resonances confirming them to be the two fluorines involved in the η^2 -coordination. We conclude that the pentafluoropyridine is coordinated $\eta^2\text{-C}_2\text{,C}_3$. Selected NMR data for complex **2** are listed in Table 4 (Scheme 12).



Scheme 12. Photochemical reaction between complex **1** and pentafluoropyridine to form complex **2**.

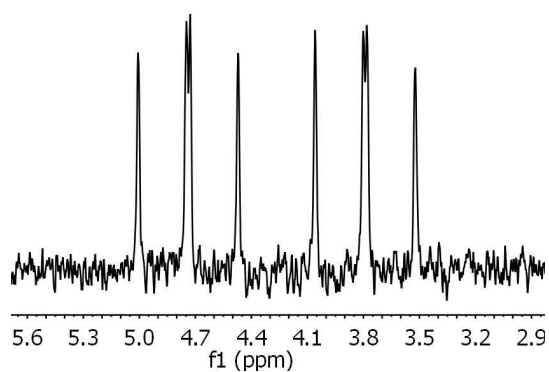
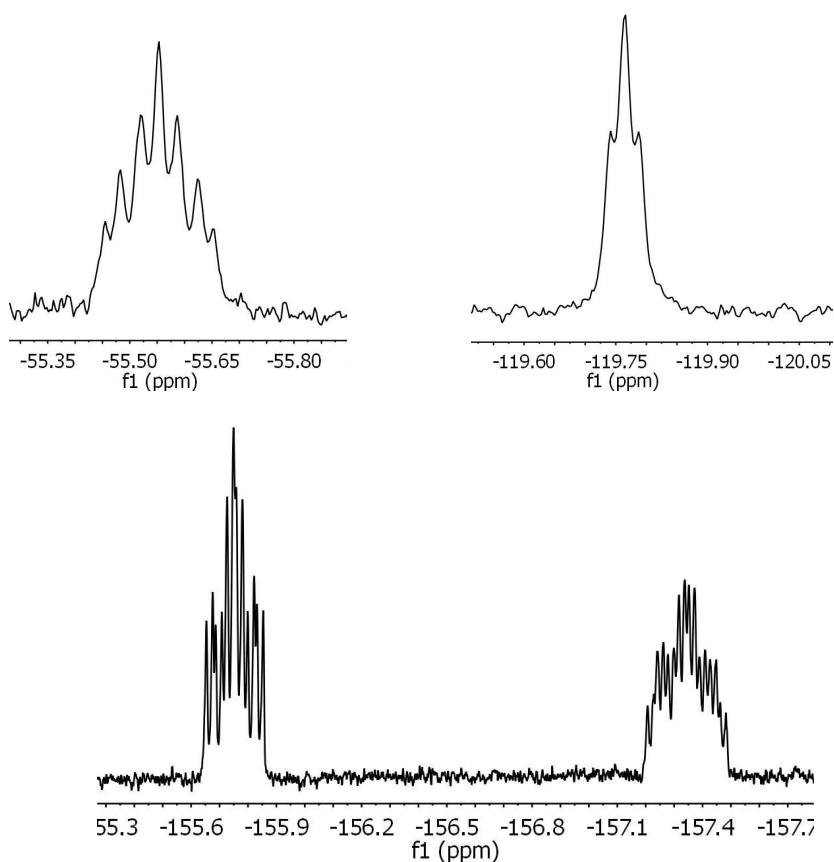


Figure 1. $^{31}\text{P}\{^1\text{H}\}$ NMR spectrum for complex **2** in C_6D_6 showing a doublet of doublets of doublets due to coupling of ^{31}P to ^{103}Rh and two inequivalent fluorines.



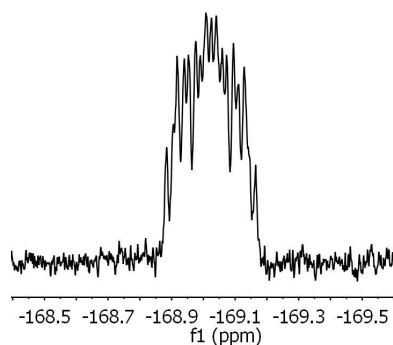


Figure 2. Enlargement of the five resonances from ^{19}F NMR spectrum in C_6D_6 belonging to the five inequivalent fluorines on the pyridyl ring.

The crystal structure of **2** was determined previously by the visiting student. It shows the coordination of pentafluoropyridine but is complicated by disorder of the pyridine ring between the C5 and the N1 due to the symmetry of the pentafluoropyridine; F5A and F5B are also disordered (Figure 3,a). Further attempts at crystallisation of **2** were tried in these studies, changing the conditions in order to obtain a different packing system and perhaps to avoid the disorder. Two crystal structure determinations were carried out, but both of them show the same disorder. The structure of **2** shows a planar $\text{C}_5\text{F}_3\text{N}$ unit with the two fluorines involved in the η^2 coordination bent out of the plane by 42.02° (Figure 3, b) in agreement with the $\text{Rh}(\eta^2 - \text{C}_6\text{F}_6)$ analogue previously reported.³¹ All the crystal structures reported in the literature of coordinated pentafluoropyridine or pyridine show the ligand bound through N,^{35,36} to our knowledge this is the only η^2 -CC-coordinated pentafluoropyridine structure reported. Johnson et al have recently reported extensive NMR characterization of η^2 - coordinated pentafluoropyridine and tetrafluoropyridine at a nickel centre.³⁷ Such complexes have often been proposed as intermediates in C-F activation reactions.^{31,32}

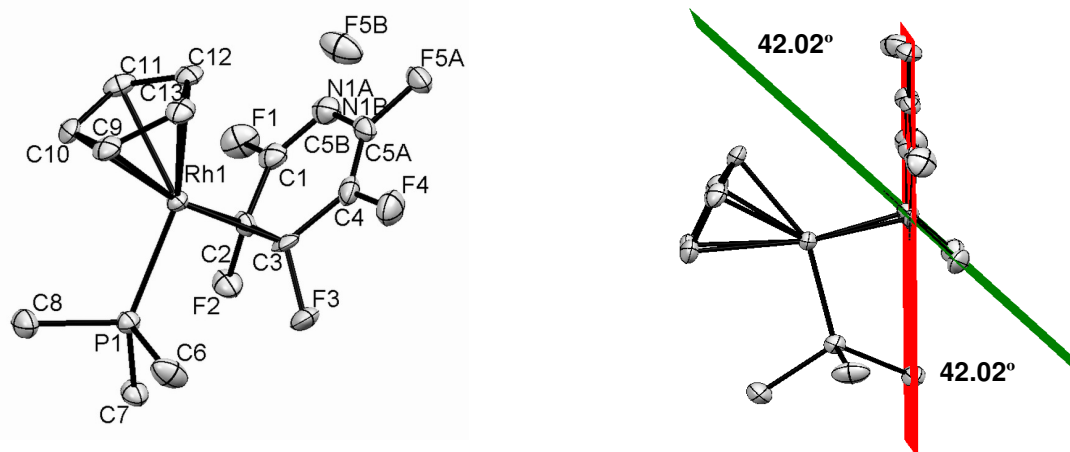


Figure 3. Left. Molecular structure of **2**. Right. Plane 1 C_2F_2 , Plane 2 C_5N , Plane 1 - Plane 2 42.02° , Hydrogen atoms are omitted for clarity. Ellipsoids for the anisotropic displacement parameters are shown at the 50% level.

Selected bond distances and angles are given in Table 1. The co-ordinated C-C bond is extended to $1.443(8)$ Å relative to free C_5F_5N [$1.379(4)$ Å]. A diene pattern is instead observed for the uncoordinated C-C bonds (Figure 4). The coordinated C-F bonds average 1.384 Å, an extension of about 0.05 Å is observed compared to C-F bond length of free pentafluoropyridine. Refinement and crystallographic data for complex **3** are reported in Table 3.

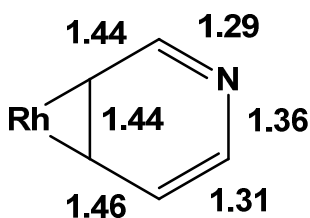


Figure 4. Bond lengths in Å for the η^2 -coordinated pyridyl moiety.

Table 1. Selected bond lengths and angles for complex **2**.

Bond length / Å	
C(2)-Rh(1)	2.042(5)
C(3)-Rh(1)	2.049(4)
C(2)-C(3)	1.443(8)
C(1)-F(1)	1.339(5)
C(2)-F(2)	1.390(5)
C(3)-F(3)	1.378(5)
C(4)-F(4)	1.339(5)

Angles between planes	
Plane 1 = RhC(2)C(3)	
Plane 2 = C(2)C(3)F(2)F(3)	
Plane 3 = C5N	
Plane 1 - Plane 2	64.60°
Plane 1 - Plane 3	73.33°
Plane 2 - Plane 3	42.02°

2.2.2 Irradiation of **1** with 2,3,5,6-tetrafluoropyridine

The irradiation of **1** in C₆D₁₂ with excess 2,3,5,6-tetrafluoropyridine **b**, ($\lambda > 290$ nm, 8 h, room temperature) leads to the clean formation of the C-H activated product. The doublet at δ 12.6 in the $^{31}\text{P}\{^1\text{H}\}$ NMR spectrum was identified as due to complex CpRh(PMe₃)(C₅F₄N)(H), **3** (Figure 5). It results from coupling to ^{103}Rh ($J_{\text{P-Rh}}$ 141.9 Hz) and these values are consistent with those found for the reaction of CpRh(PMe₃)(C₆H₅)H with partially fluorinated arenes.³⁸ In the ^1H NMR spectrum the hydride signal resonates at δ -12.9 as a doublet of doublets with $J_{\text{H-P}}$ and $J_{\text{H-Rh}}$ of 40 Hz and 22.8 Hz, respectively (Figure 6). The ^{19}F NMR spectrum is consistent with two sets of equivalent fluorine nuclei in a 1:1 ratio (Figure 7).

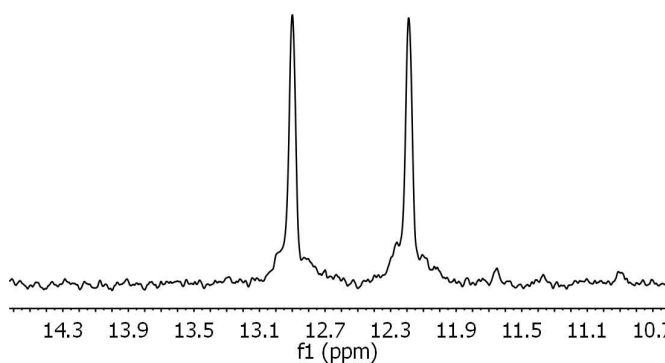


Figure 5. $^{31}\text{P}\{^1\text{H}\}$ NMR spectrum in C₆D₆ for complex **3** showing a doublet arisen from coupling to ^{103}Rh .

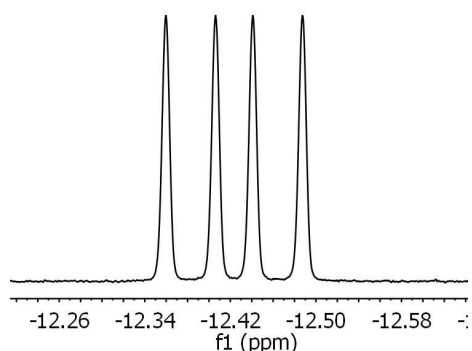


Figure 6. ^1H NMR spectrum in C_6D_6 of the hydride resonance for complex **3**. The doublet of doublets is due to coupling to ^{31}P and ^{103}Rh .

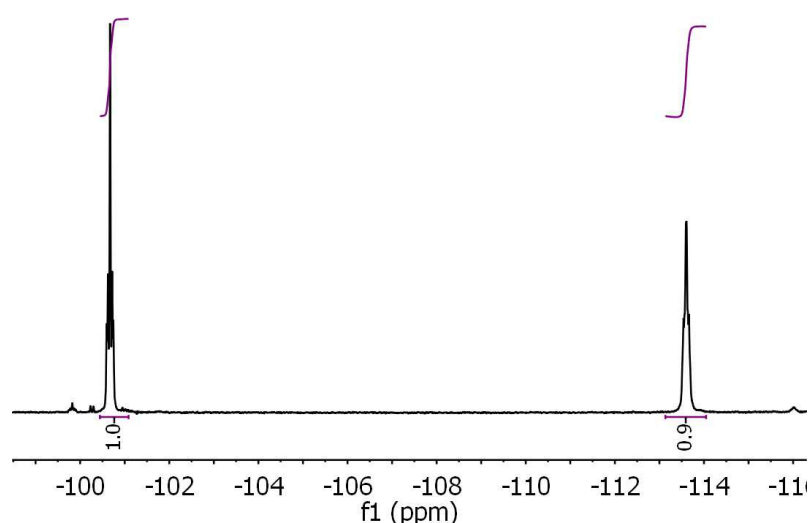
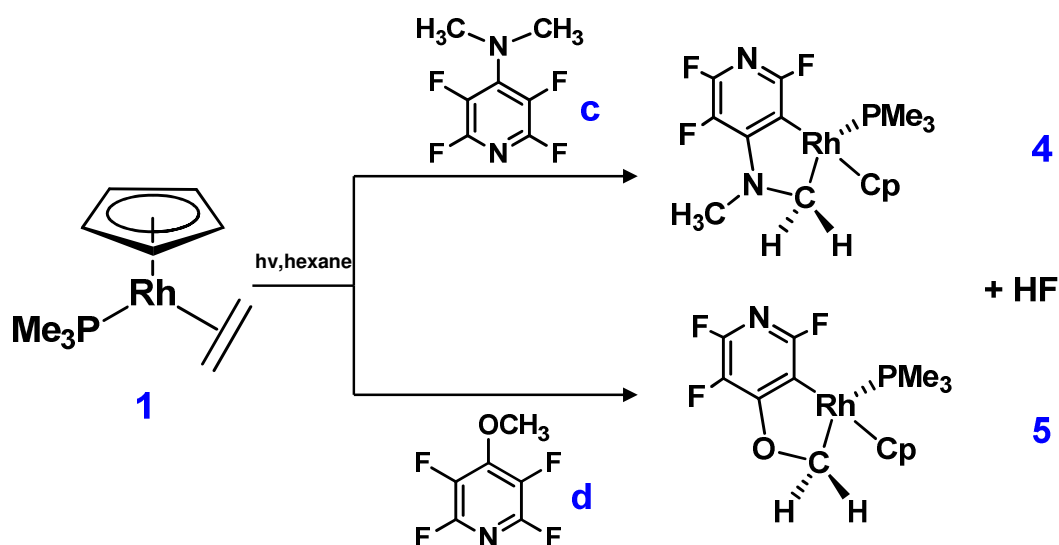


Figure 7. ^{19}F spectrum in C_6D_6 for complex **3**. The two resonances belong to the two sets of inequivalent fluorines.

2.2.3 Irradiation of **1** with 4-dimethylamino-2,3,5,6-tetrafluoropyridine

The irradiation of **1** in hexane with excess substituted tetrafluoropyridine **c**, (2,3,5,6-tetrafluoro-*N,N*-dimethylpyridin-4-aminopyridine, broadband UV, 8 h, room temperature) generates the metallacycle $[\text{Cp}(\text{PMe}_3)\text{Rh}(\kappa^2 - \text{C},\text{C}) - (\text{CH}_2\text{N}(\text{CH}_3)\text{C}_5\text{F}_3\text{N})]$, **4** with an NMR yield of 85% (Scheme 13). Upon scaling up, the complex crystallised out of the reaction mixture during photolysis as an isolable air-stable pale orange solid characterized by EI mass spectrometry, multinuclear NMR spectroscopy, X-Ray crystallography and microanalysis. The ^1H NMR spectrum (Figure 8) shows the protons of the CH_2 group of the metallacycle **4** to be diastereotopic because it is bonded to a chiral centre, Rh. The two resonances are correlated by COSY NMR

spectroscopy and appeared at δ 3.04 (ddd) and at δ 4.87 (m) with different P-H and H-H coupling constants.



Scheme 13. Photochemical reaction of complex **1** with 4-substituted tetrafluoropyridines **c**, **d** to afford metallacycles **4** and **5**.

This very low-field chemical shift for the diastereotopic proton compares with shifts of δ 6.82 and 5.24 for the diastereotopic proton of the complex $[\text{Cp}(\text{PMe}_3)\text{Rh}(\text{CH}_2\text{OC}_6\text{F}_4)]$ previously observed.³² The $^{31}\text{P}\{^1\text{H}\}$ NMR spectrum displays a doublet, with a coupling constant typical of a Rh(III) species ($J_{\text{PRh}} = 160$ Hz).³⁹ The ^{19}F NMR spectrum displays three different peaks for the three inequivalent fluorines, two at lower field for the fluorines *ortho* to nitrogen and one at higher field. Finally the ^{13}C DEPT spectrum of **4** confirms the group resonating at δ 40 as a CH_2 group (dd, $J_{\text{CRh}} = 29.8$ Hz, $J_{\text{CP}} = 13.8$ Hz). A complete set of chemical shifts and coupling constants is given in Table 4.

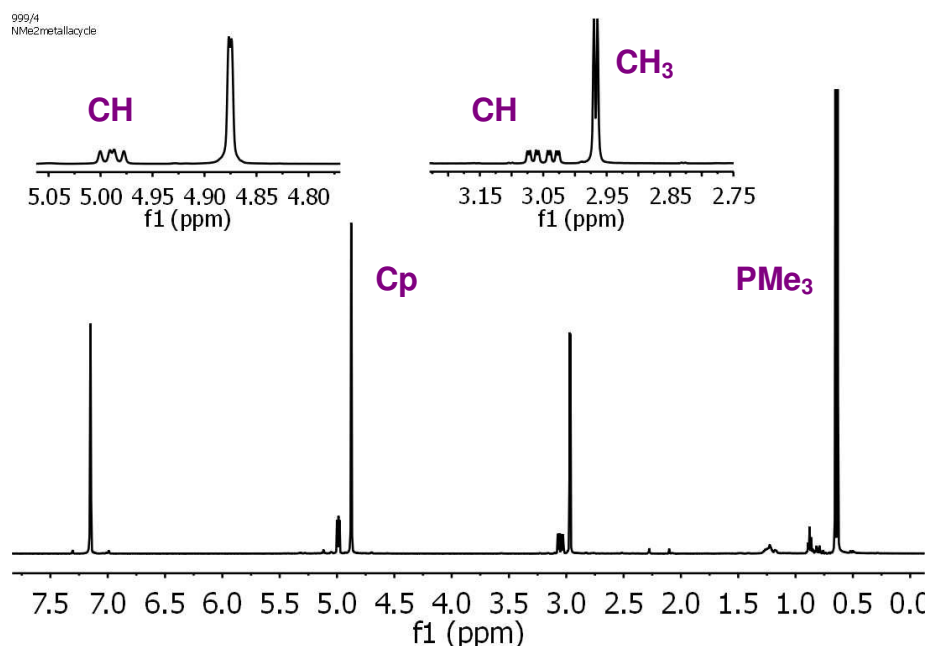


Figure 8. ^1H NMR spectrum of complex **4** in C_6D_6 .

Complex **4** was isolated as small pale orange crystals by crystallisation from hexane and its structure was determined by X-ray crystallography (Figure 9). Refinement data are summarized in Table 3. A list of selected bond lengths and angles is given in Table 2. The rhodacycle and the pyridine ring fused to it are planar as confirmed by the sum of the internal angles (539.89°). The angle C6-Rh1-C11 is $79.8(1)^\circ$, consistent with the data previously determined for a similar Cp^*Ir cyclometallated species.¹⁰ The Rh-C6 and Rh-C11 bond lengths are also consistent with bond length previously observed for the iridium complex.¹⁰

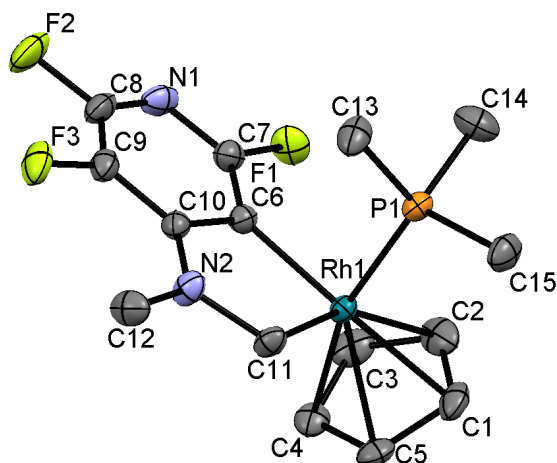


Figure 9. Molecular structure of **4**. Hydrogen atoms are omitted for clarity. Ellipsoids for the anisotropic displacement parameters are shown at the 50% level.

Table 2. Selected bond lengths and angles for complex **4**.

Bond length/ Å	
C(6)-Rh(1)	2.023(3)
C(11)-Rh(1)	2.069(3)
C(11)-N(2)	1.463(3)
C(10)-N(2)	1.346(3)
Angles / Degrees	
P(1)-Rh(1)-C(11)	89.58(7)
P(1)-Rh(1)-C(6)	87.87(7)

Table 3. Crystallographic data and refinement data for complex **2** and **4**.

	2	4
Formula	C ₁₃ H ₁₄ F ₅ NPRh	C ₁₅ H ₁₉ F ₃ N ₂ PRh
<i>M</i>	413.13	418.20
<i>a</i> /Å	10.0121(13)	8.4609(14)
<i>b</i> /Å	12.8944(16)	16.312(3)
<i>c</i> /Å	10.9517(14)	11.9985(19)
α /deg	90.00	90.00
β /deg	90.00	100.907(3)
γ /deg	90.00	90.00
<i>V</i> / Å ³	1413.9(3)	1626.1(5)
<i>T</i> /K	110(2)	110(2)
Space group	Pna21	P2(1)/c
<i>Z</i>	4	4
μ (Mo K α)/mm ⁻¹	0.71073	0.71073
Reflns meads	14753	16531
Reflns indep	4060	4045
<i>R</i> _{int}	0.0660	0.0362
FinalR [<i>I</i> > 2 σ (<i>I</i>)]	<i>R</i> ₁ = 0.0393 <i>wR</i> ₂ = 0.0922	<i>R</i> ₁ = 0.0312 <i>wR</i> ₂ = 0.0770
FinalR (all data)	<i>R</i> ₁ = 0.0439 <i>wR</i> ₂ = 0.0953	<i>R</i> ₁ = 0.0398 <i>wR</i> ₂ = 0.0809

2.2.4 Irradiation of **1** with 4-methoxy- 2,3,5,6 tetrafluoropyridine

The irradiation of **1** in hexane with excess substituted tetrafluoropyridine **d** (4-methoxy- 2,3,5,6 tetrafluoropyridine, broadband UV, 6 h, room temperature) generates the metallacycle Cp(PMe₃)Rh(κ^2 - C,C)(CH₂OC₅F₃N), **5**, with an NMR yield of 20%. The formation of **5** appeared to be blocked after that conversion; a dark film is formed on the glass wall of the NMR tube. Low temperature (-20°C) photolysis and use of a λ > 350 nm UV filter did not improve the conversion. The ¹H NMR spectrum

shows again the CH₂ group of the metallacycle **5** to be diastereotopic (Table 4). The two resonances appeared at lower field than the ones observed for **5**, δ 5.25 (ddd) and 6.90 (m), due to presence of oxygen instead than nitrogen. The ¹⁹F spectrum shows three different resonances for the three inequivalent fluorines (Figure 10). Complex **5** was isolated as small pale orange crystals by crystallisation from hexane. A crystal structure determination was attempted (Figure 11), but the refinement never converged satisfactorily because of twinning. Nevertheless, the identity of complex **5** was confirmed.

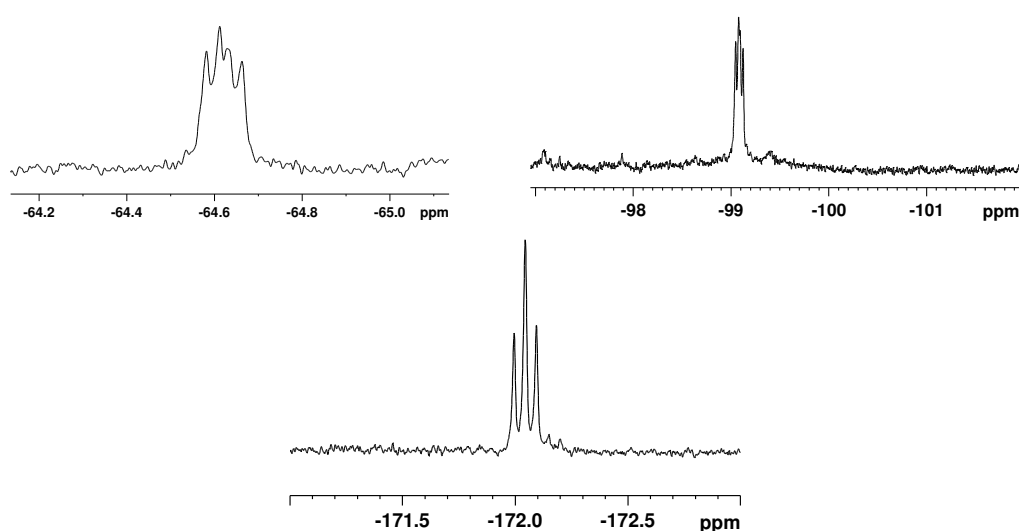


Figure 10. Three ¹⁹F resonances for complex **5** in C₆D₆.

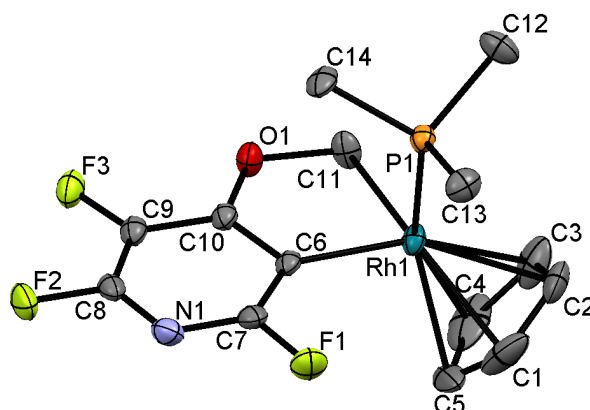


Figure 11. Molecular structure of **5**. Hydrogen atoms are omitted for clarity. Ellipsoids for the anisotropic displacement parameters are shown at the 50% level.

Table 4. NMR data in C₆D₆ for Precursor and Photoproducts δ (J/Hz).

	³¹ P{ ¹ H}	¹ H	¹⁹ F
1	4.4 (d, $J_{\text{Rh-P}}$ 200)	0.77 (d, $J_{\text{P-H}}$ 9.2, PMe ₃) 2.74 (m, C ₂ H ₄) 1.46 (m, C ₂ H ₄) 5.09 (s, Cp)	
2	3.0 (ddd, $J_{\text{Rh-P}}$ 192, $J_{\text{P-F}}$ 56, 52)	0.79 (d, $J_{\text{P-H}}$ 10.5, PMe ₃) 4.37(s, Cp)	-55.5 (m, F _A) -119.8 (t, $J_{\text{F-F}}$ 11.4, F _B) -155.7(ddd, $J_{\text{F-F}}$ 11.4, 15.3, 34.3, F _C) -157.3 (m, F _D) -169.0 (m, F _E)
3	12.6 (d, $J_{\text{Rh-P}}$ 142)	-12.9 (dd, $J_{\text{P-H}}$ 22.8, $J_{\text{Rh-H}}$ 40, Rh-H) 1.35 (d, $J_{\text{P-H}}$ 10.9, PMe ₃) 5.25 (s, Cp)	-100.7 (m, 2F) -113.6 (m, 2F)
4	13.8 (d, $J_{\text{Rh-P}}$ 158)	0.65 (d, $J_{\text{P-H}}$ 10.6, PMe ₃) 2.96 (d, $J_{\text{H-H}}$ 2.93, CH ₃) 3.04 (ddd, $J_{\text{P-H}}$ 1.93, $J_{\text{Rh-H}}$ 6.69, $J_{\text{H-H}}$ 16.06, H _A , CH ₂) 4.87 (d, $J_{\text{Rh-H}}$ 1.3, Cp) 4.98 (dd, $J_{\text{H-H}}$ 4.92, 6.71, H _B , CH ₂)	-66.5 (dd, $J_{\text{F-F}}$ 22.3, 34.2, F _A) -100.1(dd, $J_{\text{F-F}}$ 23.5, 37.9, F _B) -180.2 (t, $J_{\text{F-F}}$ 24.2, F _C)
5	14.0 (d, $J_{\text{Rh-P}}$ 159)	0.54 (d, $J_{\text{P-H}}$ 10.5, PMe ₃) 4.73 (d, $J_{\text{Rh-H}}$ 1.3, Cp) 5.12 (ddd, $J_{\text{P-H}}$ 1.42, $J_{\text{Rh-H}}$ 5.40, $J_{\text{H-H}}$ 17.4, H _A , CH ₂) 6.77 (m, H _B)	-64.6 (dd, $J_{\text{F-F}}$ 24.2, 38.1, F _A) -99.1 (dd, $J_{\text{F-F}}$ 21.2, 36.1, F _B) -172.0 (t, $J_{\text{F-F}}$ 23.7, F _C)

2.3. Mechanistic studies

2.3.1 Reaction of complex 1 with pentafluoropyridine and 2,3,5,6-tetrafluoropyridine

Reaction of complex **1** with pentafluoropyridine produces a mixture of compounds; complex **2** was identified as the only one with a coupling constant J_{PRh} characteristic of Rh(I), all the rest are Rh(III) species. The selectivity towards formation of **2** was achieved by performing photolysis at low T in hexane with a ten-fold excess of pentafluoropyridine. Variable temperature NMR spectroscopy (210 K to 320 K) was performed in order to look for any other isomer, but no new compounds were detected apart from the CpRh(PMe₃)(η^2 -C₄F₅N) complex **2**, confirming that the reaction is regioselective towards C₂-C₃ position. It was not possible to characterise all the products formed at room temperature due to decomposition of some after pumping off the reaction mixture. The unexpected presence of a hydride resonance at δ - 12.42 (dd, $J_{\text{P-H}}$ 39.9 Hz, $J_{\text{Rh-H}}$ 22.9 Hz) suggested hydrogen-source compounds being involved in the reaction mixture. The hydride containing product was identified as complex **3**. Probably reaction of C₅F₅N with some species formed in the reaction mixture led to hydrodefluorination of it to form C₅F₄HN as already reported.⁴⁰ It is clear from these experiments that complex **2** is stabilised enough for isolation and that C-F oxidative addition certainly does not occur under mild conditions. The complex appeared to be stable in solution upon heating up to 100° C. The reaction of **1** with 2,3,5,6-tetrafluoropyridine produces cleanly the C-H activation product in 100% yield. Even when the sample was over-photolysed no evidence for C-F activation was found, complex **3** was the only observed product.

2.3.2 Reaction of complex 1 with 4-substituted tetrafluoropyridines

The reaction of **1** with 4-substituted tetrafluoropyridines (OMe or NMe₂) yields metallacycles **4** and **5**. We also investigated these reactions in NMR experiments to search for reaction intermediates. The expected by-product,

free HF, was observed in the ^1H NMR spectrum as a low field broad peak at δ 14.7 (Figure 12, b). The photochemical reaction of **1** with **c** will result in initial photodissociation of C_2H_4 from **1**; possible reaction intermediates could arise by coordination of the substrate by η^2 -coordination and/or C-F or C-H oxidative addition. When the reaction is conducted in hexane or in cyclohexane- d_{12} and followed by ^1H NMR spectroscopy a hydride is detected (Figure 12, a) at δ -14 (dd, $J_{\text{P-H}} = 38.6$, $J_{\text{Rh-H}} = 28.9$ Hz) as a minor product in addition to the metallacycle. The hydride was identified as $\text{CpRh}(\text{PMe}_3)\text{H}_2$ by comparison with work done previously.⁴¹ When the reaction was followed by ^{31}P and ^{19}F NMR spectroscopy, we did not notice any evidence of a Rh(I) complex characteristic of η^2 -coordination or ^{19}F resonance at high field characteristic of a fluoride complex. Even when the reaction was carried out at 253 K and the NMR spectrum taken at 200 K, no such species were observed. In contrast to our experimental evidence, it was established before that cyclometallation occurred *via* η^2 -coordination on reaction with $\text{C}_6\text{F}_5\text{OMe}$.^{31,32}

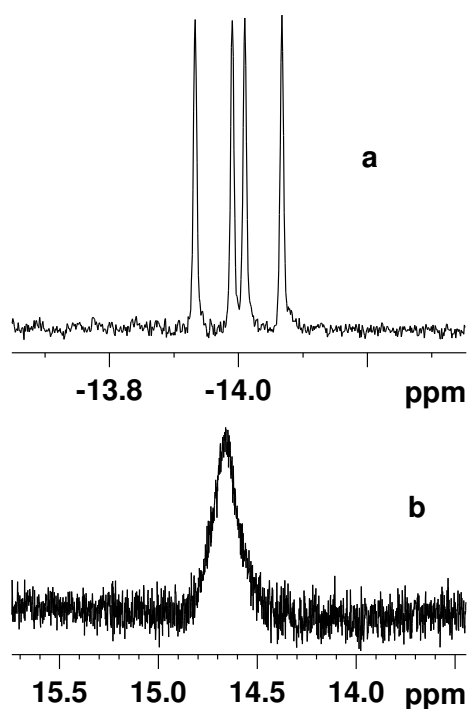


Figure 12. (a) Hydride resonance in the ^1H NMR spectrum after reaction of **1** with **b**. (b) broad peak at low field in the ^1H NMR spectrum assigned to HF.

In order to elucidate the role of the substituent on the fluoropyridine ring, we also examined the photo reactions of **1** with 4-ethyl-tetrafluoropyridine and

with 4-ethoxy-tetrafluoropyridine. Neither reaction showed any cyclometallated products. We conclude that cyclometallation requires a heteroatom substituent and a primary C-H bond as in -NMe₂ or -OMe. The preference for the metal centre to activate a primary CH bonds has already been observed by Jones et al.^{42,43}

2.3.3 Kinetic Isotopic Effect (KIE)

The isotopic effect was also explored. A large isotopic effect was reported for an Ir-PCP/ 4-methoxy-2,3,5,6-tetrafluorotoluene system to form the C-O activated product where neither a direct oxidative addition nor a simple S_N2 mechanism were observed.⁴⁴

The deuterated analogue of 2,3,5,6-tetrafluoro-4-methoxypyridine C₅NF₄OCD₃ was synthesized and fully characterized by NMR spectroscopy, mass-spectrometry and IR absorption. The irradiation of **1** in hexane with excess of both substituted tetrafluoropyridines **c** (Scheme 11, page 21) and O-CD₃, present in 1:5:5 ratio (broadband UV, 12 h, room temperature) generates a mixture of the metallacycles [CpRh(PMe₃)(CH₂OC₅F₃N)], **5**, and the deuterated analogue [CpRh(PMe₃)(CD₂OC₅F₃N)], **6**, with an NMR yield of 30%. Since the two cyclometallated species are coincident in ¹⁹F and ³¹P NMR spectra, EI Mass spectrometry was employed to determine the KIE. Reproducible results were obtained from two parallel experiments that showed a product ratio of 0.94 ± 0.04. We conclude that the KIE is very small.

2.4. Discussion

It was established that reaction of Ni(COD)₂ in the presence of excess of PEt₃ and pentafluoropyridine leads to an ortho activated Ni(F)(C₅F₄N) complex. The difference in rate of reaction between hexafluorobenzene and pentafluoropyridine was remarkable, the latter being much faster and highly regioselective.⁴⁵ DFT calculations based on a model Ni(PMe₃)₂ show that the regioselectivity derives from a neighbouring group effect with co-participation of the phosphine and the nitrogen of the pentafluoropyridine. This effect occurs only when the attack takes place in ortho-position and in the presence of a phosphine ligand (the activation takes place in 4-position when the phosphine is replaced by a carbene).⁴⁶ Para C-F activation of pentafluoropyridine with Pt(PCy₃)₂ and Pd(PCy₃)₂ forms pyridyl complexes through two different mechanisms: phosphine assistance for the platinum complex and C-F oxidative addition for the palladium one.⁴⁷ Regioselectivity is still conserved moving from Ni to Rh whereas the change in reaction rate is not relevant moving from hexafluorobenzene to pentafluoropyridine.³¹ In different behaviour from what was observed before, Rh appeared to be the suitable metal centre for isolation of the η^2 adduct as an intermediate step towards C-F oxidative addition. In order to explore the preference for C-H compared to C-F activation, reaction of complex **1** with 2,3,5,6-tetrafluoropyridine was investigated. It produces cleanly the C-H activated product, differently from what was observed for Ni(COD)₂ where C-F activation was preferred to form the ortho C-F activated isomer as the major product at room temperature.⁴⁵ Recently Johnson and co-workers isolated the C-H activated product of tetrafluoropyridine as the major species for reaction of the phenanthrene adduct (PEt₃)₂Ni(η^2 -C₁₄H₁₀) at temperatures lower than 193 K demonstrating that small changes in reaction condition could drastically influence the selectivity.³⁷

MeO and NMe₂ derivatives react at Ni(PEt₃)₂ to give C-F oxidative addition at the 2-position, the same reactivity as was shown by pentafluoropyridine and the substituents were found not to play any role in reactions at Ni centres.⁴⁸ The role played by the substituent is instead crucial in reactions of complex **1** with 4-substituted fluorinated pyridines. The complex needs a

Cp*Re(CO)₃ complex photochemically inserts into C-F bond of hexafluorobenzene with concomitant C-H activation of a methyl of the Cp* ligand to form Re(η^6 -C₆Me₄H₂)(CO)₂(C₆F₅). The reaction was found to be driven by the production of HF.⁵¹

Recently, DFT studies on Ru(NHC)(PPh₃)₃(CO)H₂ in the presence of fluorinated arenes outlined a novel mechanism where a metal hydride reacts intermolecularly with C₆F₅H by an ortho-regioselective nucleophilic attack forming HF.¹⁰

We carried out a few experiments to try to understand the route followed by our reaction: addition of CsF neither promotes the formation of the cyclometallated species nor inhibits it, this cuts out the possibility of having a base assisted mechanism. It was already established that the Rh(η^5 -C₅H₅)PMe₃ fragment activates C-H bonds selectively over C-F bonds and the C-F oxidative addition product was observed only in low temperature matrices for reaction with hexafluorobenzene. η^2 -Coordination takes place for the reaction of the same Rh fragment with a methoxy group as substituent on the fluoroarene. The reaction then proceeds through a cyclometallation pathway liberating HF. A methoxy group or a dimethylamino group seem to enhance photochemical C-F activation. Displacement of HF and ring closure would give rise to the cyclometallated species. In order to elucidate the mechanism, preliminary DFT calculations were performed by the Eisenstein group. The possible mechanistic pathways were explored (Figure 14): C-F activation followed by C-H activation and C-H activation with subsequent C-F insertion. Two different possibilities were investigated for the latter, one which involves Cp protons and the second one which involves a migration of the hydride to the pyridine ring and a fluoride passed onto the metal centre. Since calculations for the Cp-involved pathway did not find a transition state for the ring closure we excluded it and compared the two remaining. From the results obtained, the C-F/C-H pathway seems to be the favoured one (Figure 13). The first two steps are energetically less favoured, but after η^2 -coordination it goes energetically downhill towards the cyclometallation product. In contrast, C-H/C-F route is energetically favoured

in the first two steps which lead to the formation of the Rh-hydride, but it becomes energetically unfavoured towards the last steps of the mechanism.

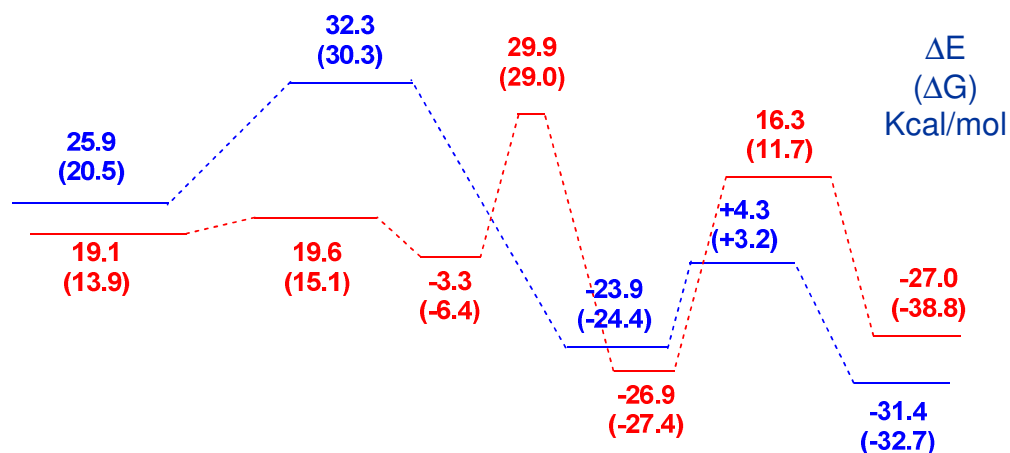


Figure 13. Energy profile for the possible mechanisms. Blue: C-F/C-H; Red: C-H/C-F.

As already mentioned, we did not succeed experimentally in obtaining evidence to choose one mechanism instead of the other. No Rh-F or η^2 – intermediates were detected in low T $^{31}\text{P}\{^1\text{H}\}$ and ^{19}F NMR and neither did in situ photolysis succeeded in finding the transient. Addition of CsF (a base which should promote C-F/C-H pathway) did not influence the reactivity; a hydride is formed during photolysis which was found not to take part in the reaction mechanism. Nevertheless, on the basis of previous results³² and results from DFT calculations, the C-F/C-H route might be the followed one. The intermediates formed are surely very short – lived species, not possible to be detected by the technique we used.

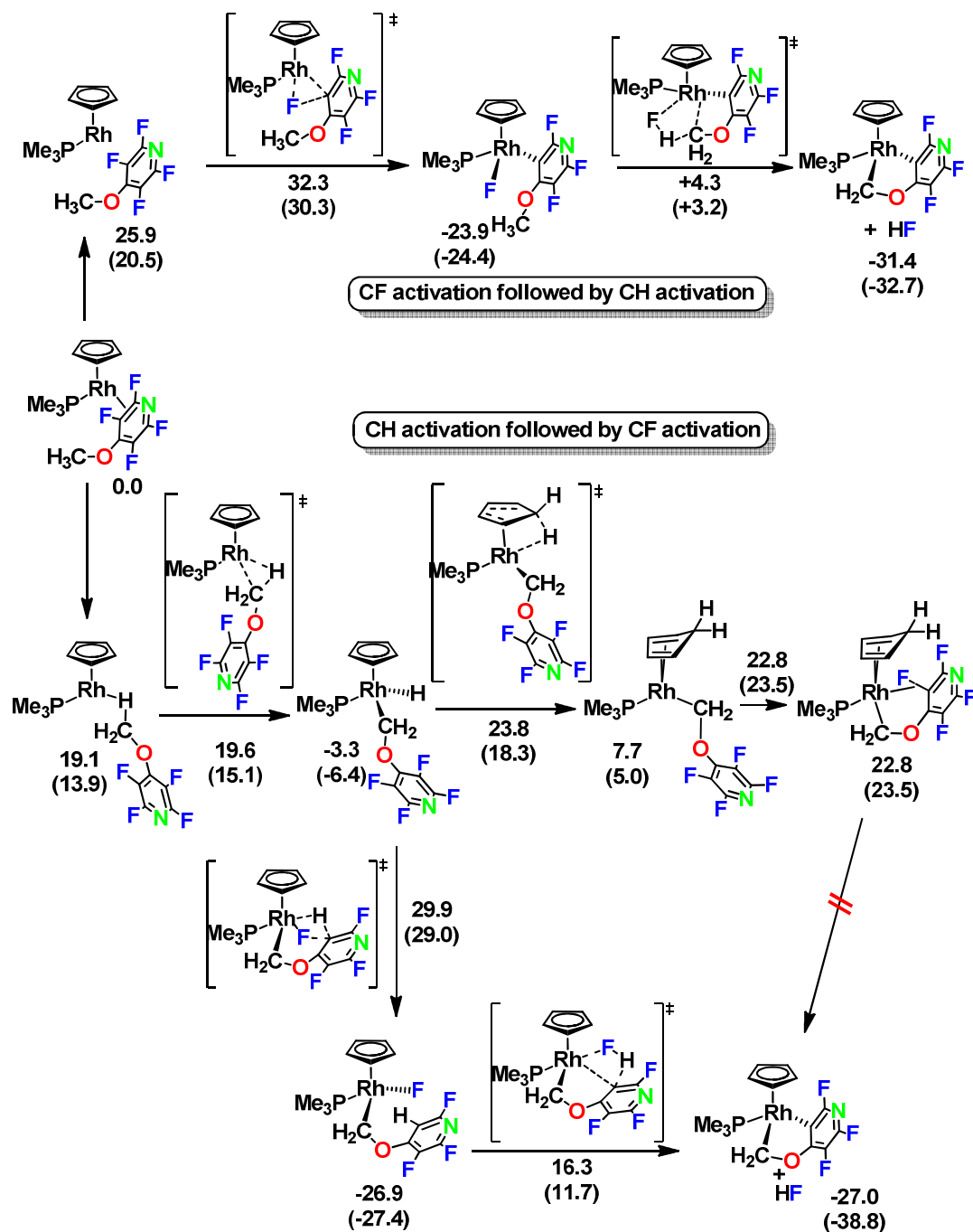
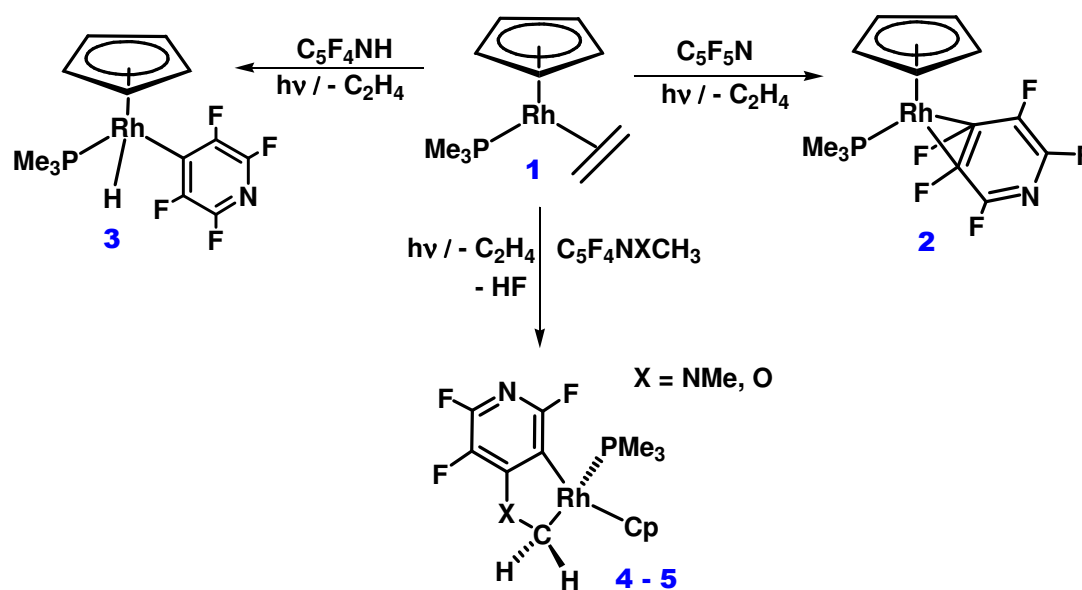


Figure 14. DFT calculations for the possible reaction mechanism. Numbers are $\Delta E/\Delta G$ in Kcal/mol.

2.5. Summary

The current experiments demonstrate the formation by photochemical reaction of $\text{CpRh}(\text{PMe}_3)(\eta^2\text{-C}_5\text{F}_5\text{N})$ as an isolable solid. Reaction with 2,3,5,6 tetrafluoropyridine was selective for C-H activation. We also show the effect of substituents on the fluoropyridine demonstrating that cyclometallation occurs to form new air- stable rhodacycle species by both CH and CF insertion (Scheme 16).



Scheme 16. Reaction of complex **1** with pyridines to afford different coordination type products.

2.6. Experimental section

2.6.1 General Procedures

All operations were performed under an argon atmosphere, either on a high-vacuum line (10^{-4} mbar) using modified Schlenk techniques, on standard Schlenk (10^{-2} mbar) lines, or in a glovebox. Solvents for general use (benzene, toluene) were of AR grade, dried by distillation over classical reagents, and stored under Ar in ampoules fitted with Young's PTFE stopcocks. Hexane was collected from the solvent purification system (equipped with two purifying columns: one alumina and one copper catalyst) and dried again by distillation. Deuterated solvents were dried by stirring over potassium and were distilled under high vacuum into small ampoules with potassium mirrors. Pentafluoropyridine and 2,3,5,6 - tetrafluoropyridine were purchased from Sigma-Aldrich and dried over molecular sieves. Photochemical reactions, at room temperature, were performed in glass NMR tubes fitted with PTFE taps, using a 125 W medium pressure mercury vapor lamp with a water filter (5 cm). UV-vis irradiations, at lower temperatures, were performed using a 300 W Oriel 66011 xenon lamp with a thermostatically controlled cooling system based on gaseous nitrogen boil-off obtained from a JEOL NMR spectrometer. All NMR spectra were recorded on Bruker AMX500 spectrometers in glass tubes fitted with Young's PTFE stopcocks. All ^1H and ^{13}C chemical shifts are reported in (δ) relative to tetramethylsilane and are referenced using the chemical shifts of residual protio solvent resonances (benzene, δ 7.15 for ^1H and δ 128.0 for ^{13}C). ^{19}F NMR spectra were recorded at 470.5 MHz and referenced to external CFCl_3 at δ 0. The $^{31}\text{P}\{^1\text{H}\}$ NMR spectra were recorded at 202.5 MHz and are referenced to external H_3PO_4 .

2.6.2 Mass spectrometry

El mass spectra were measured on a Waters Micromass GCT Premier orthogonal time-of-flight instrument set to one scan per second with resolution power of 6000 fwhm.

2.6.3 X-ray crystallography

Diffraction data for $\text{CpRh}(\text{PMe}_3)(\eta^2\text{-C}_5\text{F}_5\text{N})$ were collected at 110 K on a Bruker Smart Apex diffractometer with $\text{MoK}\alpha$ radiation ($\lambda = 0.71073 \text{ \AA}$) using a SMART CCD camera. Diffractometer control, data collection, and initial unit cell determination was performed using "SMART" (v5.625 Bruker-AXS). Frame integration and unit-cell refinement software was carried out with "SAINT+" (v6.22, Bruker AXS). Absorption corrections were applied using SADABS (v2.03, Sheldrick). The structure was solved by direct methods using SHELXS-97 (Sheldrick, 1997) and refined by full-matrix least squares using SHELXL-97 (Sheldrick, 1997).⁵² Diffraction data for $[(\eta^5\text{-C}_5\text{H}_5)(\text{PMe}_3)\text{RhCH}_2\text{N}(\text{CH}_3)\text{C}_5\text{F}_3\text{N}]$ were collected at 110 K on an Agilent SuperNova diffractometer with $\text{MoK}\alpha$ radiation ($\lambda = 0.71073 \text{ \AA}$). Data collection, unit cell determination and frame integration were carried out with "CrysalisPro". Absorption corrections were applied using crystal face-indexing and the ABSPACK absorption correction software within CrysalisPro. Structures were solved and refined using Olex2⁵³ implementing SHELX algorithms. Structures were solved by either Patterson or direct methods using SHELXS-97 and refined by full-matrix least squares using SHELXL-97. All non-hydrogen atoms were refined anisotropically. Carbon-bound hydrogen atoms were placed at calculated positions and refined using a "riding model".

2.6.4 IR experiment

The IR experiments were performed using a "Unicam RS 10000E FTIR instrument. The spectrum was recorded on a liquid film averaging sixteen scans at 1cm^{-1} resolution.

2.6.5 Synthesis and NMR Experiments

$\text{Rh}(\eta^5\text{-C}_5\text{H}_5)(\text{PMe}_3)(\text{C}_2\text{H}_4)$ was synthesized by literature procedures, but replacing TICp by LiCp.⁵⁴ 4-dimethylamino-2,3,5,6 tetrafluoropyridine and 4-methoxy- 2,3,5,6 tetrafluoropyridine were also synthesized by literature

procedures.⁵⁵ The pyridines were additionally characterised by NMR spectroscopy and EI mass spectrometry.

2.6.6 Preparation of $[(\eta^5\text{-C}_5\text{H}_5)(\text{PMe}_3)\text{Rh}(\eta^2\text{-C}_5\text{F}_5\text{N})]$, **2**

An 8 mm diameter NMR tube, fitted with a Young's tap, was charged with complex **1** (50 mg) and pentafluoropyridine (2 fold excess) in hexane and irradiated at -20 °C with an Oriel Xe arc lamp (8 h), resulting in 60% conversion to **2**. The excess of pentafluoropyridine and solvent were removed under vacuum and part of the unreacted starting material and other products were sublimed at 25 °C and 1×10^{-4} mbar onto a liquid nitrogen cold finger, leaving a brown residue. The brown residue was suspended in dry hexane, heated to 60 °C and filtered under argon. The orange solution was then cooled at -20 °C for a few days to obtain small orange crystals of complex **2**.

^1H NMR (C_6D_6 , 300 K), : δ 4.37 (s, 5H, C_5H_5), δ 0.79 (d, 9H, $J_{\text{P-H}}$ 10.6 Hz PMe_3).

$^{31}\text{P}\{^1\text{H}\}$ NMR: δ 3.09 (ddd, $J_{\text{Rh-P}}$ 192 Hz, J_{PF} 56 Hz, J_{PF} 52 Hz).

$^{13}\text{C}\{^1\text{H}\}$ NMR: δ 91.44 (t, C_5H_5), δ 21.90 (d, PMe_3), there is no indication in the spectrum of carbons corresponding to the pentafluoropyridine ring.

^{19}F NMR: F_{A} δ - 55.5 (tt, 1F), F_{B} δ - 119.8 (t, 1F), F_{C} δ - 155.7 (tdd, 1F), F_{D} δ - 157.3 (m, 1F), F_{D} δ -169.0 (m, 1F).

EI mass-spec.: m/z 412.9876 (M^+) 100% (calculated 412.9839, difference 0.4 mDa).

2.6.7 Preparation of $[(\eta^5\text{-C}_5\text{H}_5)(\text{PMe}_3)\text{Rh}(\text{C}_5\text{F}_4\text{N})\text{H}]$, **3**

An NMR tube, fitted with a Young's tap, was charged with complex **1** (15 mg) and 2,3,5,6-tetrafluoropyridine (2 fold excess) in C_6D_{12} and irradiated at room temperature (8 h), resulting in 100% conversion to **3**.

^1H NMR (C_6D_{12} , 300 K): δ 5.25 (s, 5H, C_5H_5), δ 1.35 (d, $J_{\text{P-H}}$ 12.6 Hz, 9H, PMe_3) δ - 12.42 (dd, $J_{\text{P-H}}$ 39.9 Hz, $J_{\text{Rh-H}}$ 22.9 Hz, 1H, Rh-H).

$^{31}\text{P}\{^1\text{H}\}$ NMR: δ 11.1 (dd, $J_{\text{Rh-P}}$ 142 Hz, $J_{\text{F-P}}$ 22.5 Hz).

^{19}F NMR: δ - 100.67 (m, 2F), δ - 113.7 (m, 2F).

2.6.8 Preparation of $[(\eta^5\text{-C}_5\text{H}_5)(\text{PMe}_3)\text{Rh} - (\kappa^2 \text{C,C}) \text{CH}_2\text{N}(\text{CH}_3)\text{C}_5\text{F}_3\text{N}]$, **4**

An 8 mm diameter NMR tube, fitted with a Young's tap, was charged with complex **1** (50 mg) and 4-dimethylamino-2,3,5,6 tetrafluoropyridine previously degassed, (5 fold excess) in hexane and irradiated at room temperature (8 h), resulting in 85% conversion to **3**. The excess of pyridine and solvent were pumped down under vacuum and part of the unreacted starting material and other by-products were sublimed at 25 °C and 1×10^{-4} mbar onto a liquid nitrogen cold finger, leaving a sticky brown residue. The brown residue was then washed with hexane (x 3 times), dried and dissolved in C_6D_6 in order to obtain NMR characterisation. Pure crystals appeared as light orange blocks at low T (-20 °C) from dry hexane. Suitable material for elemental analysis was obtained by washing the solid with a cold mixture of degassed ethanol/water.

^1H NMR (C_6D_6 , 300 K) : δ 4.98 (dd, CH_2 , H_b $J_{\text{H-Rh}}$ 4.7 Hz, $J_{\text{H-H}}$ 6.7 Hz), δ 4.87 (d, $J_{\text{Rh-H}}$ 1.3 Hz C_5H_5), δ 3.04 (ddd, CH_2 , H_a , $J_{\text{P-H}}$ 1.8 Hz, $J_{\text{Rh-H}}$ 6.7 Hz, $J_{\text{H-H}}$ 16 Hz), δ 2.96 (d, CH_3 $J_{\text{H-H}}$ 2.93 Hz), δ 0.65 (d, $J_{\text{P-H}}$ 10.6 Hz PMe_3).

$^{31}\text{P}\{^1\text{H}\}$ NMR: δ 13.8 (d, $J_{\text{Rh-P}}$ 158 Hz).

$^{13}\text{C}\{^1\text{H}\}$ NMR: δ 90 (t, $J_{\text{C-P}}$ 2.70 Hz, C_5H_5), 41 (ddd, $J_{\text{C-Rh}}$ 30 Hz, $J_{\text{C-P}}$ 14.3 Hz $J_{\text{C-C}}$ 1.3 Hz, CH_2), δ 40 (dd, $J_{\text{C-P}}$ 12 Hz $J_{\text{C-C}}$ 1.8 Hz, CH_3), δ 18 (d, $J_{\text{C-P}}$ 31.7 Hz PMe_3).

^{19}F NMR: F_A δ - 66.5 (dd, $J_{\text{F-F}}$ 13 Hz, 23 Hz) F_B δ -100 (dd, $J_{\text{F-F}}$ 13 Hz, 24 Hz) F_C δ - 180 (t, $J_{\text{F-F}}$ 23 Hz).

El mass-spec., m/z 418.0299 (M^+) 100%, (calculated 418.0293, difference 0.6 mDa).

Anal. Calcd. for $\text{C}_{15}\text{H}_{19}\text{N}_2\text{F}_3\text{P}_1\text{Rh}$: C, 43.08; H, 4.58; N, 6.70. Found: C, 43.21; H, 4.56; N, 6.54.

2.6.9 Preparation of $[(\eta^5\text{-C}_5\text{H}_5)(\text{PMe}_3)\text{Rh} - (\kappa^2 \text{C,C})\text{CH}_2\text{NC}_5\text{F}_3]$, **5**

An 8 mm diameter NMR tube, fitted with a Young's tap, was charged with complex **1** (50 mg) and 4-methoxy-2,3,5,6 tetrafluoropyridine previously degassed, (5 fold excess) in hexane and irradiated at room temperature (6

h), resulting in 20% conversion to **4**. The excess of pyridine and solvent were removed under vacuum and part of the unreacted starting material and other by-products were sublimed at 25 °C and 1×10^{-4} mbar onto a liquid nitrogen cold finger, leaving a brown sticky residue. The brown residue was then washed with hexane (x 3 times), dried and dissolved in C_6D_6 in order to get NMR characterisation. Crystals appeared as light orange blocks at low T (-20° C) from dry hexane.

1H NMR (C_6D_6 , 300 K) : δ 6.77 (dt, CH_2 , 1H, H_b J_{H-H} 5.3. Hz, J_{H-Rh} 1.4 Hz), δ 5.1 (ddd, CH_2 , 1H, H_a J_{P-H} 1.3 Hz, J_{Rh-H} 5.6 Hz, J_{H-H} 17.6 Hz), δ 4.73 (d, J_{Rh-H} 1.3 Hz, 5H, C_5H_5), δ 0.55 (d, J_{P-H} 10.5 Hz, 9H, PMe_3).

$^{31}P\{^1H\}$ NMR: δ 14.0 (d, J_{Rh-P} 159 Hz).

$^{13}C\{^1H\}$ NMR: δ 89.7 (t, J_{C-C} 3.2 Hz, C_5H_5), δ 17.9 (d, J_{C-P} 33Hz, PMe_3), δ 41 (ddd, J_{C-Rh} 30Hz, J_{C-P} 14.3 Hz J_{C-C} 1.3 Hz, CH_2).

^{19}F NMR: F_A δ - 64.5 (dd, J_{F-F} 13Hz, 23 Hz, 1F), F_B δ - 99 (dd, J_{F-F} 13 Hz, 23 Hz, 1F), F_C δ -171.9 (t, J_{F-F} 23 Hz, 1F).

EI mass-spec.: m/z 404.9975 (M^+) 100%, (calculated 404.9977, difference 0.2 mDa).

2.6.10 Preparation of $C_5F_4N(OCD_3)$

Na (68 mg, 2.96 mmol) was slowly added to a solution of deuterated methanol (5 ml). Upon complete reaction of Na, 500 mg of C_5F_5N (2.96 mmol) was added drop-wise and the solution was stirred and heated under reflux for 30 min. The product was treated with water (15 ml) and extracted with ether (3x10 ml). The organic extract was dried over $MgSO_4$ and the solvent removed by rotary evaporator giving a colourless oil.

2D NMR (C_6H_6 , 300 K): δ 3.28 (CD_3).

^{19}F NMR: δ - 91.9 (2 F,m) δ - 160.9 (2 F,m).

EI mass-spec.: m/z 184.0336 (M^+) 100%, (calculated 184.0339).

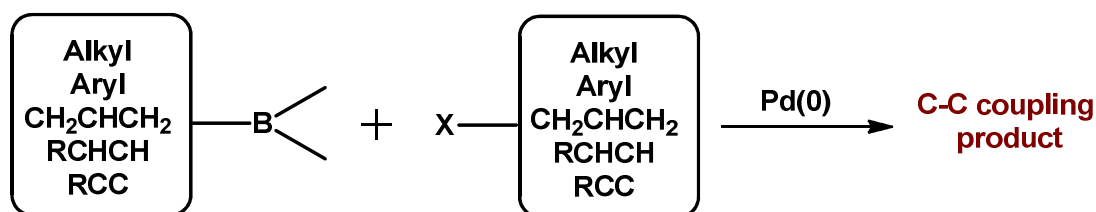
IR (liquid film) $\nu(CD)$ / cm^{-1} 2082 (s), $\nu(CF)$ / cm^{-1} 900-1000 (s), $\nu(CN)$ / cm^{-1} 1648 (s), ν (ring vibration) 1480 (s).

3 Photochemical oxidative addition of B-H bonds at Ru and Rh centers: solution photochemistry

3.1 Introduction

Borane reagents are used in a wide range of applications, especially in organic synthesis due to the versatility of boron chemistry. Organoboron compounds can in fact act either as electrophiles, because of their Lewis acidity, and as nucleophiles.¹ The interest in boron chemistry from the organometallic community has greatly expanded in the last twenty years resulting in the formation of three main areas of research: cross-coupling reactions to form C-C bonds, borylation of alkane C-H bonds, and hydroboration of alkenes.

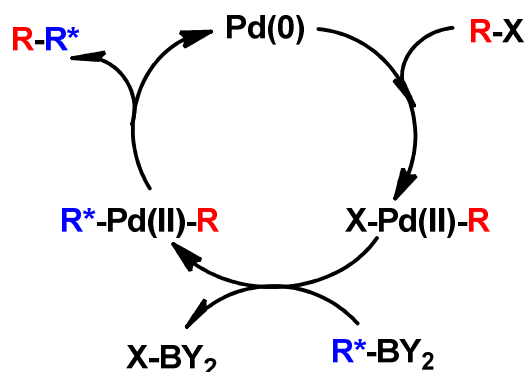
The advent of metal-catalyzed cross-coupling reactions between aryl or alkylboron compounds and organic halides has expanded the use of organoboron reagents in synthetic methodology (Scheme 1); furthermore organoboron reagents are neither water nor oxygen sensitive and can be used under mild conditions. That is the reason why these reactions are among the most used in C-C bond formation.²



Scheme 1. Schematic representation of cross-coupling reactions between an organoboron reagent and an organohalide.

Palladium(0) complexes, such as Pd(PPh₃)₄, are among the best catalysts in Suzuki-Miyaura coupling reactions, but Pd(II) precursors can also be employed to generate the active unsaturated Pd(0) species in situ. Currently, studies on Suzuki-Miyaura reactions aim to develop more efficient Pd-catalysts,³ as well as to improve methodologies to achieve more challenging targets.⁴ Scheme 2 shows the proposed catalytic cycle for C-C coupling reactions where oxidative

addition of the organo-halides takes place in first step, followed by transmetalation of the organoboron reagent to form a Pd(II) intermediate. Reductive elimination of the two organic parts leads to the formation of the C-C coupled product and regeneration of the active catalyst Pd(0).²



Scheme 2. Proposed catalytic cycle for Suzuki-Miyaura coupling reactions, Y = O, OH, OⁱPr.

Based on this main catalytic cycle, further developments have improved the understanding of the mechanism for reactions with different coupling partners; Marder and co-workers for instance, investigated by DFT calculations the reaction of aryl-halides with HBpin (for structure see Scheme 18, page 61) catalysed by Pd(0). As a result they published a novel mechanism where σ -bond metathesis takes place in the transmetalation process to afford the organoboron compound.⁵

Studies are also looking at C-C coupling methods employing less expensive metals; for example a novel, clean, one-step reductive coupling between benzyl halides and HBpin was reported involving Mg(0) as a catalyst to make benzylboronic esters in good yields.⁶

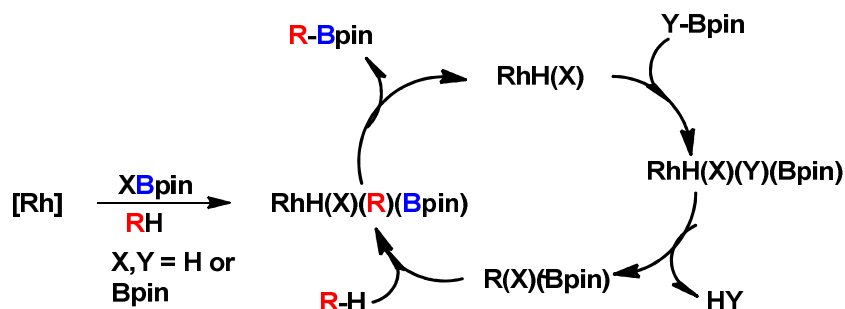
Borylations of alkyl, aryl and heteroaromatic C-H bonds have also seen an impressive development in the last two decades, especially due to the pioneering work of Hartwig and coworkers (Scheme 3). The topic has been extensively reviewed;⁷ simplistically it combines the activation of two bonds (C-H and B-H/B-B) by a metal centre to form a C-B bond. Calculations highlighted

that the process is thermodynamically⁸ and kinetically favored,⁹ the downhill energetic values are attributed to the strong σ -donation character of the boryl group which helps to deprotonate the acidic C-H bond of the σ -alkane complex formed, *plus* the presence of an empty *p*-orbital on the boron which makes the transition state for C-H bond cleavage more stable.



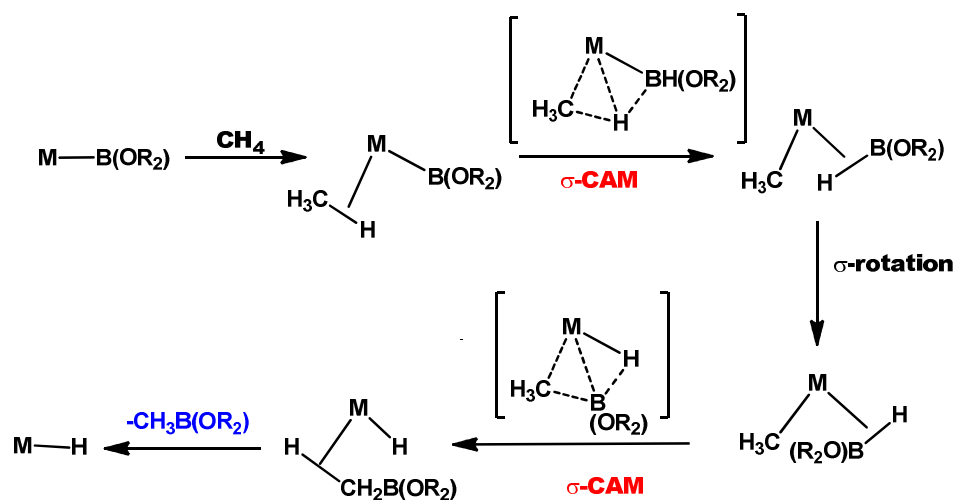
Scheme 3. General reaction scheme for borylations involving boranes and diboranes substrates.

Differently from other C-H functionalisation methodologies, C-H borylation has the unique feature of high regioselectivity; rhenium, rhodium and iridium complexes are invaluable in the regiospecific borylation of alkanes, arenes and heteroaromatics.¹⁰ The first catalytic terminal functionalisation of an alkane by $\text{Cp}^*\text{Rh}(\eta^4\text{-C}_6\text{Me}_6)$ in the presence of HBpin or B_2pin_2 (for structure see Scheme 18, page 61) was reported by Hartwig; the method afforded different organoboron compounds that are very useful in various organic syntheses.¹¹ The mechanism proposed originally involved oxidative addition of the B-H/B-B bond at the metal centre to form a rhodium-boryl-hydride complex; reductive elimination of H_2 /borane created the free coordination site for the alkane to insert and to afford a rhodium-alkyl-boryl complex (Scheme 4). Finally the product was formed by rapid and thermodynamically favored B-C coupling.



Scheme 4. General proposed mechanism for borylation reaction of primary C-H bonds via oxidative addition. X , $\text{Y} = \text{H}$ or Bpin .

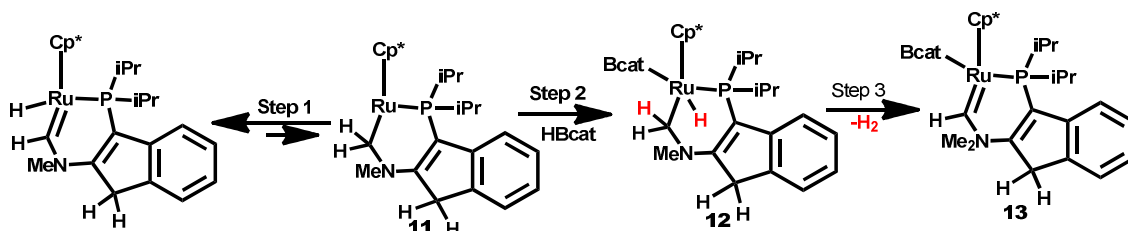
Further theoretical calculations suggested a metal assisted σ -bond metathesis mechanism (σ -CAM mechanism) for the formation of the borane complex; the latter follows rearrangement to form a complex with the suitable geometry for C-B bond formation (Scheme 5). The boryl ligand and the alkyl group need to be mutually *cis* for a second σ -bond metathesis to take place and generate the terminally functionalized alkane.⁹ The σ -CAM mechanism proposed by Perutz and Sabo-Etienne involves the participation of σ -complexes as intermediates which through dynamic rearrangement participate in the catalytic cycle at a constant oxidation state.¹²



Scheme 5. Mechanism of methane borylation with σ -CAM step.

Several studies have been carried out on the borylation of hydrocarbons by Ru complexes. $[Cp^*RuCl_2]_2$ and $[Cp^*RuCl]_4$, were found to be good catalysts to functionalize primary C-H bonds in the presence of B_2pin_2 . In contrast, they did not show high activity in aromatic C-H borylation reactions. The reactivity and dynamics of a novel ruthenium complex (Scheme 6) incorporating an unusual phosphorus-coordinated N-heterocyclic carbene was explored by Stradiotto *et al.* It was found that upon reaction with HBcat (for structure see Scheme 18, page 61), 1,2 hydrogen transfer [Step 1] occurred to give a coordinatively unsaturated species **11**, followed by oxidative cleavage of the B-H bond [Step

2] **12**, and finally loss of H₂ to generate the boryl-carbene species **13**. Notably, the reaction did not occur under similar conditions with HBpin.¹³



Scheme 6. Oxidative addition of HBcat at a Ru centre, phosphine coordinated, N-heterocyclic carbene species.

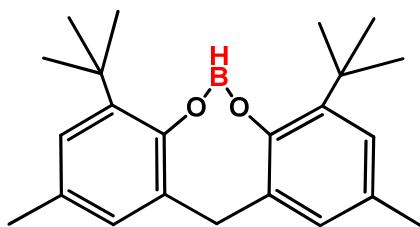
While Rh and Ru complexes provide the best tools to use in selective functionalization of aliphatic primary C-H bonds over secondary or tertiary, Ir complexes direct aromatic C-H borylation with high steric control; hence C-H bonds lacking *ortho* substituents are preferred.¹⁰ The best Ir-catalyst for these type of reactions was formed *in situ* by reacting [Ir(COD)OMe]₂ dimer with di-*t*-butyl-bipyridine in the presence of excess of diborane reagent. The reaction proceeds faster than the one to functionalize alkanes; the reason for this is the milder conditions required to generate the unsaturated intermediate.¹⁴

Electronic effects were found not to influence the selectivity of the process, but the rates were different when employing electron-rich in place of electron-poor arenes. Surprisingly, reactions were faster when electron poor reagents were employed. A highly reactive tris-boryl-Ir(III) species was isolated and proposed as intermediate.¹⁵

In contrast, electronic effects are important in Ir-catalysed C-H borylation of heteroaromatics; the α -position to the heteroatom is functionalized in a five-member heterocycle; however, the reactivity of pyridines showed selectivity for the β -position to nitrogen. The different behavior was tentatively explained by proposing nitrogen coordination of the pyridine to the metal centre which would sterically block the C-H functionalisation in alpha position.¹⁶ Finally, a highly selective method for the Ir-catalyzed directed C-H borylation was achieved introducing a hydrosilyl functionality as directing group. The methodology was

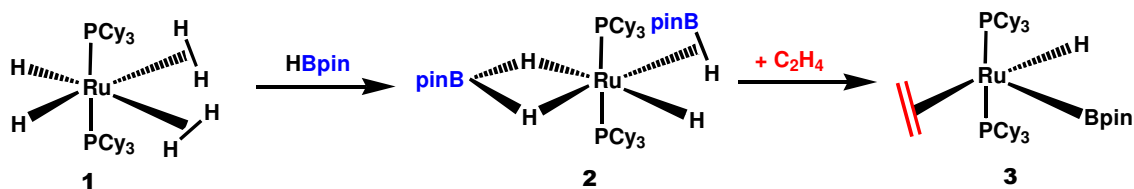
developed in first for substituted-arenes¹⁷ and expanded afterwards to N-containing heteroaromatics.¹⁸

Metal-catalyzed hydroboration of alkenes is also a much investigated field due to the vast applications of alkene boronic esters in organic synthesis. Since the first example involving rhodium and HBcat was reported in 1985¹⁹ many papers were published presenting different metals as catalysts and different boranes as boronating reagents. The [Ir(COD)Cl₂]₂ dimer was reported as a precursor to catalytic terminal hydroboration of cyclohexene and cyclopentene in the presence of B₂pin₂; the selectivity towards allylic over vinylic C-H bonds for cyclic alkenes was controlled by proper choice of reaction conditions. Preference for allyl C-H functionalisation was determined for acyclic substrates.²⁰ The same Ir-dimer was recently employed as a precursor in the reaction with an unusual bulky boron reagent (Scheme 7). The experiments afforded the desired products with aliphatic alkenes but failed with vinyl arenes.²¹



Scheme 7. Structure of the bulky dioxaborocine used in hydroboration reactions.

A study which combines hydroboration and dehydrogenative borylation of alkenes was published by Sabo-Etienne and co-workers. The complex $\text{RuH}_2(\text{H}_2)_2(\text{PCy}_3)_2$ was established to catalyze borylation of linear and cyclic alkenes in the presence of HBpin with good yields. Dehydrogenative borylation competed with hydroboration in reactions with large ring cyclic alkenes affording the diboronated products. The unsaturated complex **3**, $\text{RuH}(\text{Bpin})(\text{C}_2\text{H}_4)(\text{PCy}_3)_2$, was observed in solution and proposed as intermediate in the catalytic cycle (Scheme 8).²²



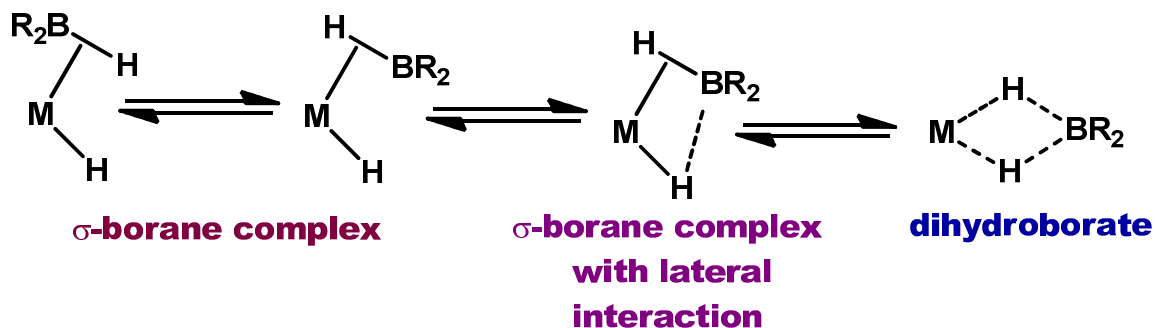
Scheme 8. Formation of the unsaturated intermediate **3** in the hydroboration reaction of $\text{RuH}_2(\text{H}_2)_2(\text{PCy}_3)_2$ in the presence of HBpin.

There is a growing interest in the earlier transition metals as inexpensive alternatives to their heavier congeners; *Wu et al.* reported a chemo-, regio-, and stereoselective Fe-catalyzed hydroboration of 1, 3-dienes to afford linear (*E*)- γ -disubstituted allylboranes. In addition to giving access to highly functionalized molecules that are otherwise very hard to synthesize, the Wu reaction showed an unprecedented reactivity for an iron catalyst.²³

The proposed catalytic cycle has still a few unsolved points and it is based on experimental studies using deuterated HBpin; the diene coordinates to the iron

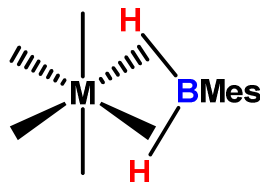
other. Many reactions have been reported where η^2 -coordination is an essential step for achieving oxidative addition or reductive elimination.

Sabo-Etienne and coworkers explored the coordination modes of the complex $\text{RuH}_2(\text{H}_2)(\text{PCy}_3)_2$ towards different boranes. The Ru complex used is a perfect illustration of an ideal balance between σ -donation and back-donation with two unstretched dihydrogen ligands that proved to be very labile. Because of the peculiar electronic features of this complex they were able to isolate a σ -complex of Ru showing HBpin coordinated in two different fashions: σ -borane and dihydroboration (Scheme 10).²⁵ Theoretical calculations on the system suggested σ -coordination as the favored mode with less acidic boranes such as HBpin and HBcat, while dihydroboration was achieved when a more Lewis acidic borane was used.²⁶



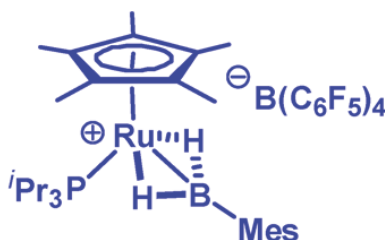
Scheme 10. Possible coordination modes of a secondary borane to a metal hydride fragment.

Further studies with $\text{RuH}_2(\text{H}_2)(\text{PCy}_3)_2$ and mesityl borane highlighted another possible coordination mode where the B-H moieties are both bound in an η^2 -fashion to the metal centre (Scheme 11).²⁷ The bis σ -bond borane ruthenium complexes present great potential for reversible hydrogen release.²⁸ Sabo-Etienne group has also recently published a borane mediated CO_2 reduction using the same Ru complex, where HBpin acts as “activator and oxygen scavenger” in reducing CO_2 to form C1 and C2 compounds such as pinBOCH₃ and pinBOCH₂OCHO.²⁹



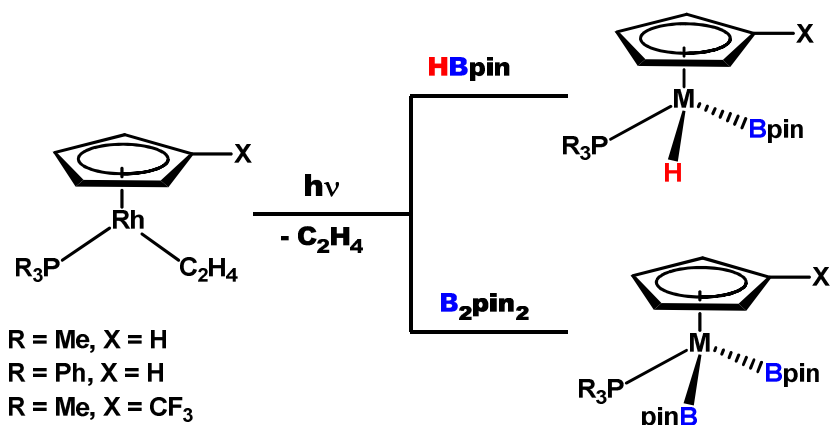
Scheme 11. Bis σ -borane complex of H_2BMes .

An unusual cationic ruthenium species was reported by Stradiotto *et al.*, showing the B-H moiety of mesitylborane also bound in a double η^2 fashion (Scheme 12).³⁰



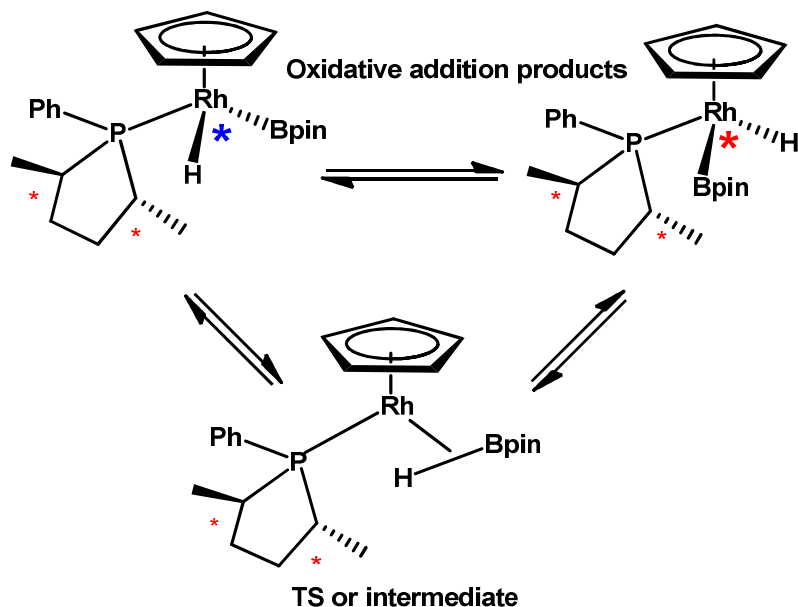
Scheme 12. Cationic Ru complex of mesitylborane.

Besides all these “fashionable” coordination modes, simple oxidative addition at the metal centre has also been reported. Hartwig and co-workers, for instance, isolated and characterized crystallographically Ir(V) boryl complexes postulating them as intermediates in the regioselective borylation of alkenes.³¹ Photochemical oxidative addition of HBpin and B_2pin_2 at CpRh-phosphine centers was investigated in our group (Scheme 13); the corresponding oxidative addition products were characterized by NMR spectroscopy and a X-ray crystal structure was obtained for the complex $\text{CpRhH}(\text{Bpin})(\text{PPh}_3)$.



Scheme 13. Photochemical reactions of CpRh-phosphine complexes in the presence of HBpin and B₂pin₂ affording the oxidative addition products.

A very weak interaction between boron and hydrogen (B...H = 2.09(2) Å) was observed in the structure; nevertheless bond lengths and angles were much closer to the ones expected for the oxidative addition process. Similar Rh(boryl)H complexes were previously crystallographically characterised by the Hartwig⁹ and Marder^{32,33} groups. Comparison between those structures and the CpRh(PPh₃)H(Bpin) complex led to conclude that different degrees of oxidative addition are achieved with respect to the electronic properties of the ligands around the metal centre.³⁴ Further studies introduced a chiral phosphine at the metal centre and allowed to identify two different isomers formed upon oxidative addition of HBpin which underwent intermolecular exchange. DFT calculations suggested a σ -borane complex as a transition state for the exchange process (Scheme 14).³⁵



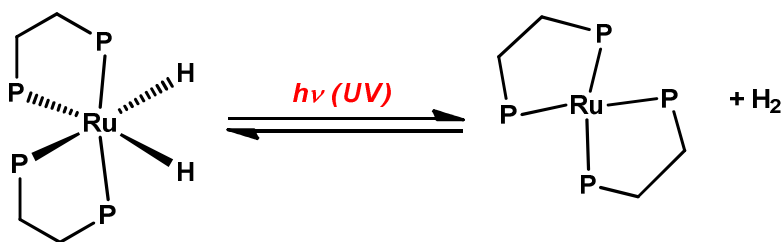
Scheme 14. Two different isomers formed in oxidative addition reactions of HBpin to a chiral phosphine-rhodium centre. The σ -compound was postulated as transition state by DFT calculations.

Finally, our group has also recently succeeded in the isolation and characterization by NMR spectroscopy of $\text{Ru}(\text{PP})_2(\text{H})(\text{Bpin})$, ($\text{PP} = \text{BPE}$ and DuPhos) complexes formed photochemically by reacting $(\text{PP})_2\text{RuH}_2$ in the presence of HBpin. The structure of the $(\text{BPE})_2\text{Ru}(\text{H})(\text{Bpin})$ complex was confirmed crystallographically, bond lengths and angles were found to be consistent with an oxidative addition product rather than a σ -borane coordination.³⁶

3.2 Results

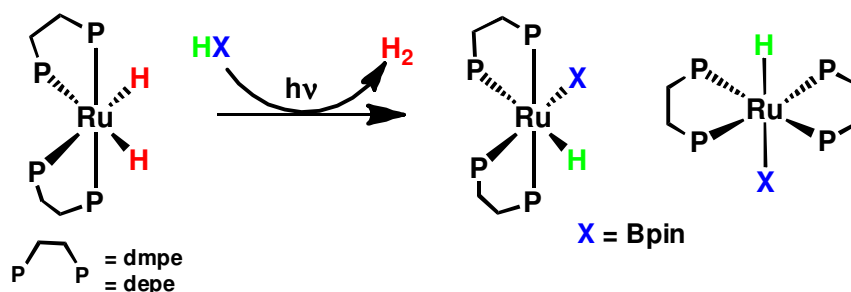
3.2.1 Ruthenium dihydride complexes

Ruthenium dihydride complexes have been extensively studied in our group. Their photolysis induces reductive elimination of dihydrogen to form a highly reactive electronically unsaturated square planar metal complex $\text{Ru}(\text{PP})_2$ (Scheme 15), followed by oxidative addition of different ligands.³⁷ Multidentate phosphine ligands are found to give greater selectivity to the photochemistry of these complexes, selectivity improves compared to the monodentate analogues due to increased kinetic stability owing to the chelate effect.



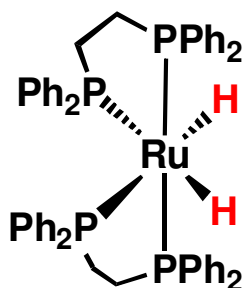
Scheme 15. Photoelimination of dihydrogen from $(\text{PP})_2\text{RuH}_2$ complexes to form the square-planar 16-electron intermediate $\text{Ru}(0)(\text{PP})_2$.

Kinetic studies of the oxidative addition at $\text{Ru}(\text{PP})_2$ (PP, depe = 1,2-bis-diethylphosphinoethane, dmpe = 1,2-bis-dimethylphosphinoethane) initiated by laser flash photolysis found that the rate constants of reaction followed the order $k(\text{H}_2) > k(\text{HBpin}) > k(\text{Et}_3\text{SiH})$; hence the regeneration of the dihydride occurs with a higher rate constant than formation of either the hydrido-boryl or hydrido-silyl complexes.^{37,38} It was also found that upon photolysis in the presence of a borane compound such as HBpin, coordinatively unsaturated complexes of the type $\text{Ru}(0)(\text{PP})_2$ undergo oxidative addition of the B-H bond to form *trans* and *cis* $\text{Ru}(\text{PP})_2(\text{H})\text{Bpin}$ (Scheme 16).



Scheme 16. Photochemical reaction of $(\text{PP})_2\text{RuH}_2$ complexes with HBpin to form *cis* and *trans* $(\text{PP})_2\text{RuH}(\text{Bpin})$.

Formation of the ruthenium boryl hydride complexes was demonstrated by the combined use of NMR spectroscopy and time resolved studies without the support of crystallographic structures for reaction of $\text{Ru}(\text{depe})_2\text{H}_2$ and $\text{Ru}(\text{dmpe})_2\text{H}_2$ in the presence of HBpin.³⁹ My studies followed the results reported in 2004, moving on to investigate the reactivity of a Ru-dihydride complex coordinated to a sterically demanding and electron poor phosphine dppe (dppe = diphenylphosphinoethane) (Scheme 17). In addition the reactivity of $\text{CpRh}(\text{C}_2\text{H}_4)_2$ towards boranes was also explored.

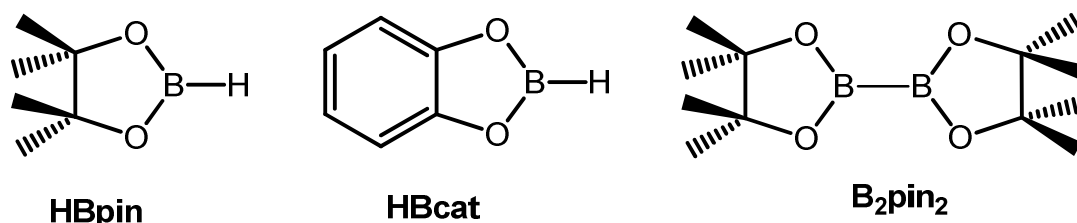


Scheme 17. Structure of the Ru complex investigated.

3.2.2 $\text{Ru}(\text{dppe})_2\text{H}_2$ in the presence of HBpin and HBcat

Scheme 17 shows the structure of the $\text{Ru}(\text{dppe})_2\text{H}_2$ complex investigated. The corresponding 4-coordinate 16-electron $\text{Ru}(\text{dppe})_2$ species is formed via photodissociation of dihydrogen; the previous studies had provided strong evidence that $\text{Ru}(\text{dppe})_2$ has a structure close to square planar, and the

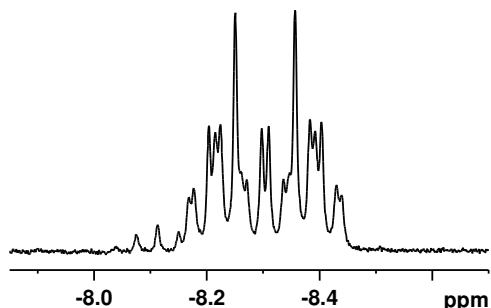
coordinatively unsaturated complex reacts with different quenching molecules.³⁷ Photolysis of the complexes is carried out in C₆D₆, at room temperature with a broadband UV source in the presence of excess of pinacolborane, HBpin, and catecholborane, HBcat (Scheme 18).



Scheme 18. Boranes used in these studies.

3.2.3 Analysis of Ru(dppe)₂H₂ complex

The NMR hydride signal of Ru(dppe)₂H₂ in the ¹H NMR spectrum is centred at δ -8.30 ppm. The signal is a second order multiplet which comprises signals of both *cis*- and *trans*- isomers in a narrow δ-range (Figure 1, top). However, recording a ¹H{³¹P} NMR spectrum, it is possible to see singlets due to each isomer. The simplified spectrum gives two peaks, one at δ -8.30, and another at δ -8.10, in a 20:1 ratio, representing *cis* and *trans* respectively (Figure 1, bottom). The two isomers are seen very clearly in the ³¹P{¹H} NMR spectrum because all phosphorus atoms in the *trans* complex are magnetically equivalent, and the signal is simply a singlet at δ 83.9. In the *cis* complex, there are two sets of two equivalent P atoms, and so we see two triplets at δ 79.5 and δ 66.2 (Figure 2).



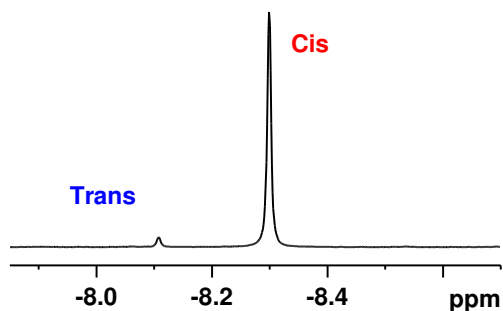


Figure 1. ^1H NMR spectrum of hydride region for complexes *cis/trans* $\text{Ru}(\text{dppe})_2\text{H}_2$ in C_6D_6 (top), and $^1\text{H}\{^{31}\text{P}\}$ NMR spectrum of hydride region for complexes *cis/trans* $\text{Ru}(\text{dppe})_2\text{H}_2$ in C_6D_6 (bottom).

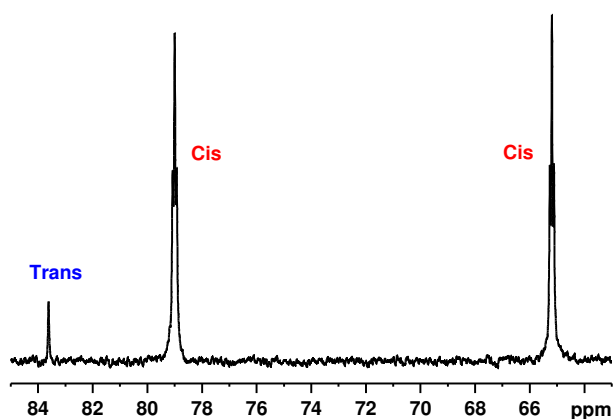


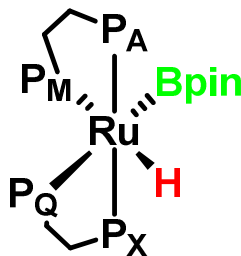
Figure 2. $^{31}\text{P}\{^1\text{H}\}$ NMR spectrum of complexes *cis*- $\text{Ru}(\text{dppe})_2\text{H}_2$ and *trans*- $\text{Ru}(\text{dppe})_2\text{H}_2$ in C_6D_6 .

3.2.4 Solution photochemistry: $\text{Ru}(\text{dppe})_2\text{H}_2$ complex with HBpin

Complex **1** does not react thermally at room temperature in the presence of an excess (10 fold) of HBpin, but a pale yellow solution of complex **1** reacted upon irradiation at room temperature for 15 hours. After that time the reaction was complete, and it was analyzed by NMR spectroscopy at room temperature.

The $^{31}\text{P}\{^1\text{H}\}$ NMR spectrum shows the formation of a single product where all of the phosphorus atoms are now magnetically inequivalent, leading to the appearance of a rather interesting ABMQ spin system. The resonances for the mutually *trans* phosphorus P^{A} and P^{X} present features of an AB quartet (Figure 3) (Scheme 19); the AB spin system is centered at δ 75.9. Each component

split into apparent doublet of doublet of doublets, with coupling constants of $J_{AM} = 21$, $J_{AQ} = 10$ Hz; and $J_{XM} = 16$ $J_{XQ} = 10$ Hz. J_{AX} was measured to be 249 Hz. There are two further resonances on the $^{31}\text{P}\{^1\text{H}\}$ NMR spectrum: a broad one at δ 57.3 assigned to the phosphorus in *trans* position to boron, P^{Q} , and a quartet at δ 53.7 for the phosphorus *trans* to the hydride, P^{M} .



Scheme 19. Scheme for a *cis* Ru boryl complex which shows four different phosphorus environments.

The ^1H spectrum shows the appearance of a new hydride resonance as a doublet of quartets at δ - 8.30 ($J_{\text{PH}} = 20.7$ Hz, 58 Hz) (Figure 4, bottom). The reaction proceeded cleanly to the formation of only one species; no other hydride resonances are present and no other products are detected on the $^{31}\text{P}\{^1\text{H}\}$ NMR spectrum. Upon decoupling from ^{31}P the doublet of quartets simplifies to a singlet confirming coupling to four inequivalent phosphorus atoms in a *cis* arrangement (Figure 4).

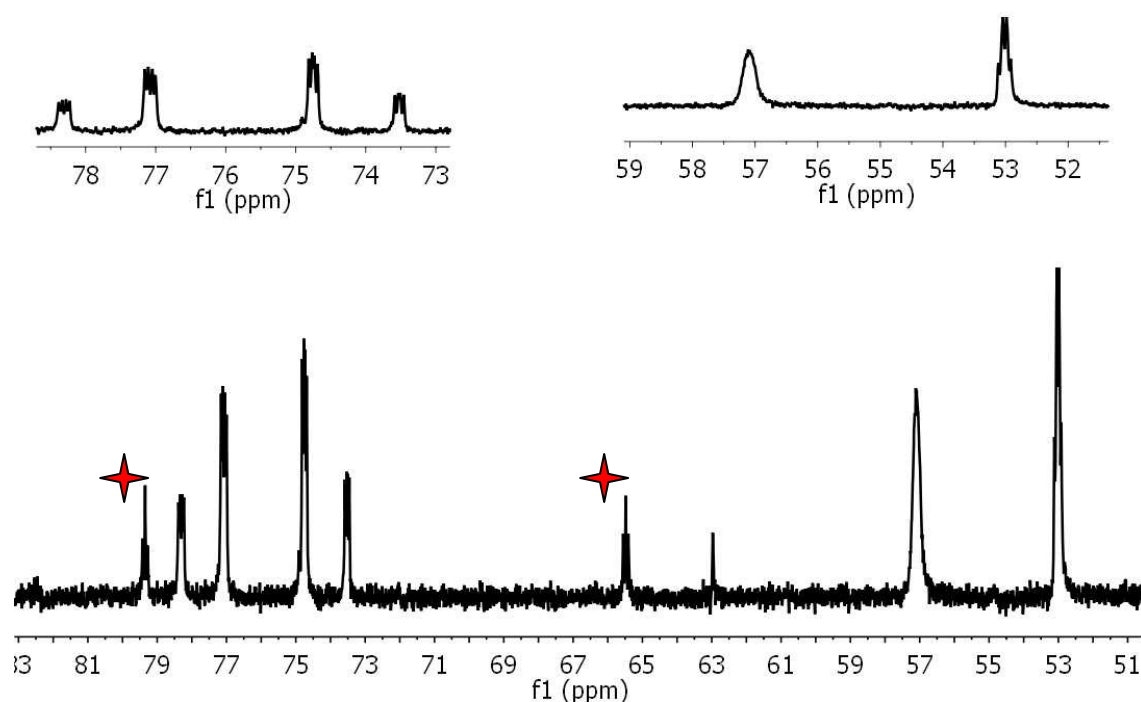


Figure 3. $^{31}\text{P}\{^1\text{H}\}$ NMR spectrum of reaction of the complex $\text{Ru}(\text{dppe})_2\text{H}_2$ with HBpin in C_6D_6 after 12 hours of photolysis at 90% of conversion. The stars referred to starting material left. Top: Enlargement of the resonances for $\text{Ru}(\text{dppe})_2\text{H}(\text{Bpin})$.

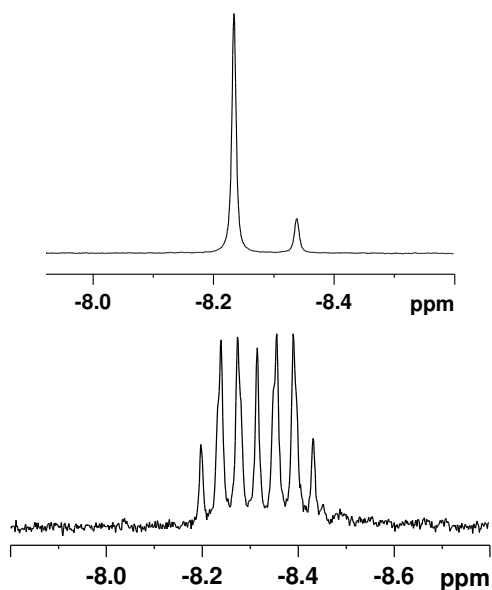


Figure 4. Hydride region of the ^1H NMR spectrum (bottom) and $^1\text{H}\{^{31}\text{P}\}$ NMR spectrum (top) of photochemical reaction of complex $\text{Ru}(\text{dppe})_2\text{H}_2$ with HBpin in C_6D_6 . The minor peak in the $^1\text{H}\{^{31}\text{P}\}$ NMR spectrum is the starting complex $\text{Ru}(\text{dppe})_2\text{H}_2$.

The $^{31}\text{P}\text{-}^1\text{H}\{^{31}\text{P}\}$ correlation spectrum shows cross peaks between the hydride for the product and the signals corresponding to the ABMQ system in the ^{31}P NMR spectrum (Figure 5). Unfortunately, no evidence of Ru-boryl resonances has been observed measuring ^{11}B NMR spectra, but we are confident because of the fact that one of the peaks in the $^{31}\text{P}\{^1\text{H}\}$ NMR spectrum (δ 57.3 ppm) appears to be broader than the rest indicative of a trans coupling with a quadrupolar nucleus. Unfortunately no resonances were detected in the ^{11}B NMR spectrum, due to the excess of HBpin and broadness of the peak corresponding to the metal boryl. Attempts to purify the complex, in order to remove the excess of ligand and obtain better ^{11}B NMR characterization failed due to regeneration of the starting material $\text{Ru}(\text{dppe})_2\text{H}_2$ upon pumping off the reaction mixture. Attempts to crystallize the complex were also unsuccessful; the product decomposes to regenerate the starting ruthenium dihydride complex when left in solution for crystallization. LIFDI mass spectrometry showed the presence of the fragment $\text{Ru}(\text{dppe})_2$, but no peak for the Ru-boryl hydride was detected. This is not surprising if it is considered that the complex appeared to be unstable under very mild conditions (solution, room temperature).

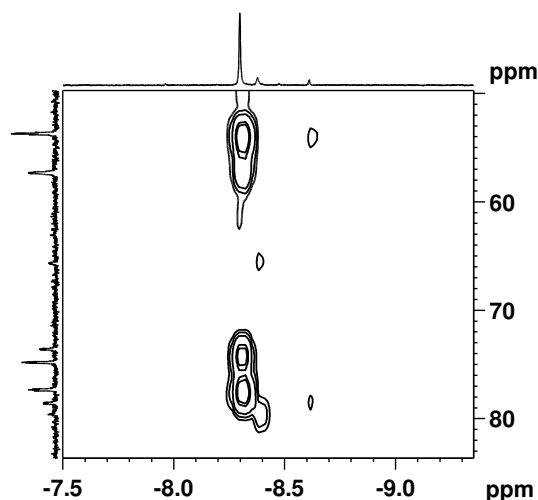
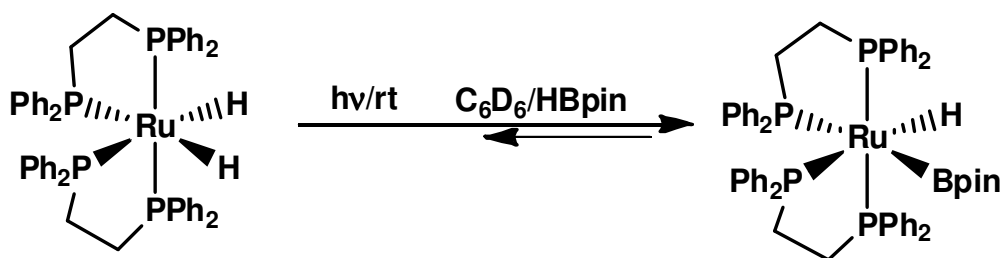


Figure 5. $^1\text{H}\{^{31}\text{P}\}\text{-}^{31}\text{P}$ NMR spectrum of photochemical reaction of complex $\text{Ru}(\text{dppe})_2\text{H}_2$ with HBpin in C_6D_6 .

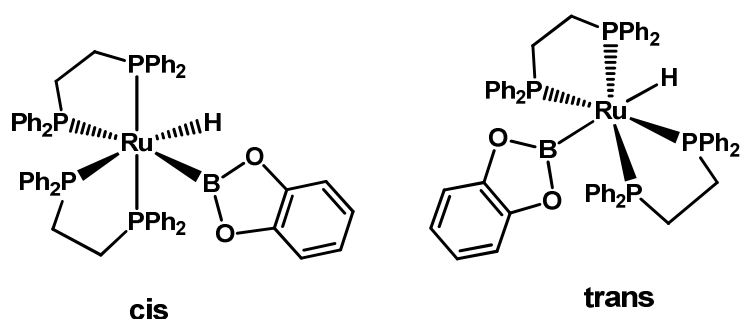
The complex was assigned as *cis*-Ru(dppe)₂H(Bpin), (Scheme 20). The ¹³C{¹H} spectrum shows a resonance at δ 79.9 assigned to the BOC carbon, considerably shifted upfield compared to free HBpin (δ 82.9). The presence of B₂pin₃ (¹¹B NMR δ 21.9) was also detected after photolysis. The solvent was changed in the attempt to stabilize the Ru boryl complex, but no difference in reactivity was observed on moving to toluene. Hexane, cyclohexane and hexamethyldisiloxane were also tried but the starting Ru dihydride complex showed low solubility in all of them. Reaction in neat HBpin did not improve the stability of the boryl-ruthenium complex formed either.



Scheme 20. Reaction scheme for oxidative addition of HBpin to RuH₂(dppe)₂ to form the *cis* isomer Ru(dppe)₂H(Bpin).

3.2.5 Solution photochemistry: Ru(dppe)₂H₂ complex with HBcat

A pale yellow solution of the complex Ru(dppe)₂H₂ in C₆D₆ was irradiated at room temperature for 30 min in the presence of 10 equivalents of HBcat. After that time the reaction was complete, and it was analyzed by NMR spectroscopy at room temperature. The complex did not react thermally in the presence of HBcat, but its photolysis in C₆D₆ led to the detection of two new hydride resonances attributed to the *cis* and *trans* isomers of the Ru(dppe)₂H(Bcat) complexes (*cis:trans* ratio is ca. 7:2) (Scheme 21) and new resonances in the ³¹P{¹H} NMR spectrum.



Scheme 21. Cis and trans isomers formed for reaction of $\text{Ru}(\text{dppe})_2\text{H}_2$ with HBcat.

The new hydride containing products resonated at δ -7.89 (*cis*, J_{PH} 20 Hz, 59.3 Hz, doublet of quartets) and δ -6.37 (*trans*, J_{PH} 19.3 Hz, quintet) in the ^1H spectrum (Figure 7). Upon ^{31}P decoupling both the hydride resonances simplified to singlets. The *cis* $\text{Ru}(\text{dppe})_2\text{H}(\text{Bcat})$ product exhibited the same ABMQ system in the $^{31}\text{P}\{^1\text{H}\}$ NMR spectrum previously observed for the *cis*-Ru-HBpin analogue and a new peak was found for the *trans* isomer as a singlet at δ 80.

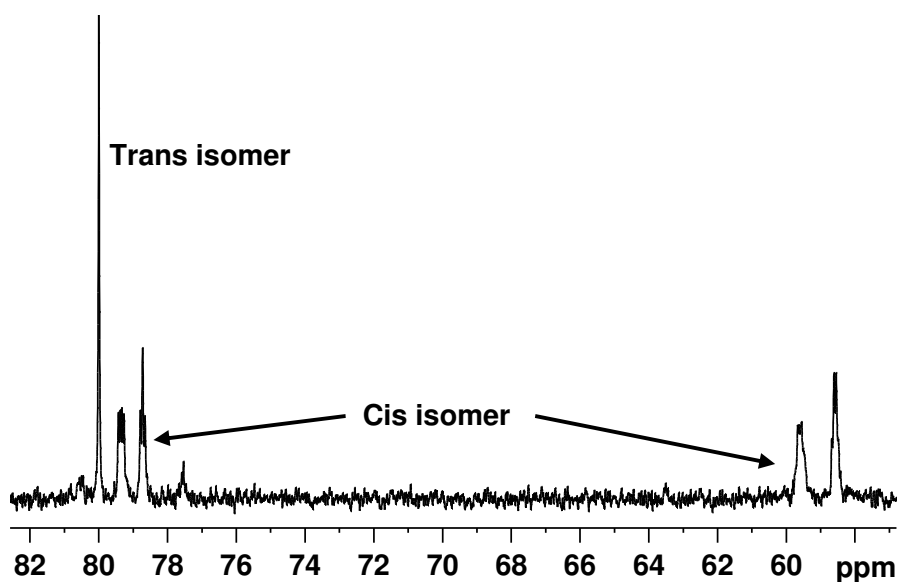


Figure 6. $^{31}\text{P}\{^1\text{H}\}$ NMR spectrum of photochemical reaction of complex $\text{Ru}(\text{dppe})_2\text{H}_2$ with HBcat in C_6D_6 showing the singlet for the *trans* isomer and the ABMQ system for the *cis* one.

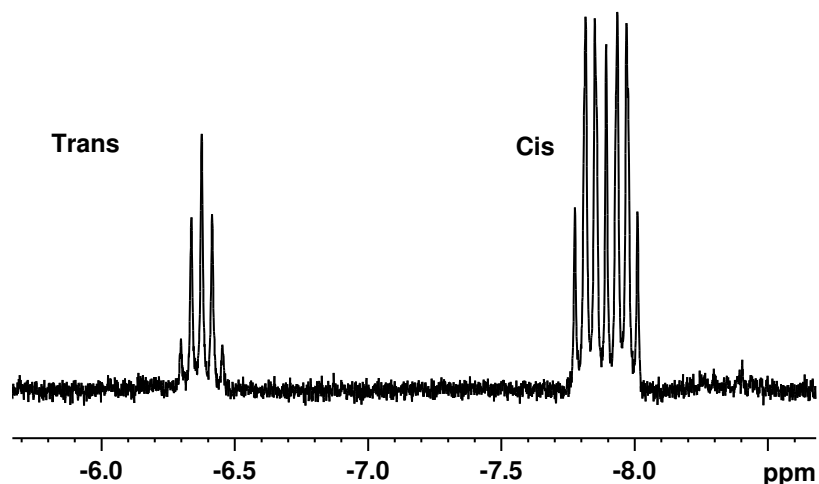


Figure 7. Hydride region of the ^1H NMR spectrum of photochemical reaction of complex $\text{Ru}(\text{dppe})_2\text{H}_2$ with HBcat in C_6D_6 to form the new species *cis*- $\text{Ru}(\text{dppe})_2\text{H}(\text{Bcat})$ and *trans*- $\text{Ru}(\text{dppe})_2\text{H}(\text{Bcat})$.

The $^{31}\text{P}\{^1\text{H}\}$ - ^1H correlation spectrum showed cross peaks between the hydrides for the products and the signals corresponding to the *cis* and *trans* species in the $^{31}\text{P}\{^1\text{H}\}$ NMR spectrum (Figure 8). Purification and isolation of the products were not possible for the same reasons mentioned for the HBpin analogue. The complex is unstable in solution and under vacuum conditions, reforming the starting material.

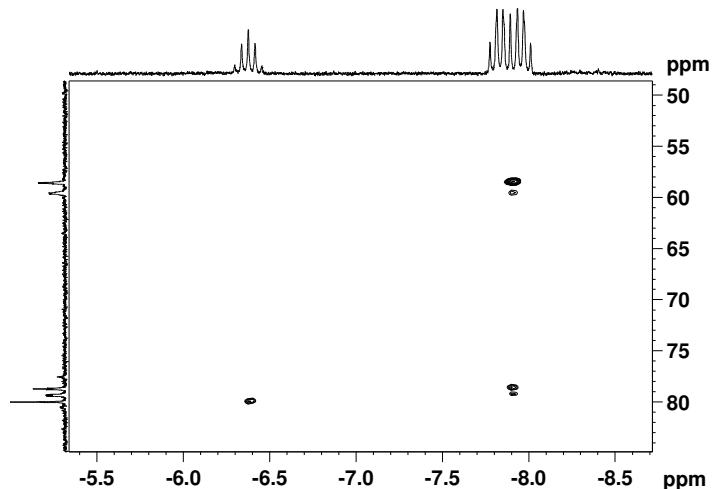


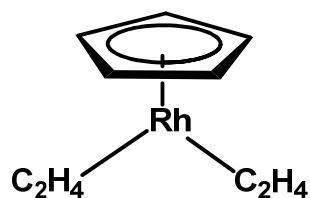
Figure 8. ^1H - $^{31}\text{P}\{^1\text{H}\}$ NMR spectrum of photochemical reaction of complex $\text{Ru}(\text{dppe})_2\text{H}_2$ with HBcat in C_6D_6 showing the ABMQ system in the $^{31}\text{P}\{^1\text{H}\}$ correlated to the *cis* hydride and a cross peak between the singlet in the $^{31}\text{P}\{^1\text{H}\}$ and the quintet resonance in the ^1H spectrum for the *trans* hydride.

3.3 Cyclopentadienyl Rh complexes in B-H and B-B activation

As already mentioned, CpRh complexes have been investigated in the presence of boranes; our group reported studies of CpRh(PR₃)(C₂H₄)₂ in the presence of HBpin and B₂pin₂³⁴ as well as investigations using chiral phosphines.³⁵

Hartwig and coworkers explored the thermal reaction of Cp^{*}Rh(C₂H₄)₂ in the presence of B₂pin₂ for the regioselective functionalization of alkanes, they found the catalyst to be very active (84% conversion to the alkyl-Bpin). However, by-products from the borylation of the alkene were detected and therefore they tested a different complex where reaction between the extruded ligand and the substrate did not take place. They found that Cp^{*}Rh(η⁴-C₆Me₆) was also an active catalyst in the same type of reaction showing a longer lifetime than the bis-ethylene analogue.¹¹

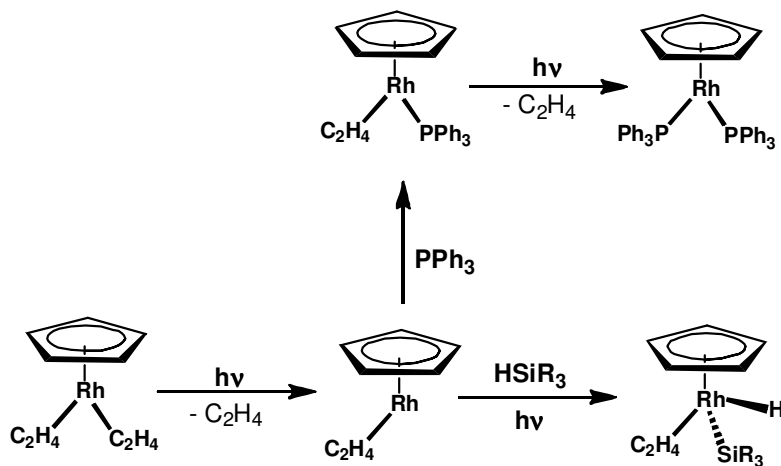
The group of Perutz has investigated an analogue of Cp^{*}Rh(C₂H₄)₂, but employing the less electron-rich and less sterically demanding C₅H₅ (Cp) as a ligand instead of C₅Me₅.



Scheme 22. Structure for the rhodium complex investigated.

It was found that under photochemical conditions CpRh(C₂H₄)₂ loses one or both the ethylene ligands and undergoes reaction with PPh₃ to form the mono or disubstituted analogues. It also showed reactivity towards thermal C-H activation of C₆H₆ at 130°C where isotopic hydrogen exchange introduced deuterium into the Cp and C₂H₄ ligand.⁴⁰ Finally reactions with silanes proceed photochemically through Si-H oxidative addition to form hydrosilylation

products.⁴¹ The mechanism was also investigated.⁴²



Scheme 23. Photoactivity of the $\text{CpRh}(\text{C}_2\text{H}_4)_2$ complex in the presence of different substrates.

The photochemical reaction of $\text{CpRh}(\text{C}_2\text{H}_4)_2$ in the presence of boranes was not explored previously, and therefore it was of interest to look at the reactivity of the complex towards HBpin and B_2pin_2 and compare the results to those reported for the Cp^* analogue.

3.3.1 Analysis of the $\text{CpRh}(\text{C}_2\text{H}_4)_2$ complex starting material

$\text{CpRh}(\text{C}_2\text{H}_4)_2$ was previously spectroscopically characterized.⁴³ The ^1H NMR spectrum exhibits a resonance at δ 4.83 for the Cp ligand and two complex doublets at δ 2.88 and δ 1.11 assigned to two protons of each coordinated C_2H_4 . The integration ratio is 5:4:4. (Figure 9). The C_2H_4 protons are broad at room temperature because of exchange.

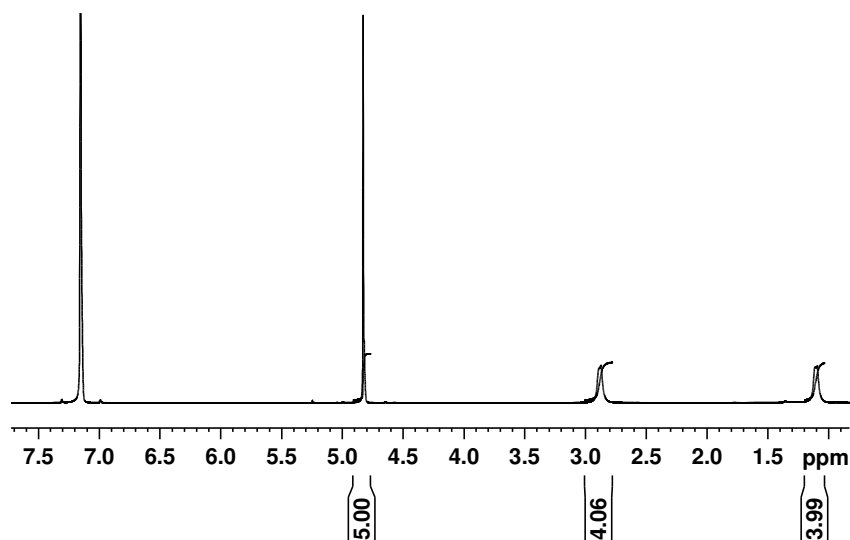
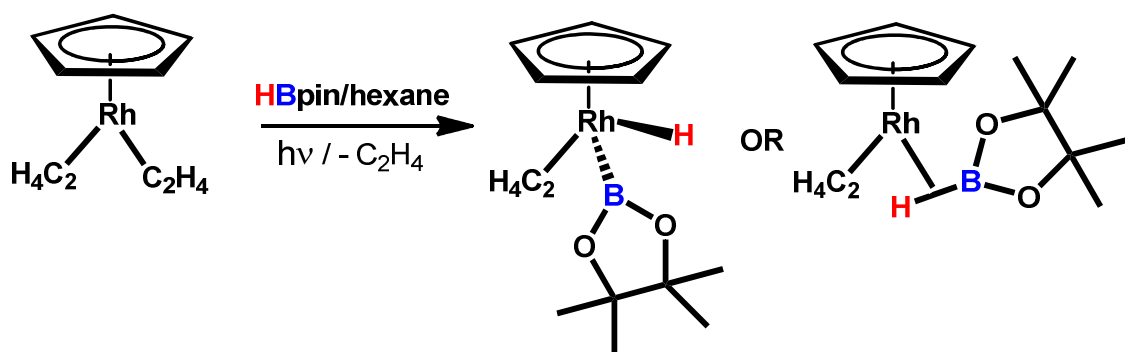


Figure 9. ^1H NMR spectrum of complex $\text{CpRh}(\text{C}_2\text{H}_4)_2$ in C_6D_6 .

3.3.2 Solution photochemistry: $\text{CpRh}(\text{C}_2\text{H}_4)_2$ complex with HBpin

Thermal reaction of complex $\text{CpRh}(\text{C}_2\text{H}_4)_2$ with excess HBpin (5 fold) in hexane did not occur, but photolysis ($\lambda > 290$ nm, 2 h, room temperature) of the same reaction mixture led to the formation of new species. A typical broad resonance at δ -14.37 was observed in the hydride region of the ^1H NMR spectrum upon following the reaction during photolysis. The full set of resonances for the new complex was determined after removal of volatile components and redissolving the brown solid in C_6D_6 . The product displays a singlet for the Cp at δ 5.17, the methyl groups on the borane ring resonate as a singlet at δ 1.09 since they are all chemically equivalent and a broad resonance is observed for the C_2H_4 group at δ 2.86. The broad peak for the hydride sharpened into a doublet upon decoupling from ^{11}B , a coupling constant of 37.7 Hz between ^{103}Rh and ^1H was also observed. ^{11}B NMR spectroscopy shows the typical broad resonance for Rh-boryl complexes at δ 39.9. Attempts to crystallize the complex failed due to its high instability in solution. The complex was found to be stable upon pumping to dryness but decomposition was observed upon leaving it in solution for a few hours. The reaction was also performed in neat HBpin in order to improve the stability, but the same behavior was detected. The by-product

B₂pin₃, formed during photolysis, was also observed in both ¹¹B and ¹H NMR spectra (¹¹B, δ21.9, ¹H, δ1.01). Because it was impossible to get a crystal structure, the identity of the product remained unclear; no distinction could be made between an oxidative addition and a σ-coordination of the B-H bond on the basis of NMR analysis. These results will be discussed later in the Chapter.



Scheme 24. Photochemical reaction of complex CpRh(C₂H₄)₂ in the presence of HBpin.

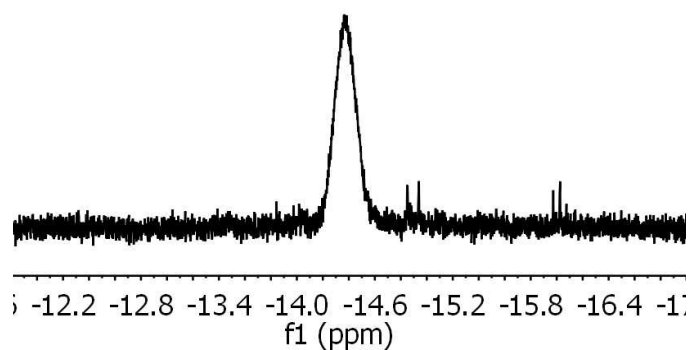


Figure 10. ¹H NMR spectrum: hydride resonance for complex CpRh(C₂H₄)H(Bpin)/CpRh(C₂H₄)(η²-HBpin). The broad peak is due to coupling to ¹¹B.

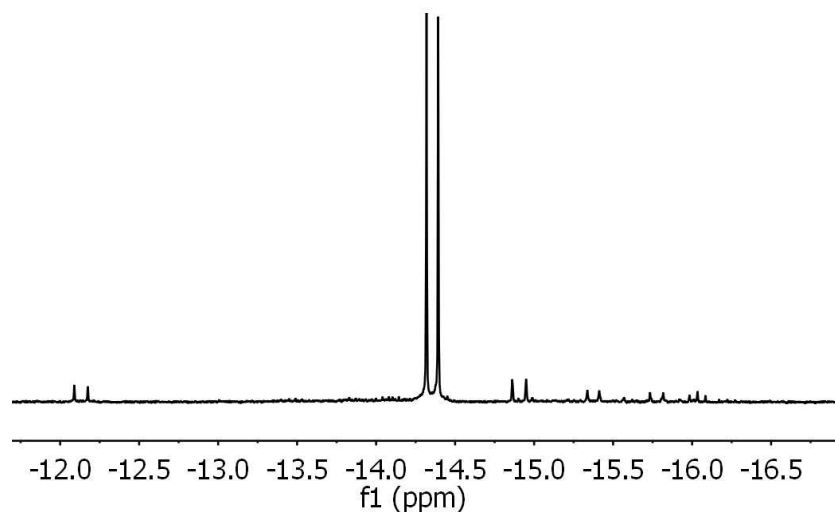
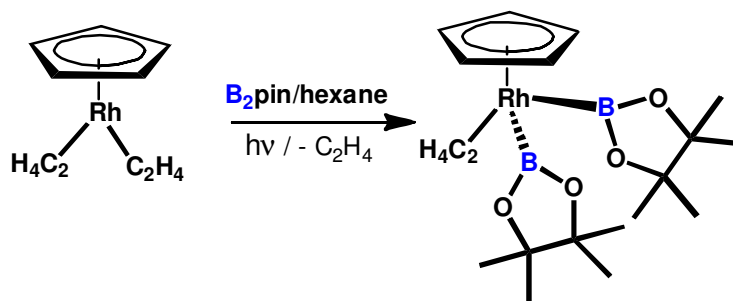


Figure 11. $\{^{11}\text{B}\}^1\text{H}$ NMR spectrum of the hydride region for complex $\text{CpRh}(\text{C}_2\text{H}_4)\text{H}(\text{Bpin})/\text{CpRh}(\text{C}_2\text{H}_4)(\eta^2\text{-HBpin})$ in C_6D_6 .

3.3.3 Solution photochemistry: $\text{CpRh}(\text{C}_2\text{H}_4)_2$ complex with B_2pin_2

Photochemical reaction of $\text{CpRh}(\text{C}_2\text{H}_4)_2$ in the presence of the diborane B_2pin_2 in a 1:1 ratio resulted in B-B oxidative addition to form one major product. The reaction mixture was pumped off and the solid redissolved in C_6D_6 . The broad peak at 37.0 ppm present in the ^{11}B NMR spectrum (Figure 12) confirmed the formation of a rhodium-boryl species; the ^1H NMR spectrum shows the presence of one major Cp resonance at δ 5.3. LIFDI mass-spectrometry elucidates the nature of the complex to be the bis-boryl rhodium complex $\text{CpRh}(\text{C}_2\text{H}_4)(\text{Bpin})_2$ formed by the photochemical reaction shown in Scheme 25. Attempts to crystallize the complex were unsuccessful since it showed high instability in solution as the Bpin analogue.



Scheme 25. Photochemical reaction of CpRh(C₂H₄)₂ and B₂pin₂.

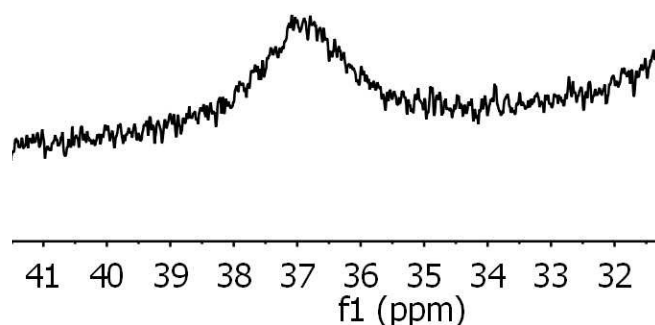


Figure 12. ¹¹B NMR spectrum showing the broad resonance for the CpRh(C₂H₄)(Bpin)₂ complex in C₆D₆.

3.3.4 Catalytic activity of CpRh(C₂H₄)₂ in the presence of HBpin and heptane

A solution of complex CpRh(C₂H₄)₂ (ca 8 mg) in the presence of excess HBpin (10 fold) in heptane was photolyzed for four hours and the reaction mixture analyzed by gas chromatography-mass spectrometry (GC-MS) to look for the borylated alkane product. The peak for the heptyl-Bpin was found in the chromatogram (*m/z* 226.2117) along with other byproducts formed by reaction of HBpin with ethylene. These preliminary results encourage the investigation of the reaction in the presence of different linear alkanes and the optimization of reaction conditions.

3.4 Discussion

Photochemical reaction of Ru(dppe)₂H₂ in the presence of the monoboron reagents HBpin and HBcat, leads to the selective formation of the B-H oxidative addition product as confirmed by NMR spectra analysis.

The reaction of Ru(dppe)₂H₂ is regioselective for the formation of the *cis* stereoisomer, unlike the Ru(dmpe)₂H₂ and the Ru(depe)₂H₂ reactions where both the isomers were observed.³⁹ Regioselectivity probably derives from the steric hindrance of the phosphine compared with Ru(dmpe)₂H₂ and Ru(depe)₂H₂. In contrast just one isomer was formed from reaction of RuH₂ complexes with bulky chiral phosphines, BPE and DuPhos in the presence of HBpin. The Ru(BPE)₂H(Bpin) structure was confirmed crystallographically and by NMR analysis.³⁶ The similarity between ³¹P{¹H} NMR coupling constants for Ru(dppe)₂H(Bpin) and the ones reported for the BPE and DuPhos analogues reinforce our proposal of B-H oxidative addition rather than C-H activation of the methyl groups on the borolane ring (Table 1).

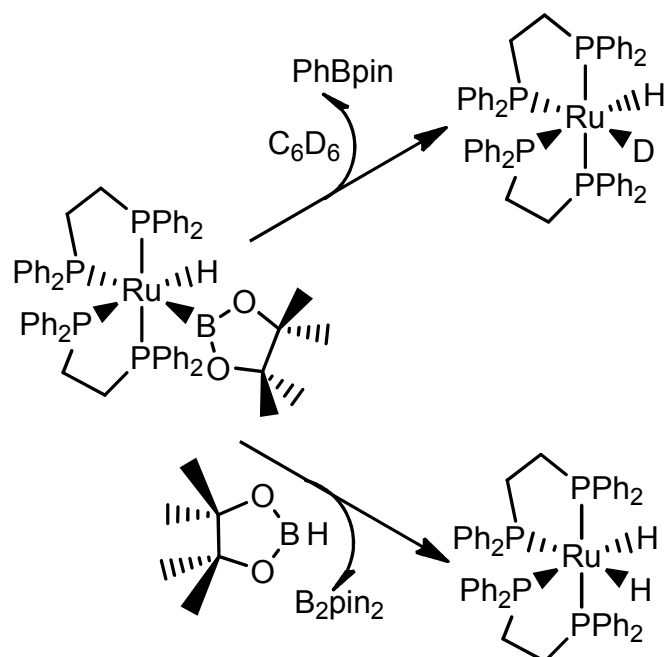
Table 1. Chemical shifts δ (ppm) and coupling constants J (Hz) for complexes Ru(BPE)₂H(Bpin), Ru(DuPhos)₂H(Bpin) and Ru(dppe)₂H(Bpin).

	Ru(BPE) ₂ H(Bpin)	Ru(DuPhos) ₂ H(Bpin)	Ru(dppe) ₂ H(Bpin)
P_A	110.2 (dt, $J_{AX} = 237$, $J_{AM} = J_{AQ} = 16$)	110.4 (dt, $J_{AX} = 239$, $J_{AM} = J_{AQ} = 14$)	77.6 (ddd, $J_{AX} = 249$, $J_{AM} = 21$, $J_{AQ} = 10$)
P_M (trans to H)	91.56 (q, $J_{MA} = 16$, $J_{MQ} = J_{MX} = 18$)	92.2 (m, overlapping with δ_X , $J_{MA} = J_{MQ} = J_{MX} = 19$)	53.7 (m)
P_Q (trans to B)	89.1 (br)	82.47 (br)	57.3 (br)
P_X	88.1 (dt, $J_{XA} = 237$, $J_{XM} = J_{XQ} = 18$)	93.0 (dt, $J_{XA} = 239$, $J_{XM} = J_{XQ} = 19$)	74.3 (ddd, $J_{AX} = 249$, $J_{XM} = 16$, $J_{XQ} = 10$)

Regeneration of starting Ru dihydride complex happens either in C₆D₆ or in neat HBpin. We hypothesized that the back reaction with the benzene regenerates the dihydride complex along with PhBpin when the reaction is in

benzene, and back reaction with HBpin reforms the starting material and possibly B_2pin_2 when the reaction is performed in neat HBpin (Scheme 26). We can also conclude that the boryl-Ru complex formed may act as a good aromatic C-H activator; possible sources of H_2 to regenerate the starting Ru dihydride complex could be HBpin itself, phenyl groups on the phosphine ligands, traces of H_2O , and OH groups from the glassware, or H_2 reductively eliminated during photolysis and still in solution (evidence of it in the 1H NMR spectrum). The instability of boryl complexes in C_6D_6 solution was already observed by Braun and coworkers.⁴⁴ According to laser flash photolysis results, (see Chapter 6), the primary reaction of $Ru(dppe)_2$ and HBpin is very fast ($k_2 = (8.9 \pm 0.3) \times 10^5 \text{ dm}^3 \text{ mol}^{-1} \text{ s}^{-1}$). Therefore the very long photolysis time needed to take the reaction to completion is due to secondary parallel reactions which take place during photolysis and compete to slow down the conversion to the product.

A complete NMR study has also been carried out on the products of the photochemical reaction between $Ru(dppe)_2H_2$ and HBcat in C_6D_6 . In contrast to the reaction with HBpin both the stereoisomers are observed. The reaction is considerably faster than the one with HBpin, and back reaction to regenerate the starting complex occurs much more slowly. Large P-H couplings and sharp hydride resonances (J_{PH} observed) are consistent with the formation of Ru(II) hydrides rather than η^2 -borane complexes which usually show very broad hydride resonances.²⁸



Scheme 26. Possible scheme for the regeneration of the starting complex $\text{Ru}(\text{dppe})_2\text{H}_2$ upon reaction with C_6D_6 or HBpin .

Even greater instability on standing in solution than the Ru-boryl complexes discussed above, is shown by the rhodium complexes formed by photochemical reaction of $\text{CpRh}(\text{C}_2\text{H}_4)_2$ in the presence of HBpin and B_2pin_2 . Attempts at crystallization were not successful, but both the products were characterized by NMR spectroscopy and LIFDI mass-spectrometry. The reactions proceed through photo-elimination of one C_2H_4 ligand to form the unsaturated reactive complex $\text{CpRh}(\text{C}_2\text{H}_4)$ which then either inserts into B-H/B-B bond to form the oxidative addition product or coordinates to it to give the η^2 adducts. Discrimination between a σ -borane complex and a hydrido(boryl) oxidative addition product can not really be achieved just on the basis of NMR spectroscopy. Since both the species exhibit quite similar chemical shifts either in ^1H and in ^{11}B NMR spectra, choosing a bonding mode on the basis of chemical shifts is not possible.⁴⁵ Analysis of B-H coupling constants is also quite uninformative; a σ -borane resonance is always too broad to allowed the determination of $J_{\text{B-H}}$. The resonance for the hydride formed after reaction of

complex $\text{CpRh}(\text{C}_2\text{H}_4)_2$ in the presence of HBpin was broad suggesting B-H bonding interaction, an estimation of the B-H coupling was attempted by measuring the width at half-height of the peak and determined to be 30 Hz. This resonance sharpened to a doublet upon ^{11}B decoupling ($J_{\text{Rh-H}} = 37.0$). Comparison with studies carried on by Hartwig and co-workers helped to confirm the nature of the products as well as to highlight the difference in reactivity moving from Cp^* to Cp as a ligand.⁹ The broad resonances observed in the ^{11}B NMR spectrum are consistent with a boryl group bound to the metal and the presence of a resonance for the C_2H_4 group in the ^1H NMR spectrum confirms that one ethene is kept by the complex after photolysis unlike what was observed for the reactions with the Cp^* analogue. The C_2H_4 group resonates at $\delta 2.86$ for the HBpin complex and at $\delta 3.09$ for the B_2pin_2 one.

Small quantities of other species were detected by ^1H and ^{11}B NMR spectroscopy; reaction of $\text{CpRh}(\text{C}_2\text{H}_4)_2$ in the presence of HBpin produces $\text{CpRh}(\text{C}_2\text{H}_4)(\text{Bpin})_2$ as minor species (evidence on LIFDI-MS) along with other by-products possibly formed by borylation of ethene. The possible Rh(V) complexes $\text{CpRhH}_2(\text{Bpin})_2$ and $\text{CpRh}(\text{Bpin})_4$ were not detected. Nevertheless, Rh(V) species were proposed as intermediates in borylation reactions of alkanes by Hartwig; experimental evidence and theoretical calculations supported the activity of these compounds in the catalytic cycle and energetically favored compared with Rh(III) intermediates.⁹ Our experiments demonstrate instead the formation of Rh(III)/Rh(I) complexes stable enough to be spectroscopically characterized. X-ray analysis was not possible due to instability in solution, in contrast to $\text{Tp}^*\text{Rh}(\text{PMe}_3)\text{H}(\text{Bpin})$ where a crystal structure determination was achieved. (See Chapter five). The complexes obtained by photochemical reaction of $\text{CpRh}(\text{C}_2\text{H}_4)_2$ in the presence of HBpin and B_2pin_2 are formed preferentially with respect to the high-valent intermediates observed for reactions of the Cp^* analogue. Preliminary results demonstrate a potential catalytic ability for the system, reaction of the $\text{CpRh}(\text{C}_2\text{H}_4)_2$ with excess HBpin in heptane resulted in the formation of the functionalized alkane.

3.5 Summary

We have demonstrated here that UV photolysis of the metal phosphine hydride complex $\text{Ru}(\text{dppe})_2\text{H}_2$ in the presence of HBpin and HBcat yields metal phosphine boryl hydrides identified by the use of NMR criteria in the absence of crystallographic data. The complex $\text{CpRh}(\text{C}_2\text{H}_4)_2$ also shows photochemical activity in the presence of HBpin and B_2pin_2 yielding the analogous borylated complexes. All of these complexes proved to be thermally unstable at ambient temperature. The $\text{CpRh}(\text{Bpin})\text{H}(\text{C}_2\text{H}_4)$ appeared to be a catalyst in the borylation of linear alkanes. Reaction of $\text{CpRh}(\text{C}_2\text{H}_4)_2$ in the presence of excess HBpin in heptane afforded the heptyl-Bpin functionalized species.

3.6 Experimental

3.6.1 General procedures

All operations were performed under a argon atmosphere, either on a high-vacuum line (10^{-4} mbar), standard Schlenk (10^{-2} mbar) lines or in a glovebox. Solvents for general use (benzene, toluene) were of AR grade, dried by distillation over sodium and stored under Ar in ampoules fitted with a Young's PTFE stopcock. Hexane was collected from the purification system and dried again by distillation. Deuterated solvents were dried by stirring over potassium and distilled under high vacuum into small ampoules with potassium mirror. HBpin and HBcat were bought by Aldrich and purified by vacuum distillation. Photochemical reactions at room temperature were performed in pyrex NMR tubes fitted with Young's PTFE stopcocks by using a Philips 125 W medium-pressure mercury vapor lamp with a water filter (5 cm).

3.6.2 Mass spectra

LIFDI mass spectra were measured on a Waters Micromass GCT Premier orthogonal time-of-flight instrument set to one scan per second with resolution power of 6000 FWHM and equipped with a LIFDI probe from LINDEN GmbH. The design is very similar to that described by Gross et al.⁴⁶ Toluene was used for tuning the instrument. The polyethylene glycol probe was kept at ambient temperature with the emitter potential at 12 kV. Activated tungsten wire LIFDI emitters (13 μm tungsten from LINDEN) were ramped manually up to 100 mA for the emitter heating current during the experiment. The m/z values are accurate to 0.01 Da. M/z values are quoted for ^{11}B and ^{103}Rh .

3.6.3 NMR spectroscopy

All standard NMR spectra were recorded on a Bruker AMX500 spectrometer, in tubes fitted with Young's PTFE stopcocks. All ^1H and ^{13}C chemical shifts are reported in ppm (δ) relative to tetramethylsilane and referenced using the chemical shifts of residual protio solvent resonances (benzene, δ 7.16 for ^1H and δ 128.06 for ^{13}C). The $^{31}\text{P}\{^1\text{H}\}$ NMR spectra were referenced to external H_3PO_4 . ^{11}B NMR spectra were referenced to external $\text{BF}_3\cdot\text{Et}_2\text{O}$.

3.6.4 Synthesis of Ru(dppe)₂H₂⁴⁷

A 250 mL Schlenk flask containing a teflon-coated magnetic stirring bar was charged with NaOH (1.00 g, 25 mmol), [RuCl₂(COD)]_x (0.352 g, 1.25 mmol) and dppe (1.03 g, 2.5 mmol) were added to the reaction vessel, the vessel was then connected to the Schlenk line, degassed and refilled with argon three times. Degassed sec-butyl alcohol (80 mL) was added via a cannula, and the reaction was then sealed and heated at 80 °C for three hours, the solution's color changed from brown to yellow. The reaction was then allowed to cool to room temperature, and degassed water (100 mL) was added to dissolve the excess NaOH. The liquid portion was removed through a cannula and the solid was washed with degassed methanol, dried in vacuum and redissolved in benzene. The solution was filtered off by cannula under an argon atmosphere, the benzene removed by evaporation under vacuum and the compound dried in vacuum.

¹H NMR (C₆D₆, 300K) δ -8.3 (m, *J*_{PH} 53, 39, 21 Hz, 2H, *cis* isomer), δ -8.1 (q, *J*_{PP} 19.4 Hz, 2H, *trans* isomer), 1.5 (m, 2H, C₂H₄), 1.7 (m, 2H, C₂H₄), 2.0 (dd, *J*_{HH} 11.6, *J*_{PH}, 34.1, 2H, C₂H₄), 2.7 (dd, *J*_{HH} 14.1, *J*_{PH}, 44.6, 2H, C₂H₄), 6.1, 7.33, 7.42, 7.73 (t, *J*_{PH} 8.2 Hz, *J*_{HH} 7.4 Hz, 4 phenyl protons each resonance), 6.76, 6.85, 6.95, the resonance of the remaining protons on the phenyls ring overlap and precise assignment was not possible, but the total integration count is consistent with the presence of 40 aryl protons.

³¹P{¹H} NMR δ 65.7 (t, *J*_{PP} 15.5 Hz 2P, *cis* isomer), 79.6 (t, *J*_{PP} 15.5 Hz 2P, *cis* isomer) 83.9 (s, 4P, *trans* isomer).

¹³C NMR δ 28.2, (dt, *J*_{CH} 20.9, 12.7 Hz, C₂H₄), 33.7, (dt, *J*_{CH} 25.1, 13.7 Hz, C₂H₄), 135.2 to 127.6, (set of resonances for the CH), 141.1 to 143.7, (set of resonances for qC of phenyl).

3.6.5 Synthesis of trans-Ru(dppe)₂H(Bpin)

An NMR tube, fitted with a Young's tap, was charged with complex Ru(dppe)₂H₂ (20 mg) and HBpin (10 fold excess) in C₆D₆ and irradiated for 15 h, resulting in 100% conversion to *trans* Ru(dppe)₂H(Bpin). Purification and isolation of the

complex was not possible because of back reaction under mild condition to regenerate the starting complex. NMR characterisation was done in C₆D₆.

¹H NMR (C₆D₆, 300 K): δ -8.3 (dq, J_{PH} 38.1, 20 Hz, RuH), δ 2.94 (m), 2.43 (m), 2.09 (m, very broad), 1.86 (m), 1.66 (m), the C₂H₄ protons are in a 2:1:1:2:1:1 integration ratio; δ 8.58, 8.31, 7.97, 7.57, 7.05, 7.02, 6.82, 6.30 (t, J_{PH} 7.9 Hz, J_{HH} 8.5 Hz, 2 phenyl protons each resonance), the resonances of the remaining protons on the phenyls ring are overlapping and precise assignment was not possible, but the total integration count is consistent with the presence of 40 aryl protons.

³¹P{¹H} NMR: δ 78.0 (AB system, ddd, J_{PP} 21 Hz P_A), 74.2 (AB system, ddd, J_{PP} 16 Hz, P_Q), δ 57.3, (b, J_{PP} 15.5 Hz 1P, trans to B) 53.7, (dd, J_{PP} 25.9 Hz; 15.7 Hz 1P).

¹³C NMR: δ 146.5 to 139.0, (set of resonances for the qC of phenyl), δ 135.4 to 128.4, (set of resonances for the CH of phenyls), δ 79.9, (s, BOC), δ 33.5, (t, J_{CH} 25.4, C₂H₄), δ 32.4, (t, J_{CH} 22.3, C₂H₄), δ 30.84, (b, C₂H₄), δ 26.72, (t, J_{CH} 20.4, C₂H₄), δ 26.06, (s, BOCMe).

3.6.6 Synthesis of trans and cis-Ru(dppe)₂H(Bcat)

An NMR tube, fitted with a Young's tap, was charged with complex Ru(dppe)₂H₂ (20 mg) and HBcat (10 fold excess) in C₆D₆ and irradiated for 30 min resulting in 100% conversion to *trans* and *cis* Ru(dppe)₂H(Bcat). Purification and isolation of the complex was not possible because of back reaction under mild condition to regenerate the starting complex. NMR characterisation was done in C₆D₆.

¹H NMR (C₆D₆, 300 K): δ -7.89 (dq, J_{PH} 59.3, 20 Hz, *cis*-RuH), δ -6.37 (q, J_{PH} 19.3, *trans*-RuH), δ 2.87 to 1.82 (set of broad multiplets for the *cis-trans* C₂H₄), δ 8.79 to 6.16 (set of multiplets for the aryl protons and the catechol ones for *cis* and *trans*, all the resonances overlap and integration was no possible.).

³¹P{¹H} NMR: δ 76 (s, *trans* isomer), 76.5 (dd) and 75.3 (t) (δ_{AB} quartet, J_{AB} = 240, J_{AM} = 21 J_{AQ} = 11, J_{BM} = J_{BQ} = 14, *cis* isomer), 56.6 (δ_M , br, P_{transB}, *cis* isomer), 55.6 (δ_Q , m, P_{transH}, *cis* isomer).

3.6.7 Synthesis of CpRh(C₂H₄)₂

The complex was prepared by standard methods,⁴³ but replacing TICp with LiCp. It was extracted with hexane, the resulting yellow solution was pumped to dryness, and the product was sublimed under vacuum onto a liquid nitrogen-cooled finger. Yield: 85%.

¹H NMR (C₆D₆) δ 1.09 (b, C₂H₄), δ 2.87 (b, C₂H₄), δ 5.17 (s, Cp).

3.6.8 Synthesis of CpRh(C₂H₄)H(Bpin)

An NMR tube, fitted with a Young's tap, was charged with complex CpRh(C₂H₄)₂ (20 mg) and HBpin (5 fold excess) in hexane and irradiated for 2 hours, resulting in 90% conversion to CpRh(C₂H₄)H(Bpin). The reaction mixture was pumped to dryness and the solid redissolved in C₆D₆ for NMR characterisation. Purification was not possible due to decomposition of the product upon passing the solution through an alumina column.

¹H NMR (C₆D₆) δ -14.34 (br, 1H, RhH), δ 1.09 (s, 12H, BO₂C₂(CH₃)₄), δ 2.86 (b, 4H, C₂H₄), δ 4.83 (s, 5H, Cp).

¹¹B NMR δ 39.9 (b).

LIFDI mass-spec: m/z 324.07 (calculated: 324.08, difference 10 mDa).

3.6.9 Synthesis of CpRh(C₂H₄)(Bpin)₂

An NMR tube, fitted with a Young's tap, was charged with complex CpRh(C₂H₄)₂ (20 mg), and B₂pin₂ (1:1 ratio) in hexane and irradiated for 3 hours, resulting in 70% conversion to CpRh(C₂H₄)(Bpin)₂. The reaction mixture was pumped to dryness and the solid redissolved in C₆D₆ for NMR characterisation. Purification was not possible due to decomposition of the product upon passing the solution through an alumina column.

¹H NMR (C₆D₆): δ 1.16 (d, 24H, BO₂C₂(CH₃)₄), δ 3.09 (d, 4H, C₂H₄), δ 5.34 (s, 5H, Cp).

¹¹B NMR (C₆D₆): δ 37.0 (b).

LIFDI mass-spec: m/z 450.162 (calculated: 450.162).

4 Oxidative addition of (*i*Pr)₂N-BH₂ at rhodium centres

4.1 Introduction

Ammonia-borane and amine-boranes contain a high percentage by weight of available hydrogen (~ 28%)¹ and they are isoelectronic with alkanes. The interest in looking at the reaction of transition metal centres in the presence of amine-boranes has increased in the last years (Scheme 1), especially considering their applications in hydrogen release and storage.² The proved capability of some homogeneous catalysts to be active in dehydrogenation of alkanes inspired the use of similar systems in reactions with amine-boranes. Many metals have been shown to be effective in this type of reactions, from early transition metals (Ti, Zr)³ to late ones (Rh and Ir).⁴⁻⁸ Metal free methods have also been recently reported by Manners and coworkers.⁹



Scheme 1. General scheme for the metal assisted dehydrogenation of amine-borane.

Primary or secondary amine-boranes have been employed in order to produce dihydrogen. Tertiary amine-boranes showed reactivity of the B-H bond to produce η^1 -coordinated metal-complexes (Figure 1).¹⁰

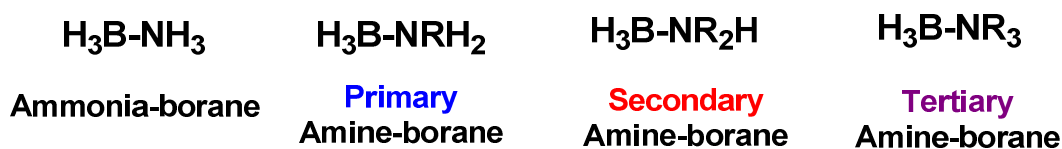
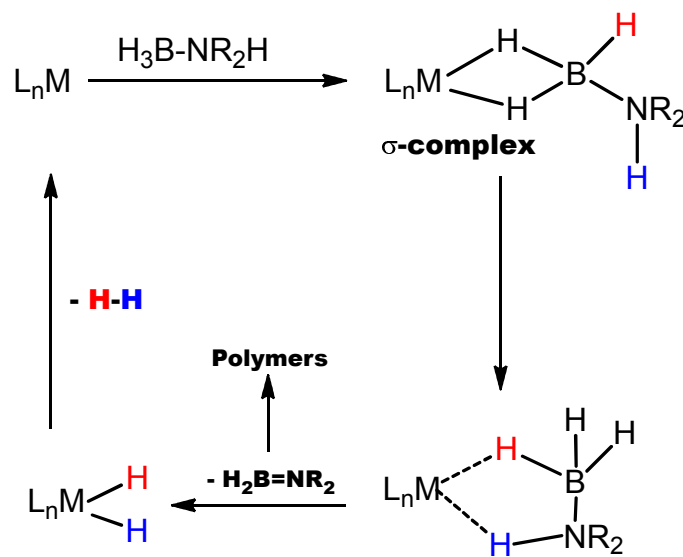


Figure 1. Structure of possible substituted amine-boranes.

The mechanism of metal-catalysed dehydrogenation reactions has been explored experimentally and theoretically,¹¹ different routes have been proposed which strongly depend on the organometallic complex employed (Scheme 2). However the nature of the intermediates involved in the catalytic cycle is relatively unknown. Recently, the first step in the insertion of an amineborane into an Ir(PCy₃)₂ centre has been reported to yield [Ir(PCy₃)₂(H)₂(η^2 -H₃BNMeHBH₂-NMeH₂)] [BAR^F₄]. Dehydrogenation to form an

aminoborane ligated complex was not observed and the reaction was found to be catalytic for the dehydropolymerization of $\text{H}_3\text{B-NMeH}_2$ to form the simplest oligomeric species.¹²



POSSIBLE MECHANISMS:

- B-H OXIDATIVE ADDITION/N-H β ELIMINATION (Ru and Ni)**
- CONCERTED N-H/B-H ACTIVATION (Ir-pincer)**
- N-H TRANSFER TO LIGAND (Ni-NHC)**

Scheme 2. Proposed mechanisms for amine-borane dehydrogenation.

The loss of dihydrogen from amine-boranes forms the corresponding amino-boranes which are isoelectronic with alkenes; the instability of these species leads to the formation of dimeric cyclic products by dehydrocoupling reactions.² The introduction of steric hindrance with bulky substituents at the nitrogen centre (ⁱPr instead of H) improved the stability of the amino-borane allowing isolation as monomeric species. The role played by these compounds in the catalytic cycle is not well defined and a deeper understanding of their reactivity towards metal centres would be useful to clarify the mechanistic pathways followed by the dehydrogenative coupling reactions.

Therefore, the interest in aminoboranes $\text{H}_2\text{B=NR}_2$, the unsaturated analogues of amine-boranes has increased; furthermore they are the basic monomers from which metal-mediated polymerisation gives access to novel materials.

Sabo-Etienne and co-workers reported the first ruthenium complex where a monomeric amino-borane coordinates to the metal centre *via* a bis(σ -B-H) bonds. They found that the thermal reaction of $\text{RuH}_2(\eta^2\text{-H}_2)_2(\text{PCy}_3)_2$ in the presence of three different amine-boranes led to the release of H_2 and coordination of the corresponding amino-borane to the unsaturated fragment (Figure 2).¹⁰

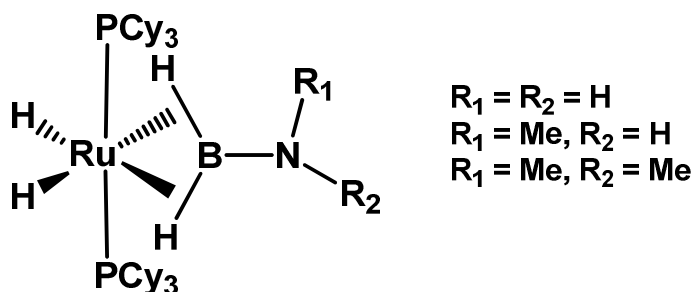


Figure 2. The bis-(σ -BH) coordination product formed by thermal reaction of complex $\text{RuH}_2(\eta^2\text{-H}_2)_2(\text{PCy}_3)_2$ in the presence of amine-borane.

The same reactivity was observed on changing the phosphine ligands at the ruthenium centre and breaking the symmetry of the complex by introducing a chloride instead of a hydride. Reaction of $\text{RuHCl}(\eta^2\text{-H}_2)(\text{P}i\text{Pr}_3)_2$ in the presence of cyclodiborazane $[\text{Me}_2\text{N-BH}_2]_2$ gave the same type of product as observed previously.¹³ The complex $\text{RuHCl}(\text{H}_2\text{BNMe}_2)(\text{P}i\text{Pr}_3)_2$ was found to be very stable under vacuum/standard conditions and did not undergo borylene formation as found for reaction of the same complex in the presence of mesityl borane.¹⁴ Comparison with the same type of complexes using osmium¹⁵ instead of ruthenium demonstrated that Ru prefers σ -coordination while osmium oxidatively adds the B-H bond of the cycloborazane.¹³

Shimoi-type complexes¹⁶ of amine-boranes have been reported by Weller group using rhodium as metal centre (Figure 3). They isolated and characterized the first Rh(I) and Rh(III) σ -amine-borane species by reacting $[\text{Rh}(\text{P}i\text{Bu}_3)_2][\text{BAr}^{\text{F}}_4]$ in the presence of DMAB (dimethylamine-borane).¹⁷

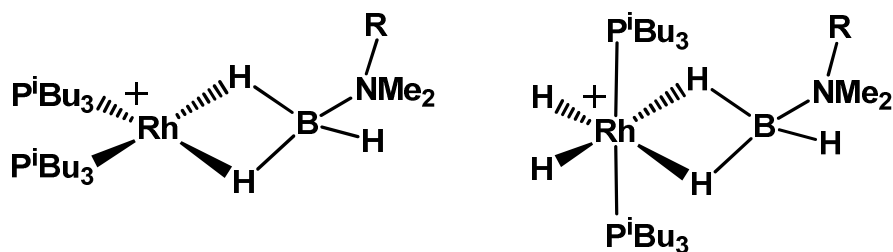


Figure 3. Structures for the Rh(I) and Rh(III) Shimoï-type complexes of amine-borane.

They also noticed different reactivity on changing the phosphine ligands.¹⁸ On introducing P^iPr_3 instead of P^iBu_3 the Rh(III) complexes formed were found to be more stable than those with P^iBu_3 .

A collaboration of Sabo-Etienne and Weller group reported a series of Ru, Ir, Rh σ -borane complexes of $H_2B-N^iPr_2$, which were characterized by NMR spectroscopy and confirmed by X-Ray analysis (Figure 4). A stronger M-B interaction was observed for the Ru/Ir complexes than for the Rh one. Theoretical calculations agreed with the experimental trend placing Ru as the metal which forms the strongest metal-boron bond.¹⁸

Aldridge and coworkers demonstrated that replacing the phosphine ligand with a carbene did not affect the reactivity; bis(σ -B-H) diisopropylaminoborane cationic rhodium and iridium complexes $[MH_2(\eta^2:\eta^2-H_2B-N^iPr_2)(IMes)_2][BAR^F_4]$ ($M = Rh, Ir, IMes=2,5-Mes_2-N_2C_3H_2$) were isolated upon dehydrogenation of diisopropylamine-borane by rhodium centres.¹⁹

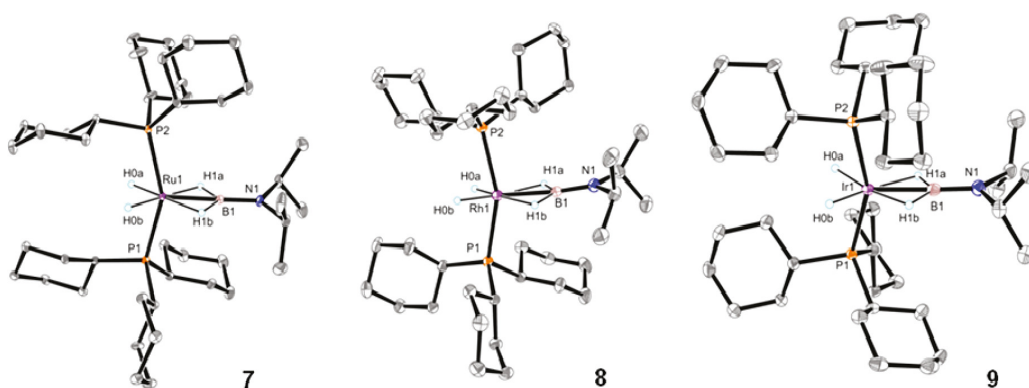


Figure 4. Crystal structures for Ru, Rh, Ir σ -borane complexes of $H_2B-N^iPr_2$.¹⁸

The same group recently reported the first example of $\text{H}_2\text{B}=\text{NCy}_2$ coordinated to a sixteen-electron Ru-complex $[\text{CpRu}(\text{PPh}_3)_2]$ via a mono (σ -B-H) bond. The capability of these ligands to act as two electron donors was shown.²⁰ The first example of oxidative addition of an amino-borane B-H bond to a metal centre was also achieved by the group of Aldridge. The $[\text{Ir}(\text{PMe}_3)_3]^+$ fragment oxidatively added $\text{H}_2\text{B}=\text{NR}_2$ ($\text{R} = i\text{Pr}, \text{Cy}$) in the first step to form an Ir-boryl hydride complex **2**; a novel mechanism was proposed for the subsequent formation of a borylene species **3** where a B-to-M α -hydride migration took place after Cl^- abstraction (Figure 5).²¹

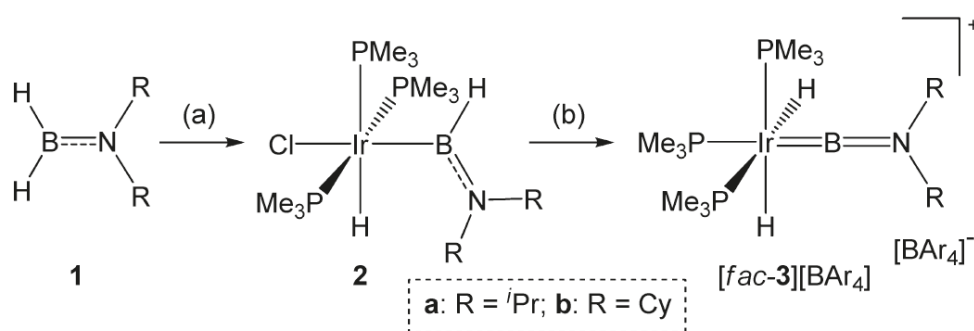
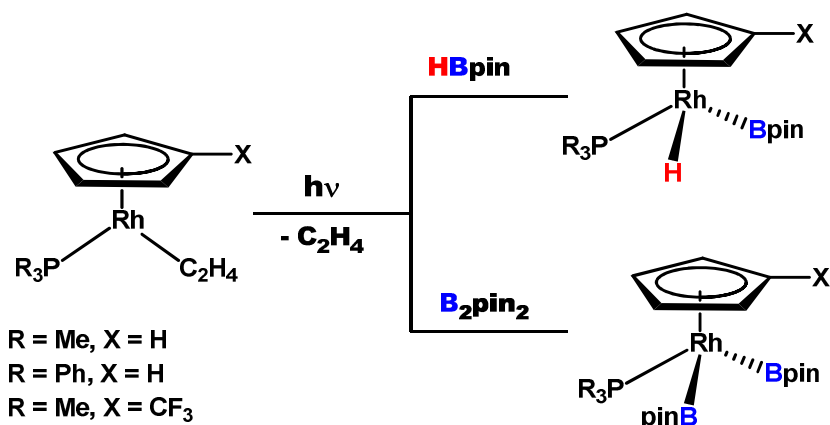


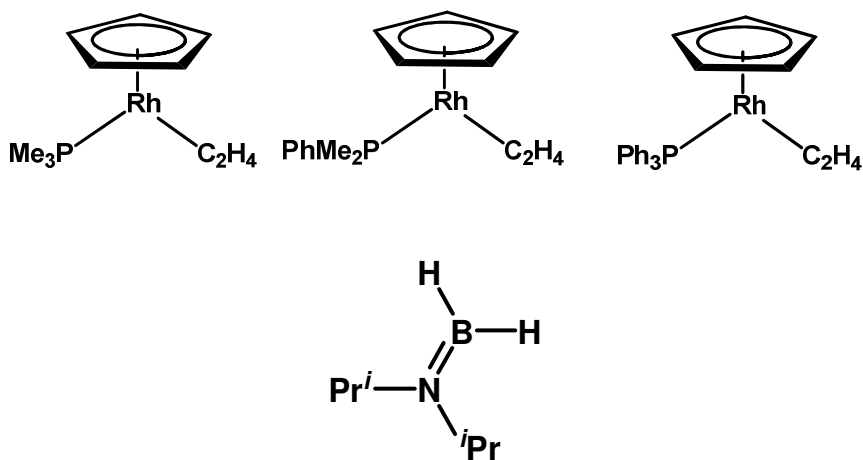
Figure 5. 2: Product formed by oxidative addition of H_2BNR_2 at Ir centre, (a) $\text{Ir}(\text{PMe}_3)_3\text{Cl}(\text{coe})$, toluene. **3:** Ir-borylene species formed by chlorine abstraction from complex **2**, (b) $\text{Na}[\text{BAR}_4]$, $\text{C}_6\text{H}_5\text{F}$.

$\text{CpRh}(\text{PR}_3)(\text{C}_2\text{H}_4)$ complexes ($\text{R} = \text{PMe}_3, \text{PPh}_3$) have been already employed in reactions with boranes.²² It has been proved that their photochemical reaction generates the unsaturated 16-electron fragment $\text{CpRh}(\text{PR}_3)$ which, in the presence of HBpin and B_2pin_2 , can insert into the B-H and B-B bond to form the oxidative addition products. The crystal structure of the complex $\text{Rh}(\eta^5\text{-C}_5\text{H}_5)(\text{H})(\text{Bpin})(\text{PPh}_3)$ was determined and a residual B...H interaction found, confirming that a partial B-H oxidative addition took place.²²



Scheme 3. Photochemical reaction of $\text{CpRh}(\text{PR}_3)$ complexes in the presence of HBpin and B_2pin_2 to give the oxidative addition products.

Considering the reactivity of the CpRh -phosphine complexes towards B-H bonds of boranes and the few examples of simple oxidative addition of amino-boranes to a 16 electron Rh centre we thought it would be interesting to explore the photochemical reactions of $\text{CpRh}(\text{PR}_3)(\text{C}_2\text{H}_4)$ complexes ($R = \text{PMe}_3, \text{PPh}_3, \text{PhMe}_2$) in the presence of $\text{H}_2\text{B}=\text{N}(\text{iPr})_2$.

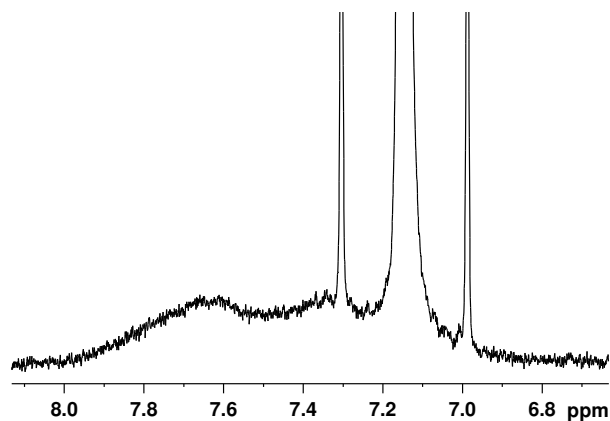


Scheme 4. Top: Structure of the $\text{CpRh}(\text{PR}_3)(\text{C}_2\text{H}_4)$ complexes investigated; Bottom: Structure of the amino-borane used in these studies.

4.2 Results

4.2.1 Photochemical reaction of $\text{CpRh}(\text{PMe}_3)(\text{C}_2\text{H}_4)$ in the presence of $\text{H}_2\text{B}=\text{N}(\text{iPr})_2$

An excess of $\text{H}_2\text{B}=\text{N}(\text{iPr})_2$ (5 fold) was added to a hexane solution of $\text{CpRh}(\text{PMe}_3)(\text{C}_2\text{H}_4)$ (10 mg). The mixture did not react thermally, but its photochemical reaction showed the appearance of a new phosphorus containing product with a $J_{\text{Rh-P}}$ of 175.8 Hz. After 3.5 hours of photolysis the reaction was complete, the reaction mixture was pumped down under vacuum and the solid redissolved in C_6D_6 . NMR characterization showed a doublet in the ^{31}P NMR spectrum at δ 12.2 as the major product (NMR yield > 98%) with a coupling constant consistent with a Rh(III) oxidation state.²² The ^1H NMR spectrum exhibits a hydride resonance as a doublet of doublets at δ - 14.7 ($J_{\text{H-Rh}} = 35.9$, $J_{\text{H-P}} = 42.0$ Hz), a single resonance for the Cp at δ 5.27 and a broad peak at δ 7.49 which sharpens to a doublet upon decoupling from ^{11}B (Figure 6), suggesting a proton remaining on the aminoborane moiety as previously observed.²¹ ^{11}B NMR spectroscopy showed the presence of a typical metal boryl peak at δ 56 (Figure 7). On the basis of this evidence we assign the new species as $\text{CpRh}(\text{PMe}_3)\text{H}(\text{BHN}(\text{iPr})_2)$. LIFDI mass spectrometry confirmed the nature of the product.



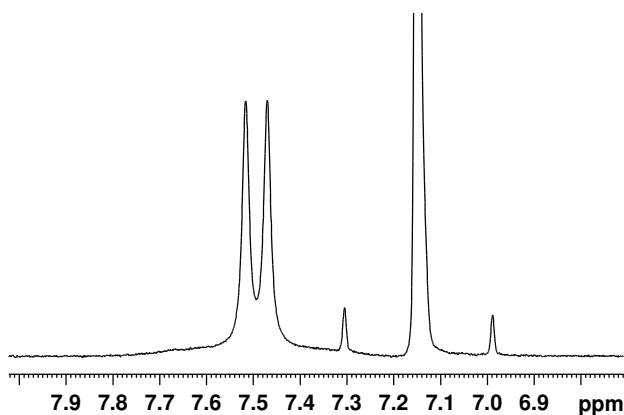


Figure 6. Top: ^1H NMR spectrum in C_6D_6 of complex $\text{CpRh}(\text{PMe}_3)\text{H}(\text{BHN}(\text{iPr})_2)$ showing the broad resonance for the B-H proton. **Bottom:** $^1\text{H}\{^{11}\text{B}\}$ NMR spectrum of the same complex showing how the resonance sharpened under ^{11}B decoupling.

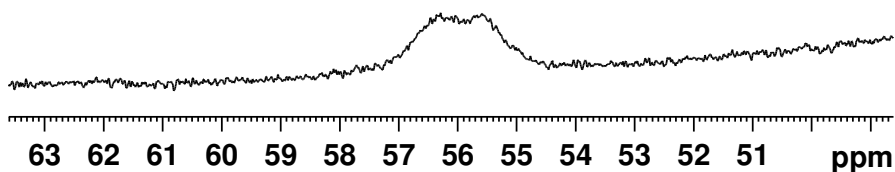


Figure 7. ^{11}B NMR spectrum showing the broad resonance for the $\text{CpRh}(\text{PMe}_3)\text{H}(\text{BHN}(\text{iPr})_2)$ complex in C_6D_6 .

4.2.2 Photochemical reaction of $\text{CpRh}(\text{PPh}_3)(\text{C}_2\text{H}_4)$ in the presence of $\text{H}_2\text{B}=\text{N}(\text{iPr})_2$

Photochemical reaction of the $\text{CpRh}(\text{PPh}_3)(\text{C}_2\text{H}_4)$ complex, (5 mg) in the presence of a 5 fold excess $\text{H}_2\text{BN}(\text{iPr})_2$ in hexane showed the same features as for the PMe_3 analogue. The $\text{CpRh}(\text{PPh}_3)(\text{C}_2\text{H}_4)$ complex exhibited low solubility in hexane, however the reaction was complete after 5 hours of photolysis. A new product appeared in the $^{31}\text{P}\{^1\text{H}\}$ NMR spectrum at $\delta 63.0$ with a J_{RhP} of 186.2 Hz (Figure 8). This peak was found to be linked to a hydride resonance in the ^1H NMR spectrum by $\{^{31}\text{P}-^1\text{H}\}$ 2D NMR spectroscopy. Selected NMR data are summarized in Table 1.

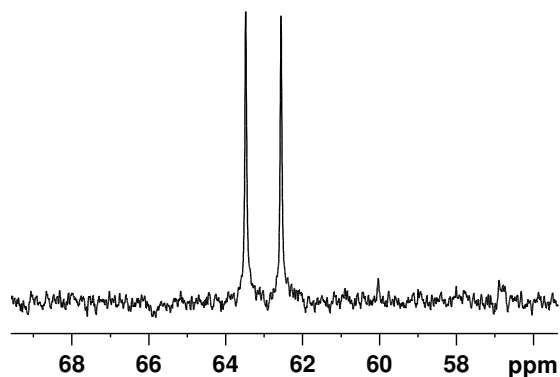


Figure 8. $^{31}\text{P}\{^1\text{H}\}$ NMR spectrum for complex $\text{CpRh}(\text{PPh}_3)\text{H}(\text{HBN}(\text{iPr})_2)$.

4.2.3 Photochemical reaction of $\text{CpRh}(\text{PMe}_2\text{Ph})(\text{C}_2\text{H}_4)$ in the presence of $\text{H}_2\text{B}=\text{N}(\text{iPr})_2$

Excess of $\text{H}_2\text{BN}(\text{iPr})_2$ (5 fold) was added to a hexane solution of $\text{CpRh}(\text{PMe}_2\text{Ph})(\text{C}_2\text{H}_4)$ (10 mg). The appearance of a new phosphorus containing product with a $J_{\text{Rh-P}}$ of 180.9 Hz was observed by $^{31}\text{P}\{^1\text{H}\}$ NMR spectroscopy. After 6 hours of photolysis the reaction was complete, the volatiles pumped down by vacuum and the solid redissolved in C_6D_6 . NMR characterization showed a doublet in the $^{31}\text{P}\{^1\text{H}\}$ NMR spectrum at δ 27.6 as major product (NMR yield > 90%) with a Rh(III) oxidation state coupling constant ($J_{\text{PRh}} = 181.6$).²² Further NMR data are reported in Table 1. ^{11}B NMR spectroscopy showed the presence of a typical metal boryl peak at δ 55.7 (Figure 9). On the basis of these evidence we assign the new species as $\text{CpRh}(\text{PMe}_2\text{Ph})\text{H}(\text{HBN}(\text{iPr})_2)$.

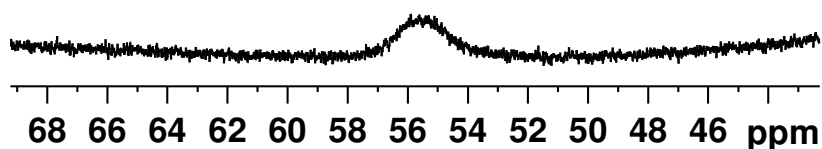


Figure 9. ^{11}B spectrum showing the broad resonance for the $\text{CpRh}(\text{PMe}_2\text{Ph})\text{H}(\text{BHN}(\text{iPr})_2)$ complex in C_6D_6 .

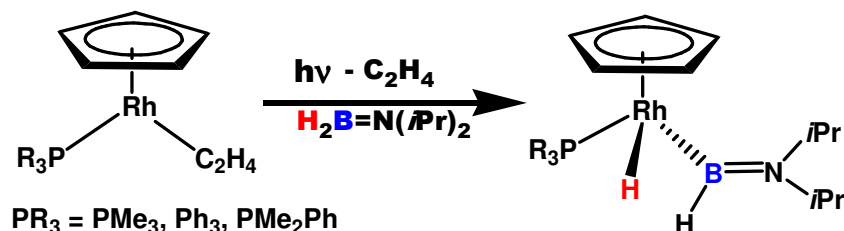
Chapter 4: Photochemical oxidative addition of aminoborane at Rh

Table 1. Selected NMR data in C₆D₆ for Precursor and Photoproducts δ (J/Hz).

	³¹ P{ ¹ H}	¹ H	¹¹ B	¹ H{ ¹¹ B}	LIFDI MS
CpRh(PMe₃)(C₂H₄)	4.4, d, J _{PRh} = 201	5.09, s, Cp	-	-	-
CpRh(PPh₃)(C₂H₄)	59.5, d, J _{PRh} = 210	5.06, s, Cp	-	-	-
CpRh(PMe₂Ph)(C₂H₄)	21.0, d, J _{PRh} = 204	5.11, s, Cp			
CpRh(PMe₃)H(BHN(<i>i</i>Pr)₂)	12.2, d, J _{PRh} = 176	- 14.7, dd, J _{H-Rh} = 35.9, J _{H-P} = 45.0, RhH 5.27, s, Cp	55.9, br	7.5, d, J _{H-P} = 22.9	357.148 Exp 357.127
CpRh(PPh₃)H(BHN(<i>i</i>Pr)₂)	63.0, d, J _{PRh} = 186	- 14.0, dd, J _{H-Rh} = 33.4, J _{H-P} = 40.3, RhH 5.30, s, Cp	56.0, br		543.176 Exp 543.174
CpRh(PMe₂Ph)H(BHN(<i>i</i>Pr)₂)	27.6, d, J _{PRh} = 182	- 14.4, dd, J _{H-Rh} = 35.1, J _{H-P} = 40.9, RhH 5.26, s, Cp	55.7, br	7.5, d, J _{H-P} = 21.4	419.14 Exp 419.14

4.3 Discussion

The photochemical reaction of the complexes $\text{CpRh}(\text{PR}_3)(\text{C}_2\text{H}_4)$, ($\text{R} = \text{PMe}_3, \text{PPh}_3, \text{PMe}_2\text{Ph}$) forms the unsaturated fragment $\text{CpRh}(\text{PR}_3)$ as previously observed.²² The sixteen electron complex $\text{CpRh}(\text{PR}_3)$ has been demonstrated to insert into the B-H bond of the diisopropyl-aminoborane by these preliminary experiments, to afford cleanly the oxidative addition product (Scheme 5), formed with a high yield (>90%). The sharp signals observed for the hydride resonances suggest oxidative addition rather than σ -coordination.¹⁸ $^1\text{H}\{^{11}\text{B}\}$ NMR spectroscopy showed the presence of the B-H proton at low field (δ 7.50) in agreement with what was observed by Aldridge *et al.*²¹ This resonance was not found for the $\text{CpRh}(\text{PPh}_3)\text{H}(\text{HBN}(\text{iPr})_2)$ probably because it overlaps with the phenyl protons of the phosphine ligand. The shape of the ^{11}B resonance for the PMe_3 complex shows coupling to ^1H ($J_{\text{BH}} = 135$ Hz), the same coupling constant is observed in the ^1H NMR spectrum on the resonance at 7.50 ppm. The capability of rhodium to activate B-H bonds of boranes has been demonstrated frequently, but we are not aware of reported oxidative addition of the B-H bond of amino-borane at rhodium centres. The literature is rich in examples of σ -coordination of amino-borane¹⁸ as well as Shimo-i-type complexes of rhodium.¹⁷ Clearly electronics and sterics of the ligands play a role in the different coordination modes. Different metal centres also give different reactivity. Reaction of the $[\text{CpRu}(\text{PR}_3)_2]^+$ fragment ($\text{R} = \text{PPh}_3$) with $\text{H}_2\text{B}=\text{NCy}_2$ afforded the mono(σ -BH) mode of amino-borane ligation.²⁰



Scheme 5. Photochemical reaction of complexes $\text{CpRh}(\text{PR}_3)(\text{C}_2\text{H}_4)$ in the presence of amino-borane to form the oxidative addition products.

These studies are encouraging for a deeper investigation of the process. It would be interesting to characterize the complexes crystallographically to see if any B...H interaction is still present. Performing the reaction in the presence of $[\text{Ph}_3\text{C}][\text{PF}_6]$ acting as hydride abstractor would show if the complexes evolve to the formation of the borylene analogues as observed by Aldridge and coworkers for the $[\text{Ir}(\text{PMe}_3)_3]^+$ system.²¹ An alternative route to the use of $[\text{Ph}_3\text{C}][\text{PF}_6]$ to create a vacant site on the metal centre could be to convert the Rh-hydride species to a Rh-chloride complexes and use $[\text{Na}][\text{BAr}_4]$ [$\text{Ar}^{\text{F}} = \text{C}_6\text{H}_3(\text{CF}_3)_2\text{-}3,5$ or $\text{ArCl} = \text{C}_6\text{H}_3\text{Cl}_2\text{-}3,5$] as chloride abstractor. The reaction of complex $\text{CpRh}(\text{PMe}_2\text{Ph})\text{H}(\text{HBN}(i\text{Pr})_2)$ in the presence of a stoichiometric amount of $[\text{Ph}_3\text{C}][\text{PF}_6]$ in THF was attempted. The reaction was monitored by low temperature NMR spectroscopy (220 K to 260 K) and the appearance of a resonance at $\delta 10.8$ as a singlet suggested the formation of a short lived species $[\text{CpRh}(\text{PMe}_2\text{Ph})(\text{HBN}(i\text{Pr})_2)]^+$ (Figure 10). The chemical shift for the B-H proton is similar to that previously observed for a C-H carbene proton of a analogue Rh complex which was found at $\delta 13.1$.²⁴ No new resonances were detected in the ^{11}B NMR spectrum at low temperature.

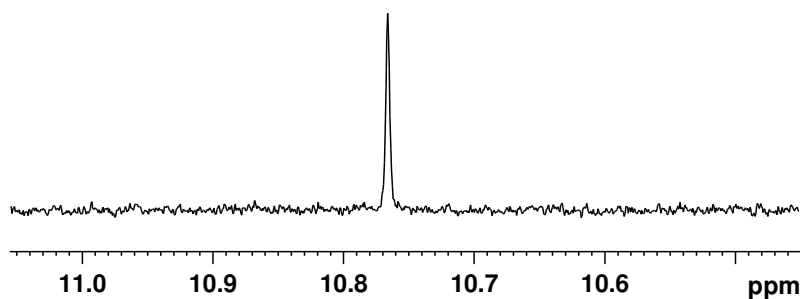


Figure 10. ^1H NMR spectrum at 240 K showing the low field peak for the cationic rhodium complex.

Although very preliminary results, they show potential for optimization and further investigations of the process. Changing the alkyl groups of the aminoborane could also be a possibility in order to assess how the reactivity will be influenced.

4.4 Photochemical reaction of $\text{CpRh}(\text{C}_2\text{H}_4)_2$ in the presence of 2-pyridine-N-methyldimethylsilazane

Silazanes are of great interest for their use in materials chemistry, especially for the preparation of non-oxidizing silicon-based ceramic materials.²⁵ Ru-catalyzed dehydrocoupling reactions of poly(N-methylsilazane) and poly(Si-methylsilazane) have been demonstrated to increase the molecular weight significantly.²⁶ The multicenter reactivity offered by these types of ligands is very interesting. Different coordination modes have been reported; lanthanocene coordinates through two or one agostic σ -Si-H interactions,^{27,28} whilst the ruthenium centre has been proved to coordinate 1,1,3,3-tetramethyldisilazane via two σ -Si-H bonds without N-coordination. The isolated Ru-complex exhibited secondary interactions between the hydrides and the silicon atoms (SISHA) which held together the structure in this unusual coordination mode.²⁹ The coordination of 2-pyridine-N-methyldimethyldisilazane at Ru centers has also been investigated by Sabo-Etienne and coworkers. They found that N-coordination of the pyridine group at the metal centre was always favored and σ -coordination was not observed.³⁰

Perutz and coworkers explored the photochemical reaction of the complex $\text{Cp}^*\text{Rh}(\text{C}_2\text{H}_4)_2$ in the presence of 1,3-divinyl-1,1,3,3-tetramethyldisiloxane, $(\text{CH}_2=\text{CHSiMe}_2)_2\text{O}$, and its disilazane analogue $(\text{CH}_2=\text{CHSiMe}_2)_2\text{-NH}$. The products were formed by coordination through the vinyl groups as for a diene and were found to undergo photoisomerization.³¹ More interestingly, complex $\text{CpRh}(\text{C}_2\text{H}_4)_2$ reacted photochemically in neat $\text{HSiMe}_2\text{OSiMe}_2\text{OSiMe}_2\text{H}$ (hexamethyltrisiloxane) to afford the Rh(V) species $\text{CpRh}(\text{SiMe}_2\text{OSiMe}_2\text{OSiMe}_2\text{H})_2\text{H}_2$ and $\text{CpRh}(\kappa^2\text{-Si,Si}(\text{SiMe}_2\text{OSiMe}_2\text{OSiMe}_2))\text{H}_2$ in a ratio 1:4.8 (Figure 11).³²

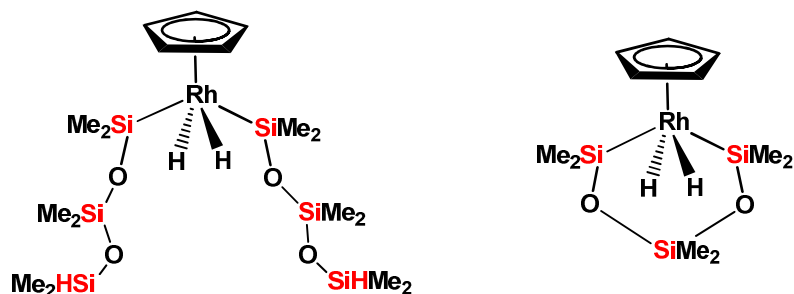


Figure 11. Products formed from photochemical reaction of $\text{CpRh}(\text{C}_2\text{H}_4)_2$ with $\text{HSiMe}_2\text{OSiMe}_2\text{H}$.

In order to determine the reactivity of Si-N containing species towards Rh, we have investigated the reactions of the CpRh centres in the presence of 2-pyridine-N-methyldimethylsilazane (Figure 12). The photochemistry of $\text{CpRh}(\text{PR}_3)(\text{C}_2\text{H}_4)$ complexes ($\text{R} = \text{PMe}_3, \text{PPh}_3$) in the presence of 2-pyridine-N-methyldimethylsilazane has been explored. The reactions appeared not to be very selective for the formation of one product; however the same reaction was repeated using the bis-ethylene analogue $\text{CpRh}(\text{C}_2\text{H}_4)_2$ and greater selectivity was achieved.

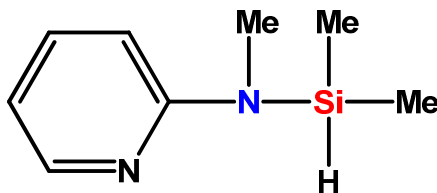


Figure 12. Structure of the silazane used in this work.

4.4.1 Results

Photochemical reaction of $\text{CpRh}(\text{C}_2\text{H}_4)_2$ (10 mg) in the presence of excess 2-pyridine-N-methyldimethylsilazane (5 fold) in hexane led to the formation of new hydride resonances (Figure 13). After 6 hours of photolysis the reaction was at 70% of conversion. The volatile components were removed and the crude material redissolved in C_6D_6 . The major product displayed a hydride resonance at δ -14.9 as a doublet, ($J_{\text{HRh}} = 30.1$ Hz), a new Cp resonance was also present in the ^1H NMR spectrum at δ 5.05. $\{^{29}\text{Si}-^1\text{H}\}$ 2D NMR spectroscopy showed the

hydride to be linked to a ^{29}Si resonance which contained two inequivalent silicon moieties (Figure 14). This species was the only silicon-containing hydride; two minor hydrides were also detected and not identified (δ - 13.6, $J_{\text{Rh-H}}$ 31.5 Hz and δ - 16.1, $J_{\text{Rh-H}}$ 19.6 Hz). The impossibility of a total removal of the silazane under vacuum conditions obscured some of the resonances. The solution was therefore passed through an alumina flash-column in order to obtain complete NMR characterization. The hydride species decomposed after attempted purification by flash chromatography and no hydride resonances were found in the ^1H NMR spectrum.

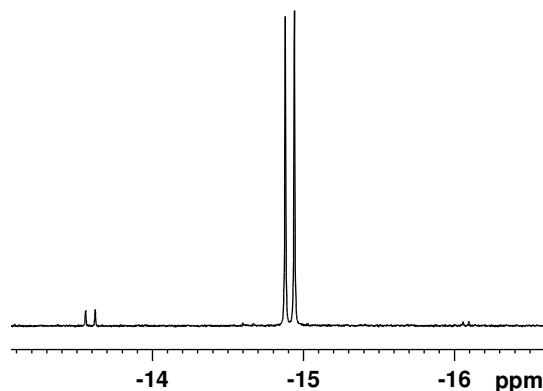


Figure 13. ^1H NMR spectrum in C_6D_6 showing the hydride region. The major doublet belongs to the silicon containing complex.

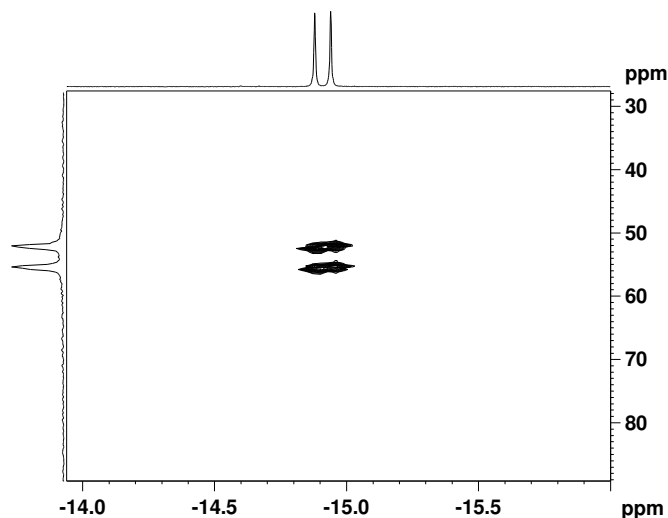


Figure 14. $\{^1\text{H}-^{29}\text{Si}\}$ 2D NMR spectrum showing correlation between the hydride resonance and the ^{29}Si signal. The ^{29}Si signal is two resonances, confirming the presence of two inequivalent ^{29}Si environments.

A solution of the reaction was left in a vial for crystallization after purification; crystals were found and were analyzed by X-ray diffraction. The resulting structure was found to be an octahedral rhodium tris-silazane complex where three silazane units are bound the metal centre through the silicon and the pyridyl – nitrogen (Figure 15). Refinement data were satisfactory as shown in Table 2.

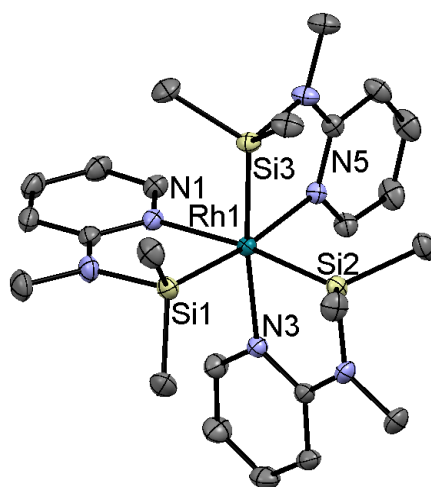


Figure 15. Crystal structure for the rhodium-tris-silazane complex; hydrogen atoms are omitted for clarity. Ellipsoids for the anisotropic displacement parameters are shown at the 50% level.

Table 2. Crystallographic data and refinement data for the rhodium tris-silazane complex.

Formula	$C_{24}H_{39}N_6RhSi_3$
<i>M</i>	598.79
<i>a</i> /Å	16.1618(6)
<i>b</i> /Å	9.5340(3)
<i>c</i> /Å	18.5846(5)
α /deg	90.00
β /deg	100.828(3)
γ /deg	90.00
<i>V</i> / Å ³	6601.3(4)
<i>T</i> /K	110(2)
Space group	$P2_1/c$
<i>Z</i>	4
μ Mo $K\alpha$ mm ⁻¹	0.663
Reflns meads	44756
Reflns indep	9319
R_{int}	0.0357
Final R [$I > 2\sigma(I)$]	$R_1 = 0.0293$

Chapter 4: Photochemical oxidative addition of aminoborane at Rh

	$wR_2 = 0.0664$
Final R (all data)	$R_1 = 0.0374$
	$wR_2 = 0.0712$

Selected distances and angles are given in Table 3. The mean Rh-Si distance of 2.2707(4) Å is slightly shorter than distances found before for $\text{RuH}\{(\text{SiMe}_2)\text{N}(\kappa\text{N-C}_5\text{H}_4\text{N})(\text{SiMe}_2\text{H})\}_3$ (Ru-Si = 2.32 Å)³⁰ as well as than those observed for the complex $\text{Tp}^*\text{RhH}(\text{Et}_2\text{SiH})(\text{PMe}_3)$ reported in Chapter five where the Rh-Si distance was found to be 2.315(2) Å. The N-Rh-Si angles are also consistent with data obtained for the $\text{RuH}\{(\text{SiMe}_2)\text{N}(\kappa\text{N-C}_5\text{H}_4\text{N})(\text{SiMe}_2\text{H})\}_3$ complex (N-Rh-Si = 80.32(6) Å).

Table 3. Selected bond lengths and angles.

Bond length / Å	
Rh1-N1	2.215(1)
Rh1-N3	2.215(1)
Rh1-N5	2.209(1)
Rh1-Si1	2.2711(5)
Rh1-Si2	2.2709(4)
Rh1-Si3	2.2702(5)
Angles / Deg	
N1-Rh1-Si1	82.57(4)
N3-Rh1-Si2	82.27(4)
N5-Rh1-Si3	82.21(4)

The crystals were redissolved in C_6D_6 in order to obtain NMR data. The ^1H NMR spectrum shows four different resonances for the pyridyl protons in a ratio 1:1:1:1, a singlet for the methyl group bound to N at δ 2.6 and two resonances for the diastereotopic methyl groups on the silicon atom at δ 0.7 and δ 0. The ^{29}Si resonance was found to be at δ 53.6 by $\{^{29}\text{Si}-^1\text{H}\}$ 2D NMR spectroscopy. The complex was further characterized by ^{13}C NMR spectroscopy and LIFDI mass-spectrometry.

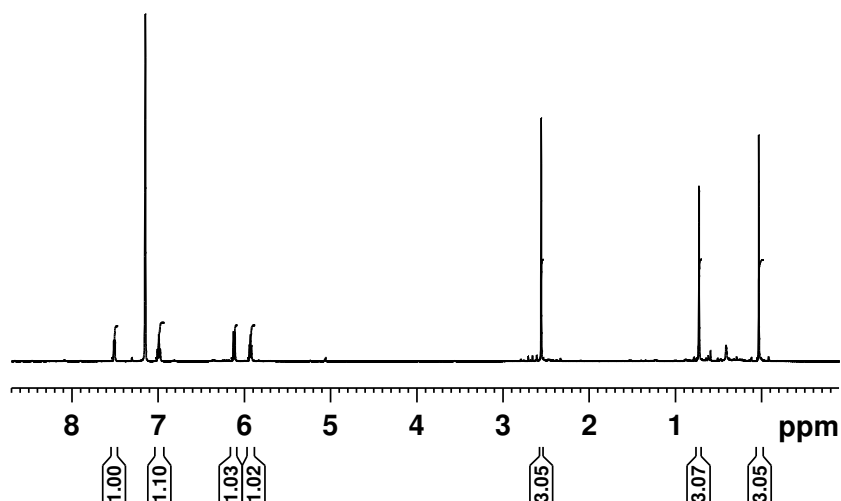
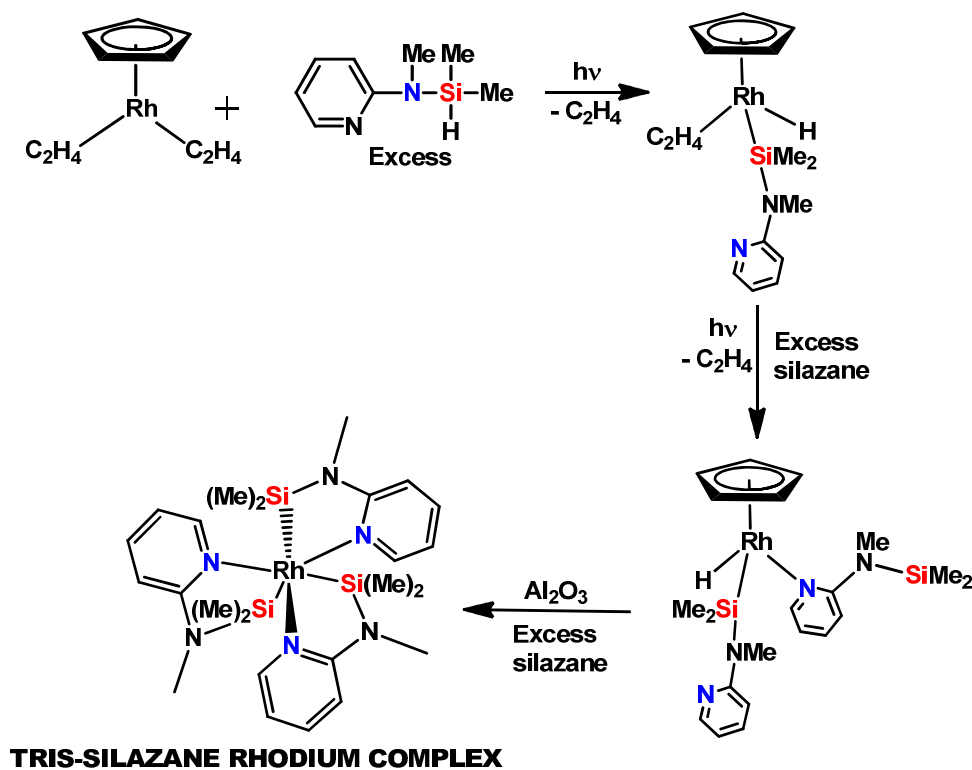


Figure 16. ^1H NMR spectrum for the rhodium-tris silazane complex in C_6D_6 .

The tris-silazane rhodium compound was probably formed by decomposition of the silicon containing product upon interaction with alumina (Scheme 6). Its formation was not observed under photochemical or thermal conditions, but it was always found in solution after attempted column purification.



Scheme 6. Proposed decomposition mechanism of the silicon containing rhodium complex leading to the formation of the Rh tris-silazane complex.

A deeper investigation of the reaction mechanism is needed in order to understand better the reactivity and fully characterize the intermediates. Low temperature photolysis could be employed in order to control better the product distribution for the reactions of the Rh(PR₃) complexes in the presence of the silazane and improve the selectivity in Si-H activation.

4.5 Summary

Photochemical oxidative addition of the B-H bond of the aminoborane H₂BN(*i*Pr)₂ has been proved to take place at CpRh(PR₃) fragments, (PR₃ = PMe₃, PMe₂Ph, PPh₃) to afford the CpRh(PR₃)H(HBN(*i*Pr)₂) complexes. The complexes were fully characterized by NMR spectroscopy and mass spectrometry. Photochemical reaction of CpRh(C₂H₄)₂ with 2-pyridine-N-methyldimethylsilazane, followed by column purification of the product yielded a cyclometallated Rh(III) complex that was characterized crystallographically.

4.6 Experimental

4.6.1 General procedures

All operations were performed under an argon atmosphere, either on a high-vacuum line (10^{-4} mbar), standard Schlenk (10^{-2} mbar) lines or in a glovebox. Solvents for general use (hexane) were of AR grade, dried by distillation over sodium and stored under Ar in ampoules fitted with a Young's PTFE stopcock. Deuterated solvents were dried by stirring over potassium and distilled under high vacuum into small ampoules with potassium mirror. $[\text{CpRh}(\text{PMe}_3)(\text{C}_2\text{H}_4)]$,³³ $[\text{CpRh}(\text{PPh}_3)(\text{C}_2\text{H}_4)]$ ³⁴ and $[\text{CpRh}(\text{PMe}_3)(\text{C}_2\text{H}_4)]$ ³⁵ complexes were synthesized by literature procedures, but replacing TICp by LiCp. $[\text{CpRh}(\text{PMe}_2\text{Ph})(\text{C}_2\text{H}_4)]$ was synthesized following literature preparative³³ by my colleague Marius Câmpian. $\text{H}_2\text{B-N}(i\text{Pr})_2$ and $\text{SiH}(\text{Me}_2)\text{-N}(\text{Me})(\text{C}_5\text{H}_4\text{N})$ were supplied by the Sabo-Etienne group in Toulouse and dried over molecular sieves. Photochemical reactions at room temperature were performed in pyrex NMR tubes fitted with Young's PTFE stopcocks by using a Philips 125 W medium-pressure mercury vapor lamp with a water filter (5 cm).

4.6.2 Mass spectra

LIFDI mass spectra were measured on a Waters Micromass GCT Premier orthogonal time-of-flight instrument set to one scan per second with resolution power of 6000 FWHM and equipped with a LIFDI probe from LINDEN GmbH. The design is very similar to that described by Gross et al.³⁶ Toluene was used for tuning the instrument. The polyethylene glycol probe was kept at ambient temperature with the emitter potential at 12 kV. Activated tungsten wire LIFDI emitters (13 μm tungsten from LINDEN) were ramped manually up to 100 mA for the emitter heating current during the experiment. m/z values are quoted for ^{11}B , ^{103}Rh and ^{28}Si . m/z values are accurate to 0.01 Da

4.6.3 X-ray crystallography

Diffraction data were collected at 110 K on an Agilent SuperNova diffractometer with MoK α radiation ($\lambda = 0.71073\text{\AA}$). Data collection, unit cell determination and frame integration were carried out with “CrysalisPro”. Absorption corrections were applied using crystal face-indexing and the ABSPACK absorption correction software within CrysalisPro. Structures were solved and refined using Olex2³⁷ implementing SHELX algorithms. Structures were solved by either Patterson or direct methods using SHELXS-97 and refined by full-matrix least squares using SHELXL-97. All non-hydrogen atoms were refined anisotropically. Carbon-bound hydrogen atoms were placed at calculated positions and refined using a “riding model”. Hydrogen atoms bound to rhodium and silicon in were found by difference map and refined.

4.6.4 NMR spectroscopy

All standard NMR spectra were recorded on a Bruker AMX500 spectrometer in tubes fitted with Young’s PTFE stopcocks. All ^1H and ^{13}C chemical shifts are reported in ppm (δ) relative to tetramethylsilane and referenced using the chemical shifts of residual protio solvent resonances (benzene, δ 7.15 for ^1H and δ 128.06 for ^{13}C). The $^{31}\text{P}\{^1\text{H}\}$ NMR spectra were referenced to external H_3PO_4 . ^{11}B NMR spectra to were referenced external $\text{BF}_3\cdot\text{Et}_2\text{O}$.

4.6.5 NMR experiments

The products were synthesized by irradiating ~ 10 mg of complex in hexane in the presence of 5 fold $\text{H}_2\text{B-N}(i\text{Pr})_2$. The reaction was taken to completion, the mixture pumped off by vacuum and the crude redissolved in C_6D_6 in order to obtain NMR characterization.

4.6.6 $\text{CpRh}(\text{PMe}_3)\text{H}(\text{BHN}(i\text{Pr})_2)$

^1H NMR (C_6D_6 , 300 K): δ - 14.7 ($J_{\text{H-Rh}} = 35.9$, $J_{\text{H-P}} = 42.01$, RhH), 1.1 (d, 9H, $^2J_{\text{PH}} = 10.1$ Hz, $\text{P}(\text{CH}_3)_3$), 1.2 (d, 6 H, $J_{\text{H-H}} = 5$ Hz, $i\text{PrCH}_3$), 1.3 (d, 6.0 H, $J_{\text{H-H}} = 6$ Hz,

*i*PrCH₃), 3.3 (sept, 1H, $J_{H-H} = 6.7$ Hz, *i*PrCH), 5.2 (sept, $J_{H-H} = 7$ Hz, 1H, *i*PrCH), 5.8 (s, 5H, Cp), 7.5 (b, 1 H, BH).

$^1\text{H}\{^{11}\text{B}\}$ NMR (C_6D_6): δ 7.5 (d, $J_{\text{PH}} = 22.9$ Hz, BH).

$^{31}\text{P}\{^1\text{H}\}$ NMR (C_6D_6): δ 12.2 (d, $J_{\text{RhP}} = 175.8$ Hz).

^{11}B NMR (C_6D_6): δ 55.9 (b, Rh-B).

^{13}C NMR (C_6D_6): δ 22.9 (dd, $J_{\text{PC}} = 32.5$, $J_{\text{RhC}} = 1.8$ Hz, PMe_3), 21.9, 23.7 (CH₃ of *i*Pr), 44.8, 55.6, (CH of *i*Pr), 87.0 (dd, $J_{\text{C-P}} = J_{\text{RhP}} = 2.7$ Hz, Cp).

Mass Spectra (LIFDI, m/z): 357.148 (100%, M⁺), exp 357.127, calcd for C₁₄H₃₀PNBRh.

4.6.7 CpRh(PPh₃)H(BHN(*i*Pr)₂)

^1H NMR (C_6D_6 , 300 K): δ - 14.0 ($J_{\text{H-Rh}} = 33.4$, $J_{\text{H-P}} = 40.3$, RhH), 1.1 (d, 6H, $J_{\text{HH}} = 6.7$ Hz, *i*PrCH₃), 1.2 (d, 6 H, $J_{\text{H-H}} = 6.0$ Hz, *i*PrCH₃), 3.1 (sept, 1 H, $J_{\text{H-H}} = 6.7$ Hz, *i*PrCH), 5.2 (sept, 1 H, $J_{\text{H-H}} = 6.7$ Hz, *i*PrCH), 5.3 (s, 5 H, Cp), 7.0 (m, 9 H, Ph), 7.7 (m, 6 H, Ph), the resonance for the B-H proton overlaps with the phenyl peaks, even upon ^{11}B decoupling was not found.

$^{31}\text{P}\{^1\text{H}\}$ NMR (C_6D_6): δ 63 (d, $J_{\text{RhP}} = 186.2$ Hz).

^{11}B NMR (C_6D_6): δ 56.0 (br, Rh-B).

^{13}C NMR (C_6D_6): 21.8, 23.7 (s, CH₃ of *i*Pr), 44.9, 55.8, (s, CH of *i*Pr), 88.6 (dd, $J_{\text{C-P}} = J_{\text{RhP}} = 2.3$ Hz, Cp), 134.2 (d, $J_{\text{PC}} = 11.1$ Hz, *o*-Ph), 138.5 (s, *m*-Ph), 138.9 (s, *p*-Ph).

Mass Spectra (LIFDI, m/z): 543.176 (100%, M⁺), exp 543.174, calcd for C₂₉H₃₆PNBRh.

4.6.8 CpRh(PMe₂Ph)H(BHN(*i*Pr)₂)

^1H NMR (C_6D_6 , 300 K): δ - 14.4 ($J_{\text{H-Rh}} = 35.1$, $J_{\text{H-P}} = 40.9$, RhH), 1.1 (d, 6 H, $J_{\text{H-H}} = 7.0$ Hz, *i*PrCH₃), 1.2 (d, 6 H, $J_{\text{H-H}} = 6.4$ Hz, *i*PrCH₃), 1.4 (d, 6 H, $J_{\text{PH}} = 9.3$ Hz, P(CH₃)₂), 3.2 (sept, 1 H, $J_{\text{H-H}} = 6.7$ Hz, *i*PrCH), 5.2 (sept, 1 H, $J_{\text{H-H}} = 6.7$ Hz, *i*PrCH), 5.3 (s, 5H, Cp), 7.1 (m, 3 H, Ph), 7.6 (m, 2 H, Ph), 7.5 (b, 1H, BH).

$^1\text{H}\{^{11}\text{B}\}$ NMR (C_6D_6): δ 7.5 (d, $J_{\text{PH}} = 21.4$ Hz, BH).

$^{31}\text{P}\{^1\text{H}\}$ NMR (C_6D_6): δ 27.6, (d, $J_{\text{RhP}} = 181.6$ Hz).

^{11}B NMR (C_6D_6): δ 55.7 (b, Rh-B).

^{13}C NMR (C_6D_6): δ 18.1 (d, $J_{\text{PC}} = 70$ Hz, PMe_2), 21.9, 27.4 (CH_3 of *i*Pr), 44.9, 55.7, (CH of *i*Pr), 87.5 (dd, $J_{\text{C-P}} = J_{\text{RhP}} = 2.5$ Hz, Cp), 130.1 (d, $J_{\text{PC}} = 9.7$ Hz, *o*-Ph), 131.3 (d, $J_{\text{PC}} = 11.4$ Hz, *m*-Ph).

Mass Spectra (LIFDI, m/z): 419.14 (100%, M^+), exp 419.14, calcd for $\text{C}_{19}\text{H}_{32}\text{PNBRh}$.

4.6.9 $\text{CpRh}((\text{SiMe}_2)\text{N}(\kappa\text{N-C}_5\text{H}_4\text{N}))_3$

^1H NMR (C_6D_6 , 300 K): δ 0 (s, 3 H, SiCH_3), 0.7 (s, 3 H, SiCH_3), 2.6 (s, 3 H, NCH_3), 5.9 (d, 1 H, $J_{\text{HH}} = 6.2$ Hz, Py), 6.1 (d, 1 H, $J_{\text{H-H}} = 8.8$ Hz, Py), 7.0 (m, 1 H, Py), 7.5 (m, 1 H, Py).

^{29}Si NMR (C_6D_6): δ 53.6.

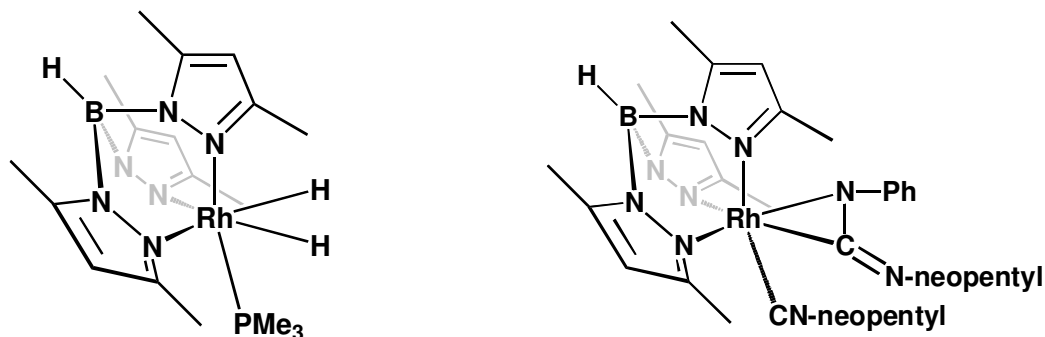
^{13}C NMR (C_6D_6): δ 3.2 (s, SiMe), 6.4 (d, SiMe), 31.9, (s, NMe), 107.3, 111.3, 137.3, 148.0 (s, C-Py), 164.3 (s, *q*C-Py).

Mass Spectra (LIFDI, m/z): 598.17 (100%, M^+), exp 598.16, calcd for $\text{C}_{24}\text{H}_{39}\text{PN}_6\text{Si}_3\text{Rh}$.

5 C-F, B-H, and Si-H activation at Tp`Rh complexes

5.1 Introduction

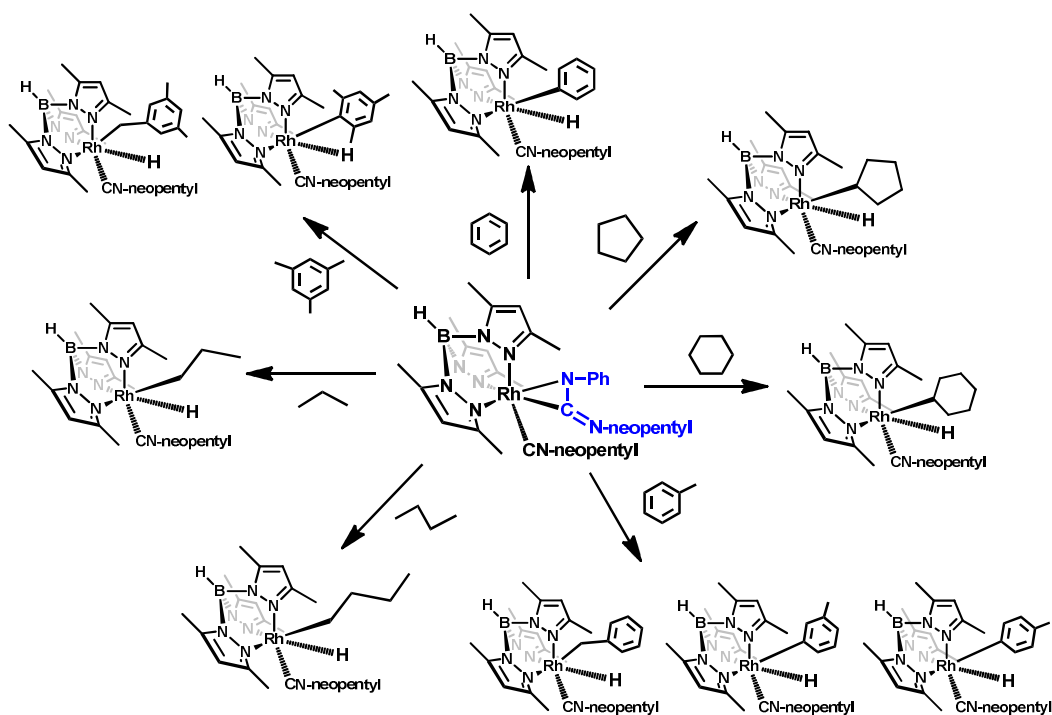
Tris(pyrazolyl)borate - metal complexes have been extensively studied since the advent of Tp ligands in organometallic chemistry in 1970.¹ The chemistry of group 9 tris(pyrazolyl)borate complexes has been reviewed in detail presenting these complexes as good activators of C-H bonds either photochemically or thermally.² This Chapter will be focused on the reactivity of Tp`Rh(PMe₃)H₂ and Tp`Rh(CNneopentyl)(η^2 -PhN=C=N-neopentyl) complexes shown in Scheme 1 where Tp` = tris(2,4 – dimethylpyrazolyl) borate.



Scheme 1. Structures of the Tp`Rh complexes investigated.

Tp`Rh(CNneopentyl)(η^2 -PhN=C=N-neopentyl) is a well known complex; synthesis and photoactive properties of the complex were reported for the first time by Jones and coworkers in 1992.³ The photochemistry of the complex was further investigated in the presence of a wide variety of ligands looking at selectivity towards C-H activation (Scheme 2). The complex showed preference towards primary C-H bonds of alkanes over secondary. Aromatic and benzylic C-H activation were also both achieved, with the aromatic C-H activated product being the thermodynamic products. Aromatic C-H activation was established to be preferred to the aliphatic one, even though aliphatic C-H bonds are weaker.

The stronger Rh-C bond formed in activation of aromatic C-H bonds was given as the reason for aromatic C-H oxidative addition over the aliphatic.⁴



Scheme 2. C-H activation achieved in photochemical reactions of complex $Tp`Rh(CNneopentyl)(\eta^2-PhN=C=N-neopentyl)$ with different aromatic and aliphatic hydrocarbons.

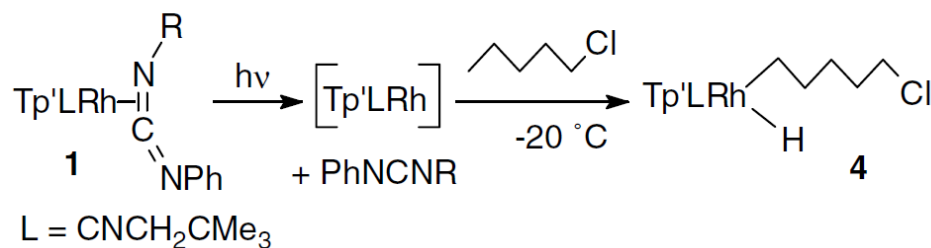
Comparison with the previously studied unsaturated fragments $Cp^*Rh(PMe_3)$ and $Cp^*Ir(PMe_3)$ highlighted a similar reactivity towards C-H bonds, suggesting that selectivity is not strongly influenced by the ligand-type or the nature of the metal centre. The combination between kinetic selectivity and reductive elimination allowed the authors to determine the thermodynamic barriers for the activation of different C-H bonds.⁴ A similar investigation was conducted for reactions of the same unsaturated fragment $Tp`Rh(CNneopentyl)$ in the presence of vinylic and allylic C-H bonds; the trend in Rh-C bond strength was found to follow the one previously determined for hydrocarbons (Scheme 3),⁵ but with a steeper gradient. In other words, although M-C bonds are weaker than H-C bonds, they strengthen more rapidly as the substituent changes.

Rh-Ph > Rh-vinyl > Rh-methyl > Rh-alkyl (1°) > Rh-cycloalkyl (2°) > Rh-benzyl > Rh-allyl

Scheme 3. Trend for Rh-C bond strengths for the activation of aliphatic, aromatic vinylic and allylic C-H bonds.

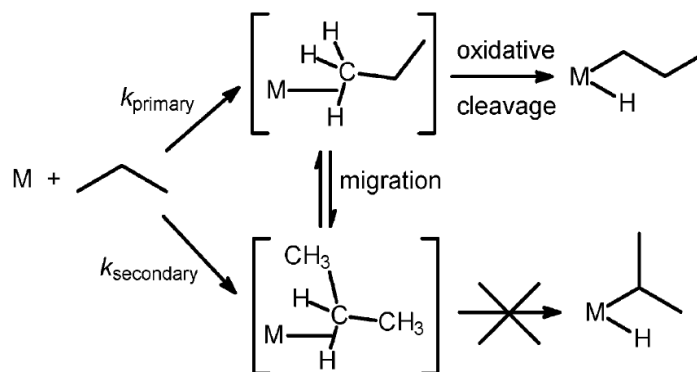
The majority of the metal-hydrides formed in reactions of complex Tp`Rh(CNneopentyl)(η^2 -PhN=C=N-neopentyl) in the presence of vinyls and allyls were observed to be thermally unstable and rearrange to the η^2 -olefin analogues. Increasing the steric hindrance of the alkene afforded stable Rh-allyl-hydrides.⁵

The behavior of the same complex in the presence of mono-chloroalkanes showed that C-H activation of the terminal methyl group was the only observed product, no evidence of C-Cl oxidative addition was detected (Scheme 4).⁶



Scheme 4. Photochemical reaction of complex Tp`Rh(CNneopentyl)(η^2 -PhN=C=N-neopentyl) in the presence of chloroalkanes.

Further experiments highlighted also a slight preference for the unsaturated fragment Tp`LRh to coordinate in the first place to secondary C-H bonds to form a σ -alkane complex. The selectivity for C-H oxidative addition of primary carbons previously observed was justified proposing a migration step from a secondary σ -alkane complex to a primary one (Scheme 5).



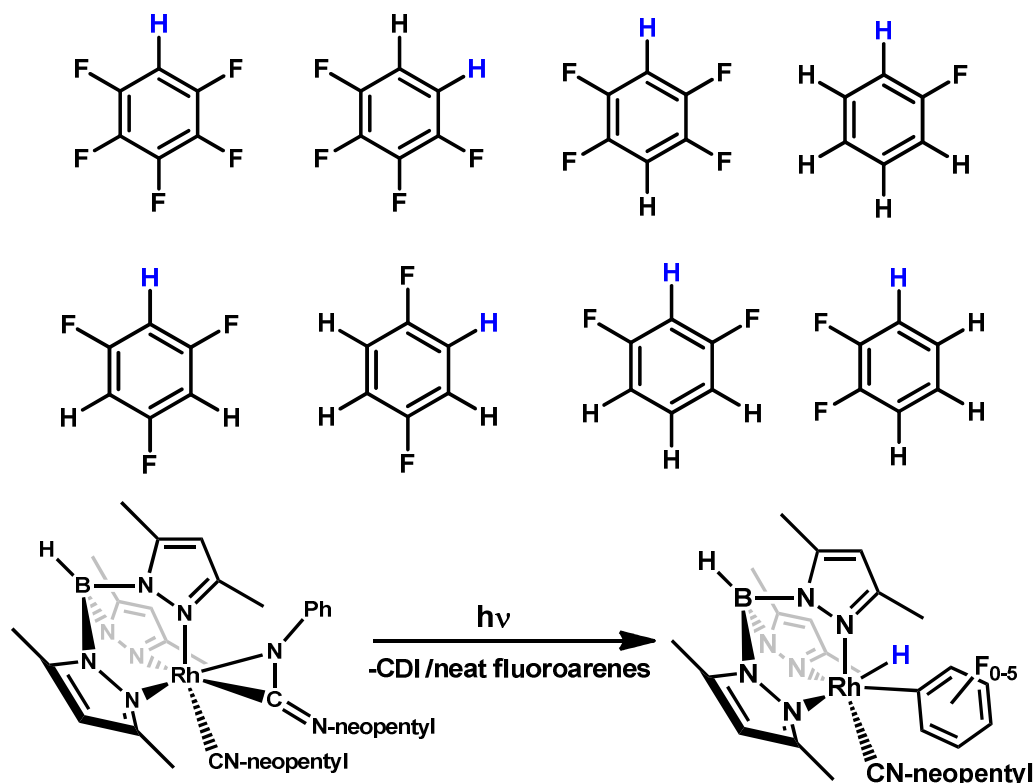
Scheme 5. Migration from a secondary σ -alkane complex to a primary one to favor the activation of primary C-H bonds in chloroalkanes.

More recently the complex $\text{Tp}^{\text{R}}\text{Rh}(\text{CNneopentyl})(\eta^2\text{-PhN}=\text{C}=\text{N-neopentyl})$ was investigated in the presence of partially fluorinated arenes in order to assess selectivity between C-H and C-F activation (Scheme 6). The results were also used to determine the thermodynamics of the process. A wide range of fluoroarenes were tested and a variety of complexes of the type $[\text{Tp}^{\text{R}}\text{Rh}(\text{CNneopentyl})(\text{aryl}^{\text{F}})\text{H}]$ were isolated.⁷ The unsaturated fragment $[\text{Tp}^{\text{R}}\text{Rh}(\text{CNneopentyl})]$, formed after photochemical loss of the carbodiimide ligand, showed selectivity towards the activation of the C-H bond and the results confirmed experimentally the theory of the ortho fluorine effect previously proposed by Perutz and Eisenstein.^{8,9} Thermodynamic selectivity was found to be controlled by the presence of ortho fluorines: all the compounds formed converted thermally to the C-H activated product with the maximum number of ortho fluorines, even when more than one isomer was kinetically formed. No evidence of C-F activation was found for reactions of the complex in neat fluorinated arenes.

The tris(pyrazolyl)borate dihydride rhodium complex $\text{Tp}^{\text{R}}\text{Rh}(\text{PMe}_3)\text{H}_2$ is “younger” than the carbodiimide analogue. It was first synthesised by hydrogenation of the ethylene precursor¹⁰ and its photochemistry was explored in the presence of C_6H_6 to afford the C-H activated product.¹¹

A direct alternative route for the synthesis of the complex was proposed by Jones and co-workers and reported in 2009.¹² They also showed the capability of the fragment $\text{Tp}^{\text{R}}\text{Rh}(\text{PMe}_3)$, formed after losing H_2 under photochemical

conditions, to activate the C-C bond of biphenylene and to be an active catalyst in the hydrogenation of the latter to form the biphenyl product.



Scheme 6. Top: Partially fluorinated arenes investigated. Bottom: Reactions of complex Tp`Rh(CNneopentyl)(η^2 -PhN=C=N-neopentyl) in the presence of partially fluorinated arenes.

Additionally, Jones` work looked at the trend in C₆D₆ reductive elimination of different Tp`Rh fragments and compared it with the Cp* ligand previously explored. The authors showed how both electronic and steric features of the ligands around the metal centre play a fundamental role in C₆H₆ reductive elimination which was established to be 250 times slower for the Tp` complex than the Cp* complex (Scheme 7). This was explained on the basis of a different steric demand of the two substituents which are electronically very similar.¹²



Scheme 7. Trend for reductive elimination of C_6H_6 between different Tp^*Rh complexes and comparison with the Cp^* previously observed. In brackets are relative rates at 100°C .

The complex was also tested in photochemical reactions with partially fluorinated arenes (Figure 1); the authors isolated and characterised a number of $\text{Tp}^*\text{Rh}(\text{PMe}_3)(\text{H})(\text{Ar}^{\text{F}})$ where C-H activation took place preferentially where the C-H bond had fluorines in ortho position (Scheme 8).¹³

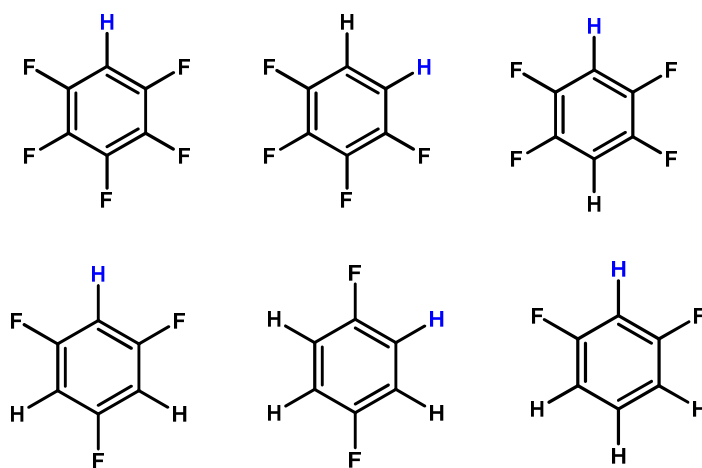
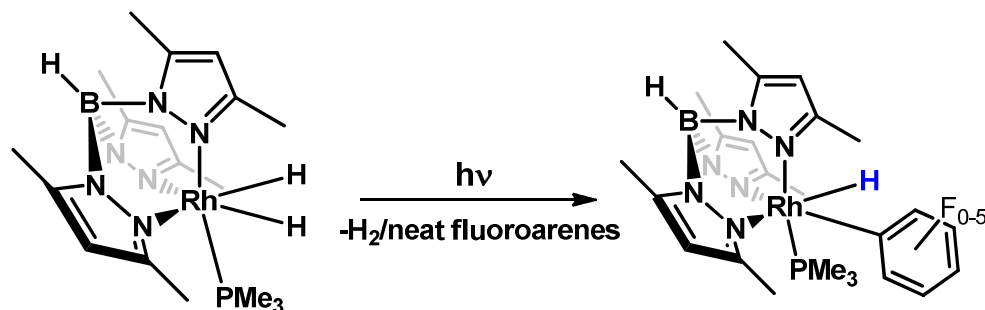


Figure 1. Partially fluoroarenes investigated in photochemical reactions of the complex $\text{Tp}^*\text{Rh}(\text{PMe}_3)\text{H}_2$.

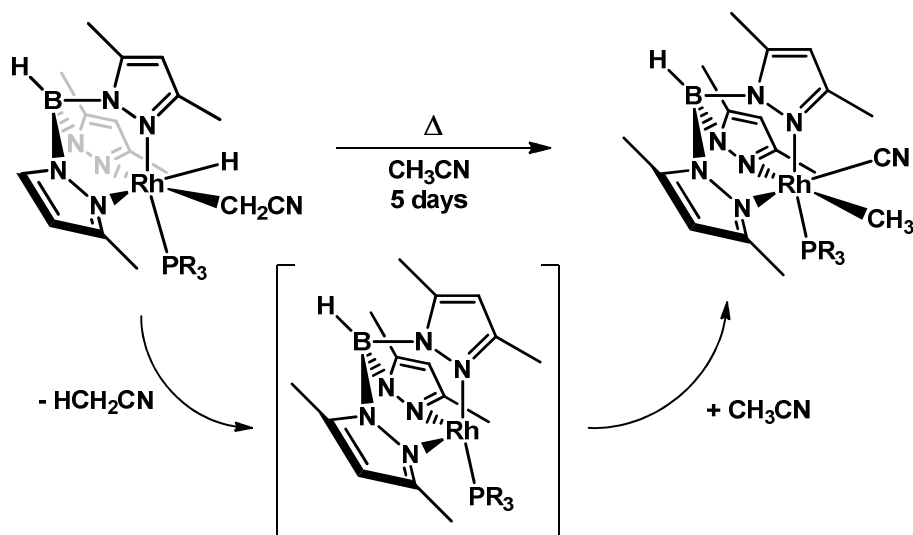


Scheme 8. Photochemical reaction of complex $\text{Tp}^*\text{Rh}(\text{PMe}_3)\text{H}_2$ in neat fluoroarenes to form the $\text{Tp}^*\text{Rh}(\text{PMe}_3)(\text{Ar}^{\text{F}})(\text{H})$ products.

The determination of the kinetics of reductive elimination for the fluoroarenes in C_6H_6 was attempted, but they were complicated by the formation of the

Tp`Rh(PMe₃)₂ complex under thermal conditions. Therefore the Tp`Rh(PMe₂Ph)H₂ complex was synthesized and used for this purpose, the “ortho fluorine effect theory” was again proved experimentally through combination of results from kinetics of reductive elimination and selectivity. Similarly to what previously observed in reaction of the Tp`Rh(CNneopentyl)(*η*²-PhN=C=N-neopentyl) complex, no C-F activation was observed for any of the fluoroarenes investigated.

Activation of C-H and C-CN bonds was also recently reported using the same Tp`Rh(PMe₃) fragment. The complex was found to undergo photochemical C-H activation of CH₃CN in first place, to form the kinetic product Tp`Rh(PMe₃)(CH₂CN)H, conversion to the thermodynamic product was then achieved by heating the reaction mixture at 100°C. This afforded the Tp`Rh(PMe₃)(CH₃)(CN) complex (Scheme 9).

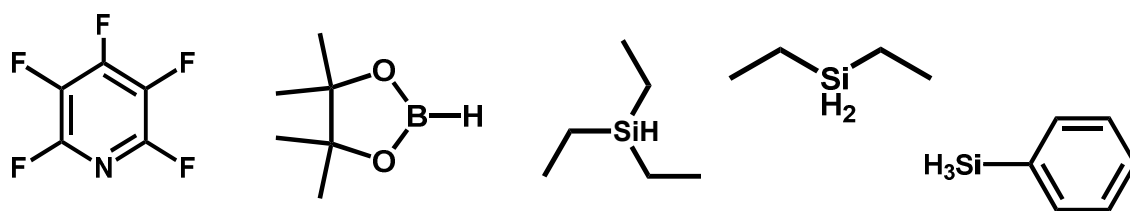


Scheme 9. Activation of C-H and C-CN bonds in reaction of complex Tp`Rh(PMe₃)Ar^FH with CH₃CN.

The extensive work done with these complexes focused mainly on aliphatic and aromatic C-H activation, but almost nothing is known about their reactivity towards different types of bonds. No reactivity towards C-F bonds was

observed by Jones *et al.* in reactions with fluorinated arenes, and the fragment $\text{Tp}^{\text{R}}\text{Rh}(\text{PMe}_3)$ appeared not to react in the presence of Et_3SiH .¹³

Our work shows the capability of these complexes to react with different bonds than C-Hs and an unexpected selectivity when a C-H bond is present within the ligand is observed. The photochemistry of both complexes was explored in the presence of $\text{C}_5\text{F}_5\text{N}$, HBpin and silanes (Scheme 10), intramolecular and intermolecular competition reactions were also carried out to see the selectivity towards one bond with respect to the other.



Scheme 10. Structures of the substrates investigated.

5.2 Results

5.2.1 Starting material Tp`Rh(PMe₃)H₂

The starting complex Tp`Rh(PMe₃)H₂ was provided by the Jones group in Rochester. It was synthesised following literature procedures.¹² The complex is a Rh(III) species, that displays a doublet in the ³¹P{¹H} NMR spectrum at δ 3.04 with a J_{PRh} of 138 Hz (Figure 2). The ¹H NMR exhibits a hydride resonance at δ -17.09 (dd, $J_{\text{RhH}} = 21$ Hz, $J_{\text{PH}} = 36$ Hz), a doublet for the PMe₃ at δ 1.21, four resonances for the CH₃ groups of the Tp` ligand in a 1:2:2:1 ratio and two signals for the CHs of the Tp` in a 2:1 ratio at δ 5.52 and 5.77 (Figure 3).

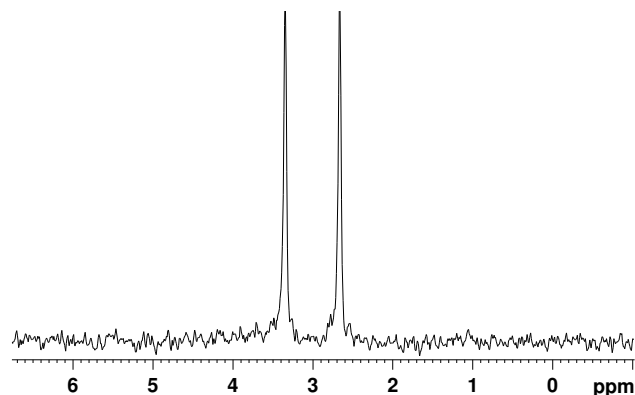


Figure 2. ³¹P{¹H} NMR spectrum in C₆D₆ for the Tp`Rh(PMe₃)H₂ starting material.

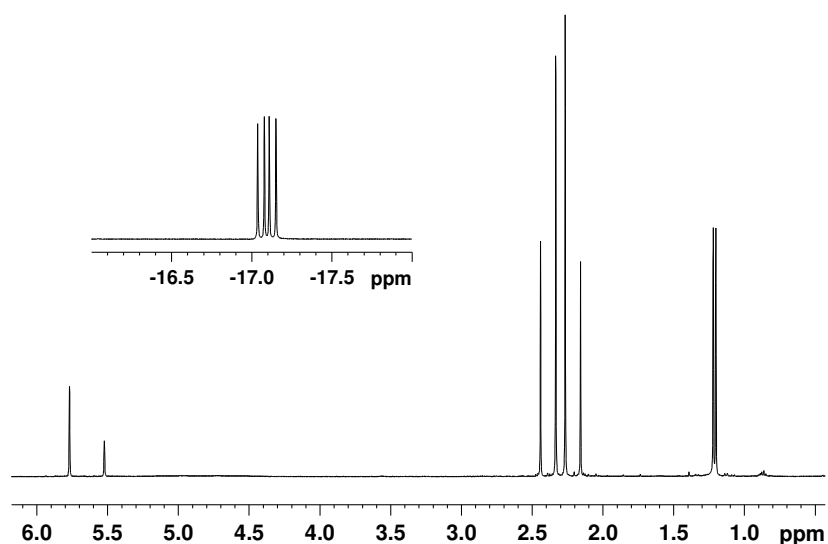


Figure 3. ¹H NMR spectrum in C₆D₆ for the Tp`Rh(PMe₃)H₂ starting material. The inset shows the hydride resonance.

5.2.2 Photochemical reaction of Tp`Rh(PMe₃)H₂ in the presence of C₅F₅N

The irradiation of Tp`Rh(PMe₃)H₂ in neat pentafluoropyridine ($\lambda > 290$ nm, 5 h, room temperature) generates one product cleanly, leading to an NMR yield for the new complex $> 80\%$. This product was purified by removing the volatiles and washing the solid with hexane; the white solid was redissolved in C₆D₆ and characterised by multinuclear NMR spectroscopy and LIFDI mass spectrometry. The ³¹P{¹H} NMR spectrum shows a resonance at δ 6.67, as a doublet of doublets ($J_{\text{RhP}} = 129$, $J_{\text{PF}} = 17$ Hz) (Figure 4). The value of J_{RhP} indicates a Rh(III) oxidation state¹⁴ and the values of J_{FP} are similar to those for Cp`Rh(C₆F₅)F(PMe₃) complexes.¹⁵

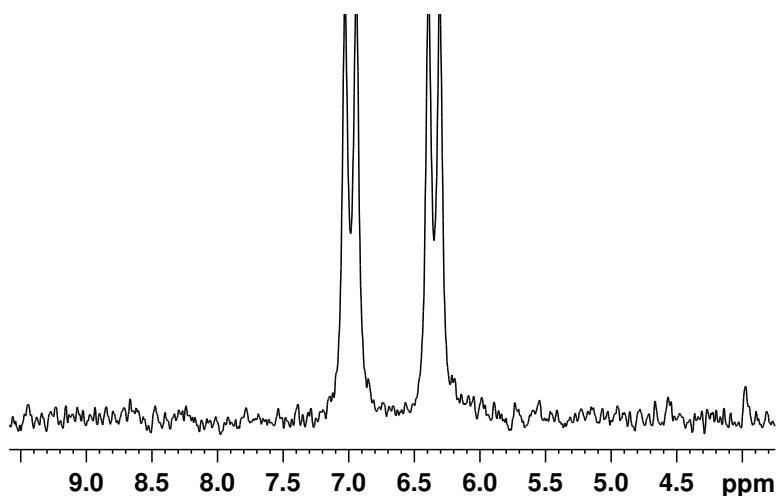


Figure 4. ³¹P{¹H} NMR spectrum of the complex Tp`Rh(C₅F₄N)(PMe₃)F.

A typical Rh-F broad resonance was found in the metal-fluoride region of the ¹⁹F NMR spectrum at δ - 429 consistent with a Rh-F bond. Low temperature ¹⁹F NMR sharpened the resonance enabling J_{RhF} to be measured as 182 Hz. The product was assigned as the Tp`Rh(C₅F₄N)(PMe₃)F complex. The presence of a second isomer was also detected by low temperature ¹⁹F NMR; the weak and broad resonance at δ - 455.4, not visible at room temperature, sharpened upon cooling (Figure 5). The two species were assigned as two ortho conformers in a 10:1 ratio. The assignment was possible by analysing the aromatic part of the ¹⁹F NMR spectrum where two sets of four inequivalent fluorines were detected

in a 10:1 ratio. The presence of only two fluorine resonances close to N discarded the possibility of having the ortho and meta isomers. The meta isomers would have displayed two peaks for fluorine atoms adjacent to nitrogen, for a total of three resonances for the two regioisomers. Instead a set of similar chemical shifts was observed (δ -85.9/84.6; 133.0/129.9; 148.3/146.6; 169.0/168.5) suggesting the two species to be rotamers. The chirality at rhodium was demonstrated by the appearance of three singlets for the Tp`-methine groups and six resonances for the inequivalent Tp`-methyls. The complexes were fully characterized by NMR spectroscopy and LIFDI mass-spectrometry.

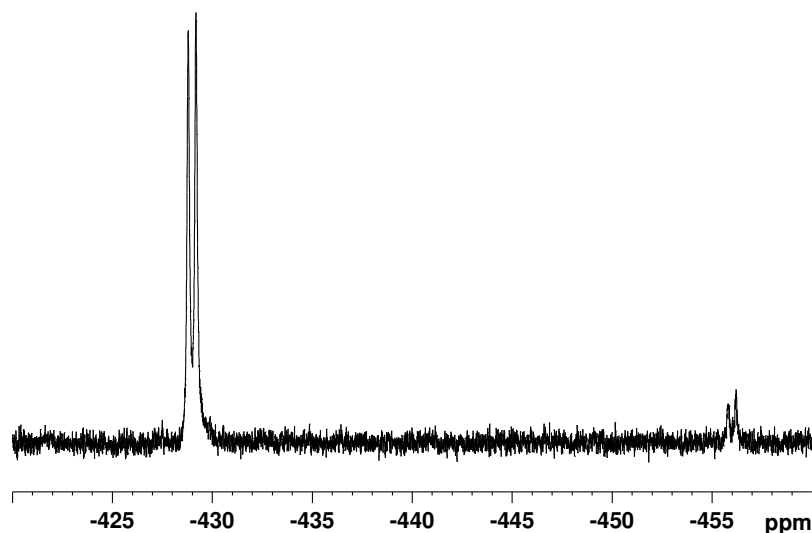


Figure 5. Low temperature ^{19}F NMR spectrum showing the presence of the two ortho conformers.

The reaction was scaled up in order to isolate the major species; crystals were obtained from a hexane solution and the structure determined to be the bifluoride analogue $\text{Tp`Rh}(\text{FHF})(2\text{-C}_5\text{NF}_4)(\text{PMe}_3)$, where a molecule of HF is coordinated to the fluoride atom (Figure 6). More details are given below.

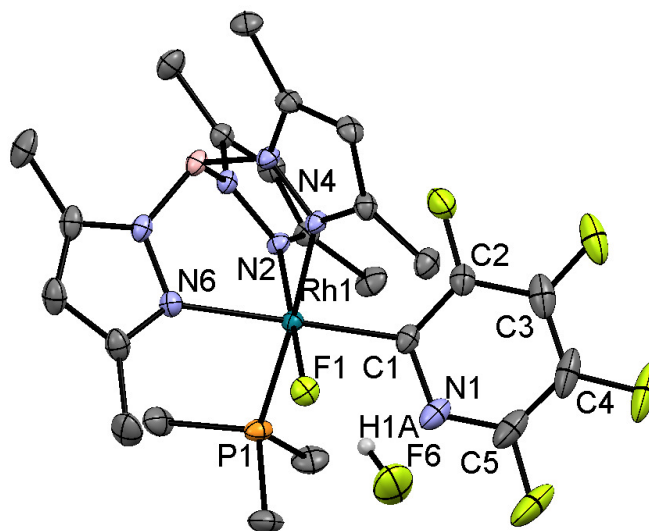


Figure 6. Crystal structure of the complex $\text{Tp}^{\text{`}}\text{Rh}(\text{FHF})(\text{C}_5\text{NF}_4)(\text{PMe}_3)$, hydrogen atoms are omitted for clarity apart from the bifluoride. Ellipsoids for the anisotropic displacement parameters are shown at the 50% level.

Spectroscopic characterization of the bifluoride complex $\text{Tp}^{\text{`}}\text{Rh}(\text{FHF})(\text{C}_5\text{NF}_4)(\text{PMe}_3)$ was also carried out. NMR analysis showed the typical features for this kind of complexes: a broad low-field resonance ($\delta 10.7$) found in the ^1H NMR spectrum which resolves to a doublet on exchanging the solvent from C_6D_6 (Figure 7) to C_7D_8 (Figure 8) due possibly to higher dryness of toluene. This resonance is assigned to the hydrogen of the FHF ligand and exhibits a large coupling ($J_{\text{HF}} = 447$ Hz) associated with the distal fluorine of the bifluoride. The $^{31}\text{P}\{^1\text{H}\}$ NMR spectrum shows a doublet of doublets at $\delta 6.70$ with very similar coupling constants to those observed for the fluoride analogue.

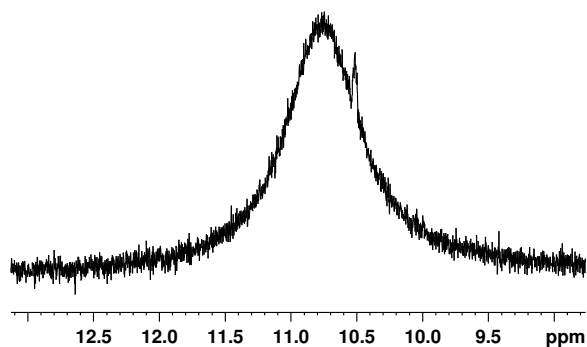


Figure 7. ^1H NMR spectrum in C_6D_6 showing the broad low field peak belonging to the bifluoride proton.

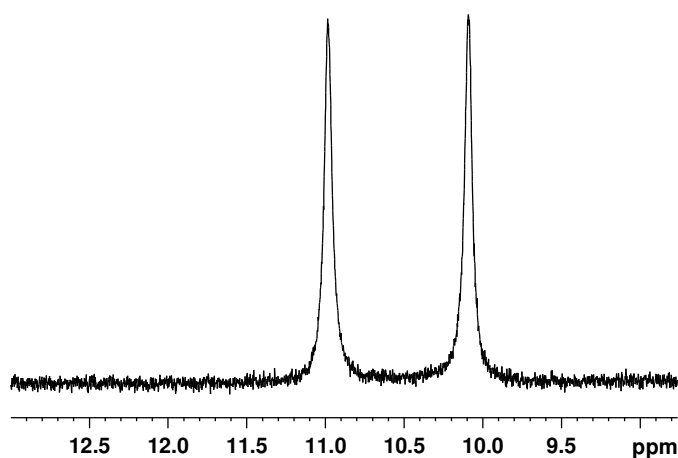


Figure 8. ^1H NMR spectrum in C_7D_8 showing a doublet at low field belonging to the bifluoride proton.

The ^{19}F NMR spectrum at 205 K shows two resonances assigned to the proximal fluorine (directly bonded to Rh) and for the distal one respectively (Figure 9). The first one resonates as a broad peak at δ 398.9 while the second one appears as a doublet at δ -178.7, showing the same large coupling constant observed in the ^1H NMR spectrum ($J_{\text{HF}} = 447$ Hz). All the NMR data for the bifluoride complex are consistent with what previously observed for the bifluoride analogues of $\text{Ru}(\text{PP})_2$.¹⁶

The crystal structure for complex $\text{Tp}^{\text{`}}\text{Rh}(\text{FHF})(2\text{-C}_5\text{F}_4\text{N})(\text{PMe}_3)$ was determined as shown in Figure 6. Refinement data were satisfactory (Table 1).

Table 1. Refinement data for complex Tp`Rh(FHF)(C₅NF₄)(PMe₃).

Formula	C ₂₃ H ₃₂ BF ₆ N ₇ PRh
<i>M</i>	834.31
<i>a</i> /Å	34.358(13)
<i>b</i> /Å	8.538(3)
<i>c</i> /Å	22.805(9)
α /deg	90.00
β /deg	99.322(4)
γ /deg	90.00
<i>V</i> / Å ³	6601.3(4)
<i>T</i> /K	110(2)
Space group	C ₂ /c
<i>Z</i>	8
μ Mo K α /mm ⁻¹	0.663
Reflns meas	16457
Reflns indep	9556
<i>R</i> _{int}	0.0252
Final <i>R</i> [<i>I</i> > 2 σ (<i>I</i>)]	<i>R</i> ₁ = 0.0356
	<i>wR</i> ₂ = 0.0785
Final <i>R</i> (all data)	<i>R</i> ₁ = 0.0458
	<i>wR</i> ₂ = 0.0831

The structure shows the presence of the bifluoride, FHF, coordinated to the rhodium; the acidic proton was not found by difference map and was located taking into account the known HF bond distance.¹⁷ Selected bond lengths and angles are summarized in Table 2.

Table 2. Selected bond lengths and angles for complex Tp`Rh(FHF)(2-C₅NF₄)(PMe₃).

Bond length / Å	
F1-Rh1	2.0107(12)
C1-Rh1	2.005(2)
N2-Rh1	2.0452(17)
N4-Rh1	2.1138(16)
N6-Rh1	2.1869(17)
P1-Rh1	2.2927(6)
F1...F6	2.334(2)
F1...H1A	1.441(1)
Angles / Deg	
P1-Rh1-F1	89.35(4)
N2-Rh1-C1	93.75(8)
N4-Rh1-C1	92.55(8)
N6-Rh1-C1	172.47(8)
Rh1-F1-F6	139.28(8)

The Rh-F bond length (2.0107(12) Å) is considerably shorter than the one observed for the [Rh(FHF)(COD)(PPh₃)] complex (2.083(2) Å). It is actually closer to the bond length observed for the fluoride analogue (2.0214(12) Å).¹⁸ This is probably reflected in a very weak hydrogen bonding between HF and the rhodium fluoride complex, as also confirmed by the fact that HF gets uncoordinated when the complex is left in solution for few days. The Rh-F...F angle was found to be 139.28(8) and it is similar to the one reported for the *trans*-[(Ph₃P)₂Rh(Ph₂PF)(FHF)].¹⁹ The F1...F6 distance is also consistent with previous observation; a distance of 2.329 Å was given for the *trans*-[(Ph₃P)₂Rh(Ph₂PF)(FHF)] complex.

Table 3. Selected torsional angles.

Torsional angles / Deg	
C5F4N-Rh1N2P1	81.35
C5F4N-Rh1N4P1	51.79
C5F4N-Rh1N6P1	42.78

A slightly distorted octahedral geometry is observed around the Rh centre, the plane of the fluoropyridine ring bisects the trispyrazolylborate group almost perfectly. A list of torsional angles is reported (Table 3). A short contact of 2.575 Å was found in the molecule between the pyridyl nitrogen and the HF proton. A molecule of pentafluoropyridine was found as solvent of crystallization.

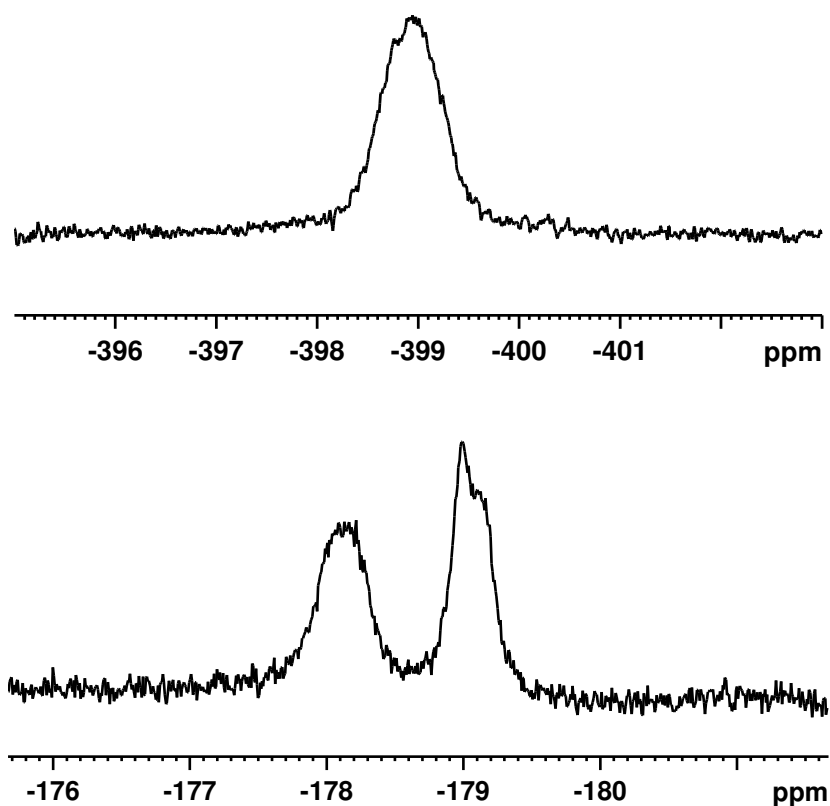


Figure 9. ^{19}F NMR spectrum of complex $\text{Tp}^{\text{R}}\text{Rh}(\text{FHF})(\text{C}_5\text{NF}_4)(\text{PMe}_3)$ showing: top, broad resonance assigned to the proximal fluorine of the bifluoride; bottom: doublet assigned to the distal fluorine of the bifluoride.

5.2.3 Photochemical reaction of complex Tp`Rh(PMe₃)H₂ in the presence of 2,3,5,6 - tetrafluoropyridine

The photochemical reaction of complex Tp`Rh(PMe₃)H₂ in neat 2,3,5,6-tetrafluoropyridine was investigated in order to explore intramolecular competition between C-H and C-F activation and to confirm the selectivity for C-H activation previously observed in partially fluorinated benzenes.²⁰ After 5 hours of photolysis the reaction reached 30% conversion; the volatiles were removed and the solid redissolved in C₆D₆. The ³¹P{¹H} NMR spectrum showed the appearance of two new products, both resonating as doublets of doublets at δ - 2.33, (dd, $J_{\text{RhP}} = 127.3$, $J_{\text{PF}} = 19.7$ Hz) and 4.6, (dd, $J_{\text{RhP}} = 132.1$, $J_{\text{PF}} = 17.5$ Hz) respectively, suggesting coupling to ¹⁰³Rh and to ¹⁹F (Figure 10). The ¹H NMR spectrum shows the presence of a new hydride resonance at δ - 15.5 (ddd, $J_{\text{RhH}} = 14.3$, $J_{\text{FH}} = 19.1$ Hz, $J_{\text{PH}} = 24.6$ Hz) (Figure 11, top), which was found linked by {¹H - ³¹P} HMQC NMR to the doublet of doublet at δ - 2.33 in the ³¹P{¹H} NMR spectrum. The coupling to ³¹P was assigned upon running ¹H{³¹P} NMR spectroscopy. This species was assigned as Tp`Rh(H)(C₅F₄N)(PMe₃). The ¹⁹F NMR spectrum shows a characteristic rhodium-fluoride peak at δ - 430.1, it appears as a doublet with a J_{FRh} of 181.3 Hz (Figure 11, bottom). On the basis of these results, we assigned the second product to the C-F activated complex Tp`Rh(F)(C₅F₃NH)(PMe₃). The aromatic proton was also detected at δ 6.2. The two products were found to be in a 1:4 ratio in favor of C-H activation, but to our surprise C-F activation also took place. This contrasts with the results in the presence of fluorinated arenes previously published, where no detection of C-F activation was mentioned.²⁰

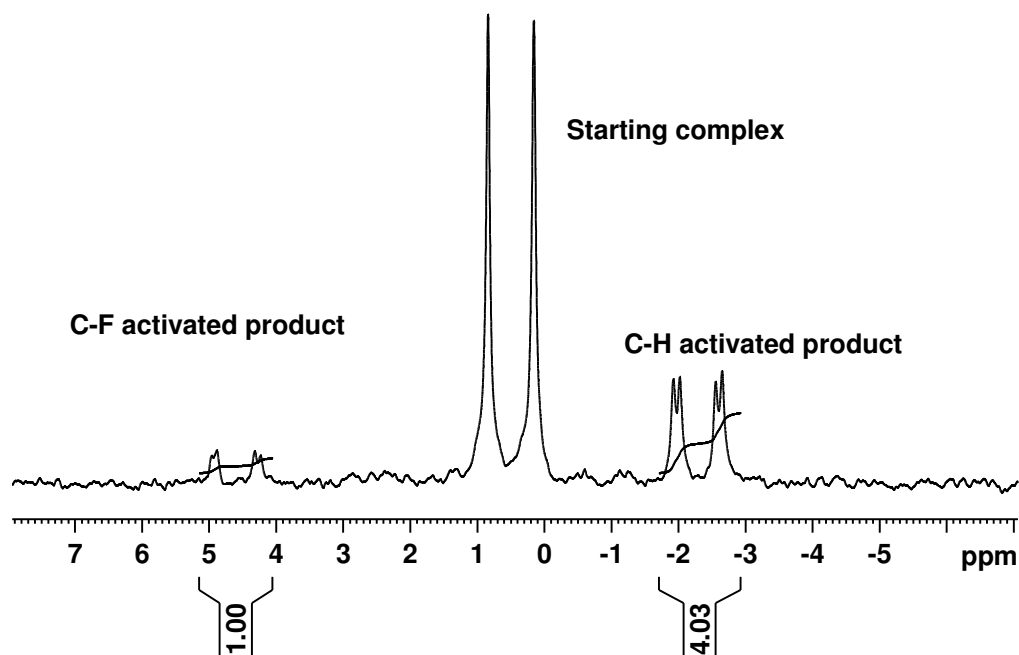


Figure 10. $^{31}\text{P}\{^1\text{H}\}$ NMR spectrum for reaction of $\text{Tp}^*\text{Rh}(\text{PMe}_3)_2\text{H}_2$ in the presence of $\text{C}_5\text{F}_4\text{HN}$ after 5 hours of irradiation.

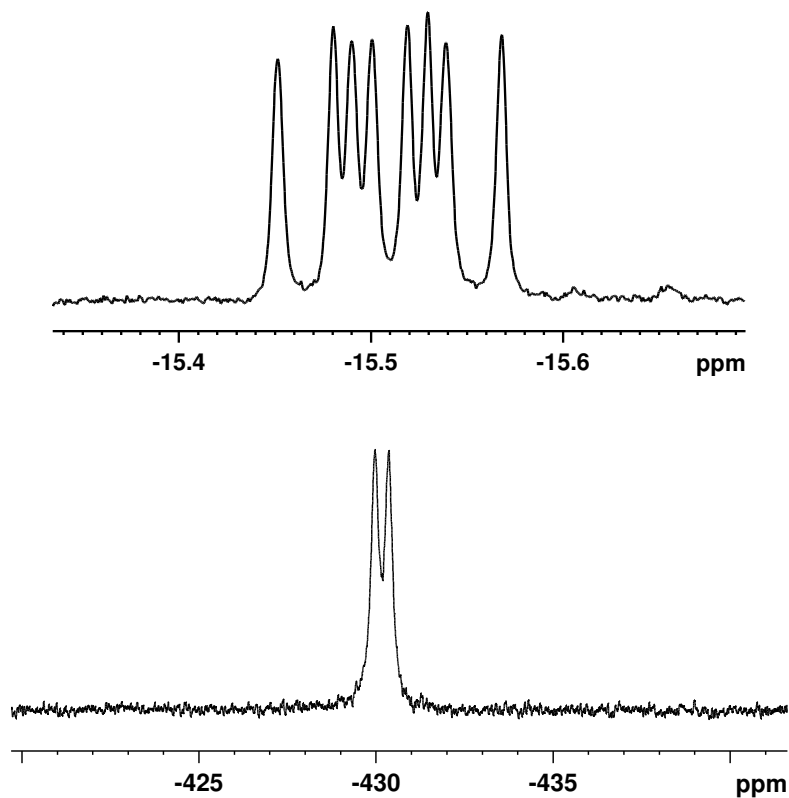


Figure 11. Top: ^1H NMR spectrum, hydride resonance for the complex $\text{Tp}^*\text{Rh}(\text{C}_5\text{F}_4\text{N})(\text{PMe}_3)_2\text{H}$ in C_6D_6 . Bottom: ^{19}F NMR spectrum, fluoride resonance for the complex $\text{Tp}^*\text{Rh}(\text{C}_5\text{F}_3\text{NH})(\text{PMe}_3)_2\text{F}$ in C_6D_6 .

5.2.4 Photochemical reaction of Tp`Rh(PMe₃)H₂ in the presence of HBpin

The irradiation of Tp`Rh(PMe₃)H₂ in neat HBpin ($\lambda > 290$ nm, 1 h, room temperature) generates cleanly one product, leading to an NMR yield for the new complex $> 90\%$. This product was purified by removing the volatiles, washing the solid with hexane and passing it through an alumina column. The solid was redissolved in C₆D₆ and the characterization was done by multinuclear NMR spectroscopy, LIFDI mass spectrometry and X-ray crystallography. The ³¹P{¹H} spectrum shows a resonance at δ 5.2, as a doublet ($J_{\text{RhP}} = 145$ Hz) (Figure 12). The value of J_{RhP} indicates a Rh(III) oxidation state typical of Rh-half-sandwich complexes.²¹ The ¹H NMR spectrum reveals a hydride resonance at δ -16.8 as a doublet of doublets ($J_{\text{Rh-H}} 25.5$, $J_{\text{P-H}} 30.9$ Hz) and finally the ¹¹B NMR spectrum shows a broad peak at 39.2 typical of a rhodium boryl species (Figure 13).

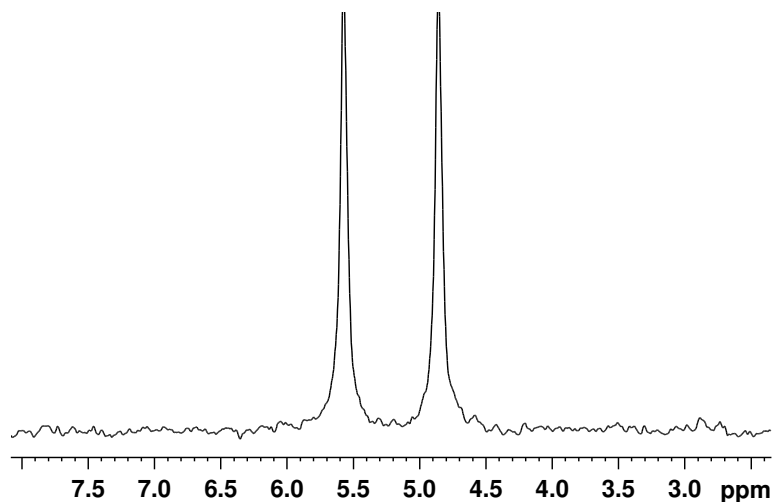


Figure 12. ³¹P{¹H} NMR spectrum for the complex Tp`RhH(Bpin)(PMe₃) in C₆D₆.

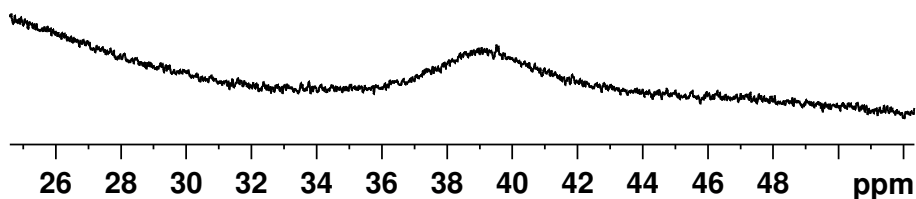


Figure 13. ^{11}B NMR spectrum of the $\text{Tp}^{\text{`}}\text{RhH}(\text{Bpin})(\text{PMe}_3)$ complex in C_6D_6 showing the typical broad resonance for metal-boryl complexes.

Finally the ^{13}C NMR spectrum reveals the quaternary carbon of the Bpin moiety at $\delta 81.8$, being upfield shifted from the free HBpin ($\delta 83.1$). We therefore assign the new species as the $\text{Tp}^{\text{`}}\text{RhH}(\text{Bpin})(\text{PMe}_3)$ complex. The crystal structure was determined and it confirmed the identity of the product (Figure 14). Refinement parameters are given below in Table 4.

Table 4. Refinement and crystallographic data for complex $\text{Tp}^{\text{`}}\text{RhH}(\text{Bpin})(\text{PMe}_3)$.

Formula	$\text{C}_{24}\text{H}_{44}\text{B}_2\text{N}_6\text{O}_2\text{PRh}$
<i>M</i>	604.15
<i>a</i> /Å	25.996(12)
<i>b</i> /Å	10.660(2)
<i>c</i> /Å	21.452(5)
α /deg	90.00
β /deg	101.455(3)
γ /deg	90.00
<i>V</i> / Å ³	5819.4(12)
<i>T</i> /K	110(2)
Space group	C2/c
<i>Z</i>	8
$\mu_{\text{Mo K}\alpha}$ mm ⁻¹	0.674
Reflns meads	11082
Reflns indep	5832
<i>R</i> _{int}	0.0249
Final <i>R</i> [<i>I</i> > 2σ(<i>I</i>)]	<i>R</i> ₁ = 0.0307
	w <i>R</i> ₂ = 0.0660
Final <i>R</i> (all data)	<i>R</i> ₁ = 0.0384
	w <i>R</i> ₂ = 0.0699

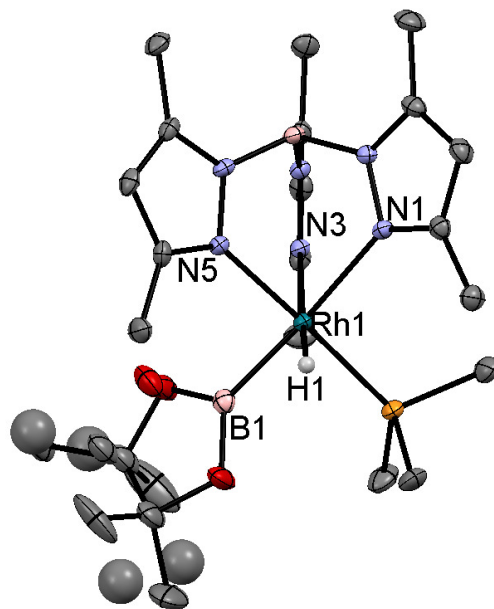


Figure 14. Crystal structure for complex Tp`RhH(Bpin)(PMe₃), hydrogen atoms are omitted for clarity except of the hydride. Ellipsoids for the anisotropic displacement parameters are shown at the 50% level.

As can be seen from Figure 14, the structure is complicated by disorder in the borolane ring; the structure was modeled with one oxygen occupying two alternative positions. These oxygens found with 88% probability in one position and 12% in the other one. Consequently, also the quaternary carbon bonded to it and the methyl groups attached to the moiety are disordered, showing the same occupancy. Selected bond lengths and angles are reported in Table 5.

Table 5. Selected bond length and angles for complex Tp`RhH(Bpin)(PMe₃).

Bond length/ Å	
B1-Rh1	2.028(3)
P1-Rh1	2.2377(7)
H1-Rh1	1.50(2)
B...H	2.43(2)
Rh-N1	2.297(2)
Rh-N3	2.241(2)
Rh-N5	2.124(2)

Angles / Deg	
B1-Rh1-H1	85.8(9)
P1-Rh1-B1	86.78(8)

The Rh-B distance was determined as 2.028(3) Å in agreement with the length previously observed for the complex $[\text{Rh}-(\eta^5\text{-C}_5\text{H}_5)(\text{H})(\text{Bpin})(\text{PPh}_3)]$.²¹ The hydride was located in the difference map and after refinement found at a distance Rh-H of 1.50(2) Å; the B...H separation was determined as 2.43(2) Å, considerably longer than what was found for the $[\text{Rh}-(\eta^5\text{-C}_5\text{H}_5)(\text{H})(\text{Bpin})(\text{PPh}_3)]$. This observation supports an oxidative addition to form a rhodium-boryl complex rather than η^2 -coordination. The B-Rh-H angle of 85.8(9) is also larger than that determined for the $[\text{Rh}-(\eta^5\text{-C}_5\text{H}_5)(\text{H})(\text{Bpin})(\text{PPh}_3)]$ complex, where a residual B...H interaction was suggested.²¹

The complex $\text{Tp`RhH}(\text{Bpin})(\text{PMe}_3)$ does not reductively eliminate HBpin under mild conditions. It proved to be stable upon heating up to 140° C in benzene solution. Decomposition was detected on pushing the reaction at higher temperatures, but no formation of the rhodium–phenyl hydride was observed.

5.2.5 Photochemical reaction of $\text{Tp`Rh}(\text{PMe}_3)\text{H}_2$ in the presence of silanes

Complex $\text{Tp`Rh}(\text{PMe}_3)\text{H}_2$ was irradiated in different neat silanes (Et_3SiH , Et_2SiH_2 and PhSiH_3) at room temperature on an NMR scale. The most thoroughly characterized reaction was that of $\text{Tp`Rh}(\text{PMe}_3)\text{H}_2$ with Et_2SiH_2 to generate $\text{Tp`RhH}(\text{Et}_2\text{SiH})(\text{PMe}_3)$ with an NMR yield of 75%. The product exhibits a characteristic doublet of doublets in the ^1H NMR spectrum ($J_{\text{HRh}} = 20.8$, $J_{\text{HP}} = 32.4$) at δ -17.9, assigned to the hydride, and a doublet in the $^{31}\text{P}\{^1\text{H}\}$ NMR spectrum at δ -0.9 with a J_{PRh} of 139.8 Hz. The $\{^1\text{H}-^{29}\text{Si}\}$ correlation linked the hydride resonance to a ^{29}Si resonance at δ 31.8, the ethyl protons also correlate to the same ^{29}Si resonance (Figure 15).

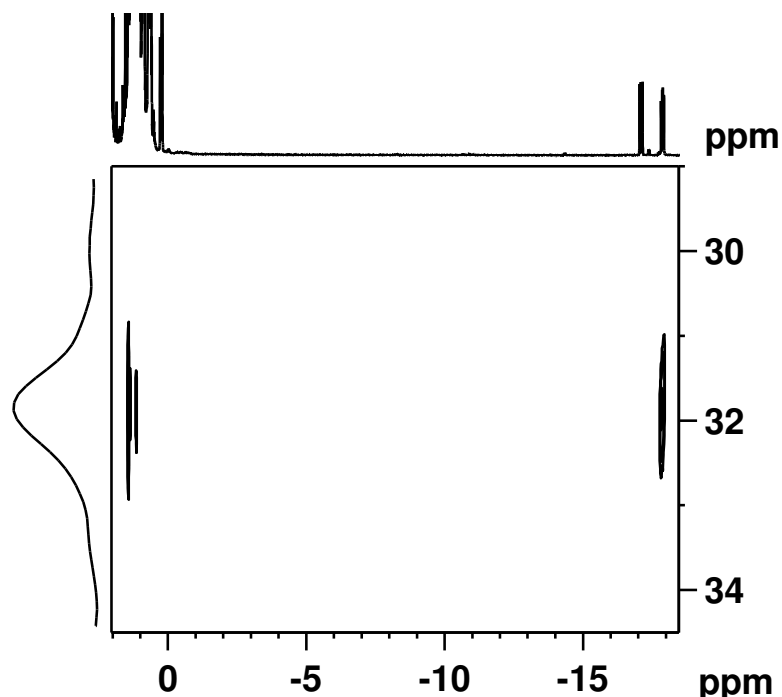


Figure 15. $\{^1\text{H}-^{29}\text{Si}\}$ 2D NMR spectrum showing correlation between the hydride resonance for the complex $\text{Tp}^{\text{`}}\text{RhH}(\text{Et}_2\text{SiH})(\text{PMe}_3)$ and the ^{29}Si signal. The ethyl protons are also linked to the ^{29}Si resonance. The second hydride belongs to starting material left.

Crystals of the complex were grown from hexane solution and the structure was confirmed as $\text{Tp}^{\text{`}}\text{RhH}(\text{Et}_2\text{SiH})(\text{PMe}_3)$ (Figure 16). Selected bond lengths and angles are reported in Table 6.

Table 6. Selected bond lengths and angles for complex $\text{Tp}^{\text{`}}\text{RhH}(\text{Et}_2\text{SiH})(\text{PMe}_3)$.

Bond length/ Å	
Si1-Rh1	2.315(1)
P1-Rh1	2.2373(8)
H1A-Rh1	1.52(3)
Si...H1A	2.62(3)
Si-H1B	1.53(3)
Rh-N1	2.247(2)
Rh-N3	2.299(3)
Rh-N5	2.124(2)

Angles / Deg	
Si1-Rh1-H1A	83.4(2)
P1-Rh1-Si1	89.89(3)

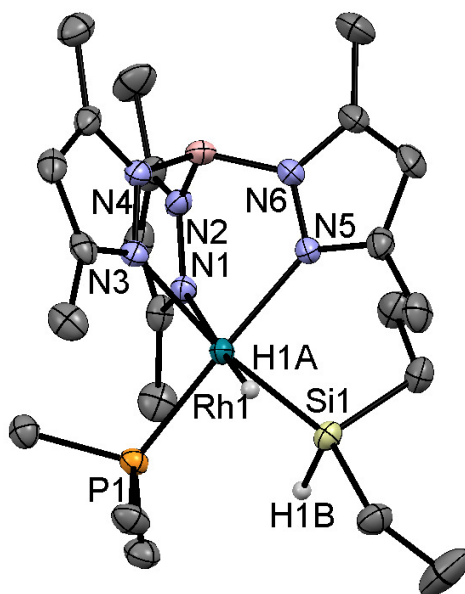


Figure 16. Crystal structure for complex Tp`RhH(Et₂SiH)(PMe₃), hydrogen atoms are omitted for clarity apart from the RhH and SiH. Ellipsoids for the anisotropic displacement parameters are shown at the 50% level.

The Rh-Si bond was found to be 2.315(2) Å, the hydride and the proton bound to the Si atom were located by difference map after refinement; the Rh-H1A bond length was determined as 1.52(3) Å and the Si...H1A distance as 2.62(3) Å. This value is considerably larger than what is expected for SISHA secondary interactions (secondary interaction between silicon and hydrogen atoms),²² confirming that a complete oxidative addition took place. The values for the P-Rh-H and the Si-Rh-H angles are 82.2(1)^o and 83.4(2)^o respectively, also confirming that no residual Si...H interaction is present.²¹

Refinement indicators for the structure are listed in Table 7. They all converged satisfactorily.

Table 7. Refinement and crystallographic parameters for complex Tp`RhH(Et₂SiH)(PMe₃).

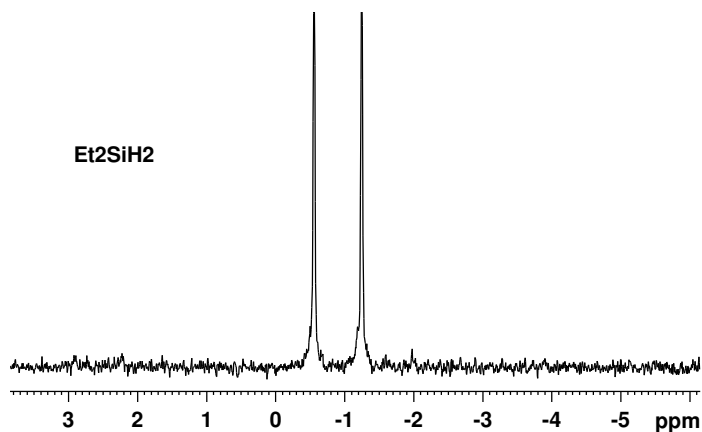
Formula	C ₂₂ H ₄₃ BN ₆ SiPRh
<i>M</i>	564.4
<i>a</i> /Å	10.840(7)
<i>b</i> /Å	11.533(9)
<i>c</i> /Å	13.546(11)
α/deg	65.602(8)
β/deg	72.784(7)
γ/deg	65.226(7)
<i>V</i> / Å ³	1384.81(18)
<i>T</i> /K	110(2)
Space group	P-1
<i>Z</i>	2
μMo Kα/mm ⁻¹	0.739
Reflns meas	12496
Reflns indep	5656
<i>R</i> _{int}	0.0294
Final <i>R</i> [<i>I</i> > 2σ(<i>I</i>)]	<i>R</i> ₁ = 0.0329
	w <i>R</i> ₂ = 0.0708
Final <i>R</i> (all data)	<i>R</i> ₁ = 0.0414
	w <i>R</i> ₂ = 0.0764

Photochemical reactions of complex Tp`Rh(H₂)(PMe₃) in the presence of other silanes led to the formation of the corresponding Tp`Rh(PMe₃)H-silyl complexes, which exhibit similar spectroscopic features to those observed for the complex reported above. All the products show hydride in the ¹H NMR spectrum which is correlated by {¹H-²⁹Si} 2D-NMR to a peak in the ²⁹Si spectrum. A selection of NMR data for all the products are reported in Table 8. They all show very similar coupling constants as confirmation that the same type of products are formed.

Table 8. NMR Spectroscopic Data (solvent C₆D₆, δ , (J/Hz)) for Products of Photoreaction of Tp`Rh(PMe₃)H₂ with Silanes.

	Tp`RhH(Et ₂ SiH)(PMe ₃)	Tp`RhH(Et ₃ Si)(PMe ₃)	Tp`RhH(PhSiH ₂)(PMe ₃)
¹ H hydride	δ -17.9 (dd) J_{HRh} = 20.8 J_{HP} = 32.4	δ -18.1 (dd) J_{HRh} = 19.7 J_{HP} = 30.9	δ -16.7 (dd) J_{HRh} = 19.9 J_{HP} = 30.6
³¹ P{ ¹ H}	δ - 0.9 (d) J_{PRh} = 139.8	δ -3.4 (d) J_{PRh} = 145.4	δ 1.9 (d) J_{PRh} = 130.9
²⁹ Si	δ 31.8	δ 31.6	δ -15.8

Reactions with diethylsilane showed more selectivity towards the formation of the silyl hydride product than the triethyl and phenyl silanes where other minor species were observed in the ³¹P{¹H} NMR spectrum that were not identified. The identity of all the rhodium-silyl products was also confirmed by LIFDI mass-spectrometry.



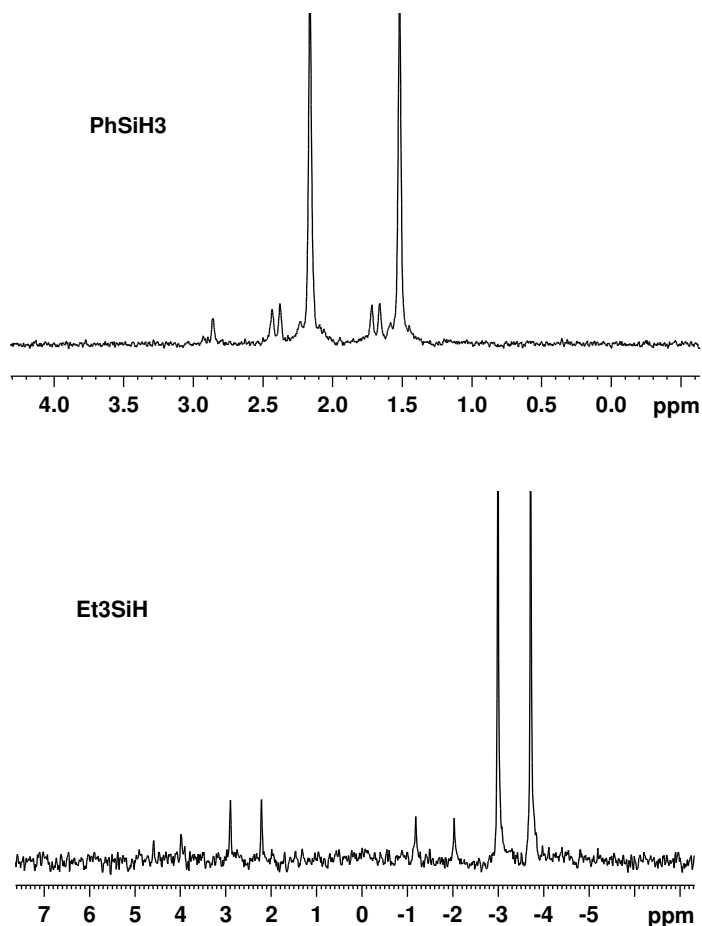


Figure 17. $^{31}\text{P}\{^1\text{H}\}$ NMR spectra for the reactions of complex $\text{Tp}^{\text{R}}\text{Rh}(\text{H}_2)(\text{PMe}_3)$ with the different silanes.

5.2.6 Starting material $\text{Tp}^{\text{R}}\text{Rh}(\text{CNneopentyl})(\eta^2\text{-PhN}=\text{C}=\text{N-neopentyl})$

$\text{Tp}^{\text{R}}\text{Rh}(\text{CNneopentyl})(\eta^2\text{-PhN}=\text{C}=\text{N-neopentyl})$, (neopentyl = $\text{CH}_2\text{C}(\text{Me}_3)$) complex was provided by Jones group. It was prepared following reported procedures.³ As shown in Figure 18, the ^1H NMR spectrum for this species is very rich. It exhibits the two singlets at high field for the neo-pentyl methyl groups in a ratio 1:1, the Tp^{R} resonances consist of a set of six singlets for the CH_3 groups and three for the CH ones indicating chirality at rhodium, and finally the CH_2 protons of the neopentyl moiety resonate between δ 3.9 and 4.4.

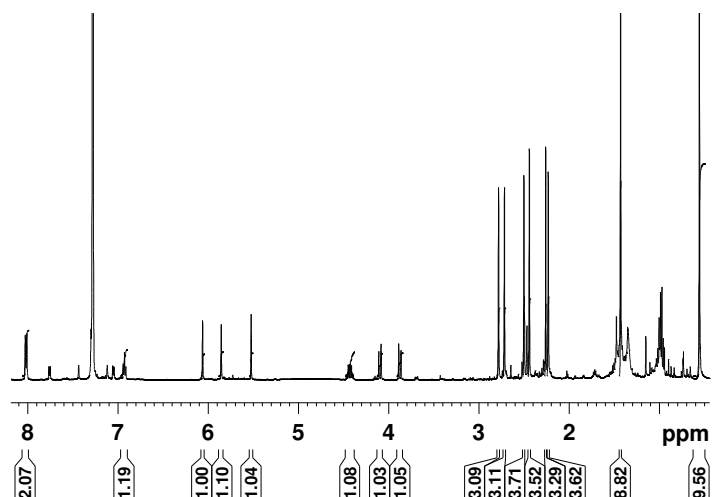


Figure 18. ^1H NMR spectrum of complex $\text{Tp}^{\text{`}}\text{Rh}(\text{CNneopentyl})(\eta^2\text{-PhN=C=N-neopentyl})$ in C_6D_6 . The spectrum shows the presence of some impurities.

5.2.7 Photochemical reaction of $\text{Tp}^{\text{`}}\text{Rh}(\text{CNneopentyl})(\eta^2\text{-PhN=C=N-neopentyl})$ in the presence of $\text{C}_5\text{F}_5\text{N}$

The irradiation of $\text{Tp}^{\text{`}}\text{Rh}(\text{CNneopentyl})(\eta^2\text{-PhN=C=N-neopentyl})$, in neat pentafluoropyridine ($\lambda > 290$ nm, 40 min, room temperature) generates three products detected by ^{19}F NMR spectroscopy. These products were purified by removing the reaction mixture and washing it with hexane; the solid was redissolved in C_6D_6 and characterised by multinuclear NMR spectroscopy and LIFDI mass spectrometry. The appearance of three sets of three resonances between δ 5.3 and δ 5.8 for the $\text{Tp}^{\text{`}}$ methine hydrogens and three sets of six resonances between δ 1.5 and δ 2.8 for the $\text{Tp}^{\text{`}}$ methyl groups indicated chirality at rhodium. The ^{19}F NMR spectrum showed three broad resonances at δ - 417.8, - 435.0 and -457.5 in the Rh-fluoride region which sharpened upon cooling down to 220 K. They all resolved as doublets with a J_{FRh} of about 148 Hz. Distinction between conformational isomerism, observed for the PMe_3 analogue, or regioisomerism could not be achieved. The products were assigned as the three isomers of the complex $\text{Tp}^{\text{`}}\text{Rh}(\text{CNneopentyl})(\text{C}_5\text{F}_4\text{N})\text{F}$ in a 4.6:2:1 ratio (Figure 19). No evidence of HF coordination was detected by ^1H NMR upon scaling up the reaction and furthermore the resonance for the $(\text{FHF})\text{Rh}(\text{PMe}_3)$ complex did not resolve upon cooling, but all the three

resonances observed here sharpened at low temperature. Attempts at crystallisation failed, the complex tends to form a non-crystalline precipitate in different conditions and using different combinations of solvents.

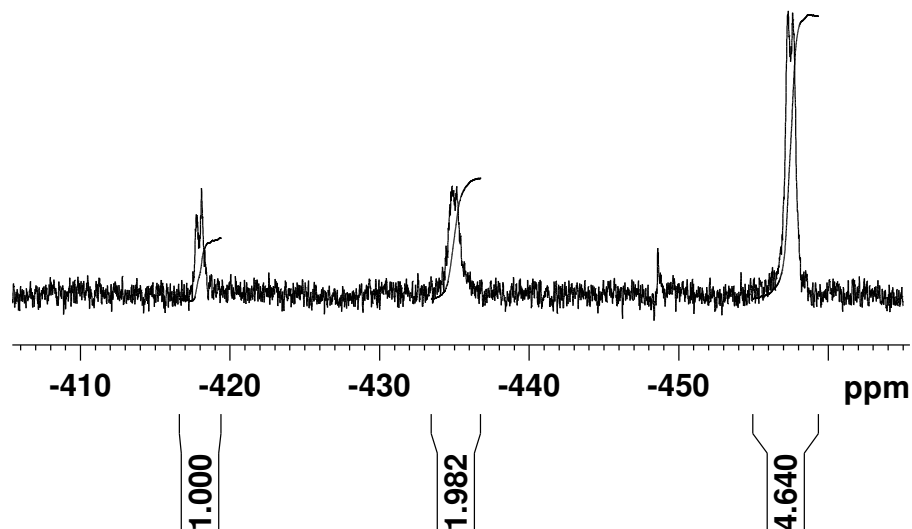


Figure 19. Low temperature ^{19}F NMR spectrum after photochemical reaction of complex $\text{Tp}^{\text{`}}\text{Rh}(\text{CNneopentyl})(\eta^2\text{-PhN}=\text{C}=\text{N-neopentyl})$ in the presence of $\text{C}_5\text{F}_5\text{N}$.

5.2.8 Photochemical reaction of $\text{Tp}^{\text{`}}\text{Rh}(\text{CNneopentyl})(\eta^2\text{-PhN}=\text{C}=\text{N-neopentyl})$ in the presence of HBpin

The irradiation of $\text{Tp}^{\text{`}}\text{Rh}(\text{CNneopentyl})(\eta^2\text{-PhN}=\text{C}=\text{N-neopentyl})$ in neat HBpin ($\lambda > 290$ nm, 40 min, room temperature) generates preferentially one product, leading to an NMR yield for the new complex $> 90\%$. The new product was purified by removing the reaction mixture, washing it with hexane and passing it through an alumina column. The solid was redissolved in C_6D_6 and characterized by multinuclear NMR spectroscopy and LIFDI mass spectrometry. The ^1H NMR spectrum reveals a hydride resonance at δ -14.2 as a doublet ($J_{\text{Rh-H}}$ 25.7 Hz) (Figure 20), the ^{11}B NMR spectrum shows a broad peak at 39.1 typical of a rhodium boryl species (Figure 21). A chiral Rh centre is also formed as confirmed by the three sets of methine resonances and six sets of methyl resonances for the $\text{Tp}^{\text{`}}$ ligand.

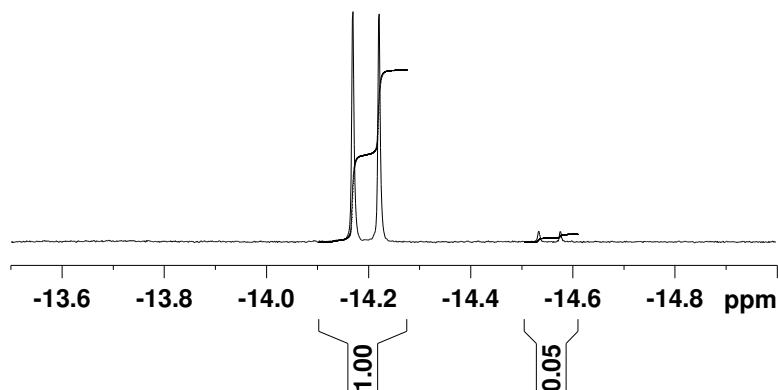


Figure 20. ¹H NMR spectrum in C₆D₆ for the photochemical reaction of complex Tp`Rh(CNneopentyl)(η^2 -PhN=C=N-neopentyl) in neat HBpin showing the hydride resonance arising from it.

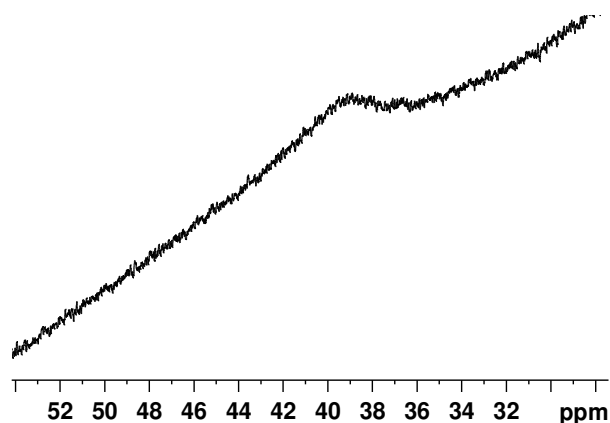


Figure 21. ¹¹B NMR spectrum showing the broad resonance for the rhodium-boryl complex.

The product was therefore assigned as Tp`Rh(CNneopentyl)(Bpin)(H). The {¹H-¹³C} correlation linked the methyl resonances of the borane ring on the ¹H spectrum to the BOC quaternary carbon on the ¹³C NMR spectrum, to reinforce our proposal of oxidative addition of the HBpin to the Rh centre (Figure 22). Reductive elimination of HBpin was tested in C₆H₆ solution, the complex was found to be stable upon heating up to 140° C, a very strong Rh-B bond is therefore formed.

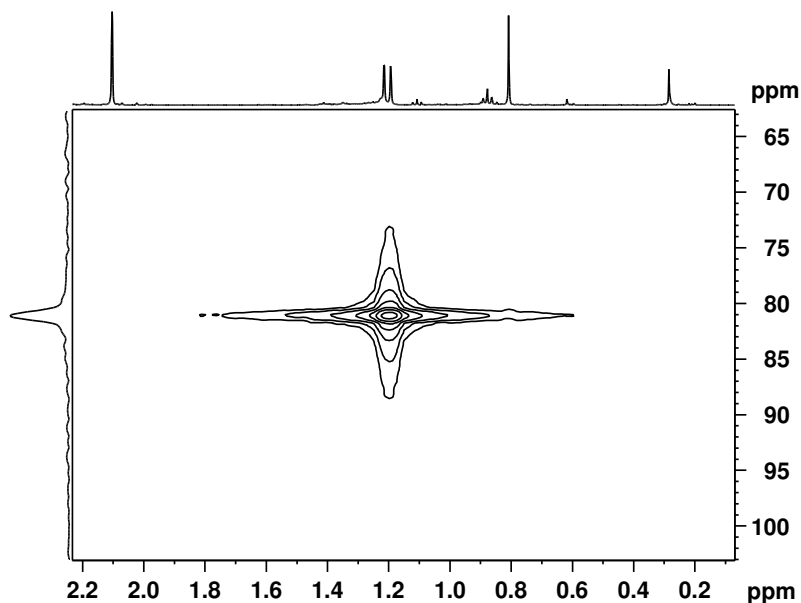


Figure 22. $\{^1\text{H}-^{13}\text{C}\}$ 2D NMR spectrum in C_6D_6 showing correlation between the BOC quaternary carbon and the methyl groups on the borane ring.

5.2.9 Photochemical reaction of $\text{Tp}^{\text{R}}\text{Rh}(\text{CNneopentyl})(\eta^2\text{-PhN}=\text{C}=\text{N-neopentyl})$ in the presence of silanes

The photochemical reactions of complex $\text{Tp}^{\text{R}}\text{Rh}(\text{CNneopentyl})(\eta^2\text{-PhN}=\text{C}=\text{N-neopentyl})$ in the presence of neat silanes were less selective towards the activation of the Si-H bond than the $\text{Tp}^{\text{R}}\text{Rh}(\text{PMe}_3)(\text{H}_2)$. All the reactions were completed within about 30 min of photolysis. Evidence of Si-H activation was observed for Et_2SiH_2 and PhSiH_3 generating products with a hydride resonance with a coupling J_{RhH} of about 20 Hz. The $\{^{29}\text{Si}-^1\text{H}\}$ 2D spectrum showed correlation between those hydrides and resonances in the ^{29}Si NMR spectrum. The NMR yield was determined to be greater than 70%. The photochemical reaction in neat Et_3SiH produced a second non silicon-linked containing product in a 1:1 ratio with the Si-H activated species, that prevented the full characterization. The formation of silane polymers or oligomers as by-products, made the full characterization of these complexes difficult; they were resistant both to high-vacuum pumping and to flash-chromatography. The identity of the rhodium silyl hydrides was also confirmed by LIFDI mass spectrometry. They

were assigned as Tp`Rh(CNneopentyl)H(Et₂SiH₂), Tp`Rh(CNneopentyl)H(PhSiH₂) and Tp`Rh(CNneopentyl)H(Et₃Si). Selected NMR data for the complexes are summarized in Table 9.

Table 9. NMR spectroscopic data (solvent C₆D₆, δ , (J/Hz)) for products of photoreaction of Tp`Rh(CNneopentyl)(η^2 -PhN=C=N-neopentyl) with silanes.

	Tp`Rh(CNneopentyl) H(Et ₂ SiH ₂)	Tp`Rh(CNneopentyl) H(PhSiH ₂)	Tp`Rh(CNneopentyl) H(Et ₃ Si)
¹ H hydride	δ -14.9 (d) $J_{\text{HRh}} = 21.5$	δ -14.1(d) $J_{\text{HRh}} = 19.7$	δ -15.3 (d) $J_{\text{HRh}} = 21.7$
²⁹ Si	δ 23.2	δ - 22.7	δ 32.8

5.2.10 Competition reactions

In order to investigate the selectivity of complex Tp`Rh(PMe₃)H₂ for the activation of C-F, B-H, and Si-H bonds against aromatic C-H bonds we conducted photochemical experiments in the presence of different volumes of two substrates simultaneously. The same ratio was observed during photolysis as well as at reaction completion. The results are summarised in Table 10.

Table 10. Results of competition reactions, measured by integration of the ³¹P{¹H} resonance. All measurements after 120 min irradiation.

	Substrates		
	C ₅ F ₅ N/C ₆ H ₆	HBpin/C ₆ H ₆	PhSiH ₃ /C ₆ H ₆
Ratio substrates	1/1	1/1	1/1
	0:1	1:3.5	1:1
Ratio substrates		5/1	
		1:1	
Ratio substrates	40/1		
	5:1		

Complex $\text{Tp}'\text{Rh}(\text{PMe}_3)_2\text{H}_2$ was irradiated in 50/50 volume of C_6H_6 and $\text{C}_5\text{F}_5\text{N}$, product formation was followed by $^{31}\text{P}\{^1\text{H}\}$ NMR spectroscopy. A total preference for activation of the C-H bond of benzene, to form the already known $\text{Tp}'\text{Rh}(\text{PMe}_3)\text{H}(\text{Ph})$,¹² was observed after 2 hours and also at completion of the reaction (Figure 23). The experiment was repeated increasing the amount of $\text{C}_5\text{F}_5\text{N}$ to 40 times more than the quantity of C_6H_6 in order to push the reaction towards activation of the C-F bond. A ratio of 5:1 between C-F and C-H activation was determined after 2 hours of photolysis.

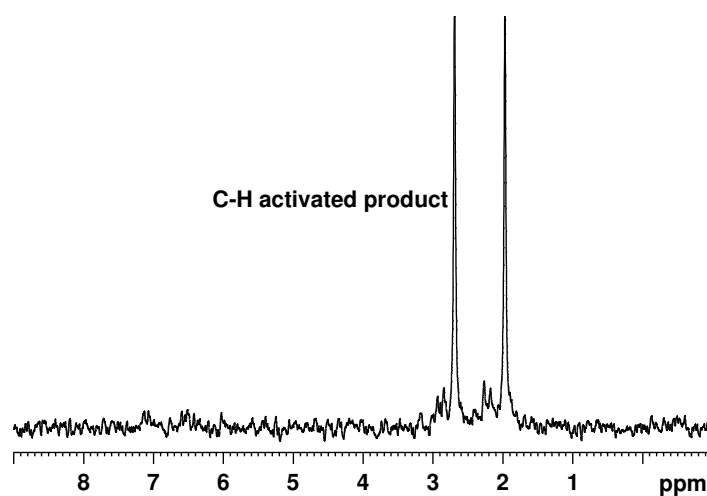


Figure 23. $^{31}\text{P}\{^1\text{H}\}$ NMR spectrum for competition reaction of $\text{Tp}'\text{Rh}(\text{PMe}_3)_2\text{H}_2$ in 50/50 volume of $\text{C}_6\text{H}_6/\text{C}_5\text{F}_5\text{N}$ at reaction completed.

Again, a preference for activation of the C-H bond of benzene was observed in 50/50 volume competition reaction between C_6H_6 and HBpin. NMR integration gave a ratio of 3.5:1 in favour of C-H activation of the aryl bond (Figure 24). Increasing the volume of HBpin by five times in the reaction mixture led to a ratio of B-H/C-H activation of 1:1, confirming that the reaction is concentration dependent.

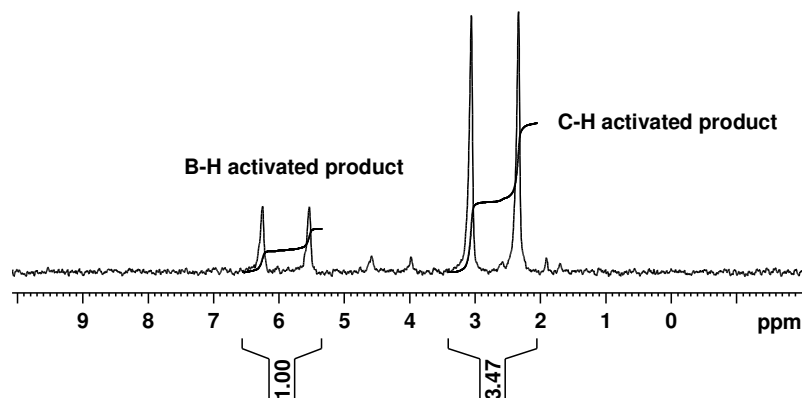


Figure 24. $^{31}\text{P}\{^1\text{H}\}$ NMR spectrum for competition reaction of $\text{Tp}'\text{Rh}(\text{PMe}_3)_2\text{H}_2$ in 50/50 volume of $\text{C}_6\text{H}_6/\text{HBpin}$ at completion of reaction.

Less selectivity was instead shown in the competition reaction performed in 50/50 volume of C_6H_6 and PhSiH_3 where $^{31}\text{P}\{^1\text{H}\}$ NMR integration gave a 1:1 ratio between C-H and Si-H activation.

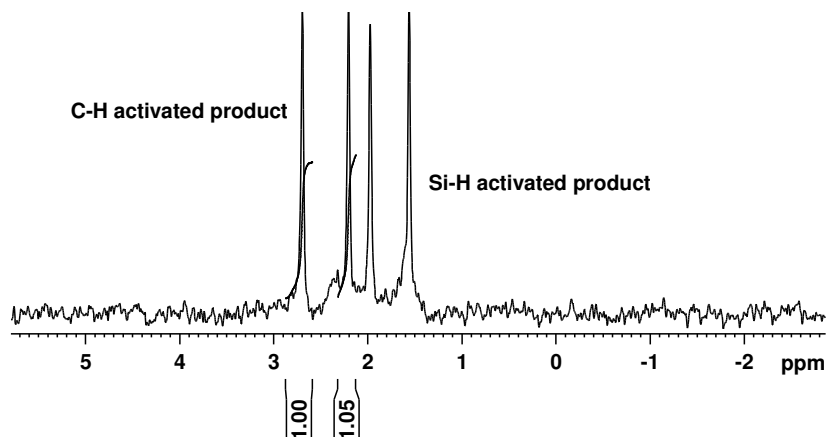


Figure 25. $^{31}\text{P}\{^1\text{H}\}$ NMR spectrum for competition reaction of $\text{Tp}'\text{Rh}(\text{PMe}_3)_2\text{H}_2$ in 50/50 volume of $\text{C}_6\text{H}_6/\text{PhSiH}_3$ at completion of reaction.

The results of competition reactions could reflect kinetic or thermodynamic selectivity. Thermal equilibration of the final products was excluded considering that the complexes were found to be stable in benzene solution heating up to 140°C . Photochemical equilibration was also explored; since the reactions were taken to relatively small conversion and the product distribution varied only slightly with photolysis time, we conclude that it did not play any role in the product ratio. However, a solution of the complex $\text{Tp}'\text{RhH}(\text{Bpin})(\text{PMe}_3)$ was photolysed in benzene solution for six hours and the reaction followed by

$^{31}\text{P}\{^1\text{H}\}$ NMR spectroscopy. The disappearance of the doublet for the Rh-boryl species and appearance of a new resonance for the Rh-phenyl species after six hours of photolysis, confirmed that the complex $\text{Tp}^{\text{R}}\text{RhH}(\text{Bpin})(\text{PMe}_3)$ absorbs at $\lambda > 290$ nm and shows photo-activity. A similar experiment was performed for $\text{Tp}^{\text{R}}\text{Rh}(\text{C}_5\text{F}_4\text{N})(\text{PMe}_3)\text{F}$ which, however was photo-stable upon photolysis in benzene solution.

5.3 Discussion

The complexes $\text{Tp`Rh}(\text{PMe}_3)_2$ and $\text{Tp`Rh}(\text{CNneopentyl})(\eta^2\text{-PhN=C=N-neopentyl})$ are well known to generate photochemically the very reactive fragments $\text{Tp`Rh}(\text{PMe}_3)$ and $\text{Tp`Rh}(\text{CNneopentyl})$ respectively. All the reactions mentioned above are conducted in neat substrates to avoid any source of C-H bonds coming from a solvent, which would be kinetically favored. To our surprise, since well known as excellent C-H activators, the complexes were selective for the activation of C-F; B-H and Si-H bonds with respect to the C-H bonds within the ligands. Rhodium-fluorides, rhodium-boryls and rhodium-silyls were therefore the major products in the reactions investigated.

The photochemical reactions of $\text{Tp`Rh}(\text{PMe}_3)_2$ in neat $\text{C}_5\text{F}_5\text{N}$ proved to be regioselective in C-F activation of the ortho position; two conformers were observed in the reaction. The $\text{Tp`Rh}(\text{CNneopentyl})(\eta^2\text{-PhN=C=N-neopentyl})$ complex showed less selectivity than the PMe_3 , three products arose and distinction between regioisomers or conformers was not possible due to the overlapping of some resonances in the aromatic part of the ^{19}F NMR spectrum. The $\text{Tp`Rh}(\text{PMe}_3)\text{F}(\text{C}_5\text{F}_4\text{N})$ acted as a trap for HF, as confirmed by the isolation of the bi-fluoride complex, the same behaviour was not seen for the CDI complex where the scaled up reaction did not produce any (FHF)-species. This could imply participation of the PMe_3 ligand in the mechanism to produce HF. Braun and co-workers have previously observed that reactions between phosphine complexes and $\text{C}_5\text{F}_5\text{N}$ hydro-defluorinate pyridines.²³ The presence in our reaction mixture of a hydride (^1H NMR: dd, δ -16.6, J_{PH} 27.4, J_{RH} 11.2 Hz, $^{31}\text{P}\{^1\text{H}\}$ NMR: d, δ 4.28, J_{PRh} 119 Hz) suggests hydrogen sources, and possibly a similar type of reaction takes place to the one observed by Braun.

Unexpectedly, the reaction in neat HBpin results in high selectivity for the activation of the B-H bond with both the starting complexes. The presence of primary C-H bonds in the ligand, activation of which is well known to happen preferentially and with a very small energy barrier,²⁴ did not affect the clean formation of rhodium-boryl hydrides. This suggests an even smaller energy

barrier for the B-H oxidative addition than C-H one, and furthermore the formation of a very strong and stable Rh-B bond. This is also confirmed by the reductive elimination experiments where the complexes are stable in C₆H₆ solution up to high temperature.

The preference for the activation of the Si-H bond was also striking compared to C-H bonds in the ligands. Even in the presence of aromatic C-H bonds (PhSiH₃), the major product was the Si-H activated complex. This confirms again that there is a smaller energy barrier for Si-H activation than C-H activation. We can conclude therefore that rhodium-silyl hydrides are the kinetic products in these types of reactions.

Competition reactions in C₆H₆ solution allowed the determination of a scale for the activation of the “hetero-bonds”, Si-H oxidative addition competes with C-H activation more effectively than does B-H activation, which competes more favorably than C-F bond cleavage. The latter is not observed at all in intermolecular competition reaction with 50/50 volume of C₆H₆ and C₅F₅N, but becomes instead competitive when the ratio between the two substrates is greatly increased in favor of pentafluoropyridine. A statistical ratio on preference for activated bond in favor of C₆H₆ was calculated. The C-H bond was activated eight times faster than the C-F ones. Competition takes place between C-H and B-H *per* activated bond (statistical ratio of 6:3.5 for C-H), while Si-H activation of phenylsilane occurred at half the rate of C-H activation of C₆H₆.

From these experiments we can conclude that $k_{\text{CH}} = k_{\text{SiH}} = 3.5 k_{\text{BH}} = 8 k_{\text{CF}}$ and if the statistical correction is taken into account the trend is $k_{\text{CH}} = 2 k_{\text{SiH}} = 1.7 k_{\text{BH}} = 0.37 k_{\text{CF}}$, therefore as shown in Table 11, the kinetically favored bonds resulted to be Si-H, and B-H.

Competition between C-H and C-F was established to happen also intramolecularly. Surprisingly the reaction of the PMe₃ complex with 2,3,5,6 - tetrafluoropyridine afforded the C-F activated product.

Table 11. Rate constants for reactions of complex Tp`Rh(PMe₃)₂ in the presence of C₆H₆, PhSiH₃, HBpin, C₅F₅N deduced from competition reactions.

	k _{CH}	k _{SiH}	k _{BH}	k _{CF}
Without statistical correction	8	8	8/3.5	1
Number of activatable bonds	6	3	1	2
With statistical correction	16/6 2.7	16/3 5.3	16/3.5 4.6	2/2 1

Comparison with the previously investigated systems CpRh(PR₃)(C₂H₄) in the presence of the same ligands (borane and silanes) highlights a very similar reactivity confirming that changing from Cp to Tp` does not influence the selectivity of the unsaturated fragment.²¹

The value of J_{RhP} for the Tp`Rh(PMe₃)(Bpin)H and Tp`Rh(H)(PMe₃)(silyl) shows a consistent decrease of 30 - 40 Hz with respect to those determined for CpRh(PMe₃) analogues. The value of J_{RhH} is also about 10 Hz smaller than the ones previously observed.²¹ The J_{RhP} coupling constants follow the order B(OR₂) (145 Hz) > H_{n-m}SiR_m (140 Hz) > C₅F₄N (128 Hz) reflecting the σ -donor strength of the ligands.²⁵

5.4 Summary

These experiments show that the Tp`RhL systems can activate a much wider variety of bonds that had been previously realized, opening up the possibilities of new applications. The complexes Tp`Rh(C₅F₄N)(PMe₃)(FHF), Tp`Rh(PMe₃)H(Bpin) and Tp`Rh(PMe₃)H(Et₂SiH) have been isolated and the crystal structures determined. The kinetic selectivity of the fragment follows the order Si-H(PhSiH₃), B-H(HBpin), C-H(C₆H₆), C-F(C₅F₅N) with a range spanning a factor of 5.4. In contrast to the compounds described in Chapter 3, the products are thermally stable.

5.5 Experimental

5.5.1 General procedures

All operations were performed under a nitrogen or argon atmosphere, either on a high-vacuum line (10^{-4} mbar), standard Schlenk (10^{-2} mbar) lines or in a glovebox. Solvents for general use (benzene) were of AR grade, dried by distillation over sodium and stored under Ar in ampules fitted with a Young's PTFE stopcock. Hexane was collected from the solvent purification system and dried again by distillation. Deuterated solvents were dried by stirring over potassium and distilled under high vacuum into small ampules with potassium mirror. Tp`Rh(PMe₃)H₂ and Tp`Rh(CNneopentyl)(η^2 -PhN=C=N-neopentyl) were supplied by William Jones group in Rochester. The fluoropyridines used were bought from Aldrich and dried over molecular sieves. HBpin was also bought from Aldrich and purified by vacuum distillation. Photochemical reactions at room temperature were performed in pyrex NMR tubes fitted with Young's PTFE stopcocks by using a Philips 125 W medium-pressure mercury vapor lamp with a water filter (5 cm).

5.5.2 Mass spectra.

The LIFDI mass spectra were measured on a Waters Micromass GCT Premier orthogonal time-of-flight instrument set to one scan per second with resolution power of 6000 FWHM and equipped with a LIFDI probe from LINDEN GmbH. The design is very similar to that described by Gross et al.²⁶ Toluene was used for tuning the instrument. The polyethylene glycol probe was kept at ambient temperature with the emitter potential at 12 kV. Activated tungsten wire LIFDI emitters (13 μ m tungsten from LINDEN) were ramped manually up to 100 mA for the emitter heating current during the experiment. m/z values are accurate to 0.01 Da. m/z values are quoted for ¹¹B, ²⁸Si.

5.5.3 X-ray crystallography

Diffraction data were collected at 110 K on an Agilent SuperNova diffractometer with MoK α radiation ($\lambda = 0.71073\text{\AA}$). Data collection, unit cell determination and

frame integration were carried out with “CrysalisPro”. Absorption corrections were applied using crystal face-indexing and the ABSPACK absorption correction software within CrysalisPro. Structures were solved and refined using Olex2²⁷ implementing SHELX algorithms. Structures were solved by either Patterson or direct methods using SHELXS-97 and refined by full-matrix least squares using SHELXL-97. All non-hydrogen atoms were refined anisotropically. Carbon-bound hydrogen atoms were placed at calculated positions and refined using a “riding model”. Hydrogen atoms bound to rhodium and silicon were found by difference map and refined.

5.5.4 NMR spectroscopy

All standard NMR spectra were recorded on a Bruker AMX500 spectrometer in tubes fitted with Young’s PTFE stopcocks. All ¹H and ¹³C chemical shifts are reported in ppm (δ) relative to tetramethylsilane and referenced using the chemical shifts of residual protio solvent resonances (benzene, δ 7.16 for ¹H and δ 128.06 for ¹³C). The ³¹P{¹H} NMR spectra were referenced to external H₃PO₄. ¹¹B NMR spectra to external BF₃·Et₂O, ¹⁹F spectra to external CFCl₃ and ²⁹Si spectra to external TMS. 2D NMR spectra were recorded with a standard HMQC pulse program varying the values of cnst2 from 2 to 200 Hz.

5.5.5 Syntheses and NMR Experiments

All the products were synthesized by irradiating ~ 10 mg of complex in neat substrates. Purification, when achieved, was done by passing the reaction mixture through an neutral alumina column. This method was efficient for the Rh- fluoride and Rh-boryl complexes, but not for the Rh-silyl products where silane polymers were formed during photolysis. Even though the purity of the complex improved after passing the solution through the column, total purification was not achieved, especially for the isonitrile complex. Some resonances were not found on the spectra because they were obscured by impurities.

5.5.6 Tp`Rh(C₅F₄N)(PMe₃)F – major rotamer

¹H NMR (C₆D₆, 300 K): 1.11 (d, J_{PH} 10.1 Hz, 9H, P(CH₃)₃), 1.37 (s, 3H, pzCH₃), 1.93 (s, 3H, pzCH₃), 2.07 (s, 3H, pzCH₃), 2.18 (s, 3H, pzCH₃), 2.24 (s, 3H, pzCH₃), 2.47 (s, 3H, pzCH₃), 5.44 (s, 1H, pzH), 5.53 (s, 1H, pzH), 5.63 (s, 1H, pzH).

¹⁹F{¹H} NMR (C₆D₆): δ - 85.9 (m, 1F), - 133.0 (m, 1 F), -148.3 (m, 1 F), -169.0 (m, 1 F), -428.8 (b, 1 F, J_{RhF} = 185, RhF).

³¹P{¹H} NMR (C₆D₆): δ 6.67, (dd, J_{RhP} = 128.7, J_{PF} = 17 Hz).

Mass Spectra (LIFDI, m/z): 645.12 (100%, M+), 625.10 (20%, [M+] - HF), exp 645.12, calcd for C₂₃H₃₁N₇PF₅BRh.

5.5.7 Tp`Rh(C₅F₄N)(PMe₃)F – minor rotamer

¹H NMR (C₆D₆, 300 K): δ 1.04 (d, J_{PH} 9.6 Hz, 9H, P(CH₃)₃), 1.32 (s, 3H, pzCH₃), 1.78 (s, 3H, pzCH₃), 1.98 (s, 3H, pzCH₃), 2.13 (s, 3H, pzCH₃), 2.22 (s, 3H, pzCH₃), 2.49 (s, 3H, pzCH₃), 5.42 (s, 1H, pzH), 5.54 (s, 1H, pzH), 5.62 (s, 1H, pzH).

¹⁹F{¹H} NMR (C₆D₆): δ -84.6 (m, 1F), -129.8 (m, 1 F), -146.6 (m, 1 F), -168.5 (m, 1 F), -455.4 (b, 1 F, J_{RhF} = 183, RhF).

³¹P{¹H} NMR (C₆D₆): δ 2.4, (dt, J_{RhP} = 125.9, J_{PF} = 17.9 Hz).

5.5.8 Tp`Rh(C₅F₄N)(PMe₃)(FHF)

¹H NMR (C₆D₆, 300 K): δ 1.13 (d, 9H, P(CH₃)₃), 1.39 (s, 3H, pzCH₃), 1.83 (s, 3H, pzCH₃), 2.11 (s, 3H, pzCH₃), 2.21 (s, 3H, pzCH₃), 2.25 (s, 3H, pzCH₃), 2.42 (s, 3H, pzCH₃), 5.40 (s, 1H, pzH), 5.49 (s, 1H, pzH), 5.59 (s, 1H, pzH), 11 (b, 1H, FHF).

¹³C NMR (C₆D₆): δ 12.4, 12.43, 13.5, 14.5, 14.8, 16.5 (s, pzCH₃), 16.08 (dd, J_{PC} = 32.5 Hz, J_{RhC} = 3 Hz, P(CH₃)₃), 107.0 (d, J_{PC} = 4.4 Hz, pzCH), 108.1 (s, pzCH), 108.2 (s, pzCH), 142.9 (d, J_{PC} = 3 Hz, pzCq), 144 (s, pzCq), 146 (s, pzCq), 151.1 (d, J_{PC} = 4 Hz, pzCq), 151.9 (s, pzCq), 152.8 (s, pzCq), Signals

assignable to the five carbons of C₅F₄N group were not detected because of multiple coupling with fluorines.

¹⁹F{¹H} NMR (C₆D₆): δ - 84.9 (m, 1F), -133.5 (m, 1F), -147.1 (m, 1F), -167.1 (m, 1F), -178.7 (d, J_{RhF} 447.6, FHF), - 398.9 (b, 1 F, RhF).

³¹P{¹H} NMR (C₆D₆): δ 6.67, (dd, J_{RhP} = 128.7, J_{PF} = 17 Hz).

Mass Spectra (LIFDI, m/z): attempts to observe parent ion failed due to loss of HF. The peak for the Tp`Rh(C₅F₄N)(PMe₃)F was observed instead.

5.5.9 Tp`Rh(C₅F₃NH)(PMe₃)F

¹H NMR (C₆D₆, 300 K): δ 1.16 (d, 9H, J_{PH} = 11.07 Hz, P(CH₃)₃), 1.42 (s, 3H, pzCH₃), 1.84 (s, 3H, pzCH₃), 2.10 (s, 3H, pzCH₃), 2.24 (s, 3H, pzCH₃), 2.26 (s, 3H, pzCH₃), 2.46 (s, 3H, pzCH₃), 5.48 (s, 1H, pzH), 5.56 (s, 1H, pzH), 5.64 (s, 1H, pzH), 6.20 (m, 1H, pyrH).

¹⁹F{¹H} NMR (C₆D₆): δ - 111.6 (m, 1 F), - 126.9 (m, 1 F), 146.3 (m, 1 F), - 430.1 (d, J_{FRh} 181.3, 1F, RhF).

³¹P{¹H} NMR (C₆D₆): δ 4.6, (dd, J_{RhP} = 132.1, J_{PF} = 17.5 Hz).

5.5.10 Tp`Rh(C₅F₄N)(PMe₃)H

¹H NMR (C₆D₆, 300 K): δ - 15.51 (ddd, J_{RhH} = 14.3, J_{FH} = 19.1 Hz, J_{PH} = 24.6 Hz, 1H, RhH), 0.94 (d, 9H, J_{PH} = 9.55 Hz, P(CH₃)₃), 1.48 (s, 3H, pzCH₃), 1.77 (s, 3H, pzCH₃), 2.01 (s, 3H, pzCH₃), 2.14 (s, 3H, pzCH₃), 2.16 (s, 3H, pzCH₃), 2.33 (s, 3H, pzCH₃), 4.68 (b, J_{BH} 113.1 Hz, 1H, pzBH), 5.34 (s, 1H, pzH), 5.55 (s, 1H, pzH), 5.80 (s, 1H, pzH).

¹⁹F{¹H} NMR (C₆D₆): δ - 100.6 (m, 2F), - 125.2 (m, 2 F).

³¹P{¹H} NMR (C₆D₆): δ - 2.33, (dd, J_{RhP} = 127.3, J_{PF} = 19.7 Hz).

5.5.11 Tp`RhH(Bpin)(PMe₃)

¹H NMR (C₆D₆, 300 K): δ - 16.77 (dd, $J_{\text{Rh-H}}$ 25.5, $J_{\text{P-H}}$ 30.9, RhH), 1.16 (s, 6H, BOC-CH₃), 1.21 (s, 6H, BOC-CH₃), 1.35 (d, 9H, $^2J_{\text{PH}}$ = 9.3 Hz, P(CH₃)₃), 2.07 (s, 3H, pzCH₃), 2.29 (s, 3H, pzCH₃), 2.30 (s, 3H, pzCH₃), 2.31 (s, 3H, pzCH₃), 2.41

(s, 3H, pzCH₃), 2.49 (s, 3H, pzCH₃), 4.75 (b, J_{BH} 121 Hz, 1H, pzBH), 5.54 (s, 1H, pzH), 5.70 (s, 1H, pzH), 5.86 (s, 1H, pzH).

¹³C NMR (C₆D₆): δ 11.34, 13.67, 13.84, 16.9, 18.03, 18.14 (s, pzCH₃), 22.14 (d, ¹J_{PC} = 33.5 Hz, P(CH₃)₃), 22.0, 25.2, 26.3, 27.7 (s, BOC-CH₃), 81.79 (s, BOC), 106.4 (d, ⁴J_{PC} = 2.8 Hz, pzCH), 106.5 (s, pzCH), 106.7 (s, pzCH), 143.8 (s, pzCq), 144.2 (s, pzCq), 144.8 (s, pzCq), 149.2 (s, pzCq), 150.2 (d, pzCq), 150.6 (s, pzCq).

¹¹B NMR (C₆D₆): δ 39.25 (b, Rh-B), -8.72 (b, pzB-H).

³¹P{¹H} NMR (C₆D₆): δ 5.25, (d, J_{RhP} = 145 Hz).

Mass Spectra (LIFDI, m/z): 604.21 (100%, M⁺), exp 604.21, calcd for C₂₄H₄₄N₆PO₂B₂Rh 604.25, difference 40 mDa.

5.5.12 Tp`RhH(Et₂SiH)(PMe₃)

¹H NMR (C₆D₆, 300 K): δ - 17.89 (dd, J_{Rh-H} 20.3, J_{P-H} 32.3, RhH), 1.14 (m, 2H, SiCH₂), 1.25 (d, 9H, ²J_{PH} = 11.1 Hz, P(CH₃)₃), 1.36 (m, 2H, SiCH₂), 1.43 (d, 6H, SiCH₃), 2.13 (s, 3H, pzCH₃), 2.19 (s, 3H, pzCH₃), 2.22 (s, 3H, pzCH₃), 2.30 (s, 3H, pzCH₃), 2.39 (s, 3H, pzCH₃), 2.52 (s, 3H, pzCH₃), 4.36 (bd, J_{PH} 15 Hz, Si-H), 5.56 (s, 1H, pzH), 5.64 (s, 1H, pzH), 5.82 (s, 1H, pzH).

²⁹Si NMR (C₆D₆): δ 31.84 (b, Rh-Si).

³¹P{¹H} NMR (C₆D₆): δ 0.87, (d, J_{RhP} = 140 Hz).

Mass Spectra (LIFDI, m/z): 564.19 (100%, M⁺), exp 564.19, calcd for C₂₂H₄₃N₆PSiBRh 564.220, difference 30 mDa.

5.5.13 Tp`RhH(PhSiH₂)(PMe₃)

¹H NMR (C₆D₆, 300 K): δ - 16.7 (dd, J_{Rh-H} 19.9, J_{P-H} 30.6, Hz, RhH), 1.17 (d, 9H, ²J_{PH} = 9.4 Hz, P(CH₃)₃), 2.14 (s, 3H, pzCH₃), 2.27 (s, 3H, pzCH₃), 2.32 (s, 3H, pzCH₃), 2.35 (s, 3H, pzCH₃), 2.37 (s, 3H, pzCH₃), 2.39 (s, 3H, pzCH₃), 4.98 (bdd, Si-H), 5.28 (m, Si-H), 5.44 (s, 1H, pzH), 5.73 (s, 1H, pzH), 5.84 (s, 1H, pzH), the phenyl resonances overlap with resonances of silanes polymers.

²⁹Si NMR (C₆D₆): δ -15.8 (b, Rh-Si).

$^{31}\text{P}\{^1\text{H}\}$ NMR (C_6D_6): δ 1.9 (d, $J_{\text{RhP}} = 131$ Hz).

Mass Spectra (LIFDI, m/z): 584.15 (100%, M^+), exp 584.19, calcd for $\text{C}_{24}\text{H}_{39}\text{N}_6\text{PSiBRh}$ 584.19, difference 40 mDa.

5.5.14 Tp`RhH(Et₃Si)(PMe₃)

^1H NMR (C_6D_6 , 300 K): δ - 18.1 (dd, $J_{\text{Rh-H}} 19.7$, $J_{\text{P-H}} 30.9$, Hz, RhH), 1.27 (d, 9H, $^2J_{\text{PH}} = 9.3$ Hz, P(CH₃)₃), 2.15 (s, 3H, pzCH₃), 2.18 (s, 3H, pzCH₃), 2.22 (s, 3H, pzCH₃), 2.27 (s, 3H, pzCH₃), 2.35 (s, 3H, pzCH₃), 2.45 (s, 3H, pzCH₃), 5.56 (s, 1H, pzH), 5.61 (s, 1H, pzH), 5.85 (s, 1H, pzH), the resonances for the ethyl group were not found due to the presence of by-products.

^{29}Si NMR (C_6D_6): δ 31.6 (b, Rh-Si).

$^{31}\text{P}\{^1\text{H}\}$ NMR (C_6D_6): δ -3.4 (d, $J_{\text{RhP}} = 145.4$ Hz).

Mass Spectra (LIFDI, m/z): 592.23 (100%, M^+), exp 592.25, calcd for $\text{C}_{24}\text{H}_{47}\text{N}_6\text{PSiBRh}$ 584.25, difference 20 mDa.

5.5.15 Tp`Rh(CNneopentyl)F(C₅F₄N)

^1H NMR (C_6D_6), 2 isomers (the quantity of the third is too small to be observed): δ , 0.55/0.77 (s, 9 H, C(CH₃)₃), 1.58 (s, 3 H, pz CH₃), 1.62 (s, 3 H, pz,CH₃), 1.89 (s, 3 H, pz CH₃), 1.97 (s, 3 H, pz CH₃), 2.02 (s, 3H, pz CH₃), 2.05 (s, 3 H, pz CH₃), 2.11 (s, 3 H, pz CH₃), 2.14 (s, 3 H, pz,CH₃), 2.18 (s, 3 H, pz CH₃), 2.21 (s, 3 H, pz CH₃), 2.72 (s, 3H, pz CH₃), 2.76 (s, 3 H, pz CH₃), 2.54 (ABq, $J_{\text{Rh-H}} 14.8$ Hz, 2 H, NCH₂), 5.45 (s, 1 H, pz H), 5.47 (s, 1 H, pz H), 5.52 (s, 1 H, pz H), 5.56 (s, 1 H, pz H), 5.69 (s, 1 H, pz H), 5.70 (s, 1 H, pz H).

^{19}F NMR (C_6D_6), 3 isomers: δ - 457 (b, 1 F, $J_{\text{RhF}} 156$ Hz, RhF regioisomer / rotamer), - 435 (b, 1 F, $J_{\text{RhF}} 150$ Hz, RhF), - 418 (b, 1 F, $J_{\text{RhF}} 153$ Hz, RhF). Aromatic fluorines: - 84.8 (m, 1 F), - 85.1 (m, 1 F), - 88.5 (m, 2 F, para isomer), - 146.8 (m, 1 F), - 147.0 (m, 1 F), - 147.6 (m, 2 F, para isomer), - 159.9 (m, 1 F), - 161.6 (m, 1 F), - 168.4 (m, 1 F), - 168.6 (m, 1 F). The distinction between different regioisomers / rotamers was not possible.

Mass Spectra (LIFDI, m/z): 666.18 (100%, M^+), exp 666.18, calcd for $\text{C}_{26}\text{H}_{33}\text{N}_8\text{F}_5\text{BRh}$ 666.18 difference 10 mDa.

5.5.16 Tp`Rh(CNneopentyl)H(Bpin)

^1H NMR (C_6D_6): δ , -14.20 (d, J_{RhH} 25.7, 1 H, RhH), 0.80 (s, 9 H, $\text{C}(\text{CH}_3)_3$), 1.19 (s, 6 H, $\text{BOC}(\text{CH}_3)_2$), 1.21 (s, 6 H, $\text{BOC}(\text{CH}_3)_2$), 2.10 (s, 3 H, pz CH_3), 2.25 (s, 3 H, pz CH_3), 2.26 (s, 3H, pz CH_3), 2.46 (s, 3 H, pz CH_3), 2.53 (s, 3 H, pz CH_3), 2.55 (s, 3 H, pz, CH_3), 2.69 (ABq, $J_{\text{Rh-H}}$ 14.0 Hz, 2 H, NCH_2), 5.64 (s, 1 H, pz H), 5.69 (s, 1 H, pz H), 5.84 (s, 1 H, pz H).

^{11}B NMR (C_6D_6): δ 39.1 (b, Rh-B), - 8.08 (b, pzB-H).

Mass Spectra (LIFDI, m/z): 625.29 (100%, M^+), exp 625.29, calcd for $\text{C}_{27}\text{H}_{46}\text{N}_7\text{O}_2\text{B}_2\text{Rh}$ 625.295, difference 5 mDa.

5.5.17 Tp`Rh(CNneopentyl)H(Et_2SiH)

^1H NMR (C_6D_6 , 300 K): δ - 14.88 (d, $J_{\text{Rh-H}}$ 20.8, RhH), 0.66 (s, 9 H, $\text{C}(\text{CH}_3)_3$), 1.06 (m, 4H, SiCH_2), 1.46 (d, 6H, SiCH_3), 2.17 (s, 3H, pz CH_3), 2.22 (s, 3H, pz CH_3), 2.28 (s, 3H, pz CH_3), 2.42 (s, 3H, pz CH_3), 2.46 (s, 3H, pz CH_3), 2.66 (s, 3H, pz CH_3), 4.36 (bd, J_{PH} 15 Hz, Si-H), 5.60 (s, 1H, pzH), 5.68 (s, 1H, pzH), 5.81 (s, 1H, pzH). The missing resonances are obscured by by-products and not found.

^{29}Si NMR (C_6D_6): δ 23.17 (b, Rh-Si).

Mass Spectra (LIFDI, m/z): 564.19 (100%, M^+), exp 564.22, calcd for $\text{C}_{22}\text{H}_{43}\text{N}_6\text{PSiBRh}$ 564.2204, difference 25.6 mDa.

5.5.18 Tp`Rh(CNneopentyl)H(PhSiH_2)

^1H NMR (C_6D_6 , 300 K): δ - 14.10 (d, $J_{\text{Rh-H}}$ 19.9, RhH), 0.59 (s, 9 H, $\text{C}(\text{CH}_3)_3$), 2.16 (s, 3H, pz CH_3), 2.23 (s, 3H, pz CH_3), 2.28 (s, 3H, pz CH_3), 2.39 (s, 3H, pz CH_3), 2.42 (s, 3H, pz CH_3), 2.52 (s, 3H, pz CH_3), 5.46 (s, 1H, pzH), 5.71 (s, 1H, pzH), 5.77 (s, 1H, pzH). The missing resonances are obscured by by-products and not found.

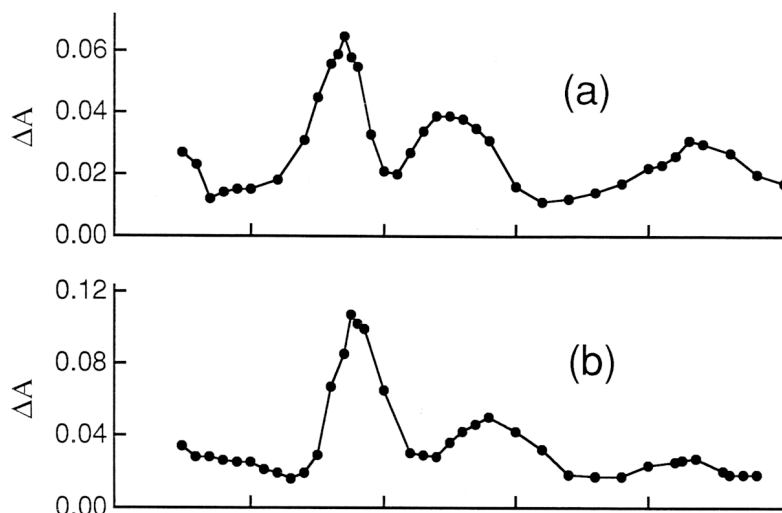
^{29}Si NMR (C_6D_6): δ -22.7 (b, Rh-Si).

Mass Spectra (LIFDI, m/z): 590.20 (100%, M+), exp 590.20, calcd for $C_{26}H_{38}N_7PSiBRh$ 590.210, difference 10 mDa.

6. Laser flash studies of Ru(PP)₂H₂ complexes

6.1. Introduction

The steady state and laser flash photochemistry of *cis* or *trans*-[Ru(drpe)₂(H)₂] (drpe = R₂PCH₂CH₂PR₂, R = CH₃ (dmpe), C₂H₅ (depe), C₆H₅ (dppe), C₂F₅ (dfepe)) type complexes has been studied intensively in our group.¹⁻⁹ By employing inert matrices and laser flash experiments, it has been demonstrated that the loss of H₂ and formation of a transient [Ru(drpe)₂] with a square planar configuration at Ru occurs upon irradiation with broad band UV light. The intermediates [Ru(drpe)₂] are exceptionally well suited to transient absorption investigation, since they exhibit a rich optical absorption spectrum with several bands spanning the visible region. A multiband UV/Vis spectrum with a low energy absorption band between 800 and 735 nm was determined for the primary photoproducts M(drpe)₂ (M = Ru,³ drpe = dmpe, depe, dppe; M = Os,¹ drpe = dmpe) (Figure 1).



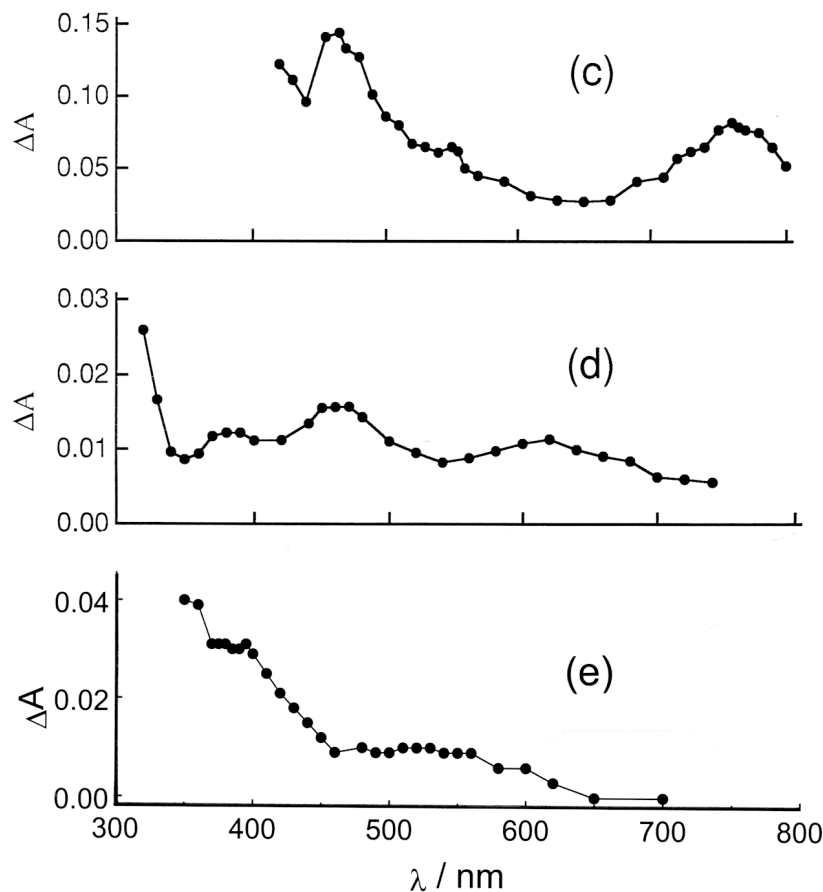


Figure 1. Transient UV/Vis spectra measured after solution laser flash photolysis (a)(d) 400 ns after flash and (e) 300 ns after flash. (a) Spectrum of Ru(dmpe)₂ in cyclohexane under argon, (b) spectrum of Ru(depe)₂ in heptane under 11 torr of H₂, (c) spectrum of Ru(dppe)₂ in cyclohexane under 760 torr of H₂, (d) spectrum of Ru(dfepe)₂ under 760 torr of H₂ and (e) spectrum of Ru(dmpm)₂ under 100 torr of H₂.³

The long wavelength bands have been assigned to a $M(d_z^2) - M(p_z)$ transition by comparison with isoelectronic square planar Rh and Ir species.¹⁰ Theoretical calculations also supported this assignment.¹¹ Square planar complexes exhibit bands at low energy with high extinction coefficients ($\epsilon \approx 800 - 15000 \text{ dm}^3 \text{ mol}^{-1} \text{ cm}^{-1}$) which is much too intense for a d-d transition typical of octahedral complexes (ϵ between $10 - 100 \text{ dm}^3 \text{ mol}^{-1} \text{ cm}^{-1}$).¹⁰ The lowest energy band in Rh (I) and Ir (I) chelating diphosphine complexes $[M(dppe)_2]^+$ and $[M(diphos)_2]^+$ (diphos = Ph₂PCH=CHPPh₂) were assigned to the allowed transition $a_{1g}(d_z^2) \rightarrow a_{2u}(p_z)$ in D_{4h} symmetry.¹⁰

Figure 2 shows the molecular orbital diagram for these complexes; the lowest

band was interpreted in terms of $a_{1g}(d_z^2) \rightarrow a_{2u}(p_z)$ transition and the next transition to higher energy to $e_g(d_{xz,yz}) \rightarrow a_{2u}(p_z)$. The two lowest energy absorption bands arise therefore from different orbital types as demonstrated by low temperature excitation polarisation experiments on the same compounds where different signs of polarisation were observed.¹² Perutz *et al.* suggested that the $d_z^2 - p_z$ transition should move to higher energy in D_{2d} symmetry due to the fact that the p_z orbital acquires b_2 symmetry and becomes σ antibonding.^{3,5}

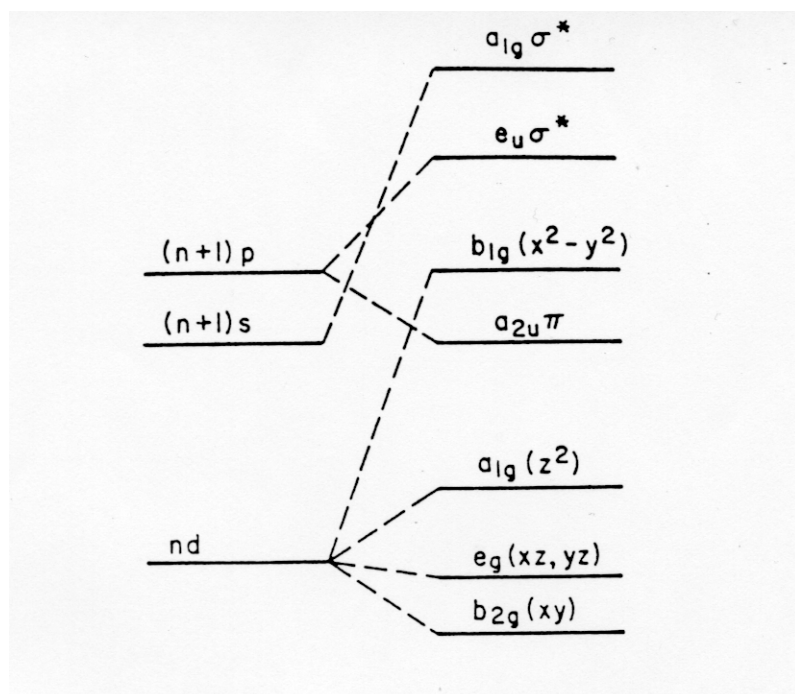
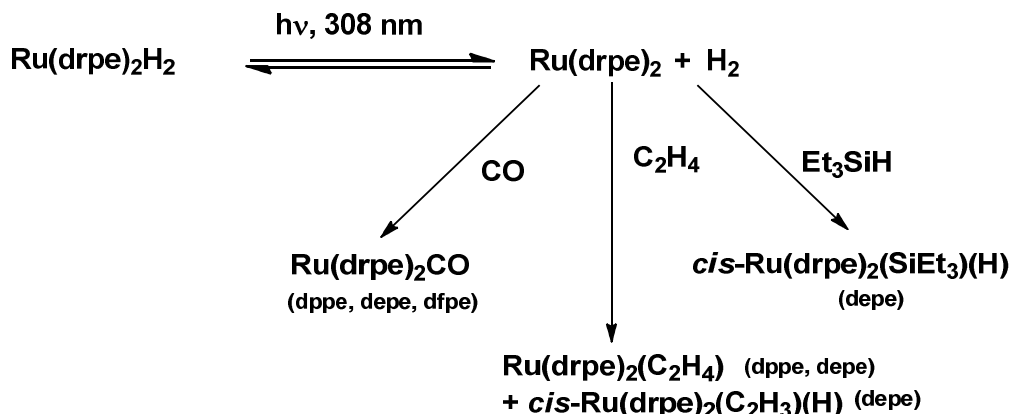


Figure 2. The molecular orbital energy diagram proposed for a square planar MP_4 complex with a $^1A_{1g}$ ground state assuming D_{4h} symmetry.¹²

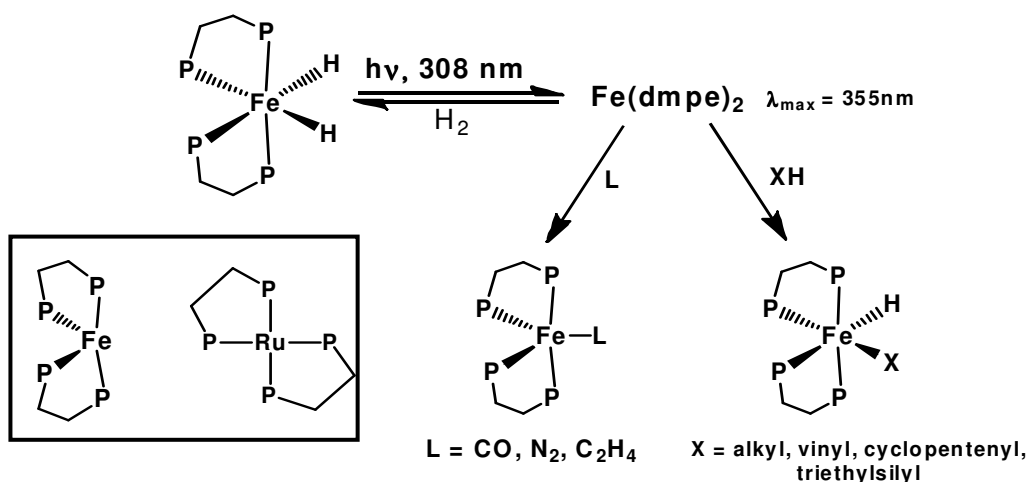
The reaction rates measured in the presence of substrates (H_2 , CO , Et_3SiH , C_2H_4 , $HBpin$ (pin = pinacolate)) are influenced by the nature of the substituent on the phosphorus atom and by the substrate resulting an increase in reactivity in the order: $Ru(dfepe)_2 < Ru(dppe)_2 < Ru(depe)_2 < Ru(dmpe)_2$. Steady-state solution photochemistry revealed that the transient species reacts with substrates to give addition or oxidative addition products (Scheme 1) but no products were observed due to the activation of solvent (C_6D_6 , THF, heptane).^{3,6,7}



Scheme 1. Reactions of Ru(drpe)₂ complexes with different quenching ligands.

The effect of a C₁ bridge in place of a C₂ bridge has also been reported,¹³ and it has been shown that competing photodissociation of phosphine is favored in solution over the dissociation of the dihydride ligand for *cis*-[Ru(PMe₃)₄(H)₂].⁸ The same methodology has also been applied to Fe(dmpe)₂H₂ and Os(dmpe)₂H₂.^{1,2}

Fe(dmpe)₂H₂ contrasts with its Ru analogue both spectroscopically and in its reactivity (Scheme 2). Fe(dmpe)₂ shows, in fact, just one UV-vis band at very short wavelength (355 nm in solution) and rate constants for the reaction of Fe(dmpe)₂ with H₂ and Et₃SiH are considerably smaller than the ones observed for Ru(dmpe)₂ by a factor of 7500. It readily reacts with benzene and toluene (k_2 ca 10⁶ dm³ mol⁻¹ s⁻¹), as well as with alkanes (k_2 in the range of 10 – 10² dm³ mol⁻¹ s⁻¹), the different reactivity leads to the conclusion that the transient species adopts a different geometry than Ru(dmpe)₂ (Scheme 2, inset). The structure of the Ru(dmpe)₂ was proposed to be square planar *D*_{2h} whereas that of the Fe(dmpe)₂ is probably puckered *C*_{2v}.



Scheme 2. Scheme for reaction of Fe(dmpe)₂H₂ in the presence of different substrates. Inset: different geometries adopted by the Ru and Fe transients.

Laser flash photolysis of Os(dmpe)₂H₂ fully agreed with data previously observed for Ru(dmpe)₂H₂; the intermediate Os(0) is generated within the laser flash and it reacts with CO and H₂ with essentially no energetic barrier towards the formation of the photoproducts. Reactions with different substrates (C₂H₄, Et₃SiH, N₂) were also observed, giving second order rate constants all close to 10⁸ dm³ mol⁻¹ s⁻¹. The UV-vis spectrum indicated a structure close to square planar showing a striking resemblance to that of Ru(dmpe)₂ (Figure 3).

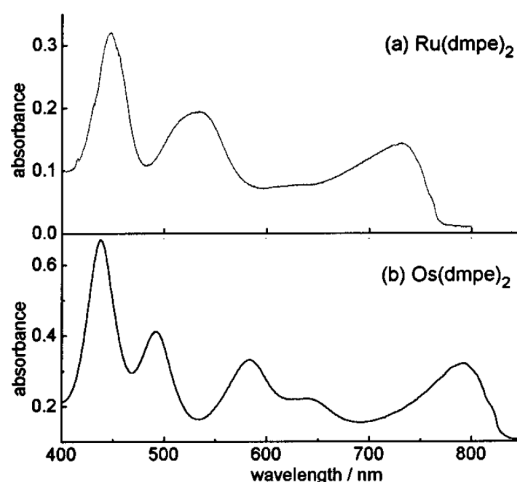
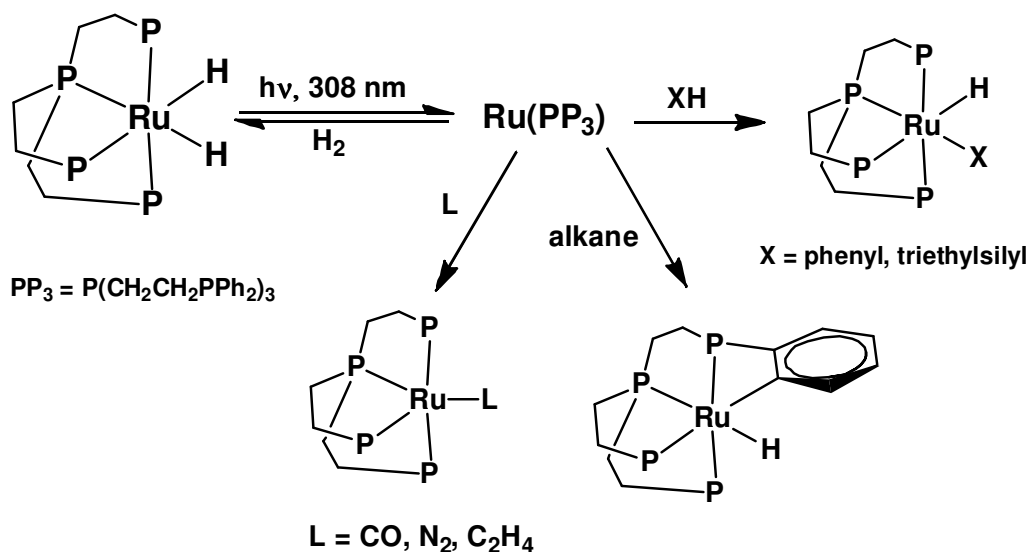


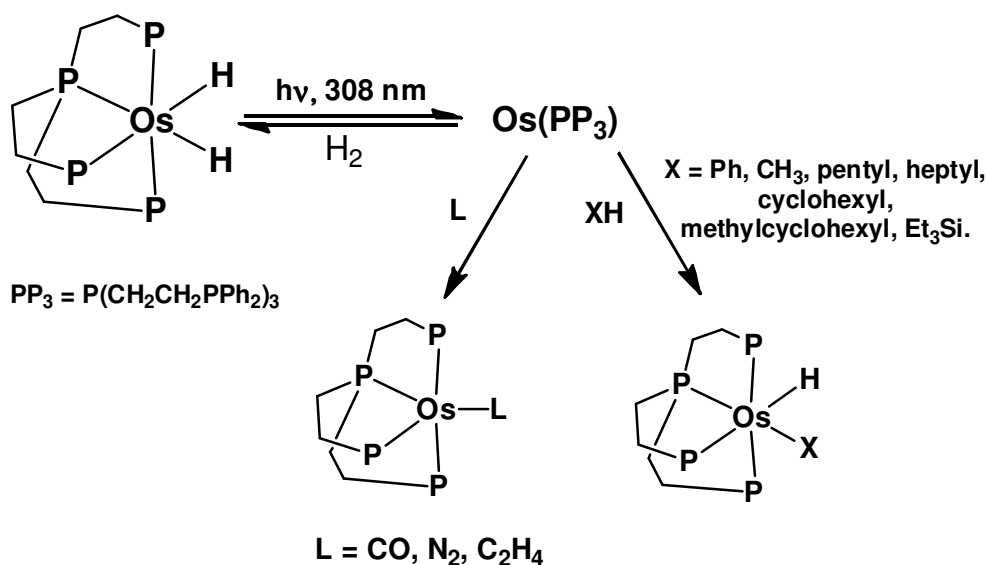
Figure 3. UV- vis spectra for complex Ru(dmpe)₂, a, and Os(dmpe)₂, b in low temperature matrix.

Laser flash photolysis was also employed on dihydride complexes of tetradentate phosphines [M(PP₃)(H)₂] (M = Ru, Os; PP₃ = P(CH₂CH₂PPh₂)₃). Notably, [Ru(PP₃)] undergoes cyclometalation in the absence of substrate and oxidative addition with benzene (Scheme 3), whereas [Os(PP₃)] does not undergo cyclometalation but forms oxidative addition products with alkanes and with benzene (Scheme 4).⁹



Scheme 3. Reaction scheme for RuH₂ complexes with tetradentate phosphines.

A narrow range of rate constants, going for Ru(PP₃) from 10⁵ dm³ mol⁻¹ s⁻¹ to 10⁶ dm³ mol⁻¹ s⁻¹ and for Os(PP₃) from 10³ dm³ mol⁻¹ s⁻¹ to 10⁶ dm³ mol⁻¹ s⁻¹ outlined a lack of selectivity towards the substrates in contrast with the behavior of the bidentate Ru analogues. Despite this, the reactivity of tetradentate ligand Ru/Os complexes was enhanced relative to bidentate with regards to Et₃SiH and C₆H₆, as a result of a reduced selectivity toward hydrogen. Closely related bidentate complexes Ru(dppe)₂ and Ru(depe)₂ did not show reactivity in the presence of C₆H₆.



Scheme 4. Reaction scheme for laser flash photolysis of Os(PP₃)H₂ complexes in the presence of different ligands.

The UV-vis spectrum for the M(PP₃) transients showed a single absorption maximum at 350 nm (M = Ru) and 390 nm (M = Os) respectively, in contrast with those of Ru(drpe)₂³ and Os(dmpe)₂¹ but consistently with the UV/vis spectrum of Fe(dmpe)₂ which exhibits a single maximum.² A different geometry, than the square planar typical of M⁰ complexes, is therefore proposed for the Os/Ru (PP₃) transients. The change reflects the enforced C_{3v} or C_s structure and the likely agostic interaction of a phenyl group. This change in conformation successfully prepared the M(PP₃) transient for C-H and Si-H activation, lowering the energy barrier in comparison with the square planar analogues. Figure 4 shows a schematic summary of the rate constants for reactions of M(PP₃) in comparison with those for Fe(dmpe)₂, Ru(depe)₂ and Ru(dppe)₂.

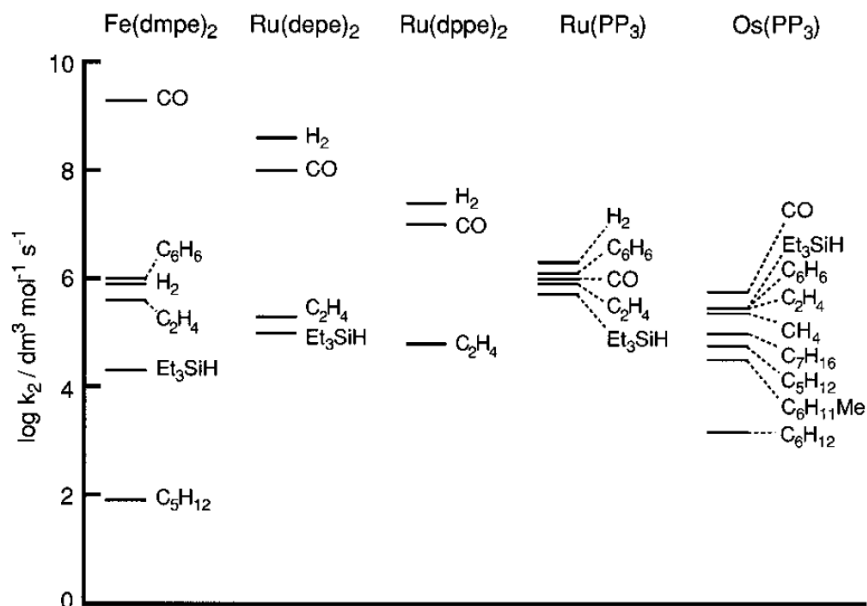
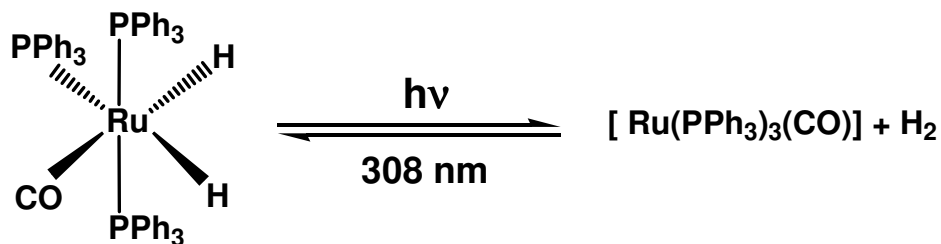


Figure 4. Schematic diagram comparing the rate constants for the investigated complexes.⁹

The related ruthenium carbonyl dihydride complexes [Ru(PPh₃)₃(CO)(H)₂] and [Ru(etp)(CO)(H)₂] (etp = PhP(CH₂CH₂PPh₂)₂) were studied by laser flash photolysis and revealed reductive elimination of the hydride ligands^{14,15} (Scheme 5), but when a carbene is incorporated [Ru(PPh₃)₂(IEt₂Me₂)(CO)(H)₂] (IEt₂Me₂ = 1,3-bis(ethyl)-4,5-dimethylimidazol-2-ylidene) the photochemistry is different; loss of both H₂ and PPh₃ was observed.¹⁶



Scheme 5. Photochemistry of ruthenium carbonyl dihydride.

Further mechanistic information has been obtained by employing para-hydrogen induced polarization (PHIP) of NMR spectra.¹⁷ Competing loss of

ligands also occurs in Ru(0) complexes such as [Ru(dppe)(PPh₃)(CO)₂].¹⁶ For [Ru(PPh₃)₃(CO)(H)₂] and [Ru(PH₃)₄(H)₂] complexes, DFT studies of photodissociation of H₂ showed fast (100 fs) elimination when the system is constrained to freeze the Ru-H and H-H distances.¹¹ In another report, DFT calculations showed that the calculated UV-Vis spectra of [Ru(PH₃)₄] reproduce the experimental ones with a square planar geometry around ruthenium.¹⁸ The reactivity of [Ru(PH₃)₄] was modeled for addition of H₂ and CO and found to be very exothermic in both cases, with an η^1 approach for H₂ to the [Ru(PH₃)₄] at an early stage of the reaction which changes to η^2 at later stages while elongation of the H...H distance also occurs late in the reaction profile (Figure 5).¹¹

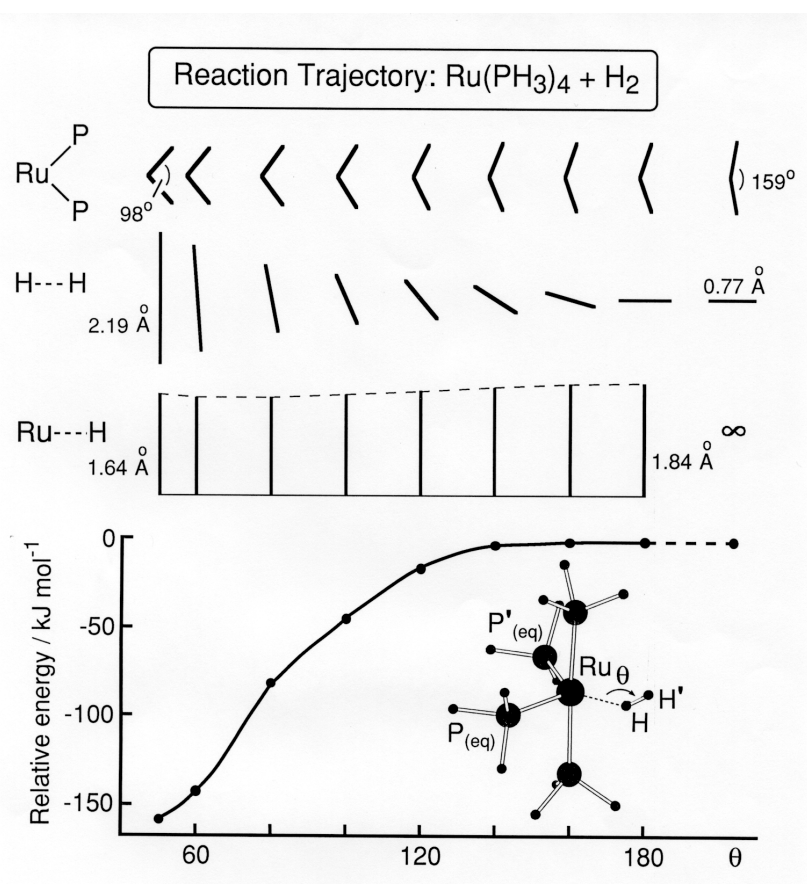


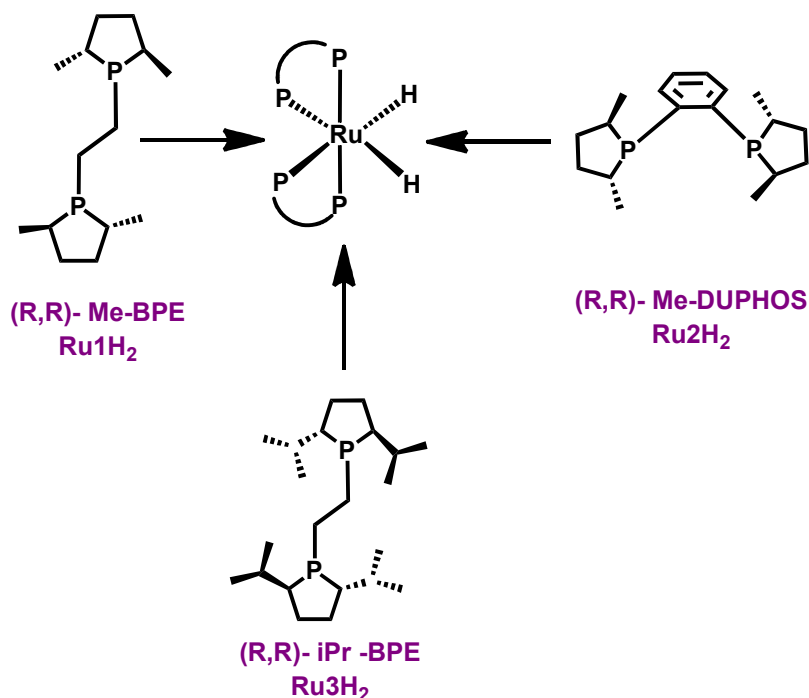
Figure 5. Calculated reaction profile and representation of changes for the η^1 and η^2 approaches of H₂ to [Ru(PH₃)₄].¹¹

π -Acceptor ligands were found to contribute to the tendency for d⁸ ML₄ systems to deviate from square planar geometry as observed for Ru(CO)₄ and Ru(CO)₂(PH₃)₂.¹⁹ The very small deviation from square planarity of Ru(PH₃)₄ is consistent with the weak π -acceptor capability of the phosphine ligands. The metal centre also plays a role in distortion from square planar geometry. [Rh(CO)₂(PH₃)₂]⁺ has a square planar geometry, while the isoelectronic Ru(CO)₂(PH₃)₂ exhibits a C_{2v} structure promoted by strong π -back donation from the high-lying metal based orbitals. The metal-based orbitals for the Rh cation are significantly lower in energy than those of Ru.¹¹ This demonstrates that the presence of a π -acceptor ligand is a necessary but not sufficient condition for a non planar d⁸ ML₄ complex.^{20,21}

6.2. Results

6.2.1. Λ -[cis-Ru((R,R)-Me-BPE)₂(H)₂] and Δ -[cis-Ru((S,S)-Me-DuPHOS)₂(H)₂]: laser flash studies

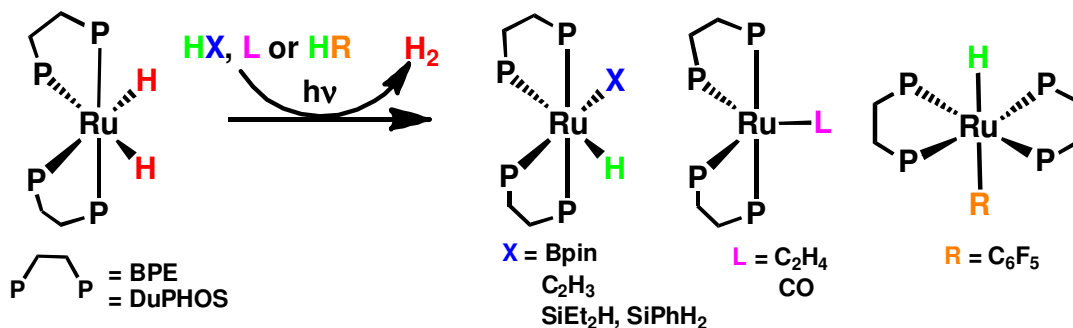
The dihydride complexes Λ -[cis-Ru((R,R)-Me-BPE)₂(H)₂], **Ru1H₂**, Λ -[cis-Ru((R,R)-Me-DuPHOS)₂(H)₂], **Ru2H₂** and Λ -[cis-Ru((R,R)-ⁱPr-BPE)₂(H)₂], **Ru3H₂** have been synthesized and fully characterized by Dr Marius Campian, and their photo-induced reactions studied (Scheme 6). BPE and DuPHOS²² phosphine ligands were chosen in order to test the diastereoselectivity of the photoreactions with the combination of stereogenic centres on the ligands and the metal. These particular phosphines are suitable because they contain no functionalities other than alkyl and aryl groups; they contain the same phospholane ring, {PhP(2*R*,5*R*-Me₂C₄H₆)}, as that used in previous studies at Rh.²³



Scheme 6. Different phosphines used for the Ru(PP)₂H₂ complexes investigated.

The reactions investigated included examples of B-H, Si-H, and C-H bond activation to [Ru(PP*)₂], as well as addition of CO and C₂H₄. This work showed

that the ligands control the configuration at the metal and exercise steric control over substrate attack (Scheme 7). My contribution to this work aimed to look at the laser flash photolysis of complexes **Ru1H₂** and **Ru2H₂** in solution.



Scheme 7. Scheme for reactions of **Ru1H₂** and **Ru2H₂** in the presence of different quenching ligands.

The transient photochemistry of **Λ -R,R-Ru1H₂** and **Λ -R,R-Ru2H₂** was investigated on nanosecond and microsecond timescales in order to determine the UV/vis spectra of the reaction intermediates of the type [Ru(PP)₂] and to determine the rates of reaction of the intermediates with hydrogen and with the substrates used in the steady-state reactions.

Reactions were initiated with a XeCl laser (308 nm, 10 ns pulsewidth) and spectra were recorded point-by-point in cyclohexane solution at 295 K.

The spectra of the transient species formed from **Λ -R,R-Ru1H₂** and **Λ -R,R-Ru2H₂** were recorded under a hydrogen atmosphere (1 atm) in order to ensure the complete reversibility of the reaction. The transient spectra derived from both the dihydride complexes exhibit at least three absorption maxima between 400 nm and 800 nm and resemble those recorded previously for other complexes of the type [Ru(PP)₂].³ The decay kinetics of the transients were measured at each of the maxima confirming that they were indistinguishable and that they rose within the instrument response time. They are assigned to a single intermediate in each case, [Ru(BPE)₂] and [Ru(DuPHOS)₂], respectively. The most intense lies at 500 nm for [Ru(BPE)₂] and 560 nm for [Ru(DuPHOS)₂];

there is a long wavelength feature at 740 nm for [Ru(BPE)₂] and at 700 nm for [Ru(DuPHOS)₂] (Figure 6 a, b).

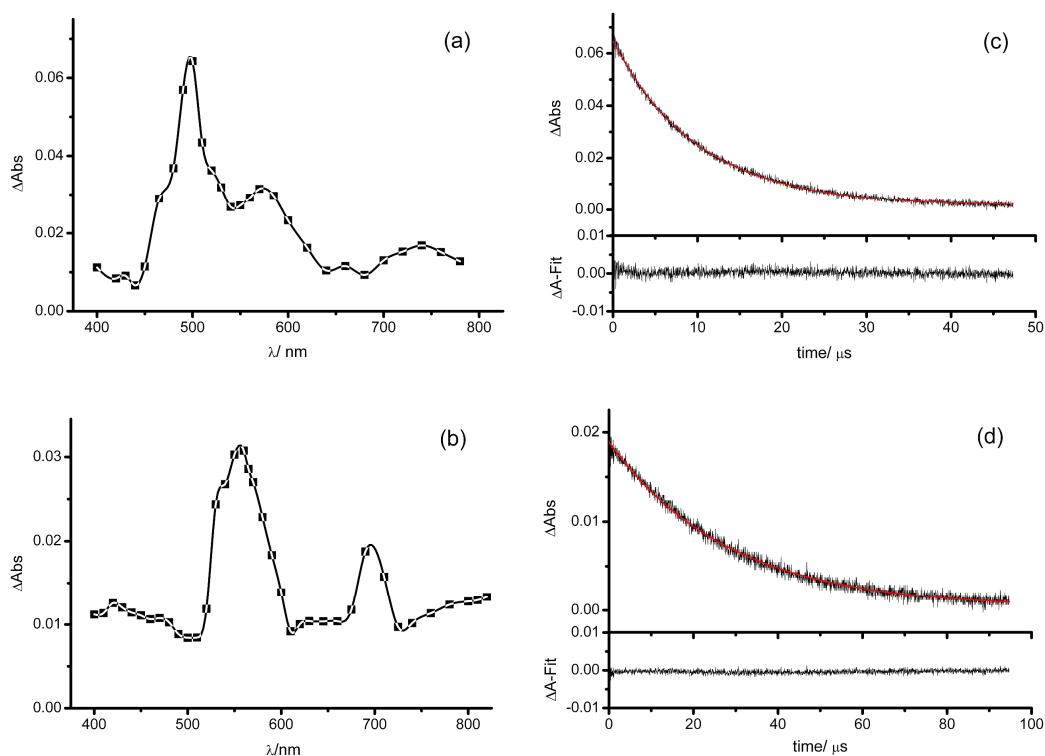


Figure 6. Left: transient UV-Vis spectra measured point-by-point at 295 K in cyclohexane on laser flash photolysis under 1 atm H₂ (308 nm) of: (a) Λ -*R,R*-Ru1H₂ and (b) Λ -*R,R*-Ru2H₂. Right: transient decay after photolysis of (c) Λ -*R,R*-Ru1H₂ recorded at 500 nm and (d) Λ -*R,R*-Ru2H₂ followed at 560 nm. The red lines show the fit to first order kinetics. The difference between the observed and the fitted decays are shown under the transient decays.

Laser flash photolysis of Λ -*R,R*-Ru1H₂ and Λ -*R,R*-Ru2H₂ under argon results in the formation of the transient species which decay with pseudo-first-order kinetics over a timescale of hundreds of microseconds ($1.1 \times 10^4 \text{ s}^{-1}$) for Λ -*R,R*-Ru1H₂ or even milliseconds ($2.6 \times 10^3 \text{ s}^{-1}$) for Λ -*R,R*-Ru2H₂. However, after laser flash photolysis of Λ -*R,R*-Ru1H₂ and Λ -*R,R*-Ru2H₂ under a hydrogen atmosphere, the transient absorbance returns to the baseline restoring the initial absorbance, indicating back reaction with H₂. The transients decay with pseudo-first-order kinetics (Figure 6 c, d) on a timescale of *ca* 40 μ s (Λ -*R,R*-Ru1H₂) and *ca* 100 μ s (Λ -*R,R*-Ru2H₂).

Complexes Λ -*R,R*-Ru1H₂ and Λ -*R,R*-Ru2H₂ have also been tested under higher pressures of hydrogen (from 1 to 5 bar) (Table 1), and both of the resulting transients showed a linear dependence of k_{obs} on $p(\text{H}_2)$ (Figure 7). The second order rate constants, k_2 , for the regeneration of the precursor in the presence of hydrogen were determined to be $(1.8 \pm 0.1) \times 10^7 \text{ dm}^3 \text{ mol}^{-1} \text{ s}^{-1}$ for [Ru(BPE)₂] and $(5.6 \pm 0.4) \times 10^6 \text{ dm}^3 \text{ mol}^{-1} \text{ s}^{-1}$ for [Ru(DuPHOS)₂]. The solubility of H₂ was taken as $4.7 \times 10^{-3} \text{ mol dm}^{-3} \text{ atm}^{-1}$.²⁴

The kinetic isotopic effects (KIE) were investigated, under different deuterium pressures (from 1 bar to 5 bar, Figure 7, Table 1). The KIEs are small for both intermediates but slightly greater for [Ru(DuPHOS)₂] (1.6 ± 0.1) than for complex [Ru(BPE)₂] (1.2 ± 0.1) (Table 2). The error bars represent statistical 95% confidence limits derived from the measurements shown. The second order rate constant for reaction of [Ru(DuPHOS)₂] with H₂ was also determined in benzene as solvent and was found to be insignificantly different from the value measured in cyclohexane. The spectra and reactivity of [Ru(PP*)₂] toward hydrogen are consistent with prompt photoelimination of H₂ and thermal regeneration of [Ru(PP*)₂(H)₂] at room temperature under H₂ (Scheme 3).

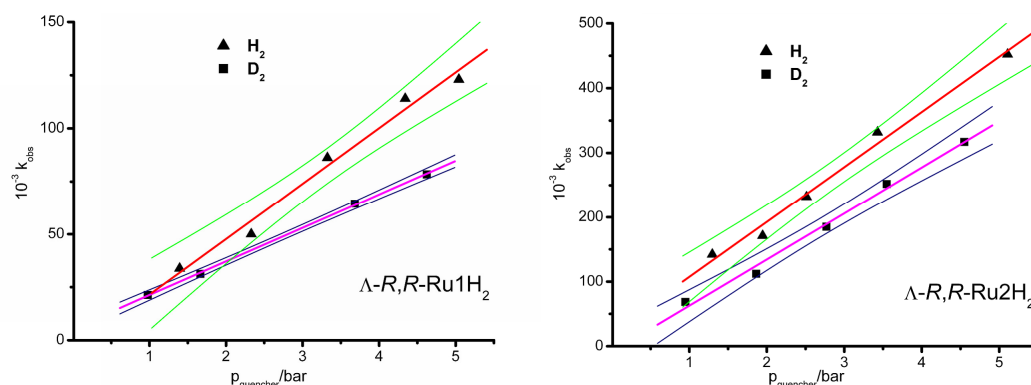
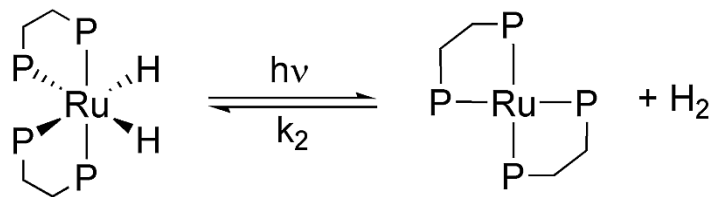


Figure 7. Plots of pseudo-first-order rate constants for the decay of the transients obtained upon laser flash photolysis (308 nm) of complexes Λ -*R,R*-Ru1H₂ and Λ -*R,R*-Ru2H₂ in cyclohexane vs the pressure of quenching gas (H₂ and D₂). The lines through the points show the best fits and the colored lines show the 95% confidence limits.



Scheme 8. Photodissociation of H₂ and regeneration of the starting material upon laser flash photolysis.

Laser flash photolysis in the presence of HBpin, PhSiH₃ and C₆F₅H of Λ -*R,R*-Ru1H₂ and Λ -*R,R*-Ru2H₂ resulted in rapid quenching of the transient both for Λ -*R,R*-Ru1H₂ and Λ -*R,R*-Ru2H₂. The formation and the decay of the transients were followed at the absorption maximum under Ar with a range of quencher concentrations (Table 1). The measured absorbance differences always return to the baseline after several microseconds, indicating that the transient complex is completely consumed leading to the Ru(II) product.

Table 1. Pseudo-first-order rate constants for reaction of transient species at 295 K in cyclohexane with different quenching ligands.

pH ₂ , bar/k _{obs} , s ⁻¹			
Ru(BPE) ₂ – H ₂		Ru(DuPHOS) ₂ – H ₂	
1.296	1.42×10 ⁵	1.394	3.38×10 ⁴
1.946	1.71×10 ⁵	2.33	5.0×10 ⁴
2.513	2.32×10 ⁵	3.324	8.62×10 ⁴
3.429	3.32×10 ⁵	4.341	1.14×10 ⁵
5.108	4.52×10 ⁵	5.042	1.23×10 ⁵

pD ₂ , bar/k _{obs} , s ⁻¹			
Ru(BPE) ₂ – D ₂		Ru(DuPHOS) ₂ – D ₂	
0.949	6.85×10 ⁴	0.978	2.13×10 ⁴
1.864	1.12×10 ⁵	1.664	3.12×10 ⁴

2.769	1.85×10 ⁵	3.683	6.45×10 ⁴
3.548	2.52×10 ⁵	4.624	7.84×10 ⁴
4.55	3.17×10 ⁵		

[HBpin], M/k _{obs} , s ⁻¹		[PhSiH ₃], M/k _{obs} , s ⁻¹	
Ru(BPE) ₂ – HBpin		Ru(BPE) ₂ – PhSiH ₃	
0.039	1.08×10 ⁴	0.4	3.52×10 ⁵
0.075	1.84×10 ⁴	0.8	5.71×10 ⁵
0.22	3.25×10 ⁴	1.23	9.26×10 ⁵
0.44	4.95×10 ⁴	1.66	1.06×10 ⁶
0.59	6.90×10 ⁴	2.14	1.38×10 ⁶

[HBpin], M/k _{obs} , s ⁻¹		[PhSiH ₃], M/k _{obs} , s ⁻¹		[C ₆ F ₅ H], M/k _{obs} , s ⁻¹	
Ru(DuPHOS) ₂ – HBpin		Ru(DuPHOS) ₂ – PhSiH ₃		Ru(DuPHOS) ₂ – C ₆ F ₅ H	
0.0331	1.35×10 ³	0.4	5.71×10 ⁴	0.03	1.64 ×10 ³
0.0825	1.75×10 ³	0.72	1.00×10 ⁵	0.18	2.44×10 ³
0.241	4.00×10 ³	0.8	1.09×10 ⁵	0.5401	3.87×10 ³
0.481	6.25×10 ³	1.23	1.48×10 ⁵	0.9	4.61×10 ³
0.646	7.69×10 ³				

Plots of k_{obs} against [HBpin] were linear and gave second-order rate constants for Λ -***R,R***-Ru1H₂ of $(9.90 \pm 0.6) \times 10^4 \text{ dm}^3 \text{ mol}^{-1} \text{ s}^{-1}$ and $(1.05 \pm 0.5) \times 10^4 \text{ dm}^3 \text{ mol}^{-1} \text{ s}^{-1}$ for Λ -***R,R***-Ru2H₂ (Figure 8). Analogous measurements with PhSiH₃ (Figure 9) showed that the transient is quenched 10 times faster than in the presence of HBpin (Table 2). A rate constant k_2 of $(3.06 \pm 0.6) \times 10^3$ was determined for the reaction of [Ru(DuPHOS)₂] in the presence of pentafluorobenzene (Figure 10). The corresponding measurement was not possible for [Ru(BPE)₂] since no reaction occurs.

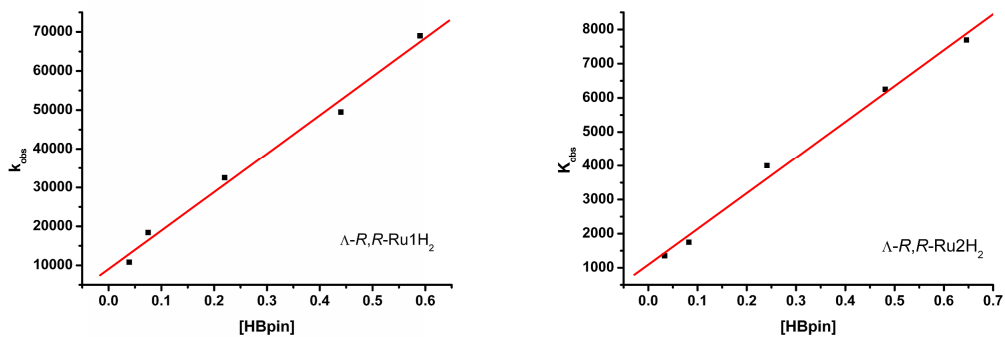


Figure 8. Plot of the pseudo first order rate constants, k_{obs} vs the concentration of HBpin: Δ -*R,R*-Ru1H₂ – left, Δ -*R,R*-Ru2H₂ – right.

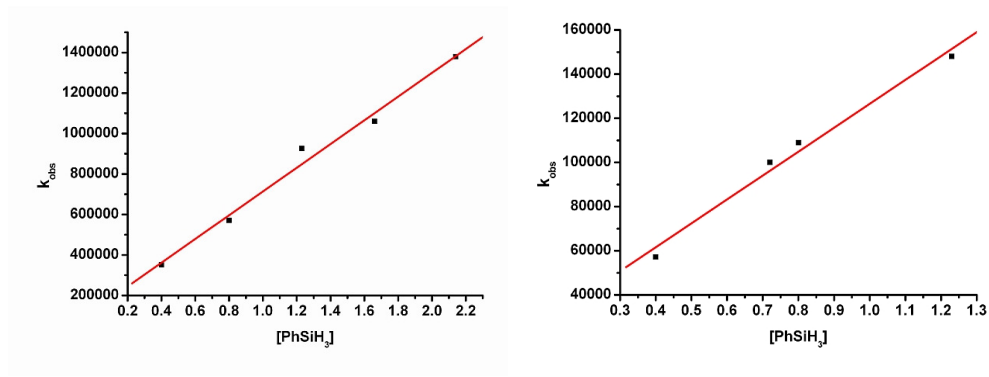


Figure 9. Plot of the pseudo first order rate constants, k_{obs} vs the concentration of PhSiH₃: Δ -*R,R*-Ru1H₂ – left, Δ -*R,R*-Ru2H₂ – right.

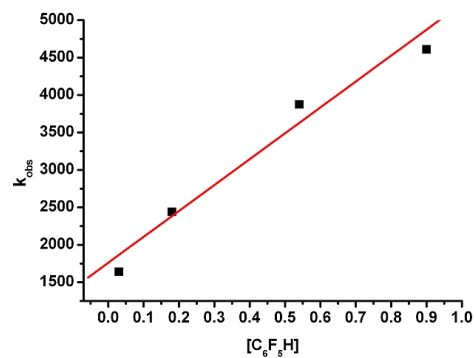


Figure 10. Plot of the pseudo first order rate constants, k_{obs} vs the concentration of C₆F₅H: Δ -*R,R*-Ru2H₂ – right.

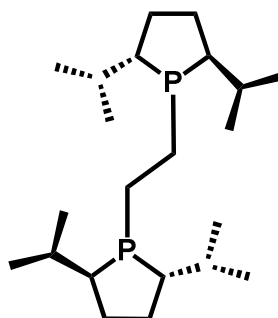
The effect of ethene (1 atm) on the transient kinetics was investigated for Λ -*R,R*-Ru2H₂. The transient decayed with pseudo-first order kinetics back to the baseline. Similar results were obtained with a cyclohexane solution of Λ -*R,R*-Ru2H₂ under 1 atm of CO. The values are not very different from those obtained under an Ar atmosphere and the characteristic residual absorbance of Ru(0) complexes was not observed, suggesting that these substrates are poor quenchers for [Ru(DuPHOS)₂].

Table 2. Second-order rate constants and kinetic isotope effects for reaction of transient species at 295 K in cyclohexane

Quencher	$k_2, \text{dm}^3 \text{mol}^{-1} \text{s}^{-1}$	
	Λ - <i>R,R</i> -Ru1H ₂	Λ - <i>R,R</i> -Ru2H ₂
H ₂	$(1.8 \pm 0.1) \times 10^7$	$(5.6 \pm 0.4) \times 10^6$
D ₂	$(1.52 \pm 0.07) \times 10^7$	$(3.37 \pm 0.05) \times 10^6$
$k_{\text{H}_2}/k_{\text{D}_2}$	1.2 ± 0.1	1.6 ± 0.1
PhSiH ₃	$(5.9 \pm 0.4) \times 10^5$	$(1.10 \pm 0.9) \times 10^5$
HBpin	$(9.90 \pm 0.6) \times 10^4$	$(1.05 \pm 0.5) \times 10^4$
C ₆ F ₅ H	-	$(3.06 \pm 0.6) \times 10^3$

6.3. Λ -[cis-Ru((R,R)-iPr-BPE)₂(H)₂], Ru₃H₂: preliminary laser flash study

Preliminary studies were carried out on Λ -**R,R-Ru₃H₂** complex, the isopropyl analogue of Λ -**R,R-Ru₁H₂**. The difference between the two complexes is just in the phospholane ligand which contains isopropyl substituents on the ring instead of methyls (Scheme 9).



Scheme 9. Structure of the phosphine used for **Ru₃H₂** complex.

6.3.1. Transient spectra

The spectrum of the transient species formed from Λ -[cis-Ru((R,R)-iPr-BPE)₂(H)₂], Λ -**R,R-Ru₃H₂**, was recorded under a hydrogen atmosphere (1 atm) in order to ensure the complete reversibility of the reaction. The transient spectra exhibit two absorption maxima, the first one and more intense at 480 nm, the second one at 770 nm, as observed for the complexes Λ -**R,R-Ru₁H₂** and Λ -**R,R-Ru₂H₂** (Figure 11, left).

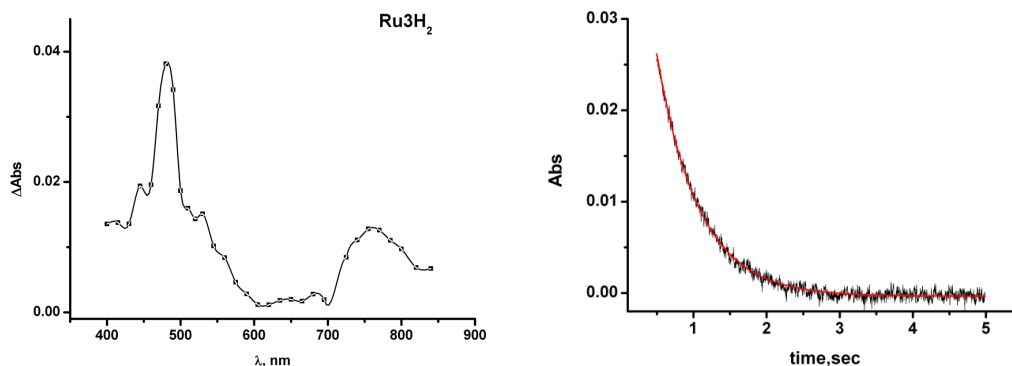


Figure 11. Left: transient UV-Vis spectra measured point-by-point at 298 K in cyclohexane on laser flash photolysis under 1 atm H₂ (308 nm) of Λ -*R,R*-Ru₃H₂. Right: transient decay after photolysis of Λ -*R,R*-Ru₃H₂ recorded at 470 nm under 1 atm of H₂ at 298 K.

6.3.2. LFP in the presence of Hydrogen

The transient decays back to the baseline with a pseudo-first-order kinetics on a second timescale (Figure 11, right). Pressure dependence studies gave a linear plot of k_{obs} versus [H₂] (Figure 12). k_2 for the regeneration of the precursor in the presence of hydrogen was determined to be $(1.3 \pm 0.1) \times 10^2 \text{ dm}^3 \text{ mol}^{-1} \text{ s}^{-1}$.

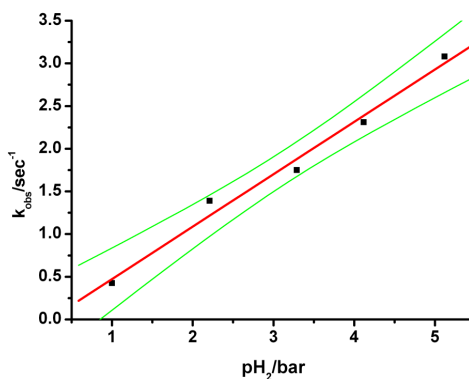


Figure 12. Plots of pseudo-first-order rate constants for the decay of the transient obtained upon laser flash photolysis (308 nm) of complexes Λ -*R,R*-Ru₃H₂ in cyclohexane vs the pressure of hydrogen. The line through the points show the best fits and the colored lines show the 95% confidence limits.

6.4. Ru(dppe)₂H₂: Laser Flash studies in the presence of HBpin

The laser flash photolysis of the complex Ru(dppe)₂H₂ was previously studied and rate constants determined in the presence of hydrogen and tertiary silanes.³ In these studies, LFP of Ru(dppe)₂H₂ was carried out in the presence of different concentrations of HBpin in cyclohexane (Table 3). The Ru⁰P₄ transient decayed with pseudo first order kinetics restoring the original absorbance (Figure 13, left). The second order rate constant k_2 , of $(8.9 \pm 0.3) \times 10^5 \text{ dm}^3 \text{ mol}^{-1} \text{ s}^{-1}$ was obtained from the plot of k_{obs} against the concentration of the quencher HBpin (Figure 13, right). Laser flash photolysis of Ru(dppe)₂H₂ in the presence of HBcat was not successful.

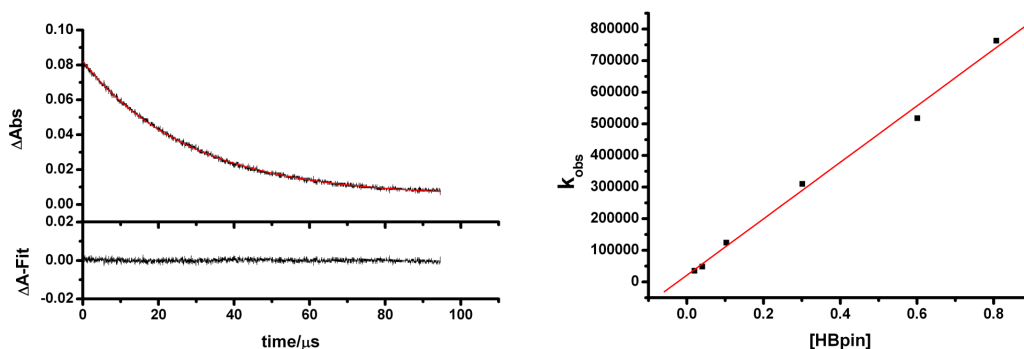


Figure 13. Left: transient decay after photolysis of Ru(dppe)₂H(Bpin) recorded at 470 nm at 298 K. Right: plot of the pseudo first order rate constants, k_{obs} vs the concentration of HBpin.

Table 3. Pseudo-first-order rate constants for reaction of transient species Ru(dppe)₂ at 295 K in cyclohexane with HBpin.

[HBpin], M/k _{obs} , s ⁻¹	
Ru(dppe) ₂ - HBpin	
0.02	3.51×10 ⁴
0.04	4.85×10 ⁴
0.103	1.24×10 ⁵
0.301	3.1×10 ⁵
0.601	5.18×10 ⁵
0.807	7.63×10 ⁵

6.5. Discussion

The primary photochemical step in the reaction of [Ru(PP^{*})₂]H₂ is reductive elimination of dihydrogen as proved by the observation of the characteristic multiband UV/vis spectra³ of the 4-coordinate [Ru(PP^{*})₂] within the instrumental rise time (< 20 ns) on laser flash photolysis of **Λ-R,R-Ru1H₂**, **Λ-R,R-Ru2H₂** and **Λ-R,R-Ru3H₂**. Similar multiband spectra for [Ru(PP)₂] have been observed previously for PP = dmpe, depe, dppe, dfep and have been shown to be characteristic of an approximate square planar geometry. The lowest energy band was previously assigned to a d_{z²}-p_z transition;³ it is observed at 740 nm, 700 nm and 750 nm for **Λ-R,R-Ru1H₂**, **Λ-R,R-Ru2H₂** and **Λ-R,R-Ru3H₂** respectively, close to observations on the analogues Ru(dmpe)₂H₂, Ru(depe)₂H₂ and Ru(dppe)₂H₂ which present bands up to 760 nm. At higher energy, we note that the most intense absorption band of **Λ-R,R-Ru2H₂** is red-shifted significantly (560 nm) relative to the spectra of the other complexes; **Λ-R,R-Ru1H₂** shows it at 520 nm and **Λ-R,R-Ru3H₂** at 480 nm. The crystal structures of the *trans* complexes provide models for the structures of [Ru(BPE)₂] and [Ru(DuPHOS)₂]. In *trans*-**R,R-Ru1(Cl)₂** and *trans*-**R,R-Ru1(Br)(H)**, the [Ru(BPE)₂] moiety approximates to D₂ symmetry while the

[Ru(DuPHOS)₂] moiety of *trans-R,R*-Ru₂(C₆F₅)(H) shows a significant twisting of Ru-P(1)-P(2) relative to Ru-P(3)-P(4) (18.4°) (Figure 14). This torsion may account for the shift observed in the UV/vis spectrum.

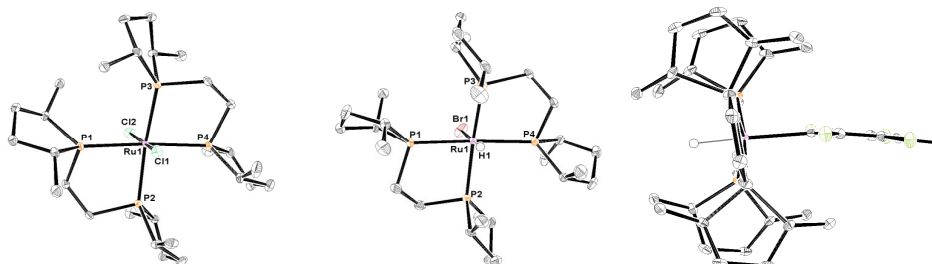


Figure 14. From the left: molecular structures of *trans-R,R*-Ru₁(Cl)₂; *trans-R,R*-Ru₁(Br)(H) and *trans-R,R*-Ru₂(C₆F₅)(H).²⁶

6.5.1. Kinetics

The reactivity of the intermediates [Ru(BPE)₂] and [Ru(DuPHOS)₂] has been explored by transient kinetics. The second order rate constant for back reaction of [Ru(BPE)₂] with H₂ ($(1.8 \pm 0.1) \times 10^7 \text{ dm}^3 \text{ mol}^{-1} \text{ s}^{-1}$) is similar to that for [Ru(dppe)₂] but substantially smaller than those for [Ru(dmpe)₂] and [Ru(depe)₂].³ The rate constant for reaction of [Ru(DuPHOS)₂] with H₂ is three times smaller than that for reaction with [Ru(BPE)₂]. The kinetic isotope effects (KIE) for these reactions are 1.18 ± 0.08 and 1.63 ± 0.12 , respectively. These reactions have very small barriers that are almost certainly created by steric hindrance and the KIE is correspondingly small.

The rate constants for reaction of the three oxidative addition substrates with [Ru(BPE)₂] span a factor of 200 and follow the order H₂ > PhSiH₃ > HBpin. The corresponding rate constants for reaction of [Ru(DuPHOS)₂] are between three and nine times smaller, but follow the same order (Figure 15, Table 2). Notably, this order still applies if a statistical correction is applied for the number of hydrogen atoms available for activation. The rate constant for reaction of [Ru(DuPHOS)₂] with C₆F₅H was even smaller than for other substrates (1800

times smaller than for reaction with H₂). The reaction rate with Et₂SiH₂ was too slow to determine by these methods.

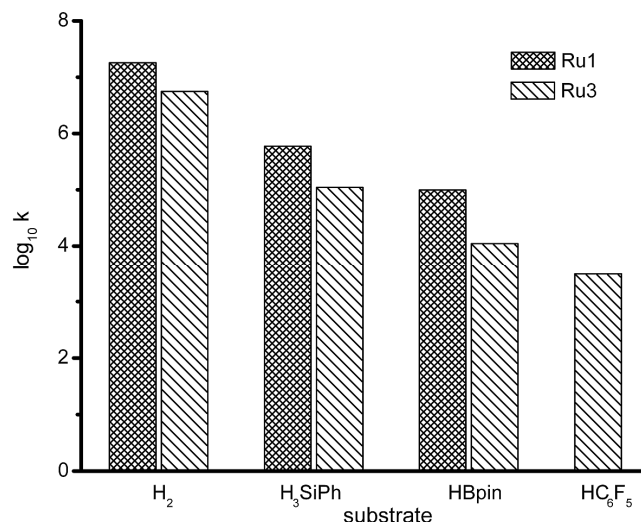


Figure 15. Plot of log₁₀ k₂ versus the different quencher for Λ -*R,R*-Ru1H₂ (stipple) and Λ -*R,R*-Ru2H₂ (hatched) where k₂ is the second order rate constant.

The reason that the reactions of [Ru(BPE)₂] and [Ru(DuPHOS)₂] are slower than those of [Ru(dmpe)₂] and [Ru(depe)₂] almost certainly lies with blocking action of the methyl substituents on the phospholane rings (Figure 16). Examination of the crystal structures of Λ -*R,R*-Ru1H₂ and Λ -*R,R*-Ru2H₂ indicates that the steric constraints are greater for Λ -*R,R*-Ru1H₂, but it is [Ru(DuPHOS)₂] that reacts more slowly, probably because the C₆H₄ link is more rigid than the CH₂CH₂ link between the phosphorus atoms.

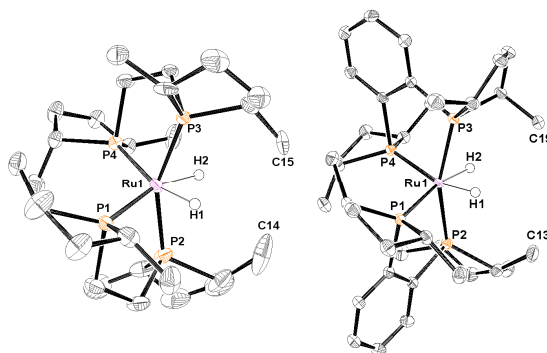


Figure 16. Molecular structures of Λ -*R,R*-Ru1H₂ (left) and Λ -*R,R*-Ru2H₂ (right) (50%

thermal ellipsoids), all hydrogen atoms omitted for clarity except for H(1) and H(2). Note that one phospholane ring in Λ -***R,R***-Ru1H₂ is disordered; just one form is shown.²⁶

In addition to transient kinetic measurements, my colleague Marius Câmpian performed competition reactions in which the photoreaction of Λ -***R,R***-Ru1H₂ or Λ -***R,R***-Ru2H₂ was followed in the presence of two substrates. These tests demonstrated that the selectivity PhSiH₃ > HBpin > Et₂SiH₂ can be observed in steady state photochemical experiments, just as in transient spectroscopy. However, exchange between substrates also occurs on photolysis of Λ -***R,R***-Ru1(Et₂SiH)(H) in the presence of HBpin or PhSiH₃ indicating that the product distribution represents a photostationary state.

Very surprisingly complex Λ -***R,R***-Ru3H₂ appears to react 100000 times slower with H₂ than Λ -***R,R***-Ru1H₂ ($(1.8 \pm 0.1) \times 10^7 \text{ dm}^3 \text{ mol}^{-1} \text{ s}^{-1}$). Isopropyl groups are sterically more demanding than methyl groups; as a result reaction with a small substrate such as hydrogen takes place on the second timescale. Moreover this very low timescale could suggest an agostic interaction taking place between the metal centre and the isopropyl groups which would enhance the selectivity. Steady state photolysis with Λ -***R,R***-Ru3H₂ was not successful due to the need for very long photolysis times and lack of selectivity in product formation. The validity of the data measured by laser flash photolysis for complex Λ -***R,R***-Ru3H₂ could be called into question due to errors in the estimation of the pseudo first order rate constants. Diffusion of species outside the monitoring beam is a source of errors for slow kinetics measurements.²⁵ Nevertheless, the good linear fit obtained by plotting k_{obs} against pressure of H₂ for complex Λ -***R,R***-Ru3H₂ encourages confidence in the validity of the experiment. It would be interesting to carry out kinetic experiments with complex Λ -***R,R***-Ru3H₂ and different quenching ligands. Since laser flash photolysis is not the best tool to look at such slow kinetics, a rapid scan UV-spectrometer set up with a flash lamp could be used to get rate constants.

In order to complete the reactivity trend of Ru(PP)₂H₂ complexes, laser flash photolysis for the reaction of the Ru(dppe)₂H₂ complex in the presence of HBpin

was also explored. A return to the pre-flash level indicates that the oxidative addition of HBpin is complete within less than 100 μs for a concentration of HBpin of 0.02 M. This is consistent with the formation of a Ru(II) species. As expected the rate constant for reaction of Ru(dppe)₂H₂ lies between the ones observed previously for Ru(dmpe)₂H₂ and Ru(depe)₂H₂⁶ and those previously discussed for the Ru(BPE)₂ and Ru(DuPHOS)₂ dihydride species²⁶(Table 4).

Table 4. Second order rate constants, $k_2 \text{ dm}^3 \text{ mol}^{-1} \text{ s}^{-1}$, for reaction of RuH₂ complexes with HBpin and H₂.

	Ru(dmpe) ₂	Ru(depe) ₂	Ru(dppe) ₂	Ru(BPE) ₂	Ru(DuPHOS) ₂
HBpin	(1.3±0.2)×10 ⁹	(1.3±0.1)×10 ⁷	(8.9±0.3)×10 ⁵	(9.9±0.6)×10 ⁴	(1.1±0.5)×10 ⁴
H ₂	(6.2±0.3)×10 ⁹	(1.3±0.1)×10 ⁷	(2.4±0.2)×10 ⁷	(1.8±0.1)×10 ⁷	(5.6±0.4)×10 ⁶

Reductive elimination of the dihydrogen occurs within the instrumental rise time (< 20 ns) upon flash photolysis for all the complexes shown in Table 4. There is clearly a trend in the k_2 values (Figure 17), which are larger for complexes with less bulky phosphines, (*e.g.* dmpe and depe) for both the reactions with HBpin and H₂. Ru(dppe)₂ shows 10 times more reactivity towards HBpin than the BPE analogue. The Ru(DuPHOS)₂ is almost 100 times slower in reaction with HBpin than the Ru(dppe)₂ complex; this difference in reactivity can surely be explained by the use of stereogenic phosphines BPE and DuPHOS where the methyl substituent on the phospholane ring exercise a blocking action, congesting the access for the ligands towards the unsaturated metal centre.

The reduction in reactivity towards HBpin observed on going from Ru(dmpe)₂ to Ru(dppe)₂ spans a factor of 1500 and it is probably due to the sum of a steric effect played by the bulkier dppe bidentate phosphine and the smaller electron donation from the ligand to the Ru centre. The same trend is observed for reactions with H₂ (Table 4, Figure 17), Ru(dppe)₂ is again less reactive than Ru(depe)₂ and Ru(dmpe)₂, the rate constants for complexes Ru(BPE)₂ and Ru(DuPHOS)₂ are still smaller than for Ru(dppe)₂. However, since hydrogen is

a really small ligand, the blocking action exercised by the methyl groups on the phospholane ring is less significant than in reactions with HBpin (Figure 17). A reduction in rate constant by a factor of 80 is in fact observed from Ru(dppe)₂ to Ru(DuPHOS)₂ for reactions with HBpin, while rate constants for reactions with hydrogen span just a factor of 4. On the other hand, a huge effect is observed with Ru(ⁱPr-BPE)₂ in which the rate constant for reaction with H₂ is massively reduced.

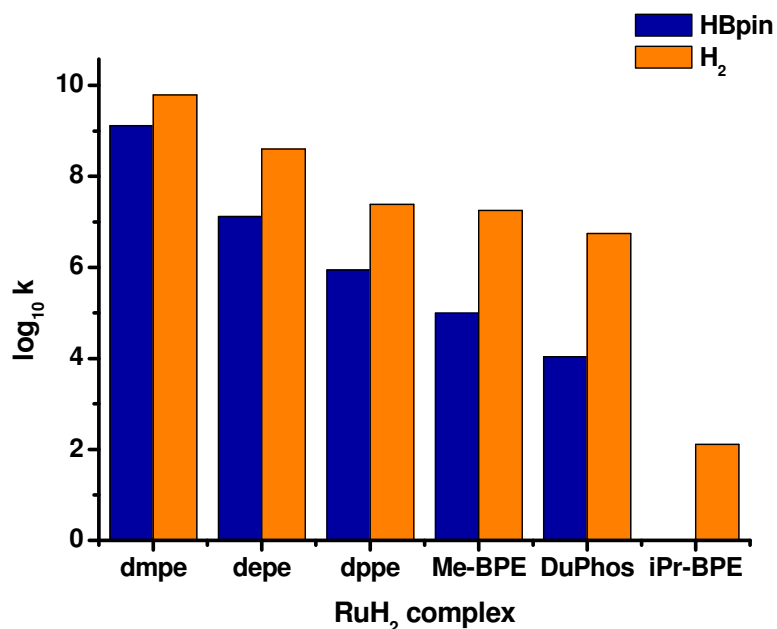


Figure 17. Plot of $\log_{10} k_2$ versus the different Ru(PP)₂H₂ complexes in the presence of HBpin (blue) and H₂ (orange) where k is the second order rate constant.

6.6. Summary

We can conclude that the primary photoproducts of Ru(drpe)₂H₂ (drpe = dppe, BPE, DuPhos and ⁱPr-BPE) are the 4-coordinate complexes Ru(drpe)₂. Each of the complexes Ru(drpe)₂ exhibits a multiband UV-visible spectrum including a long-wavelength band assigned to a M(d_{z²)–M(p_z) transition. The spectra are characteristic of a structure close to square planar. The reactivity of the complexes increases in the order Ru(ⁱPr-BPE) < Ru(duphos)₂ < Ru(BPE)₂ < Ru(dppe)₂. The 2nd order rate constants follow the order H₂ > H₃SiPh > HBpin.}

6.7. Experimental

6.7.1. General procedures

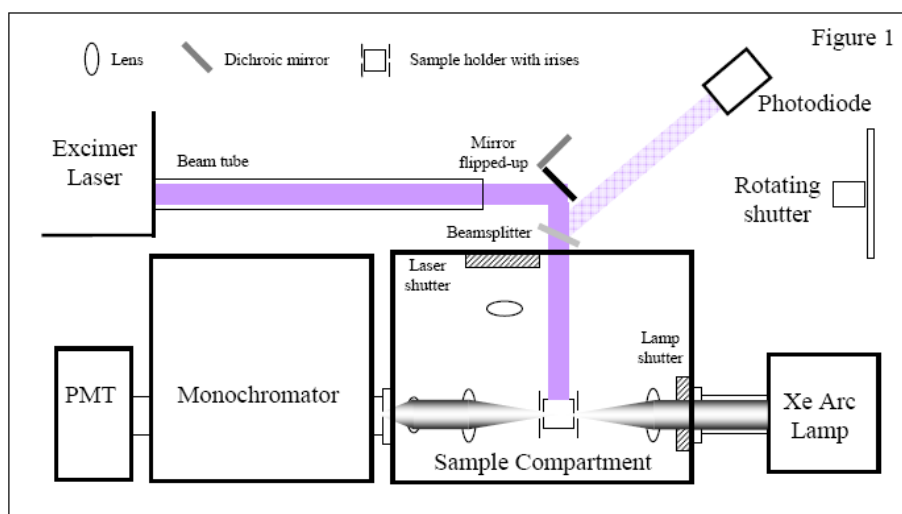
All operations were performed under an argon atmosphere on a high-vacuum line (10^{-4} mbar), or in a glovebox. Solvents for general use (cyclohexane, benzene) were of AR grade, dried by distillation over sodium and stored under Ar in ampoules fitted with a Young's PTFE stopcock. Cyclohexane used for LFP experiments was dried in the same way and used just for LFP experiments to avoid contaminations. HBpin was bought from Aldrich and purified by vacuum distillation. Λ -*R,R*-Ru1H₂, Λ -*R,R*-Ru2H₂, Λ -*R,R*-Ru3H₂ were synthesized by Dr. Marius Câmpian as reported in the literature²⁶ and Ru(dppe)₂H₂ was prepared as reported in Chapter three.²⁷

6.7.2. Laser Flash Photolysis.

Samples were prepared exclusively in the glove box. They were loaded into a quartz cuvette (10 mm path-length) fitted with a Young's PTFE stopcock, a degassing bulb, and a greaseless Young's connection. The complex (ca 2-3 mg) was dissolved in cyclohexane (5 mL) in an argon-filled glove box with a concentration selected to have an absorbance at the laser wavelength (308 nm) between 0.6 and 0.85 checked by UV/vis. Liquid quenchers were added with a micro liter syringe to the solution containing the complexes. The solution was then degassed by freeze-pump-thaw cycle (3 times) on a high-vacuum Schlenk line before being backfilled with the appropriate gas. The gaseous quencher (or argon) was admitted up to 1 atm pressure on the high vacuum Schlenk line. For high pressure work the window edges of the cuvette were flamed to secure the seal and the Young's connection was replaced by a glass-to-metal seal and a Swagelok™ fitting. The gas was admitted on a high pressure line and the pressure measured with an MKS Baratron capacitance manometer. The cell was held in a metal container for safety. A single sample was used for each run with increasing gas pressure. The results were consistent with a corresponding run with decreasing gas pressure. The variable pressure measurements were

performed on two different samples each for H₂ and D₂ and were carried out side-by-side on the same day. The gases were of Research Grade: deuterium 99.96 atom % D, Isotec; hydrogen N5.5, BOC; argon N5.5, BOC.

The apparatus consists of an excimer laser (MPB Technologies Inc, MSX-250) operating at 308 nm (XeCl) as the exciting source, coupled to an Applied Photophysics laser kinetic spectrometer with a Xe arc lamp (XM-300-5 HS made by ORC) as a white light source (Scheme 10). The laser pulse (ca 11 ns) is focused into a beam of ca 1-mm diameter and directed through the sample together with the monitoring beam in a collinear arrangement by means of a quartz beam splitter. Light falling on the photomultiplier detector is sampled by a Tektronix TDS 520 oscilloscope and transferred to a computer for data analysis and storage. Transient decays are usually analyzed as 15 shot averages. The computer is used to fire the laser and the oscilloscope is triggered by diverting part of the laser beam and focusing onto a photodiode. Transient spectra are obtained by the point-by-point method and correspond to difference spectra after particular fixed times following the laser flash. The samples were maintained at 295 K.



Scheme 10. Schematic representation of the LFP apparatus.

7 X-Ray Crystallography

7.1 Introduction

Single crystal X-ray diffraction is nowadays one of the most frequently used techniques for the structural characterisation of molecules. The technique has evolved immensely in the last 50 years coupled to the improvement of computer power and lead to extraordinary results in different areas of research; many Nobel Prizes in chemistry have been awarded for work based on crystallographic results.¹ Obtaining a structure at atomic resolution is very good evidence; knowing the geometry of the compounds you are investigating is helpful to understand the reactivity for further studies. The great majority of organic, organometallic and inorganic molecular structures have been also determined in this way; the number of structures deposited in the CSD clearly reflects the potential of this technique. I considered fundamental at my stage of study to have a deeper understanding of the strength, the precision and the limitations of X-ray crystallography and be trained in doing it. In this Chapter the crystallographic analysis of some of the structures obtained in the group is attempted. Different ruthenium and rhenium complexes are structurally analysed and compared to data already known in the literature.

7.2 Crystal structure analysis

7.2.1 Ruthenium hydride complexes

Complexes **1** and **2** (Figure 1) are ruthenium hydride compounds formed by photochemical reactions of the analogue Λ -[cis-Ru((R,R)-Me-BPE)₂(H)₂] and Λ -[cis-Ru((R,R)-Me-DuPHOS)₂(H)₂] species in the presence of phenyl silane and pentafluorobenzene respectively. Their crystal structures have been determined by X-ray diffraction and the results interpreted. Crystallographic data for complexes **1** and **2** are reported in Table 1.

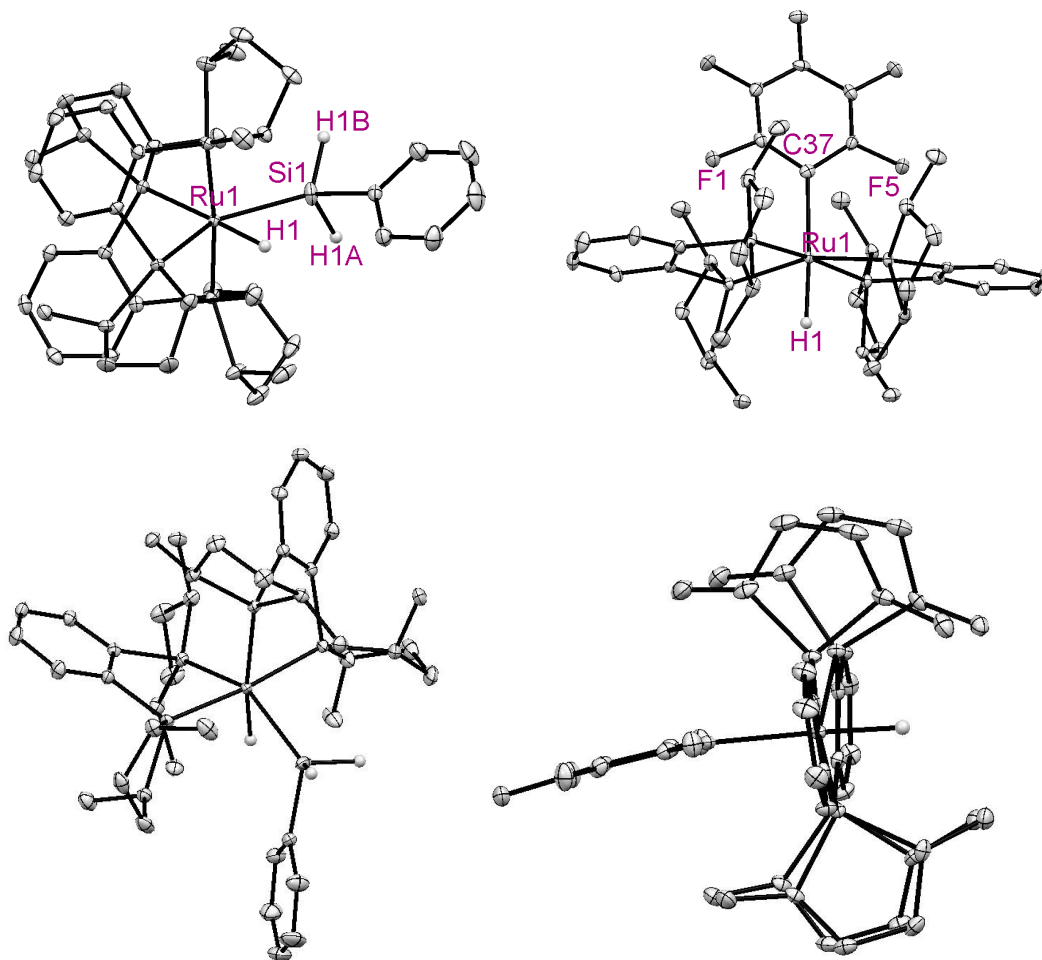


Figure 1. Molecular structure of Δ -R,R-Ru(PhSiH₂)(H), **1** (left, top-bottom), and trans-R,R-Ru(C₆F₅)(H), **2** (right, top-bottom). Hydrogen atoms are omitted for clarity apart than the hydrides and the hydrogens bounded to the silicon. Ellipsoids for the anisotropic displacement parameters are shown at the 50% level.

Both the complexes **1** and **2** crystallised in the space group P2₁. They belong to a monoclinic crystal system with a primitive lattice. The P2₁ space group is enantiomorphic with two fold axes, 2 (no improper rotation are present), as well as polar axes (every operation leaves more than one common point unmoved) and it has a two-one screw axis where a two fold rotation and a translation are combined together. Complex **1** shows optical activity, as suggested by the space group of crystallization.

Table 1. Crystallographic data for complexes **1** and **2**.

	1	2
Formula	C ₄₂ H ₆₄ P ₄ RuSi	C ₄₂ H ₅₇ F ₅ P ₄ Ru
<i>M</i>	821.97	881.83
<i>a</i> /Å	11.6044(3)	12.525(14)
<i>b</i> /Å	16.5646(2)	12.651(13)
<i>c</i> /Å	12.0137(3)	12.530(13)
α /deg	90.00	90.00
β /deg	118.031(3)	92.913(10)
γ /deg	90.00	90.00
<i>V</i> / Å ³	2038.40(8)	1982.84(4)
<i>T</i> /K	110(2)	110(2)
Space group	P2 ₁	P2 ₁
Crystal system	Monoclinic	Monoclinic
<i>Z</i>	2	2
Reflns meads	18688	14233
Reflns indep	11806	8822
<i>R</i> _{int}	0.0222	0.0222
Final <i>R</i> [<i>I</i> > 2 σ (<i>I</i>)]	<i>R</i> ₁ = 0.0273	<i>R</i> ₁ = 0.0257
	w <i>R</i> ₂ = 0.0584	w <i>R</i> ₂ = 0.0530
Final <i>R</i> (all data)	<i>R</i> ₁ = 0.0307	<i>R</i> ₁ = 0.0278
	w <i>R</i> ₂ = 0.0600	w <i>R</i> ₂ = 0.0541
Goof on <i>F</i> ²	1.015	1.035

Unit cell dimensions and angles are consistent with a monoclinic crystal system where α should be equal to γ and both equal to 90°. The presence of a two-fold axis also confirms the minimum rotation symmetry required for the molecule to crystallise in this system.

Both the data sets merged satisfactorily as confirmed by the low values of *R*_{int} (0.0222 for both complexes) and the discrepancy indices showed a very good agreement between the calculated models and the observed ones. Goodness of Fit was for both complex **1** and **2** close to 1 (1.015 and 1.035 respectively), demonstrating again that a consistent model was created. Finally, no major peak or holes were found in the electron density map. The Ru-H and Si-H hydrogen atoms were located by difference map and refined. The remaining hydrogens were placed at fixed distances with a riding model.

Table 2 shows some of the main bond lengths and angles, no anomalies were detected with the values being consistent with what was previously observed for

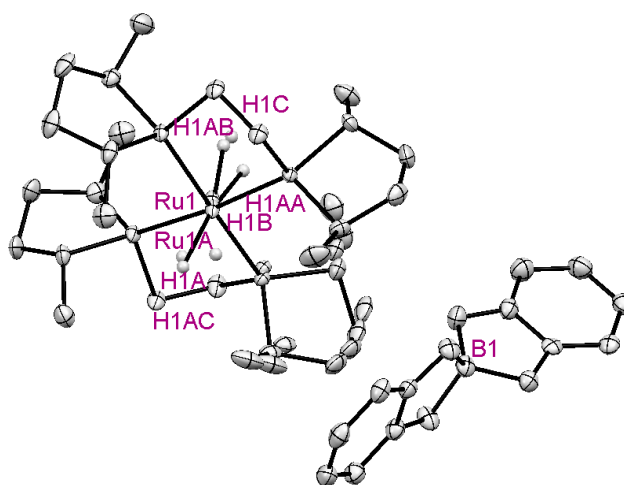
analogous Ru species. The Ru-Si and Ru-H bond lengths of 2.4064(6) Å and 1.52(3) Å are in agreement with those found in [Ru(PMe₃)₄(SiR₃)(H)].² The hydride-silicon distance H(1)⋯Si(1) to 2.20(4) Å indicates a residual interaction between the Si and H resulting in less complete oxidative cleavage of the Si-H bond.³ The absolute configuration is Δ, opposite to that of the starting material Λ-[*cis*-Ru((*R,R*)-Me-DuPHOS)₂(H)₂]. The rigid benzene backbone makes the access of phenyl silane to the ruthenium center difficult. The residual interaction is reflected also in the angles P(1)-Ru(1)-Si(1) (146.61(2)°) and P(4)-Ru(1)-Si(1) (111.57(2)°) which are very different compared to those in Λ-R₂Ru1(PhSiH₂)(H) of 164.14(3)°, 87.12(2)° where oxidative addition is complete and no residual interactions are observed.⁴

The Ru-C bond length (2.229(2) Å) for complex **2** lies in between those reported for the other known similar structures which are trans-[Ru(dmpe)₂(C₆F₅)(H)],⁵ and a *cis* carbene complex [Ru(dppp)(ICy)(CO)(C₆F₅)(H)].⁶ For complexes **X** and **Y** the C₆F₅ plane almost bisects the C-C bonds of the C₆H₄ units of the DuPHOS ligands. The angle between the plane defined by the C₆F₅ group and the Ru-H bond vector is 6.39°, and the angle between the same plane and the one defined by the RuP₄ skeleton is 81.63°, the arene moiety results almost perpendicular to the RuP₄ part. The RuP₄ skeleton is significantly distorted from planarity, with a torsional angle of 18.4° between the planes Ru-P(1)-P(2) and Ru-P(3)-P(4). The hydride was located at 1.68(2) Å from Ru, compared to a Ru-H distance of 1.59(5) Å found in the Ru(dmpe)₂(C₆F₅)H.⁵

Table 2. Selected Bond Lengths (Å) and Angles (deg) for complexes **1** and **2**.

Bond (Å)	Δ - <i>R,R</i> -Ru2 (PhSiH ₂)(H), 1	Bond (Å)	<i>trans</i> - <i>R,R</i> - Ru2(C ₆ F ₅)(H), 2
Ru-H(1)	1.52(3)	Ru-H(1)	1.68(2)
Ru-Si	2.4064(6)	Ru-C	2.229(2)
Si···H(1)	2.20(4)		
Angles (deg)		Angles (deg)	
P(1)-Ru-Si	146.61(2)	P(1)-Ru-C	91.93(6)
P(4)-Ru-Si	111.57(2)	P(4)-Ru-C	92.11(6)
P(4)-Ru-H(1)	171.7(9)	P(4)-Ru-H(1)	88.6(8)

7.2.2 Ruthenium hydride dihydrogen complexes

**Figure 2.** Molecular structure of [Ru(BPE)₂(H₂)(H)]⁺[Bcat₂]⁻, **3**. Hydrogen atoms are omitted for clarity apart from the hydride and dihydrogen. Ellipsoids for the anisotropic displacement parameters are shown at the 50% level.

Compounds **3** (Figure 2) and **4** (Figure 5) are ruthenium dihydrogen hydride complexes obtained by thermal reaction of the Ru(BPE)₂H₂ precursor with HBcat and HBAr^F₄. Complex **3** crystallized in an orthorhombic crystal system where all the three angles are 90° and there are no restrictions on unit cell lengths. As shown in Table 3, *a* is different from *b* which is different from *c*.

Table 3 Crystallographic data for complexes **3** and **4**.

	3	4
Formula	C ₄₁ H ₆₉ BCl ₂ O ₄ P ₄ Ru	C ₆₀ H ₇₁ BF ₂₄ P ₄ Ru
<i>M</i>	932.62	1483.93
<i>a</i> /Å	11.4288(3)	13.1108(5)
<i>b</i> /Å	13.3751(3)	13.1152(6)
<i>c</i> /Å	28.8585(8)	22.1948(10)
<i>α</i> /deg	90.00	104.829(4)
<i>β</i> /deg	90.00	92.187(4)
<i>γ</i> /deg	90.00	118.293(4)
<i>V</i> / Å ³	2038.40(8)	1982.84(4)
T/K	110(2)	110(2)
Space group	P2 ₁ 2 ₁ 2 ₁	P1
Crystal system	Orthorhombic	Triclinic
<i>Z</i>	4	2
Reflns meads	20794	31471
Reflns indep	13722	24661
<i>R</i> _{int}	0.0245	0.0424
Final <i>R</i> [<i>I</i> > 2σ(<i>I</i>)]	<i>R</i> ₁ = 0.0435	<i>R</i> ₁ = 0.0863
	w <i>R</i> ₂ = 0.0895	w <i>R</i> ₂ = 0.2370
Final <i>R</i> (all data)	<i>R</i> ₁ = 0.0522	<i>R</i> ₁ = 0.0933
	w <i>R</i> ₂ = 0.0951	w <i>R</i> ₂ = 0.2524
Goof on <i>F</i> ²	1.067	1.069

P2₁2₁2₁ has three mutually perpendicular C₂ axes and is one of the enantiomorphic point groups. The asymmetric unit carries a solvent molecule of crystallization (CH₂Cl₂) and there are four repeating building blocks in the unit cell (*Z* = 4). Figure 2 shows the Ortep diagram of the [Ru(BPE)₂(H₂)(H)]⁺ cation plus the counter ion B(cat)₂⁻. The closest contact with the counter ion occurs at 2.51 Å between the oxygen of the borolane ring and a hydrogen atom of the methyl group of the phospholane moiety. The metal centre appears to be disordered over two sites (Ru1, Ru1A; Figure 3); the disorder was successfully modeled with 80:20 occupancy. The phosphorus atom P3 is also disordered over two positions along with the phospholane moiety (Figure 3). Hydride and dihydrogen ligands were not found by difference maps and were located by comparison with the [Ru(η²-H₂)H(DuPHOS-Me)₂]⁺ previously reported.⁷ They lie trans to each other and are disordered with 80% probability in one position and 20% in the other one (Figure 4).

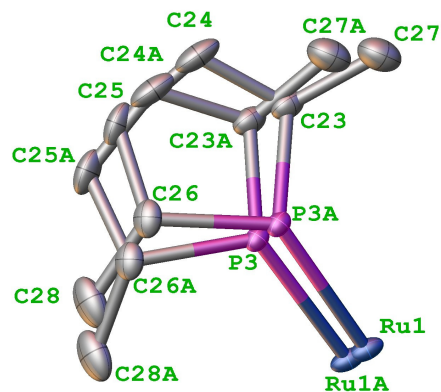


Figure 3. Phospholane moiety of complex **3** showing the disorder. Hydrogen atoms are omitted for clarity. Ellipsoids for the anisotropic displacement parameters are shown at the 50% level.

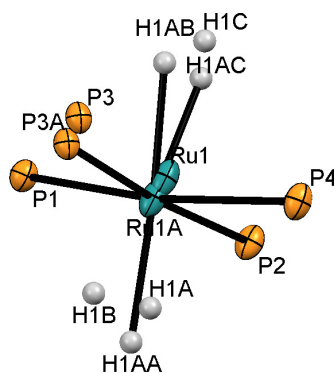


Figure 4. $[\text{Ru}(\text{PP})_2(\text{H}_2)(\text{H})]$ fragment for complex **3** showing the disorder of the metal centre Ru1 / Ru1A, hydrides H1AA / H1C and dihydrogen H1AB-H1AC / H1B-H1A ligands.

The dihydrogen ligand appears almost totally eclipsed by the P2-Ru1-P3 unit as already observed in the DuPHOS complex, and bond lengths are consistent with those found for the DuPHOS analogue (Table 4).

Refinement indicators for complex **3** are quite satisfactory; Goodness of Fit is very close to 1; R factors are low enough to be confident about the correctness of the structure and the low value for R_{int} proves that the data merged very well (Table 3).

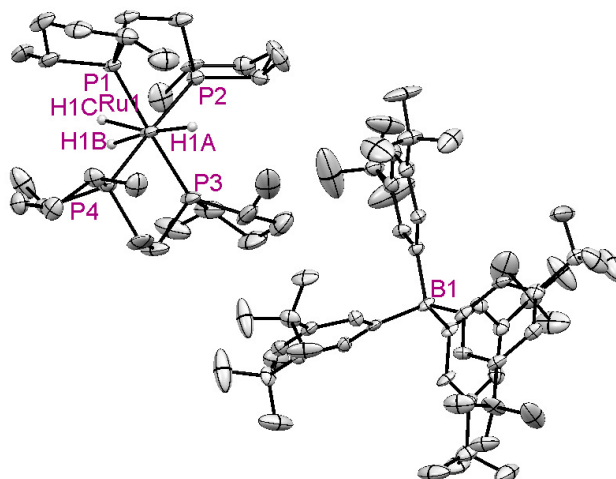


Figure 5. Molecular structure of $[\text{Ru}(\text{BPE}_2)(\text{H}_2)(\text{H})]^+[\text{BAR}_4^{\text{F}}]^-$, **4**. Hydrogen atoms are omitted for clarity apart from the hydride and dihydrogen. Ellipsoids for the anisotropic displacement parameters are shown at the 50% level.

Complex **4** is analogous to complex **3**, but with a different counter ion. The data set was much poorer than for complex **3** since the crystals were very thin plates; refinement indicators are in fact worse (Table 3). The structure is not disordered as observed for complex **3**; the shortest contact between the anion and cation occurs at 2.60 Å, between a fluorine atom of the BAR_4^{F} cation and a hydrogen atom on the phospholane moiety.

The molecule crystallizes in a triclinic crystal system; it exhibits a primitive lattice in a P1 space group where no rotational symmetry and cell dimensions restrictions are required.

Table 4 shows a comparison between selected bond lengths for complexes **3** and **4** with the previously reported $[\text{Ru}(\text{DuPHOS})_2(\text{H}_2)\text{H}][\text{PF}_6]^-$, **X**. Bond lengths are very similar, even though $[\text{Ru}(\text{BPE})_2(\text{H}_2)\text{H}]^+$ complexes **3** and **4** show shorter Ru-P interactions than the previously reported ones. The differences in Ru-H distances are not statistically significant, but the differences in Ru-P distances are significant. Thus the mean Ru-P distances for **3**, **4**, and **X** are 2.3356, 2.323 and 2.365 respectively. This is possibly a consequence of smaller steric constraints because of the absence of the phenyl moiety on the phospholane bridge which reduces backbonding.

Table 4. Selected bond lengths (Å) for complexes **3** and **4** and comparison with the [Ru(DuPHOS)₂(H₂H)]⁺ complex, **X**, previously reported.

	3	4	X
Ru-H1A	1.90(1)	1.928(7)	1.93(9)
Ru-H1B	1.77(9)	1.78(6)	1.78(7)
Ru-H1C	1.80(1)	1.77(6)	1.78(7)
Ru-P1	2.3536(12)	2.320(3)	2.393(14)
Ru-P2	2.3302(11)	2.322(3)	2.372(12)
Ru-P3	2.3332(14)	2.317(3)	2.350(4)
Ru-P4	2.3253(12)	2.333(3)	2.346(4)

7.2.3 Rhenium Carbonyl compounds.

Rhenium tricarbonyl compounds are well known for their photophysical properties and recently for their applications in solar energy conversion.^{8,9} Our group has explored these compounds as catalysts in CO₂ to CO photoreduction either used as single components¹⁰ or as part of photoactive dyads.¹¹ The molecular structures of complexes Re(CO)₃(4,4'-BMCbpy)(OPF₂O) **5**, [Re(CO)₃(bpy)(Pic)][PF₆] **6** and [Re(CO)₃(4,4'-BMCbpy)(NCCH₃)][PF₆] **7** were characterized by X-ray diffraction (Figure 6) and the results interpreted. The 4,4'-BMCbpy displays two methoxy carbonyls (BMC) group as substituents on the bipyridyl ring for complexes **5** and **7**.

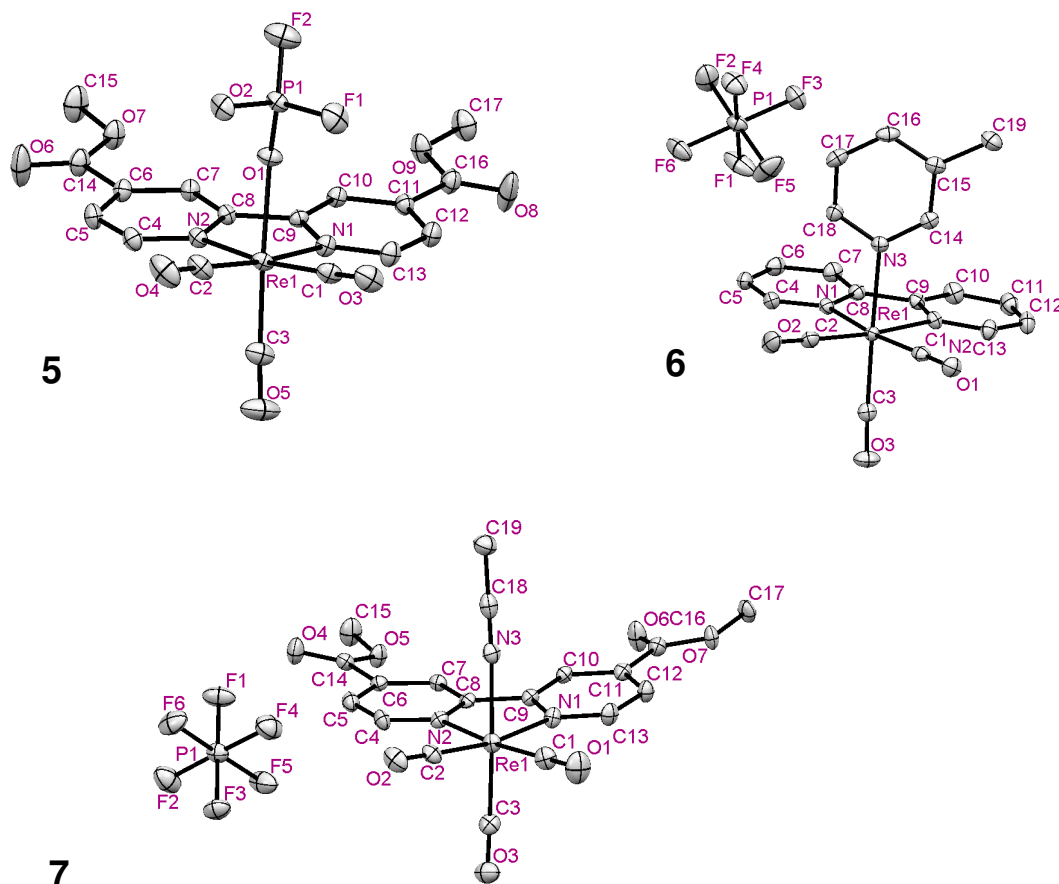


Figure 6. Molecular structure of $\text{Re}(\text{CO})_3(5,5\text{'-BMCbpy})(\text{OPF}_2\text{O})$, **5** (top left); $[\text{Re}(\text{CO})_3(\text{bpy})(\text{Pic})][\text{PF}_6]$, **6** (top right); and $[\text{Re}(\text{CO})_3(5,5\text{'-BMCbpy})(\text{NCCH}_3)][\text{PF}_6]$, **7** (bottom). Hydrogen atoms are omitted for clarity. Ellipsoids for the anisotropic displacement parameters are shown at the 50% level.

Refinement indicators were good for all the three complexes (Table 5), and no disorder was showed by any of the structures. $P2_1/c$ was determined as space group of crystallisation for all the complexes; this is a monoclinic crystal system with primitive lattice. The space groups have a two-fold screw axis and a glide plane perpendicular to b , finally an inversion centre is present and therefore $P2_1/c$ is one of the centrosymmetric space groups (Figure 7).

Table 5. Crystallographic data for complexes **5**, **6** and **7**.

	5	6	7
Formula	C ₁₇ H ₁₂ N ₂ O ₉ F ₂ ReP	C ₁₉ H ₁₅ F ₆ N ₃ O ₃ PRe	C ₁₉ H ₁₅ F ₆ N ₃ O ₇ PRe
<i>M</i>	643.46	664.51	728.51
<i>a</i> /Å	12.9895(5)	13.1006(4)	10.3451(5)
<i>b</i> /Å	12.1469(2)	11.27050(13)	14.1259(5)
<i>c</i> /Å	14.2301(11)	14.57937(17)	16.5788(9)
<i>α</i> /deg	90.00	90.00	90.00
<i>β</i> /deg	113.667(7)	98.5041(14)	101.453(6)
<i>γ</i> /deg	90.00	90.00	90.00
<i>V</i> /Å ³	2056.44(18)	2128.98(7)	1982.84(4)
T/K	110(2)	110(2)	110(2)
Space group	P2 ₁ /c	P2 ₁ /c	P2 ₁ /c
Crystal system	monoclinic	monoclinic	monoclinic
<i>Z</i>	4	4	4
Reflns measd	23575	20436	9564
Reflns indep	8049	6851	4781
<i>R</i> _{int}	0.0364	0.0267	0.0226
Final <i>R</i> [<i>I</i> > 2σ(<i>I</i>)]	<i>R</i> ₁ = 0.0289	<i>R</i> ₁ = 0.0200	<i>R</i> ₁ = 0.0263
	w <i>R</i> ₂ = 0.0647	w <i>R</i> ₂ = 0.0405	w <i>R</i> ₂ = 0.0578
Goof on <i>F</i> ²	1.055	1.039	1.041

Complex **5** is neutral while complexes **6** and **7** are cationic with PF₆⁻ as counter ion. The shortest interaction between anion and cation occurs at 2.639 Å for complex **6** and at 2.609 Å for complex **7**.

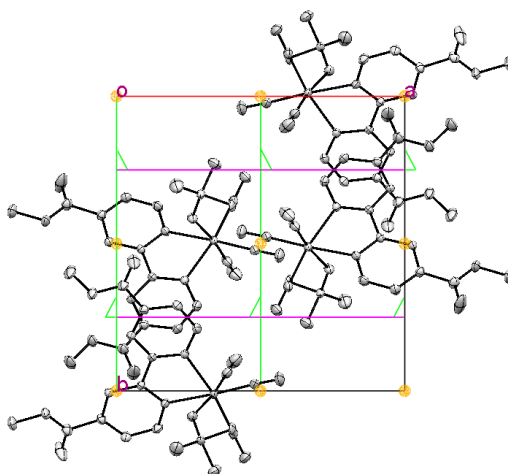


Figure 7. View of the crystal packing in P2₁/c for complex **5** along *b* with representation of the symmetry elements. Green: Two-fold screw axes; Pink: Glide planes perpendicular to *b*; Light orange: Inversion centers.

Selected bond distances and angles are listed in Table 5; the two ionic complexes **6** and **7** exhibit very similar bond lengths with the exception of the Re-X distance, where X is the picoline nitrogen for **6** and the acetonitrile nitrogen for complex **7**. This bond length is significantly shorter for complex **7** but consistent with what was previously reported for Re-NC(CH₃) complexes.¹² Bond distances for complex **5** are also similar to the one observed for complexes **6** and **7** apart from the Re-C_{Ax} bond which is the shortest for complex **5**, but the longest for the other two complexes. This could be explained assuming a smaller *trans*-effect exercised by the difluorophosphate ligand compared with the picoline or acetonitrile ligands. The Re-N_(bpy) bond lengths for **5-7** are comparable with Re-sp² nitrogen bond lengths (2.14 to 2.18 Å),¹³ however Re-N_(picoline) (2.2081(18) Å) is longer compared with the other ones in this analysis and with the one reported in the literature for the complex *cis*-[ReCl(picoline)(en)₂]²⁺.¹⁴ Such elongated bond length has been observed for the complex [H₄Re₃(CO)₉L][LH]⁺ (L = α-picoline) which shows a Re-N distance of 2.235(15) Å.¹⁵

Table 6. Selected Bond Lengths (Å) and Angles (deg) for complexes **5**, **6** and **7**.

Complex	5 (X=O)	6 (X=N)	7 (X=N)
Re-N1	2.172(2)	2.1730(17)	2.176(3)
Re-N2	2.148(2)	2.1672(17)	2.168(3)
Re-C _{Ax}	1.903(3)	1.933(2)	1.930(4)
Re-C _{Eq}	1.930(3)	1.918(2)	1.918(4)
Re-C _{Eq}	1.921(3)	1.917(2)	1.924(4)
Re-X(ligand)	2.1541(19)	2.2081(18)	2.120(4)
N1-Re-N2	74.76(8)	75.14(7)	75.48(11)
N1-Re-X	78.66(8)	84.15(6)	83.21(12)
N2-Re-X	79.23(8)	85.74(7)	81.64(12)

While N1-Re-N2 angles are very similar for all the three compounds, N1-Re-X and N2-Re-X angles are considerably smaller for complex **5** than for complexes **6** and **7**. The structure of **5** appears as a strongly distorted octahedron. Crystallographic data¹⁶ previously reported for the $\text{Re}(\text{CO})_3(\text{bpy})(\text{OPF}_2\text{O})$ complex are comparable to those observed for complex **5** with the only exception of the Re-O bond which is 0.03 Å shorter in our studies confirming stronger interaction with the rhenium centre.

The O-Re-P angle is also significantly different; it was observed to be 133.2(9) Å for the $\text{Re}(\text{CO})_3(\text{bpy})(\text{OPF}_2\text{O})$ complex and it is 138.98(12) for complex **5** suggesting a stronger steric repulsion.¹⁶

Overlay of the structures **5** and **7** (Figure 8) highlighted the different orientation of one of the methoxy-carbonyl group on the bipyridyl ring for complex **7** (green, COOCH_3 on the right). Short interactions between one H on the methyl group with the anion PF_6^- in the crystal packing blocked the COOCH_3 arm and consequently it is rotated about 90° compared to the same fragment in structure **5** (red).

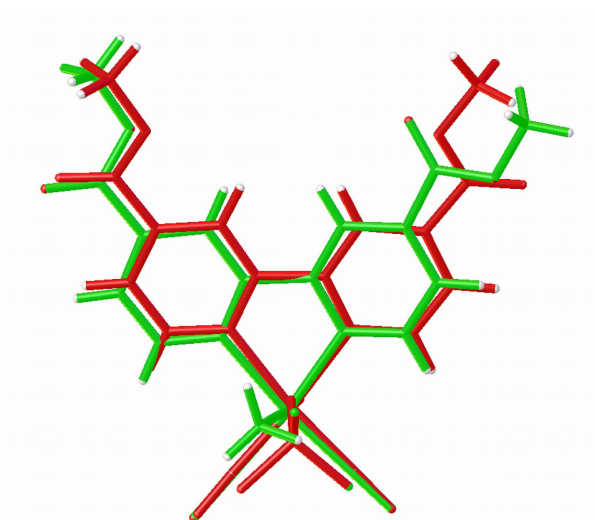


Figure 8. Overlay of Re, O1, O2 and O3 atoms of the carbonyl ligands of $\text{Re}(\text{CO})_3(4,4\text{'-BMCbpy})(\text{OPF}_2\text{O})$ **5**, (red) and $[\text{Re}(\text{CO})_3(4,4\text{'-BMCbpy})(\text{NCCH}_3)][\text{PF}_6]$ **7**, (green), showing the different orientation of the two COOCH_3 ligands.

8 SUMMARY AND CONCLUSIONS

The aim of this thesis was the investigation of the photochemical behavior of Rh and Ru phosphine complexes in the presence of a variety of bonds (C-H, C-F, B-H, B-B, Si-H) to determine new mechanistic routes in those processes. The full characterization and isolation of new compounds has been presented along with mechanistic findings.

8.1 C-F

1. Cleavage of C-F bonds was achieved at rhodium metal centres. Both $\text{CpRh}(\text{PMe}_3)(\text{C}_2\text{H}_4)$ and $\text{Tp}^*\text{Rh}(\text{PMe}_3)_2$ has been demonstrated to act as good C-F activators. While the former gives a cyclometallation product in the presence of 4-substituted tetrafluoropyridines (OMe, NMe₂), the latter proceeds through intermolecular oxidative addition to form the Rh-F analogue in its photochemical reaction with $\text{C}_5\text{F}_5\text{N}$. Upon scaling up the reaction, crystals were obtained; the crystal structure demonstrated that the $\text{Tp}^*\text{Rh-F}$ complex acts as trap for HF since a molecule of HF was found coordinated to the fluoride, held by hydrogen bonding. In contrast, the reaction of the $\text{CpRh}(\text{PMe}_3)(\text{C}_2\text{H}_4)$ complex in the presence of $\text{C}_5\text{F}_5\text{N}$ allowed isolation of the $\eta^2\text{-C}_2, \text{C}_3$ -pyridine complex and no C-F activation was detected upon photochemical or thermal conditions. C-F activation at Tp^*Rh centres is regioselective for the ortho position whereas the $\text{CpRh}(\text{PMe}_3)$ fragment inserts into the C-F bond at the meta position of the 4-substituted tetrafluoropyridines. Mechanistic studies suggested that a five membered ring is preferred to a six membered and that cyclometallation takes place only if the substituent in four-position contains a primary carbon at the β -position. From these results we can conclude that the nature of the ligands around the metal centre is fundamental in determining one coordination mode rather than the other, while Cp allows η^2 coordination in the presence of $\text{C}_5\text{F}_5\text{N}$, Tp^* directs intermolecular oxidative addition; this is probably due to the different steric bulk of the two ligands.

8.2 B-H

1. Irradiation of the complex $\text{Ru}(\text{dppe})_2\text{H}_2$ in the presence of substrates containing a B-H bond (HBpin and HBcat) leads to the formation of new Ru-boryl *cis*- $\text{Ru}(\text{dppe})_2\text{H}(\text{Bpin})$ and *cis*- $\text{Ru}(\text{dppe})_2\text{H}(\text{Bcat})$ compounds along with byproducts. The species were found to be unstable under vacuum conditions and therefore isolation and purification was not achieved; nevertheless comparison of the NMR data and the coupling constants with those of ruthenium boryl complexes previously characterized crystallographically supports our hypothesis of oxidative addition of the B-H bond. The broadness of one of the peaks in $^{31}\text{P}\{^1\text{H}\}$ NMR spectrum for both the complexes *cis* $\text{Ru}(\text{dppe})_2\text{H}(\text{Bpin})$ and *cis* $\text{Ru}(\text{dppe})_2\text{H}(\text{Bcat})$ strongly suggests a phosphorus trans to boron.
2. In contrast, photochemical reaction of complexes $\text{Tp}^*\text{Rh}(\text{PMe}_3)\text{H}_2$ and $\text{Tp}^*\text{Rh}(\text{CNneopentyl})(\eta^2\text{-PhN=C=N-neopentyl})$ in neat HBpin leads to the formation of two stable Rh-boryl complexes fully characterized by multinuclear NMR spectroscopy and mass spectrometry. The structure of $\text{Tp}^*\text{Rh}(\text{PMe}_3)\text{H}(\text{Bpin})$ was determined crystallographically. The Rh-B bond was found to be very stable even at high temperature (140°C). Surprisingly the activation of the B-H bond occurs in preference to C-H activation of the alkyl groups on the substituent for both the starting complexes.
3. Interestingly, the complex $\text{CpRh}(\text{C}_2\text{H}_4)_2$ reacts in the presence of HBpin and B_2pin_2 under photochemical conditions to extrude one ethylene and to form the corresponding boron containing adduct characterized by NMR spectroscopy and mass spectrometry. No crystals were obtained because of the instability of the products in solution (few hours). The lack of structural information made the distinction between a σ -coordination and an oxidative addition path for the reaction with HBpin impossible. Nevertheless preliminary calculation suggested η^2 coordination as favorite. The catalytic ability of the system was tested in the presence of heptane and the functionalized heptyl-Bpin detected by GC-MS.
4. Three different $\text{CpRh}(\text{PR}_3)(\text{C}_2\text{H}_4)$, ($\text{R} = \text{PMe}_3, \text{PMe}_2\text{Ph}, \text{PPh}_3$) complexes were photolysed in hexane solution in the presence of $\text{H}_2\text{BN}(\text{iPr})_2$. The reactions

cleanly formed the B-H activated products $\text{CpRh}(\text{PR}_3)\text{H}(\text{BHN}(i\text{Pr})_2)$ which were characterized by multinuclear NMR spectroscopy. The Rh centres did not show any reactivity toward N coordination or C-H activation of the $i\text{Pr}$ groups.

8.3 Si-H

1. Irradiation of $\text{Tp}^*\text{Rh}(\text{PMe}_3)\text{H}_2$ and $\text{Tp}^*\text{Rh}(\text{CNneopentyl})(\eta^2\text{-PhN}=\text{C}=\text{Nneopentyl})$ in the presence of silanes (Et_2SiH_2 , Et_3SiH , PhSiH_3) was also investigated. The reactions were selective for the activation of the Si-H bond; new Rh-silyl complexes were formed and characterized spectroscopically. The crystal structure for the $\text{Tp}^*\text{Rh}(\text{PMe}_3)\text{H}(\text{Et}_2\text{SiH})$ was determined, no residual Si...H interaction were found.

8.4 LFP

1. Laser flash photolysis of the complexes **Ru1**, *cis*- $[\text{Ru}((R,R)\text{-Me-BPE})_2(\text{H})_2]$, **Ru2**, *cis*- $[\text{Ru}((R,R)\text{-Me-DuPHOS})_2(\text{H})_2]$ and **Ru3**, *cis*- $[\text{Ru}((R,R)\text{-}^i\text{Pr-BPE})_2(\text{H})_2]$ demonstrates that the primary photoproducts are the four-coordinate complexes $\text{Ru}(\text{PP})_2$. Each of the complexes $\text{Ru}(\text{PP})_2$ exhibits multibands UV-vis spectra which are characteristic of a structure close to square planar. A long wavelength band is included in all the spectra assigned to a $M(d_z^2) - M(p_z)$ transition. The reactivity of the complexes decreased in the order **Ru1** > **Ru2** > **Ru3**. The rates of their reactions with H_2 , D_2 , HBpin, and PhSiH_3 were measured by transient kinetics. Rate constants are significantly faster for **Ru1** than for **Ru2** and follow the substrate order $\text{H}_2 > \text{D}_2 > \text{PhSiH}_3 > \text{HBpin}$. The rate constant for reaction of **Ru3** with H_2 span a factor 100000 from that of **Ru1**.

9 Future work

- The isolation of the B-H activation products in reactions of both $\text{Ru}(\text{dppe})_2\text{H}_2$ and $\text{CpRh}(\text{C}_2\text{H}_4)_2$ complexes. Conversion to metal-boryl halide could be an option to improve the stability and allow isolation. IR spectroscopy of the Ru- and Rh-boryl complexes looking for the B-H stretch and same analysis in the presence of deuterated HBpin could also be performed.

- Further investigation of the reactions of $\text{CpRh}(\text{PR}_3)(\text{C}_2\text{H}_4)$ complexes with the amino-borane substrate in the presence of hydride abstractor compound to see the next step after oxidative addition in coordination modes. Structural determination of the B-H oxidative addition products.
- Follow up the catalytic potential towards the functionalization of alkanes in the presence of HBpin shown by the $\text{CpRh}(\text{C}_2\text{H}_4)_2$ system. The reaction conditions need to be optimized and yields quantified.
- Carry out kinetic experiments with complex $\Lambda\text{-}R,R\text{-Ru3H}_2$ and different quenching ligands by a rapid scan UV-spectrometer set up with a flash lamp.

I. Appendix to chapter seven

I.II. Crystals and their internal structure

A crystal is a highly ordered structure, where the assembly of identical molecules which form it, are repeated by 3D translation. The repeating building-block in three dimensions is called a unit cell and it is defined by 3 unit cell lengths (a, b, c), and 3 angles (α, β, γ), (Figure 1, a). In a simplified manner (for a primitive lattice) each unit cell contains the equivalent of one *lattice point*; replacing each repeating unit with a lattice point leads to a *crystal lattice* (Figure 1, b). In the crystal lattice every point is generated by the translational symmetry of the starting point such as the view in a given direction from each point is identical with the view in the same direction from any other lattice point.

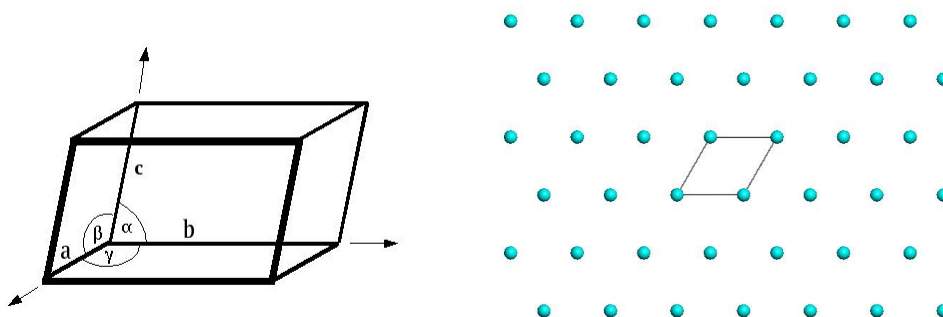


Figure 1. (a) Representation of a unit cell where a, b, c are the unit cell lengths and α, β, γ the angles.¹ (b) Schematic representation of a crystal lattice where every point is a lattice point.²

The unit cell usually carries internal symmetry, the smallest part of the unit cell to which symmetry elements are applied is called asymmetric unit. The internal symmetry characterises the space group of the crystal, 230 possible combinations exists, and therefore there are 230 space groups allowed in the solid state.³ A space group arises from the different allowed combinations between crystal system, lattice centering, point groups and symmetry:

- The lengths and angles of the unit cell are restricted to certain values depending on the symmetry. Crystals can have rotational symmetry of only 2, 3,

4 and 6. Based on these restrictions, there are seven types of crystal symmetry called the seven crystal systems (Table 1).

Table 1. Crystal systems with point group symmetry restrictions and cell-dimensions restrictions.

Crystal system	Rotational symmetry elements	Restriction on unit cell
Triclinic	none	none
Monoclinic	One two-fold rotation axis.	$\alpha = \gamma = 90^\circ$
Orthorhombic	Three two-fold rotation axes.	$\alpha = \beta = \gamma = 90^\circ$
Tetragonal	One four-fold rotation axis.	$a = b$ $\alpha = \beta = \gamma = 90^\circ$
Rhombohedral	One three-fold rotation axis.	$a = b = c$ $\alpha = \beta = \gamma \neq 90^\circ$
Hexagonal	One six-fold-rotation axis.	$a = b, \alpha = \beta = 90^\circ \gamma = 120^\circ$
Cubic	Four three-fold rotation axes.	$a = b = c$ $\alpha = \beta = \gamma = 90^\circ$

- A crystal system can be primitive, *P*, where there is a lattice point only at the eight corners of the unit cell; face centred *F* with lattice points at the centre of all the faces; face centred *A*, *B* and *C*, if only one pairs of opposite faces has lattice points. Finally body centred, *I*, where there is a lattice point at the very centre of the unit cell. A combination between the seven crystal systems and the lattice centring gives the 14 *Bravais lattices*.
- The sum of the 32 point groups, which describes in term of symmetry an isolate object, plus translational symmetry (e.g. simple translation, screw axes and glide planes) gives as result the space group. A space group may be considered as the result of operation that converts the asymmetric unit into an infinitely extending pattern (crystal lattice).

I.III. X-ray in crystallography and diffraction

In order to “see” a molecular structure at atomic resolution we need to use radiation comparable or smaller than the distance between atoms, and considering that a C-H bond is $\sim 1.1 \text{ \AA}$, X-rays produce the suitable wavelength (0.1 to 100 \AA) for this type of investigation.

Figure 2 shows the electromagnetic spectrum; high frequency radiation such as X-rays have shorter wavelength and therefore higher energy. X-rays are scattered by the electrons in the atoms; upon interaction with the electric component of the beam, electrons start to oscillate behaving as a source of radiation with the same wavelength as that of the incident X-ray.

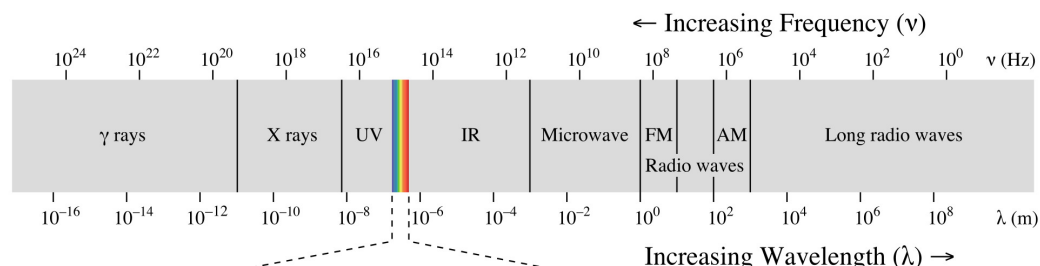
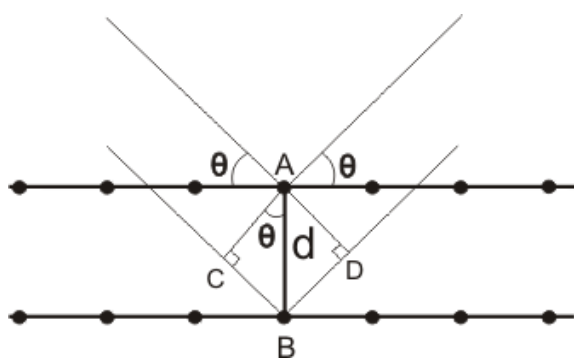


Figure 2. Electromagnetic spectrum of light.⁴

Scattering by a single molecule is too weak to be detected and the high energy of X-rays would degrade the molecule before a meaningful scattering pattern can be recorded. The use of crystals solves this problem, in fact the scattering of many molecules present in the crystalline sample is amplified by constructive interference and the damage of a small proportion of the molecules by the ionizing radiation can be accepted. Furthermore, no lenses can focus such high energy electromagnetic radiation and recombine it physically to form an image; therefore the position and intensity of the scattered rays are recorded by a detector (with the unavoidable loss of the phase information). An image is then created mathematically as the result of calculation carried out on a time-averaged electron density map where atomic positions are locations of electron density, and concentration of electron density distinguishes the atoms. The need to split the process into two parts (recording the X-ray pattern and

recombining it by maths) lead to the loss of some information; since intensity is proportional to the square of wave amplitude, this information is retained while relative phases are lost. To obtain a 3D image of the molecules, position, amplitude and phase for every reflection need to be known. The electron density map cannot be computed by a Fourier series without knowing the phase. The different methods for solving the phase problem are based on estimating the position of some of the atoms to obtain approximate values for the phases; improvement of the accuracy of the phase is achieved at a later stage during refinement. Only the asymmetric unit is refined since the rest of the molecules in the unit cell are related by crystallographic symmetry. Direct methods and the Patterson function are the two methods used to get an estimate of the phases in small molecule X-ray crystallography.

Diffraction from the crystal produces a scattering pattern which is the result of the scattering average unit cell, but only sampled at discrete points at angles when Bragg's law is fulfilled. Diffraction maxima occur when the distance between imaginary planes of atoms is such that paths from successive planes differ by an integral number of wavelengths. The scattered X-rays then interfere constructively and produce a reflection (Figure 3).



$$n\lambda = 2d \sin\theta$$

n = integer number
 λ = wavelength of radiation
 d = perpendicular space between the lattice planes
 θ = complement of the angle of incidence.

Figure 3. (Left) Geometric representation of Bragg's law; (Right) Bragg's law.

Miller indices (h,k,l), classify every allowed diffracted beam (or every reflection) from the origin (0,0,0); they increase in number as the distance from the centre increases. The Miller indices specify a single reflection and correspond to the set of planes that slice the unit cell in different directions (Figure 4). The three

integers are needed to specify the orientation of the planes with respect to the unit cell dimensions (a, b, c).

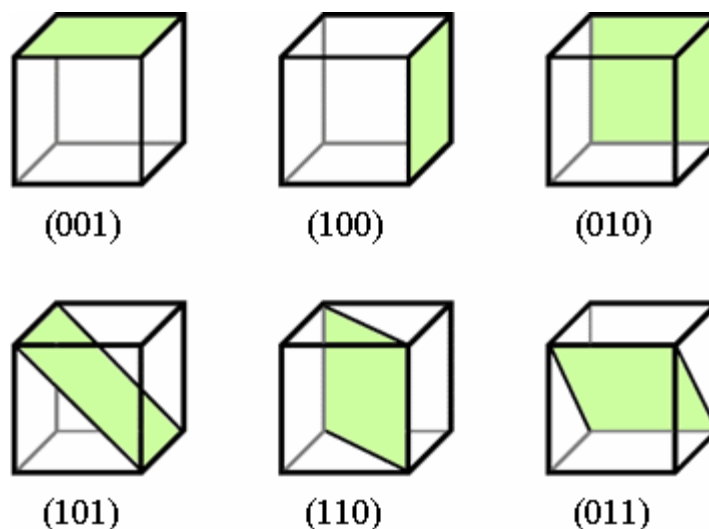


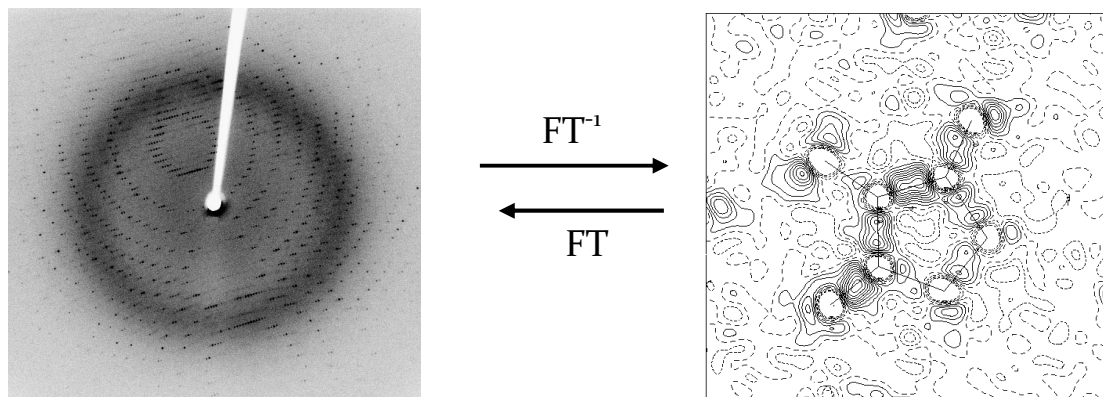
Figure 4. Miller indices in cubic crystals.

A crystal lattice and its diffraction pattern are geometrically related in a reciprocal (or more intuitively should be said “inverse”) way, such that widely spaced reflections are observed for unit cells with small dimensions and *vice versa*. For the same reason, reflections closer to the origin will carry less detailed information compared with reflections at higher angle, as high order reflections will slice the unit cell into more parts. Every diffracted beam accounts for contributions from each bit of the structure and it is mathematically described by the structure factor F . The level of details obtained depends on the resolution. The resolution is the process of distinguish individual parts of objects when examined with a radiation. For small molecules the major of X-ray structures are determined to a resolution of 0.8 – 1.0 Å, each atom therefore can be fairly distinguished.

The conversion of a diffraction pattern to an image in real space (full 3D electron density of the unit cell) can be achieved using a reverse Fourier transform (Scheme 1) where each structure factor (F_{hkl}) contains amplitude, position and phase information (Equation 1; FT^{-1}). The intensity and position of

every reflection are measured experimentally while the phases must be calculated with any of the available methods.

The forward Fourier transform (Equation 2; FT) of the electron density is the diffraction pattern, hence, once the electron density model has been built a calculated diffraction pattern can be created to improve the phases and validate the crystallographic process (Scheme 1).



Scheme 1. Schematic representation of the use of the Fourier Transform in crystal structure determination. The two pictures are not related to each other.⁵

$$F_{(hkl)} = \sum f_j(\theta) \exp[2\pi i (hx_j + ky_j + lz_j)] \quad (\text{FT})$$

Equation 1.

$$\rho_{(xyz)} = 1/V \sum_{\text{All } h,k,l} |F_{(hkl)}| \exp[-2\pi i (hx + ky + lz)] \quad (\text{FT}^{-1})$$

Equation 2.

Finally, materials commonly used to generate X-rays are copper and molybdenum with wavelengths of 1.54 Å and 0.71 Å, respectively. These metal targets are bombarded with electrons to cause electrons from core orbitals to be ejected and to be replaced by electrons from higher energy orbitals. The energy released from this process cause emission of radiation from where X-rays are generated. A number of devices between the source and the detector (monochromator, collimators and mirrors) will improve the beam quality. If a much more intense X-ray beam is needed, synchrotron radiations are available

to collect X-ray diffraction data. Figure 5 shows a schematic flowchart with all the steps needed during a crystal structure determination, every step will be briefly analysed.

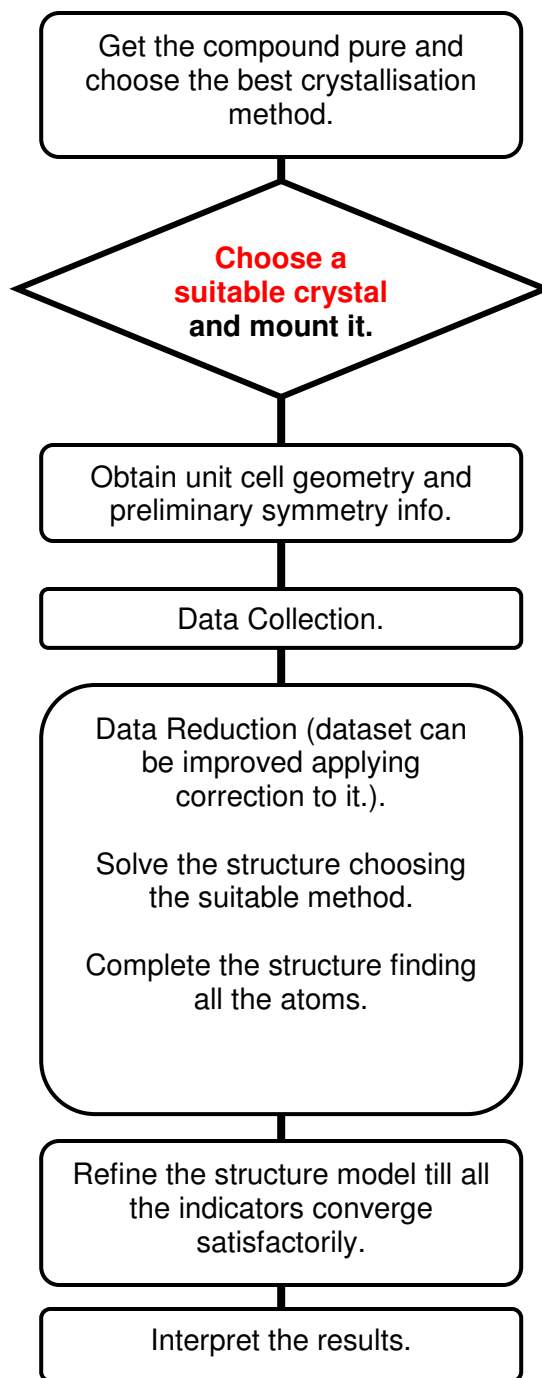


Figure 5. Flowchart for the steps of a crystal structure determination.

I.IV. Purification and crystal growth.

Once the desired compound has been identified and characterised in solution, the first step in order to get crystals is crystallisation, a process which is not always successful. An initial bulk recrystallization of a substance can commonly be insufficient to obtain single crystals for XRD and therefore, different methods of recrystallization may need to be employed.

Solution methods with careful choice of solvents are commonly used, as well as slow evaporation of solvent and slow cooling. The choice of the solvent is fundamental. It needs to be kept in mind that “like dissolves like”, e.g. polar compounds dissolved in polar solvents have to be layered with non polar solvents. From my experience benzene is a good solvent for crystallisation as well as hexane even though long alkyl chains are discouraged since they might cause disorder in the lattice. However, every compound is unique and generalising is not a good rule for growing crystals. Combinations of solvents need to be tested, with regard to the physical and chemical properties of the substance to be crystallised. Crystal growth can be time consuming. Crystallisation is the sum of three different stages controlled by kinetic and thermodynamic factors: nucleation, growth and cessation of growth.

1. *Nucleation*: nucleation is the initial process and the most critical. Enthalpy and entropy play against each other in this step, aggregation of molecules to form nuclei is in fact entropically disfavoured and the gain in enthalpy due to initial aggregation is small. Therefore the “potential” crystal needs to overcome a free energy barrier in order to grow. The use of a saturated solution is the way to reach the top of the energetic hill and eventually start the descent to the formation of ordered crystals. There are two different types of nucleation, homogeneous and heterogeneous. The first one involves just the same species participating in the process while in the latter; it is the surface of particles such as dust that favour the crystallisation process.

2. *Growth*: once the nucleation has happened, the second step is the growth phase, a process that is thermodynamically favored. The growth occurs when there is not enough energy for new nuclei to form but there is a high

compound concentration that helps the crystal in the growth process (metastable phase).

3. *Cessation of growth*: no more molecules are added to the crystals. Two factors influence this stage: no more compound left or introduction of impurities which make the process thermodynamically unfavourable.

Listed below are some of the common crystallisation methods we perform in our lab to get suitable crystals of organometallic compounds.

- **Slow evaporation of solvent.**

Slow evaporation is one of the most used and easiest methods for crystallisation of organometallic compounds. It does not always give the best quality crystals, slow evaporation might in fact produce crystals stuck to each other since the crystallisation starts only when little solvent is left. Crystals might also grow when stuck to the vessel wall, making it harder to get the crystal without damaging it.

- **Solvent layering.**

The compound is dissolved in a solvent where it is soluble and layered with another one where it appears insoluble. It is essential not to physically disturb the vessel for at least more than a week in order to get good size crystals.

- **Slow cooling.**

The crystals are formed very slowly; therefore the cooling time needs to be reduced. There are different ways of achieving a reduction in cooling time, placing the vessel in another container can help as well as adding some insulating protection. Very often this method is combined with other ones, solvent layering/slow cooling is quite usual.

These are just a few of the methods that can be used for growing crystals; vapour diffusion, sublimation, thermal gradient and many more could also work.

I.V. Choose a suitable crystal

The crystal must be a single one, where all the unit cells are identical and aligned in the same direction. In reality all the crystals have imperfections; the smallest is the “mosaic spread” (range of misalignment of unit cells), the biggest

is the chance to get a well diffracting single crystal. The first check takes place under the microscope, where the crystallographer looks for regular polyhedral shapes with well defined edges; a microscope with a polariser also helps in choosing the right crystal. When dealing with air-sensitive compounds it is vital to use an argon atmosphere to prevent decomposition. Once the crystal is coated with oil is mostly safe, unless it is of extreme air sensitivity where special manipulations are required. The crystal is “fished” on a loop and the loop mounted on a goniometer head which allows the crystal to be centred in the X-ray beam. The goniometer head is positioned between the X-ray source and the detector and allow the crystal to be rotated in three directions (ϕ , ω , χ) during data-collection (Figure 6). The detector can also rotate (θ , Figure 6) (four-circle diffractometer).

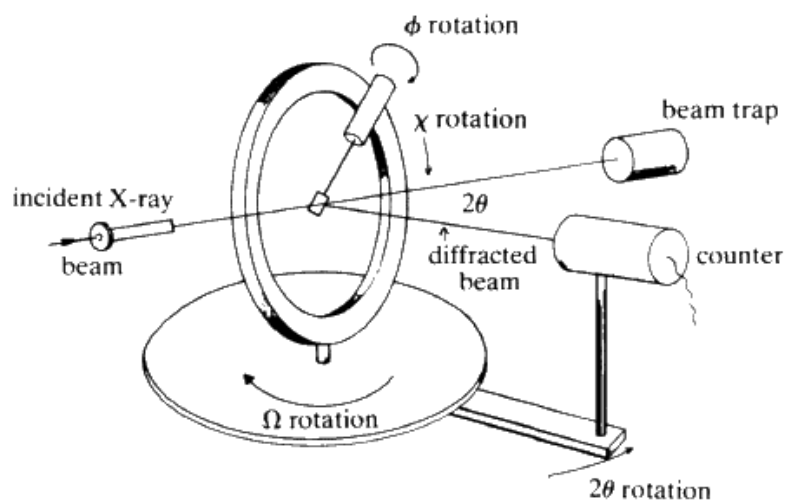


Figure 6. Schematic diagram of a four circle diffractometer.⁶

Before moving to the next step of the process, a “still image” of the crystal is acquired in order to get an idea about the quality: if the spots are well separated, there are no signs of twinning, and the crystal diffracts to a satisfactory angle ($> 50^\circ$), it is worth performing a unit cell run.

I.VI. Obtaining unit cell geometry and preliminary symmetry information

Using a diffractometer equipped with an area detector gives the possibility of obtaining information about unit cell and symmetry for the crystal in few minutes. The quality of the diffraction pattern can be assessed from the pre-experiment and considering the internal symmetry a data collection strategy will be suggested by the software. The purpose of an ideal data collection is to obtain a data set that is 100% complete, with high quality data to as high resolution as possible. This is clearly not achievable in reality, since the quality of the data depends on many factors (diffraction resolution, mosaicity, internal order, internal symmetry and noise). A good agreement (> 80%) between the reflections observed experimentally during pre-experiment and those fitted in the chosen unit cell will be indicative of obtaining a good quality data set for the full experiment.

I.VII. Data acquisition

A data collection can take few hours or maybe a day, depending on the quality of the crystal, on acquisition of redundant data, on the maximum Bragg angle to be measured and on the space group. The crystallographer must take some decisions about the intended strategy; every case is different, but mostly a data set need to have completeness as closer as possible to 100%, the Bragg angle measured has to be greater than 50° (*circa* 0.8 \AA) and the signal to noise ratio, $I/\sigma(I)$, greater than 15. Other parameters can be varied with respect to the individual case. The result of the data acquisition is a set of reflections, each with different Miller indices (hkl) and recorded intensities (I).

I.VIII. Data reduction, solving the structure and refinement

The frames collected are processed in this step. All the reflections are measured and their intensity and positions recorded. Absorption correction is also carried out in order to improve the quality of the data, each reflection will

be affected differently by X-ray absorption since the latter vary with the rotation of the crystal. At this stage any systematic error occurred during data acquisition, will be also treated. The outcome of the data reduction is therefore a unique set of data where all the symmetry-related reflections are merged and averaged. The intensities are estimated along with the standard uncertainty and converted to structure factors. The right space group is also determined.

One measure of how well the data merge together is given by the term R_{int} . Global data quality check starts together with data reduction; in fact R_{int} below 0.1 is a satisfactory value for starting the refinement process. R_{int} is defined as:

$$R_{int} = \frac{\sum [\sum |F_j^2 - \langle F \rangle|]}{\sum [\sum F_j^2]}$$

Equation 3.

where the inner sums are over the symmetry-equivalent reflections and the outer sums are over the unique hkl data (Equation 3). At this stage the “phase problem” becomes relevant. As already mentioned, since it is not possible to build a 3D image of the electron density without information about the phase, the phase term in the Fourier transform cannot be solved. Estimating the position of some of the atoms (especially those with more electrons) is the way of solving the phase problem. Obtaining approximate values for the phases will allow generation of a set of different structure factors and comparison of these with the experimental will optimize the accuracy of the phase at a later stage during refinement. The different methods for solving the phase problem are based on this basic concept.

Two of the commonly used methods to solve the “phase problem” for small molecules are Direct methods and Patterson methods. Direct methods work better for structures with heavy atoms, while Patterson is better used for structures where atoms have equal number of electrons. While the first one attempts to work out the phases of reflections considering just the most intense diffracted beams (based on the conditions that electron density must be or positive or zero everywhere only certain values of the phases are allowed), the

second build a map of electron density peaks, with the peaks representing the end points of vectors between atoms and having common origin.

The refinement (“playing” with positions and vibrations) can be started once an approximate model has been built, and it consists in systematically varying the atomic parameters in order to get the best agreement between the observed structure factors F_0 and the calculated ones, F_C . While varying the F_C , F_0 remains fixed, and the aim is to minimize the sum of the squares of the deviations of the experimentally observed values from their respective calculated (Least Squares method). Least Square refinement can be done on F (Equation 4) or on F^2 (Equation 5), the latter becoming nowadays more popular and important. The sums are taken over h,k,l.

$$\sum w (|F_0| - |F_C|)^2$$

Equation 4.

$$\sum w (F_0^2 - F_C^2)^2 \quad w = 1/\sigma^2 (F_0^2)$$

Equation 5.

The calculations needs to be iterated until the change in the parameters are insignificant and convergence is achieved. This is because the linear approximation improves as the final solution is approached. The parameters that need to be refined include the coordinates of the model (x,y,z of every atom), the displacement parameters (isotropic and anisotropic), occupancies (if more than one conformation is seen) and twin fraction (if twinning is present). Refinement also accelerates with the introduction of constraints and restraints, which means that fewer variables to be refined. Hydrogen atoms, for instance, are usually placed in calculated positions (restrained), in fact the information carried by the hydrogen parameters usually has large errors because of their weak contribution to the diffraction. As the refinement process converges, its correctness must be checked. A consistent number of statistical parameters exist in order to produce a correct structure determination.

R factors (discrepancy indices, R and $wR2$) are useful but not definitive indices of correctness. As shown in Equation 6 and Equation 7 residual factors are an assessment of the agreement between the calculated diffraction pattern and the observed one.

The $wR2$ is a discrepancy factor where the weights are included and the calculation is carried out over F^2 instead than F . If the data set is good, small molecules usually refine to R values of 0.05 or even lower, while $wR2$ will be roughly double the value of R . The sums are taken over h,k,l .

$$R = \frac{\sum | |F_0| - |F_c| |}{\sum |F_0|}$$

Equation 6.

$$wR2 = \left[\frac{\sum w(F_0^2 - F_c^2)^2}{\sum w(F_0^2)^2} \right]^{1/2}$$

Equation 7.

Goodness of fit also shows how reliable the standard deviations of the positional and displacement parameters of the atoms really are and for a correct weighting scheme it should be close to unity. Finally no fluctuations should be present on the electron density map and no anomalies in the geometry of the structure.

II. LIST OF ABBREVIATIONS

Chemicals

HBpin	pinacol borane, 4,4,5,5-tetramethyl- 1,3,2,-dioxaborolane
B ₂ pin ₂	bis(pinacolato)diborane, 4,4,4',4',5,5,5',5'-octamethyl-2,2'-bi-1,3,2- dioxaborolane
B ₂ pin ₃	(μ -2-pinacolato- <i>O,O'</i>)-bis(pinacolato- <i>O,O'</i>)diboron
Cat	catecholato, 1,2-O ₂ C ₆ H ₄
Me	methyl, CH ₃
Et	ethyl, CH ₂ CH ₃
<i>i</i> Pr	iso-propyl, CH(CH ₃) ₂
Cp	cyclopentadienyl, η^5 -C ₅ H ₅
Cp*	pentamethylcyclopentadienyl, η^5 -C ₅ Me ₅
Ph	phenyl, C ₆ H ₅
Dppe	diphenylphosphinoethane
Depe	diethylphosphinoethane
Dmpe	dimethylphosphinoethane
BPE	{C ₂ H ₄ P(2 <i>R</i> ,5 <i>R</i> -Me ₂ C ₄ H ₆)}
DuPhos	{PhP(2 <i>R</i> ,5 <i>R</i> -Me ₂ C ₄ H ₆)}
<i>i</i> PrBPE	{(C ₂ H ₄)P(2 <i>R</i> ,5 <i>R</i> - <i>i</i> Pr ₂ C ₄ H ₆)}
IMes	2,5-Mes ₂ -N ₂ C ₃ H ₂
IEt ₂ Me ₂	1,3-bis(ethyl)-4,5-dimethylimidazol-2-ylidene
COD	1,5-cyclooctadiene
Ru1H ₂	Λ -[cis-Ru((<i>R,R</i>)-Me-BPE) ₂ (H) ₂]
Ru2H ₂	Λ -[cis-Ru((<i>R,R</i>)-Me-DuPHOS) ₂ (H) ₂]
Ru3H ₂	Λ -[cis-Ru((<i>R,R</i>)- <i>i</i> Pr-BPE) ₂ (H) ₂]
Tp`	tris(2,4 – dimethylpyrazolyl) borate

CDI	carbodiimide, η^2 -PhN=C=N-neopentyl
Pic	picoline

Units

Å	ångström
atm	atmosphere
Hz	hertz
h	hours
K	kelvin
s	second
J	joule
mol	mole
g	gram
mg	milligram

Spectroscopy

IR	infra red
UV	ultra violet
Vis	visible
LFP	laser flash photolysis
MS	mass spectroscopy
EI	electron impact
LIFDI	liquid injection field desorption/ionization
NMR	nuclear magnetic resonance
COSY	correlation spectroscopy
HMQC	heteronuclear multiple quantum coherence
δ	chemical shift (in ppm)

ppm	parts per million
J	coupling constant
s	singlet
d	doublet
t	triplet
q	quartet
m	multiplet
br	broad
dd	doublet of doublets
ddd	doublet of doublet of doublets
dt	doublet of triplets

Special terms

DFT	density functional theory
KIE	kinetic isotopic effect
MLCT	metal to ligand charge transfer
LMCT	ligand to metal charge transfer
LF	ligand field
FT	fourier transform

III. Bibliography

CHAPTER ONE

- (1) Balzani, V.; Bergamini, G.; Campagna, S.; Puntoriero, F., *Photochemistry and Photophysics of Coordination Compounds I* **2007**, *280*, 1-36.
- (2) Perutz, R. N.; Torres, O.; Vlček, A. J., *Dissociative Photochemistry of Metal Carbonyls in Comprehensive Inorganic Chemistry, in press*, **2012**.
- (3) Campian, M. V.; Perutz, R. N.; Procacci, B.; Thatcher, R. J.; Torres, O.; Whitwood, A. C., *J. Am. Chem. Soc.* **2012**, *134*, 3480-3497.
- (4) Campian, M. V.; Clot, E.; Eisenstein, O.; Helmstedt, U.; Jasim, N.; Perutz, R. N.; Whitwood, A. C.; Williamson, D., *J. Am. Chem. Soc.* **2008**, *130*, 4375-4385.
- (5) Geoffroy, G. L.; Wrighton, M. S., *Organometallic Photochemistry; Academic Press: New York*, **1979**.
- (6) Perutz, R. N.; Turner, J. J., *J. Am. Chem. Soc.* **1975**, *97*, 4791-4800.
- (7) Roberts, D. A.; Geoffroy, G. L., *J. Organomet. Chem.* **1981**, *214*, 221-231.
- (8) Ampt, K. A. M.; Burling, S.; Donald, S. M. A.; Douglas, S.; Duckett, S. B.; Macgregor, S. A.; Perutz, R. N.; Whittlesey, M. K., *J. Am. Chem. Soc.* **2006**, *128*, 7452-7453.
- (9) Baerends, E. J.; Rosa, A., *Coord. Chem. Rev.* **1998**, *177*, 97-125.
- (10) Feldman, J. D.; Peters, J. C.; Tilley, T. D., *Organometallics* **2002**, *21*, 4050-4064.
- (11) Perutz, R. N., *Pure Appl. Chem.* **1998**, *70*, 2211-2220.
- (12) Chrisope, D. R.; Park, K. M.; Schuster, G. B., *J. Am. Chem. Soc.* **1989**, *111*, 6195-6201.
- (13) Janowicz, A. H.; Bergman, R. G., *J. Am. Chem. Soc.* **1983**, *105*, 3929-3939.
- (14) Wax, M. J.; Stryker, J. M.; Buchanan, J. M.; Kovac, C. A.; Bergman, R. G., *J. Am. Chem. Soc.* **1984**, *106*, 1121-1122.
- (15) Hoyano, J. K.; Graham, W. A. G., *J. Am. Chem. Soc.* **1982**, *104*, 3723-3725.
- (16) Hoyano, J. K.; McMaster, A. D.; Graham, W. A. G., *J. Am. Chem. Soc.* **1983**, *105*, 7190-7191.
- (17) Jones, W. D.; Feher, F. J., *Organometallics* **1983**, *2*, 686-687.
- (18) Jones, W. D.; Feher, F. J., *Organometallics* **1983**, *2*, 562-563.
- (19) Jones, W. D.; Feher, F. J., *J. Am. Chem. Soc.* **1984**, *106*, 1650-1663.
- (20) Jones, W. D.; Feher, F. J., *Inorg. Chem.* **1984**, *23*, 2376-2388.
- (21) Jones, W. D.; Feher, F. J., *J. Am. Chem. Soc.* **1985**, *107*, 620-631.

- (22) Haddleton, D. M.; Mccamley, A.; Perutz, R. N., *J. Am. Chem. Soc.* **1988**, *110*, 1810-1817.
- (23) Rest, A. J.; Whitwell, I.; Graham, W. A. G.; Hoyano, J. K.; McMaster, A. D., *J. Chem. Soc., Chem. Commun.* **1984**, 624-626.
- (24) Rest, A. J.; Whitwell, I.; Graham, W. A. G.; Hoyano, J. K.; McMaster, A. D., *J. Chem. Soc., Dalton Trans.* **1987**, 1181-1190.
- (25) Bloyce, P. E.; Rest, A. J.; Whitwell, I.; Graham, W. A. G.; Holmesmith, R., *J. Chem. Soc., Chem. Commun.* **1988**, 846-848.
- (26) Haddleton, D. M.; Perutz, R. N., *J. Chem. Soc., Chem. Commun.* **1985**, 1372-1373.
- (27) Belt, S. T.; Grevels, F. W.; Klotzbucher, W. E.; Mccamley, A.; Perutz, R. N., *J. Am. Chem. Soc.* **1989**, *111*, 8373-8382.
- (28) Bromberg, S. E.; Lian, T. Q.; Bergman, R. G.; Harris, C. B., *J. Am. Chem. Soc.* **1996**, *118*, 2069-2072.
- (29) Haddleton, D. M.; Perutz, R. N.; Jackson, S. A.; Upmacis, R. K.; Poliakov, M., *J. Organomet. Chem.* **1986**, *311*, C15-C20.
- (30) Weiller, B. H.; Wasserman, E. P.; Bergman, R. G.; Moore, C. B.; Pimentel, G. C., *J. Am. Chem. Soc.* **1989**, *111*, 8288-8290.
- (31) Jones, W. D., *Acc. Chem. Res.* **2003**, *36*, 140-146.
- (32) Periana, R. A.; Bergman, R. G., *J. Am. Chem. Soc.* **1986**, *108*, 7332-7346.
- (33) Belt, S. T.; Duckett, S. B.; Helliwell, M.; Perutz, R. N., *J. Chem. Soc., Chem. Commun.* **1989**, 928-930.
- (34) Belt, S. T.; Dong, L. Z.; Duckett, S. B.; Jones, W. D.; Partridge, M. G.; Perutz, R. N., *J. Chem. Soc., Chem. Commun.* **1991**, 266-269.
- (35) Crabtree, R. H., *Angew. Chem. Int. Ed.* **1993**, *32*, 789-805.
- (36) Hall, C.; Perutz, R. N., *Chem. Rev.* **1996**, *96*, 3125-3146.
- (37) Lersch, M.; Tilset, M., *Chem. Rev.* **2005**, *105*, 2471-2526.
- (38) Bercaw, J. E.; Chen, G. S.; Labinger, J. A.; Lin, B. L., *Organometallics* **2010**, *29*, 4354-4359.
- (39) Calladine, J. A.; Duckett, S. B.; George, M. W.; Matthews, S. L.; Perutz, R. N.; Torres, O.; Khuong, Q. V., *J. Am. Chem. Soc.* **2011**, *133*, 2303-2310.
- (40) Ruiz, J.; Bentz, P. O.; Mann, B. E.; Spencer, C. M.; Taylor, B. F.; Maitlis, P. M., *J. Chem. Soc., Dalton Trans.* **1987**, 2709-2713.

- (41) Duckett, S. B.; Haddleton, D. M.; Jackson, S. A.; Perutz, R. N.; Poliakoff, M.; Upmacis, R. K., *Organometallics* **1988**, *7*, 1526-1532.
- (42) Duckett, S. B.; Perutz, R. N., *Organometallics* **1992**, *11*, 90-98.
- (43) Brookhart, M.; Grant, B. E.; Lenges, C. P.; Prosenc, M. H.; White, P. S., *Angew. Chem. Int. Ed.* **2000**, *39*, 1676-1679.
- (44) Corey, J. Y., *Chem. Rev.* **2011**, *111*, 863-1071.
- (45) Campian, M. V.; Harris, J. L.; Jasim, N.; Perutz, R. N.; Marder, T. B.; Whitwood, A. C., *Organometallics* **2006**, *25*, 5093-5104.
- (46) Corey, J. Y.; Braddock-Wilking, J., *Chem. Rev.* **1999**, *99*, 175-292.
- (47) Alcaraz, G.; Sabo-Etienne, S., *Coord. Chem. Rev.* **2008**, *252*, 2395-2409.
- (48) Hoyano, J. K.; Elder, M.; Graham, W. A. G., *J. Am. Chem. Soc.* **1969**, *91*, 4568-4569.
- (49) Hartwig, J. F.; He, X. M., *Angew. Chem. Int. Ed.* **1996**, *35*, 315-317.
- (50) Hartwig, J. F.; He, X. M., *Organometallics* **1996**, *15*, 5350-5358.
- (51) He, X. M.; Hartwig, J. F., *Organometallics* **1996**, *15*, 400-407.
- (52) Chen, H. Y.; Hartwig, J. F., *Angew. Chem. Int. Ed.* **1999**, *38*, 3391-3393.
- (53) Waltz, K. M.; Hartwig, J. F., *Science* **1997**, *277*, 211-213.
- (54) Hartwig, J. F.; Cook, K. S.; Hapke, M.; Incarvito, C. D.; Fan, Y. B.; Webster, C. E.; Hall, M. B., *J. Am. Chem. Soc.* **2005**, *127*, 2538-2552.
- (55) Hartwig, J. F.; Muhoro, G. N.; He, X. M.; Eisenstein, O.; Bosque, R.; Maseras, F., *J. Am. Chem. Soc.* **1996**, *118*, 10936-10937.
- (56) Pandey, K. K., *Coord. Chem. Rev.* **2009**, *253*, 37-55.
- (57) Brookhart, M.; Green, M. L. H.; Parkin, G., *Proc. Natl. Acad. Sci. U. S. A.* **2007**, *104*, 6908-6914.
- (58) Braun, T.; Wehmeier, F., *Eur. J. Inorg. Chem.* **2011**, 613-625.
- (59) Jones, W. D.; Partridge, M. G.; Perutz, R. N., *J. Chem. Soc., Chem. Commun.* **1991**, 264-266.
- (60) Higgitt, C. L.; Klahn, A. H.; Moore, M. H.; Oelckers, B.; Partridge, M. G.; Perutz, R. N., *J. Chem. Soc., Dalton Trans.* **1997**, 1269-1280.
- (61) Selmecky, A. D.; Jones, W. D.; Partridge, M. G.; Perutz, R. N., *Organometallics* **1994**, *13*, 522-532.
- (62) Osman, R.; Perutz, R. N.; Rooney, A. D.; Langley, A. J., *J. Phys. Chem.* **1994**, *98*, 3562-3563.
- (63) Pattison, D. I., D. Phil Thesis, University of York, 1997.

- (64) Hall, C.; Jones, W. D.; Mawby, R. J.; Osman, R.; Perutz, R. N.; Whittlesey, M. K., *J. Am. Chem. Soc.* **1992**, *114*, 7425-7435.
- (65) Whittlesey, M. K.; Mawby, R. J.; Osman, R.; Perutz, R. N.; Field, L. D.; Wilkinson, M. P.; George, M. W., *J. Am. Chem. Soc.* **1993**, *115*, 8627-8637.
- (66) Cronin, L.; Nicasio, M. C.; Perutz, R. N.; Peters, R. G.; Roddick, D. M.; Whittlesey, M. K., *J. Am. Chem. Soc.* **1995**, *117*, 10047-10054.
- (67) Nicasio, M. C.; Perutz, R. N.; Walton, P. H., *Organometallics* **1997**, *16*, 1410-1417.
- (68) Nicasio, M. C.; Perutz, R. N.; Tekkaya, A., *Organometallics* **1998**, *17*, 5557-5564.
- (69) Osman, R.; Pattison, D. I.; Perutz, R. N.; Bianchini, C.; Casares, J. A.; Peruzzini, M., *J. Am. Chem. Soc.* **1997**, *119*, 8459-8473.
- (70) Callaghan, P. L.; Fernandez-Pacheco, R.; Jasim, N.; Lachaize, S.; Marder, T. B.; Perutz, R. N.; Rivalta, E.; Sabo-Etienne, S., *Chem. Commun.* **2004**, 242-243.
- (71) Norrish, R. G. W.; Porter, G., *Nature* **1949**, *164*, 658-658.

CHAPTER TWO

- (1) Sun, A. D.; Love, J. A., *Dalton Trans.* **2010**, *39*, 10362-10374.
- (2) Amii, H.; Uneyama, K., *Chem. Rev.* **2009**, *109*, 2119-2183.
- (3) Torrens, H., *Coord. Chem. Rev.* **2005**, *249*, 1957-1985.
- (4) Albrecht, M., *Chem. Rev.* **2010**, *110*, 576-623.
- (5) Pratihar, J. L.; Pattanayak, P.; Patra, D.; Rathore, R.; Chattopadhyay, S., *Inorg. Chim. Acta* **2011**, *367*, 182-186.
- (6) Bottcher, H. C.; Graf, M.; Sunkel, K.; Salert, B.; Kruger, H., *Inorg. Chem. Commun.* **2011**, *14*, 377-379.
- (7) Guard, L. M.; Ledger, A. E. W.; Reade, S. P.; Ellul, C. E.; Mahon, M. F.; Whittlesey, M. K., *J. Organomet. Chem.* **2011**, *696*, 780-786.
- (8) Wu, W. T.; Wu, W. H.; Ji, S. M.; Guo, H. M.; Zhao, J. Z., *Dalton Trans.* **2011**, *40*, 5953-5963.
- (9) Pandiarajan, D.; Ramesh, R., *Inorg. Chem. Commun.* **2011**, *14*, 686-689.
- (10) Panetier, J. A.; Macgregor, S. A.; Whittlesey, M. K., *Angew. Chem. Int. Ed.* **2011**, *50*, 2783-2786.
- (11) Vazquez-Garcia, D.; Fernandez, A.; Lopez-Torres, M.; Rodriguez, A.; Gomez-Blanco, N.; Viader, C.; Vila, J. M.; Fernandez, J. J., *J. Organomet. Chem.* **2011**, *696*, 764-771.

- (12) Pandya, S. U.; Moss, K. C.; Bryce, M. R.; Batsanov, A. S.; Fox, M. A.; Jankus, V.; Al Attar, H. A.; Monkman, A. P., *Eur. J. Inorg. Chem.* **2010**, 1963-1972.
- (13) Wu, W. T.; Cheng, C. H.; Wu, W. H.; Guo, H. M.; Ji, S. M.; Song, P.; Han, K. L.; Zhao, J. Z.; Zhang, X.; Wu, Y. B.; Du, G. T., *Eur. J. Inorg. Chem.* **2010**, 4683-4696.
- (14) Wu, W. T.; Wu, W. H.; Ji, S. M.; Guo, H. M.; Zhao, J. Z., *Eur. J. Inorg. Chem.* **2010**, 4470-4482.
- (15) Li, X. Y.; Sun, H. J.; Yu, F. L.; Florke, U.; Klein, H. F., *Organometallics* **2006**, *25*, 4695-4697.
- (16) Lian, Z.; Xu, X. F.; Sun, H. J.; Chen, Y.; Zheng, T. T.; Li, X. Y., *Dalton Trans.* **2010**, *39*, 9523-9529.
- (17) Arroyo, M.; Bernes, S.; Ceron, M.; Cortina, V.; Mendoza, C.; Torrens, H., *Inorg. Chem.* **2007**, *46*, 4857-4867.
- (18) Wang, T. G.; Love, J. A., *Organometallics* **2008**, *27*, 3290-3296.
- (19) Boutadla, Y.; Davies, D. L.; Jones, R. C.; Singh, K., *Chem. Eur. J.* **2011**, *17*, 3438-3448.
- (20) Boutadla, Y.; Davies, D. L.; Macgregor, S. A.; Poblador-Bahamonde, A. I., *Dalton Trans.* **2009**, 5887-5893.
- (21) Boutadla, Y.; Al-Duaij, O.; Davies, D. L.; Griffith, G. A.; Singh, K., *Organometallics* **2009**, *28*, 433-440.
- (22) Aullon, G.; Chat, R.; Favier, I.; Font-Bardia, M.; Gomez, M.; Granell, J.; Martinez, M.; Solans, X., *Dalton Trans.* **2009**, 8292-8300.
- (23) Umeda, N.; Hirano, K.; Satoh, T.; Shibata, N.; Sato, H.; Miura, M., *J. Org. Chem.* **2011**, *76*, 13-24.
- (24) Li, H.; Li, Y.; Zhang, X. S.; Chen, K.; Wang, X.; Shi, Z. J., *J. Am. Chem. Soc.* **2011**, *133*, 15244-15247.
- (25) Oonishi, Y.; Hosotani, A.; Sato, Y., *J. Am. Chem. Soc.* **2011**, *133*, 10386-10389.
- (26) Hyster, T. K.; Rovis, T., *J. Am. Chem. Soc.* **2010**, *132*, 10565-10569.
- (27) Braun, T.; Wehmeier, F., *Eur. J. Inorg. Chem.* **2011**, 613-625.
- (28) Arisawa, M.; Suzuki, T.; Ishikawa, T.; Yamaguchi, M., *J. Am. Chem. Soc.* **2008**, *130*, 12214-12215.
- (29) Noveski, D.; Braun, T.; Neumann, B.; Stammler, A.; Stammler, H. G., *Dalton Trans.* **2004**, 4106-4119.
- (30) Teltewskoi, M.; Panetier, J. A.; Macgregor, S. A.; Braun, T., *Angew. Chem. Int. Ed.* **2010**, *49*, 3947-3951.

- (31) Belt, S. T.; Duckett, S. B.; Helliwell, M.; Perutz, R. N., *J. Chem. Soc., Chem. Commun.* **1989**, 928-930.
- (32) Ballhorn, M.; Partridge, M. G.; Perutz, R. N.; Whittlesey, M. K., *Chem. Commun.* **1996**, 961-962.
- (33) Jones, W. D.; Partridge, M. G.; Perutz, R. N., *J. Chem. Soc., Chem. Commun.* **1991**, 264-266.
- (34) Belt, S. T.; Helliwell, M.; Jones, W. D.; Partridge, M. G.; Perutz, R. N., *J. Am. Chem. Soc.* **1993**, *115*, 1429-1440.
- (35) Basu, S.; Arulsamy, N.; Roddick, D. M., *Organometallics* **2008**, *27*, 3659-3665.
- (36) Holtcamp, M. W.; Henling, L. M.; Day, M. W.; Labinger, J. A.; Bercaw, J. E., *Inorg. Chim. Acta* **1998**, *270*, 467-478.
- (37) Hatnean, J. A.; Johnson, S. A., *Organometallics* **2012**, *31*, 1361-1373.
- (38) Selmecky, A. D.; Jones, W. D.; Partridge, M. G.; Perutz, R. N., *Organometallics* **1994**, *13*, 522-532.
- (39) Campian, M. V.; Harris, J. L.; Jasim, N.; Perutz, R. N.; Marder, T. B.; Whitwood, A. C., *Organometallics* **2006**, *25*, 5093-5104.
- (40) Braun, T.; Noveski, D.; Ahijado, M.; Wehmeier, F., *Dalton Trans.* **2007**, 3820-3825.
- (41) Partridge, M. G., PhD thesis, University of York.
- (42) Tanabe, T.; Evans, M. E.; Brennessel, W. W.; Jones, W. D., *Organometallics* **2011**, *30*, 834-843.
- (43) Vetter, A. J.; Jones, W. D., *Polyhedron* **2004**, *23*, 413-417.
- (44) Choi, J.; Choliy, Y.; Zhang, X. W.; Emge, T. J.; Krogh-Jespersen, K.; Goldman, A. S., *J. Am. Chem. Soc.* **2009**, *131*, 15627-15629.
- (45) Cronin, L.; Higgitt, C. L.; Karch, R.; Perutz, R. N., *Organometallics* **1997**, *16*, 4920-4928.
- (46) Nova, A.; Reinhold, M.; Perutz, R. N.; Macgregor, S. A.; McGrady, J. E., *Organometallics* **2010**, *29*, 1824-1831.
- (47) Jasim, N. A.; Perutz, R. N.; Whitwood, A. C.; Braun, T.; Izundu, J.; Neumann, B.; Rothfeld, S.; Stammler, H. G., *Organometallics* **2004**, *23*, 6140-6149.
- (48) Dransfield, T. A.; Nazir, R.; Perutz, R. N.; Whitwood, A. C., *J. Fluorine Chem.* **2010**, *131*, 1213-1217.
- (49) Whittlesey, M. K.; Perutz, R. N.; Moore, M. H., *Chem. Commun.* **1996**, 787-788.
- (50) Edelbach, B. L.; Jones, W. D., *J. Am. Chem. Soc.* **1997**, *119*, 7734-7742.

- (51) Klahn, A. H.; Moore, M. H.; Perutz, R. N., *J. Chem. Soc., Chem. Commun.* **1992**, 1699-1701.
- (52) Sheldrick, G. M., *Acta Crystallographica Section A* **2008**, *64*, 112-122.
- (53) Dolomanov, O. V.; Bourhis, L. J.; Gildea, R. J.; Howard, J. A. K.; Puschmann, H., *J. Appl. Crystallogr.* **2009**, *42*, 339-341.
- (54) Werner, H.; Feser, R., *J. Organomet. Chem.* **1982**, *232*, 351-370.
- (55) Banks, R. E.; Burgess, J. E.; Cheng, W. M.; Haszeldine, R. N., *J. Chem. Soc.* **1965**, 575-581.

CHAPTER THREE

- (1) Segawa, Y., *Science* **2006**, *314*, 1683-1683.
- (2) Miyaura, N.; Suzuki, A., *Chem. Rev.* **1995**, *95*, 2457-2483.
- (3) Baszczyk, I.; Gniewek, A.; Trzeciak, A. M., *J. Organomet. Chem.* **2012**, *710*, 44-52.
- (4) Avitia, B.; MacIntosh, E.; Muhia, S.; Kelson, E., *Tetrahedron Lett.* **2011**, *52*, 1631-1634.
- (5) Lam, K. C.; Marder, T. B.; Lin, Z. Y., *Organometallics* **2010**, *29*, 1849-1857.
- (6) Pintaric, C.; Olivero, S.; Gimbert, Y.; Chavant, P. Y.; Dunach, E., *J. Am. Chem. Soc.* **2010**, *132*, 11825-11827.
- (7) Mkhalid, I. A. I.; Barnard, J. H.; Marder, T. B.; Murphy, J. M.; Hartwig, J. F., *Chem. Rev.* **2010**, *110*, 890-931.
- (8) Rablen, P. R.; Hartwig, J. F., *J. Am. Chem. Soc.* **1996**, *118*, 4648-4653.
- (9) Hartwig, J. F.; Cook, K. S.; Hapke, M.; Incarvito, C. D.; Fan, Y. B.; Webster, C. E.; Hall, M. B., *J. Am. Chem. Soc.* **2005**, *127*, 2538-2552.
- (10) Hartwig, J. F., *Chem. Soc. Rev.* **2011**, *40*, 1992-2002.
- (11) Chen, H. Y.; Schlecht, S.; Semple, T. C.; Hartwig, J. F., *Science* **2000**, *287*, 1995-1997.
- (12) Perutz, R. N.; Sabo-Etienne, S., *Angew. Chem. Int. Ed.* **2007**, *46*, 2578-2592.
- (13) Rankin, M. A.; MacLean, D. F.; McDonald, R.; Ferguson, M. J.; Lumsden, M. D.; Stradiotto, M., *Organometallics* **2009**, *28*, 74-83.
- (14) Boller, T. M.; Murphy, J. M.; Hapke, M.; Ishiyama, T.; Miyaura, N.; Hartwig, J. F., *J. Am. Chem. Soc.* **2005**, *127*, 14263-14278.
- (15) Ishiyama, T.; Takagi, J.; Ishida, K.; Miyaura, N.; Anastasi, N. R.; Hartwig, J. F., *J. Am. Chem. Soc.* **2002**, *124*, 390-391.
- (16) Takagi, J.; Sato, K.; Hartwig, J. F.; Ishiyama, T.; Miyaura, N., *Tetrahedron Lett.*

2002, *43*, 5649-5651.

- (17) Boebel, T. A.; Hartwig, J. F., *J. Am. Chem. Soc.* **2008**, *130*, 7534-7535.
- (18) Robbins, D. W.; Boebel, T. A.; Hartwig, J. F., *J. Am. Chem. Soc.* **2010**, *132*, 4068-4069.
- (19) Mannig, D.; Noth, H., *Angew. Chem. Int. Ed.* **1985**, *24*, 878-879.
- (20) Olsson, V. J.; Szabo, K. J., *J. Org. Chem.* **2009**, *74*, 7715-7723.
- (21) Hunter, N. M.; Vogels, C. M.; Decken, A.; Bell, A.; Westcott, S. A., *Inorg. Chim. Acta* **2011**, *365*, 408-413.
- (22) Caballero, A.; Sabo-Etienne, S., *Organometallics* **2007**, *26*, 1191-1195.
- (23) Wu, J. Y.; Moreau, B.; Ritter, T., *J. Am. Chem. Soc.* **2009**, *131*, 12915-12917.
- (24) Harder, S.; Spielmann, J., *J. Organomet. Chem.* **2012**, *698*, 7-14.
- (25) Montiel-Palma, V.; Lumbierres, M.; Donnadiou, B.; Sabo-Etienne, S.; Chaudret, B., *J. Am. Chem. Soc.* **2002**, *124*, 5624-5625.
- (26) Lachaize, S.; Essalah, W.; Montiel-Palma, V.; Vendier, L.; Chaudret, B.; Barthelat, J. C.; Sabo-Etienne, S., *Organometallics* **2005**, *24*, 2935-2943.
- (27) Alcaraz, G.; Clot, E.; Helmstedt, U.; Vendier, L.; Sabo-Etienne, S., *J. Am. Chem. Soc.* **2007**, *129*, 8704-8705.
- (28) Alcaraz, G.; Grellier, M.; Sabo-Etienne, S., *Acc. Chem. Res.* **2009**, *42*, 1640-1649.
- (29) Bontemps, S.; Vendier, L.; Sabo-Etienne, S., *Angew. Chem. Int. Ed.* **2012**, *51*, 1671-1674.
- (30) Hesp, K. D.; Kannemann, F. O.; Rankin, M. A.; McDonald, R.; Ferguson, M. J.; Stradiotto, M., *Inorg. Chem.* **2011**, *50*, 2431-2444.
- (31) Kawamura, K.; Hartwig, J. F., *J. Am. Chem. Soc.* **2001**, *123*, 8422-8423.
- (32) Lam, W. H.; Shimada, S.; Batsanov, A. S.; Lin, Z. Y.; Marder, T. B.; Cowan, J. A.; Howard, J. A. K.; Mason, S. A.; McIntyre, G. J., *Organometallics* **2003**, *22*, 4557-4568.
- (33) Lam, W. H.; Lam, K. C.; Lin, Z. Y.; Shimada, S.; Perutz, R. N.; Marder, T. B., *Dalton Trans.* **2004**, 1556-1562.
- (34) Campian, M. V.; Harris, J. L.; Jasim, N.; Perutz, R. N.; Marder, T. B.; Whitwood, A. C., *Organometallics* **2006**, *25*, 5093-5104.
- (35) Campian, M. V.; Clot, E.; Eisenstein, O.; Helmstedt, U.; Jasim, N.; Perutz, R. N.; Whitwood, A. C.; Williamson, D., *J. Am. Chem. Soc.* **2008**, *130*, 4375-4385.
- (36) Campian, M. V.; Perutz, R. N.; Procacci, B.; Thatcher, R. J.; Torres, O.; Whitwood, A. C., *J. Am. Chem. Soc.* **2012**, *134*, 3480-3497.
- (37) Cronin, L.; Nicasio, M. C.; Perutz, R. N.; Peters, R. G.; Roddick, D. M.; Whittlesey,

- M. K., *J. Am. Chem. Soc.* **1995**, *117*, 10047-10054.
- (38) Hall, C.; Jones, W. D.; Mawby, R. J.; Osman, R.; Perutz, R. N.; Whittlesey, M. K., *J. Am. Chem. Soc.* **1992**, *114*, 7425-7435.
- (39) Callaghan, P. L.; Fernandez-Pacheco, R.; Jasim, N.; Lachaize, S.; Marder, T. B.; Perutz, R. N.; Rivalta, E.; Sabo-Etienne, S., *Chem. Commun.* **2004**, 242-243.
- (40) Seiwel, L. P., *J. Am. Chem. Soc.* **1974**, *96*, 7134-7135.
- (41) Haddleton, D. M.; Perutz, R. N., *J. Chem. Soc., Chem. Commun.* **1985**, 1372-1373.
- (42) Duckett, S. B.; Perutz, R. N., *Organometallics* **1992**, *11*, 90-98.
- (43) Belt, S. T.; Duckett, S. B.; Haddleton, D. M.; Perutz, R. N., *Organometallics* **1989**, *8*, 748-759.
- (44) Teltewskoi, M.; Panetier, J. A.; Macgregor, S. A.; Braun, T., *Angew. Chem. Int. Ed.* **2010**, *49*, 3947-3951.
- (45) Alcaraz, G.; Sabo-Etienne, S., *Coord. Chem. Rev.* **2008**, *252*, 2395-2409.
- (46) Linden, H. B., *Eur. J. Mass Spectrom.* **2004**, *10*, 459-468.
- (47) Bautista, M. T.; Cappellani, E. P.; Drouin, S. D.; Morris, R. H.; Schweitzer, C. T.; Sella, A.; Zubkowski, J., *J. Am. Chem. Soc.* **1991**, *113*, 4876-4887.

CHAPTER FOUR

- (1) DOE, U. S.; (http://www.sc.doe.gov/bes/reports/files/NHE_rpt.pdf).
- (2) Staubitz, A.; Robertson, A. P. M.; Manners, I., *Chem. Rev.* **2010**, *110*, 4079-4124.
- (3) Clark, T. J.; Russell, C. A.; Manners, I., *J. Am. Chem. Soc.* **2006**, *128*, 9582-9583.
- (4) Jaska, C. A.; Temple, K.; Lough, A. J.; Manners, I., *J. Am. Chem. Soc.* **2003**, *125*, 9424-9434.
- (5) Jaska, C. A.; Manners, I., *J. Am. Chem. Soc.* **2004**, *126*, 2698-2699.
- (6) Hebden, T. J.; Denney, M. C.; Pons, V.; Piccoli, P. M. B.; Koetzle, T. F.; Schultz, A. J.; Kaminsky, W.; Goldberg, K. I.; Heinekey, D. M., *J. Am. Chem. Soc.* **2008**, *130*, 10812-10820.
- (7) Karahan, S.; Zahmakiran, M.; Ozkar, S., *Chem. Commun.* **2012**, *48*, 1180-1182.
- (8) Denney, M. C.; Pons, V.; Hebden, T. J.; Heinekey, D. M.; Goldberg, K. I., *J. Am. Chem. Soc.* **2006**, *128*, 12048-12049.
- (9) Robertson, A. P. M.; Leitao, E. M.; Manners, I., *J. Am. Chem. Soc.* **2011**, *133*, 19322-19325.

- (10) Alcaraz, G.; Vendier, L.; Clot, E.; Sabo-Etienne, S., *Angew. Chem. Int. Ed.* **2010**, *49*, 918-920.
- (11) Butera, V.; Russo, N.; Sicilia, E., *Chem. Eur. J.* **2011**, *17*, 14586-14592.
- (12) Johnson, H. C.; Robertson, A. P. M.; Chaplin, A. B.; Sewell, L. J.; Thompson, A. L.; Haddow, M. F.; Manners, I.; Weller, A. S., *J. Am. Chem. Soc.* **2011**, *133*, 11076-11079.
- (13) Benac-Lestrille, G.; Hemstedt, U.; Vendier, L.; Alcaraz, G.; Cot, E.; Sabo-Etienne, S., *Inorg. Chem.* **2011**, *50*, 11039-11045.
- (14) Alcaraz, G.; Clot, E.; Helmstedt, U.; Vendier, L.; Sabo-Etienne, S., *J. Am. Chem. Soc.* **2007**, *129*, 8704-8705.
- (15) Esteruelas, M. A.; Fernandez-Alvarez, F. J.; Lopez, A. M.; Mora, M.; Onate, E., *J. Am. Chem. Soc.* **2010**, *132*, 5600-5601.
- (16) Shimoi, M.; Nagai, S.; Ichikawa, M.; Kawano, Y.; Katoh, K.; Uruichi, M.; Ogino, H., *J. Am. Chem. Soc.* **1999**, *121*, 11704-11712.
- (17) Douglas, T. M.; Chaplin, A. B.; Weller, A. S., *J. Am. Chem. Soc.* **2008**, *130*, 14432-14433.
- (18) Alcaraz, G.; Chaplin, A. B.; Stevens, C. J.; Clot, E.; Vendier, L.; Weller, A. S.; Sabo-Etienne, S., *Organometallics* **2010**, *29*, 5591-5595.
- (19) Tang, C. Y.; Smith, W.; Thompson, A. L.; Vidovic, D.; Aldridge, S., *Angew. Chem. Int. Ed.* **2011**, *50*, 1359-1362.
- (20) Vidovic, D.; Addy, D. A.; Kramer, T.; McGrady, J.; Aldridge, S., *J. Am. Chem. Soc.* **2011**, *133*, 8494-8497.
- (21) O'Neill, M.; Addy, D. A.; Riddlestone, I.; Kelly, M.; Phillips, N.; Aldridge, S., *J. Am. Chem. Soc.* **2011**, *133*, 11500-11503.
- (22) Campian, M. V.; Harris, J. L.; Jasim, N.; Perutz, R. N.; Marder, T. B.; Whitwood, A. C., *Organometallics* **2006**, *25*, 5093-5104.
- (23) Campian, M. V.; Perutz, R. N.; Procacci, B.; Thatcher, R. J.; Torres, O.; Whitwood, A. C., *J. Am. Chem. Soc.* **2012**, *134*, 3480-3497.
- (24) Ballhorn, M.; Partridge, M. G.; Perutz, R. N.; Whittlesey, M. K., *Chem. Commun.* **1996**, 961-962.
- (25) Kroke, E.; Li, Y. L.; Konetschny, C.; Lecomte, E.; Fasel, C.; Riedel, R., *Materials Science & Engineering R-Reports* **2000**, *26*, 97-199.
- (26) Blum, Y. D.; McDermott, G. A.; Hirschon, A. S., *Inorganic and Organometallic Oligomers and Polymers* **1991**, 161-175.

- (27) Eppinger, J.; Spiegler, M.; Hieringer, W.; Herrmann, W. A.; Anwander, R., *J. Am. Chem. Soc.* **2000**, *122*, 3080-3096.
- (28) Klimpel, M. G.; Gorlitzer, H. W.; Tafipolsky, M.; Spiegler, M.; Scherer, W.; Anwander, R., *J. Organomet. Chem.* **2002**, *647*, 236-244.
- (29) Ayed, T.; Barthelat, J. C.; Tangour, B.; Pradere, C.; Donnadieu, B.; Grellier, M.; Sabo-Etienne, S., *Organometallics* **2005**, *24*, 3824-3826.
- (30) Grellier, M.; Ayed, T.; Barthelat, J. C.; Albinati, A.; Mason, S.; Vendier, L.; Coppel, Y.; Sabo-Etienne, S., *J. Am. Chem. Soc.* **2009**, *131*, 7633-7640.
- (31) Brown, S. S. D.; Heaton, S. N.; Moore, M. H.; Perutz, R. N.; Wilson, G., *Organometallics* **1996**, *15*, 1392-1404.
- (32) Heaton, S., PhD thesis, University of York.
- (33) Werner, H.; Feser, R., *J. Organomet. Chem.* **1982**, *232*, 351-370.
- (34) Oliver, A. J.; Graham, W. A. G., *Inorg. Chem.* **1971**, *10*, 1165-1169.
- (35) Belt, S. T.; Duckett, S. B.; Haddleton, D. M.; Perutz, R. N., *Organometallics* **1989**, *8*, 748-759.
- (36) Gross, J. H.; Nieth, N.; Linden, H. B.; Blumbach, U.; Richter, F. J.; Tauchert, M. E.; Tompers, R.; Hofmann, P., *Analytical and Bioanalytical Chemistry* **2006**, *386*, 52-58.
- (37) Dolomanov, O. V.; Bourhis, L. J.; Gildea, R. J.; Howard, J. A. K.; Puschmann, H., *J. Appl. Crystallogr.* **2009**, *42*, 339-341.

CHAPTER FIVE

- (1) Trofimenko, S., *Acc. Chem. Res.* **1971**, *4*, 17-22.
- (2) Crossley, I. R., *Organotransition Metal Chemistry of Poly(Pyrazolyl)Borates, Pt 1* **2008**, *56*, 199-321.
- (3) Hessell, E. T.; Jones, W. D., *Organometallics* **1992**, *11*, 1496-1505.
- (4) Jones, W. D.; Hessell, E. T., *J. Am. Chem. Soc.* **1993**, *115*, 554-562.
- (5) Wick, D. D.; Jones, W. D., *Organometallics* **1999**, *18*, 495-505.
- (6) Vetter, A. J.; Jones, W. D., *Polyhedron* **2004**, *23*, 413-417.
- (7) Evans, M. E.; Burke, C. L.; Yaibuathes, S.; Clot, E.; Eisenstein, O.; Jones, W. D., *J. Am. Chem. Soc.* **2009**, *131*, 13464-13473.
- (8) Clot, E.; Besora, M.; Maseras, F.; Megret, C.; Eisenstein, O.; Oelckers, B.; Perutz, R. N., *Chem. Commun.* **2003**, 490-491.
- (9) Clot, E.; Megret, C.; Eisenstein, O.; Perutz, R. N., *J. Am. Chem. Soc.* **2009**, *131*, 7817-7827.

- (10) Nicasio, M. C.; Paneque, M.; Perez, P. J.; Pizzano, A.; Poveda, M. L.; Rey, L.; Sirol, S.; Taboada, S.; Trujillo, M.; Monge, A.; Ruiz, C.; Carmona, E., *Inorg. Chem.* **2000**, *39*, 180-188.
- (11) Paneque, N.; Perez, P. J.; Pizzano, A.; Poveda, M. L.; Taboada, S.; Trujillo, M.; Carmona, E., *Organometallics* **1999**, *18*, 4304-4310.
- (12) Wick, D. D.; Jones, W. D., *Inorg. Chim. Acta* **2009**, *362*, 4416-4421.
- (13) Tanabe, T.; Brennessel, W. W.; Clot, E.; Eisenstein, O.; Jones, W. D., *Dalton Trans.* **2010**, *39*, 10495-10509.
- (14) Belt, S. T.; Duckett, S. B.; Helliwell, M.; Perutz, R. N., *J. Chem. Soc., Chem. Commun.* **1989**, 928-930.
- (15) Jones, W. D.; Partridge, M. G.; Perutz, R. N., *J. Chem. Soc., Chem. Commun.* **1991**, 264-266.
- (16) Jasim, N. A.; Perutz, R. N.; Foxon, S. P.; Walton, P. H., *J. Chem. Soc., Dalton Trans.* **2001**, 1676-1685.
- (17) Checinska, L.; Grabowski, S. J., *Chem. Phys.* **2006**, *327*, 202-208.
- (18) Vicente, J.; Gil-Rubio, J.; Bautista, D.; Sironi, A.; Masciocchi, N., *Inorg. Chem.* **2004**, *43*, 5665-5675.
- (19) Macgregor, S. A.; Roe, D. C.; Marshall, W. J.; Bloch, K. M.; Bakhmutov, V. I.; Grushin, V. V., *J. Am. Chem. Soc.* **2005**, *127*, 15304-15321.
- (20) Tanabe, T.; Brennessel, W. W.; Clot, E.; Eisenstein, O.; Jones, W. D., *Dalton Trans.* **2010**, *39*, 10495-10509.
- (21) Campian, M. V.; Harris, J. L.; Jasim, N.; Perutz, R. N.; Marder, T. B.; Whitwood, A. C., *Organometallics* **2006**, *25*, 5093-5104.
- (22) Lachaize, S.; Sabo-Etienne, S., *Eur. J. Inorg. Chem.* **2006**, 2115-2127.
- (23) Braun, T.; Noveski, D.; Ahijado, M.; Wehmeier, F., *Dalton Trans.* **2007**, 3820-3825.
- (24) Vetter, A. J.; Flaschenriem, C.; Jones, W. D., *J. Am. Chem. Soc.* **2005**, *127*, 12315-12322.
- (25) Zhu, J.; Lin, Z. Y.; Marder, T. B., *Inorg. Chem.* **2005**, *44*, 9384-9390.
- (26) Linden, H. B., *Eur. J. Mass Spectrom.* **2004**, *10*, 459-468.
- (27) Dolomanov, O. V.; Bourhis, L. J.; Gildea, R. J.; Howard, J. A. K.; Puschmann, H., *J. Appl. Crystallogr.* **2009**, *42*, 339-341.

CHAPTER SIX

- (1) Nicasio, M. C.; Perutz, R. N.; Tekkaya, A., *Organometallics* **1998**, *17*, 5557-5564.
- (2) Whittlesey, M. K.; Mawby, R. J.; Osman, R.; Perutz, R. N.; Field, L. D.; Wilkinson, M. P.; George, M. W., *J. Am. Chem. Soc.* **1993**, *115*, 8627-8637.
- (3) Cronin, L.; Nicasio, M. C.; Perutz, R. N.; Peters, R. G.; Roddick, D. M.; Whittlesey, M. K., *J. Am. Chem. Soc.* **1995**, *117*, 10047-10054.
- (4) Nicasio, M. C.; Perutz, R. N.; Walton, P. H., *Organometallics* **1997**, *16*, 1410-1417.
- (5) Hall, C.; Jones, W. D.; Mawby, R. J.; Osman, R.; Perutz, R. N.; Whittlesey, M. K., *J. Am. Chem. Soc.* **1992**, *114*, 7425-7435.
- (6) Callaghan, P. L.; Fernandez-Pacheco, R.; Jasim, N.; Lachaize, S.; Marder, T. B.; Perutz, R. N.; Rivalta, E.; Sabo-Etienne, S., *Chem. Commun.* **2004**, 242-243.
- (7) Perutz, R. N., *Chem. Soc. Rev.* **1993**, *22*, 361-369.
- (8) Montiel-Palma, V.; Perutz, R. N.; George, M. W.; Jina, O. S.; Sabo-Etienne, S., *Chem. Commun.* **2000**, 1175-1176.
- (9) Osman, R.; Pattison, D. I.; Perutz, R. N.; Bianchini, C.; Casares, J. A.; Peruzzini, M., *J. Am. Chem. Soc.* **1997**, *119*, 8459-8473.
- (10) Geoffroy, G. L.; Wrighton, M. S.; Hammond, G. S.; Gray, H. B., *J. Am. Chem. Soc.* **1974**, *96*, 3105-3108.
- (11) Macgregor, S. A.; Eisenstein, O.; Whittlesey, M. K.; Perutz, R. N., *J. Chem. Soc., Dalton Trans.* **1998**, 291-300.
- (12) Andrews, L. J., *Inorg. Chem.* **1978**, *17*, 3180-3182.
- (13) Hartwig, J. F.; Andersen, R. A.; Bergman, R. G., *Organometallics* **1991**, *10*, 1710-1719.
- (14) Montiel-Palma, V.; Pattison, D. I.; Perutz, R. N.; Turner, C., *Organometallics* **2004**, *23*, 4034-4039.
- (15) Colombo, M.; George, M. W.; Moore, J. N.; Pattison, D. I.; Perutz, R. N.; Virrels, I. G.; Ye, T. Q., *J. Chem. Soc., Dalton Trans.* **1997**, 2857-2859.
- (16) Ampt, K. A. M.; Burling, S.; Donald, S. M. A.; Douglas, S.; Duckett, S. B.; Macgregor, S. A.; Perutz, R. N.; Whittlesey, M. K., *J. Am. Chem. Soc.* **2006**, *128*, 7452-7453.
- (17) Blazina, D.; Dunne, J. P.; Aiken, S.; Duckett, S. B.; Elkington, C.; McGrady, J. E.; Poli, R.; Walton, S. J.; Anwar, M. S.; Jones, J. A.; Carteret, H. A., *Dalton Trans.* **2006**, 2072-2080.
- (18) Vendrell, O.; Moreno, M.; Lluch, J. M., *J. Chem. Phys.* **2004**, *121*, 6258-6267.

- (19) Elian, M.; Hoffmann, R., *Inorg. Chem.* **1975**, *14*, 1058-1076.
- (20) Hoffmann, R.; Minot, C.; Gray, H. B., *J. Am. Chem. Soc.* **1984**, *106*, 2001-2005.
- (21) Ogasawara, M.; Macgregor, S. A.; Streib, W. E.; Folting, K.; Eisenstein, O.; Caulton, K. G., *J. Am. Chem. Soc.* **1996**, *118*, 10189-10199.
- (22) Burk, M. J., *J. Am. Chem. Soc.* **1991**, *113*, 8518-8519.
- (23) Campian, M. V.; Clot, E.; Eisenstein, O.; Helmstedt, U.; Jasim, N.; Perutz, R. N.; Whitwood, A. C.; Williamson, D., *J. Am. Chem. Soc.* **2008**, *130*, 4375-4385.
- (24) Wilhelm, E.; Battino, R., *Chem. Rev.* **1973**, *73*, 1-9.
- (25) Cassidy, J. F.; Long, C., *J. Photochem. Photobiol., A* **1990**, *54*, 1-10.
- (26) Campian, M. V.; Perutz, R. N.; Procacci, B.; Thatcher, R. J.; Torres, O.; Whitwood, A. C., *J. Am. Chem. Soc.* **2012**, *134*, 3480-3497.
- (27) Bautista, M. T.; Cappellani, E. P.; Drouin, S. D.; Morris, R. H.; Schweitzer, C. T.; Sella, A.; Zubkowski, J., *J. Am. Chem. Soc.* **1991**, *113*, 4876-4887.

CHAPTER SEVEN

- (1) http://www.nobelprize.org/nobel_prizes/chemistry/.
- (2) Dioumaev, V. K.; Yoo, B. R.; Procopio, L. J.; Carroll, P. J.; Berry, D. H., *J. Am. Chem. Soc.* **2003**, *125*, 8936-8948.
- (3) Lachaize, S.; Sabo-Etienne, S., *Eur. J. Inorg. Chem.* **2006**, 2115-2127.
- (4) Campian, M. V.; Perutz, R. N.; Procacci, B.; Thatcher, R. J.; Torres, O.; Whitwood, A. C., *J. Am. Chem. Soc.* **2012**, *134*, 3480-3497.
- (5) Whittlesey, M. K.; Perutz, R. N.; Moore, M. H., *Chem. Commun.* **1996**, 787-788.
- (6) Reade, S. P.; Acton, A. L.; Mahon, M. F.; Martin, T. A.; Whittlesey, M. K., *Eur. J. Inorg. Chem.* **2009**, 1774-1785.
- (7) Schlaf, M.; Lough, A. J.; Morris, R. H., *Organometallics* **1997**, *16*, 1253-1259.
- (8) Takeda, H.; Ishitani, O., *Coord. Chem. Rev.* **2010**, *254*, 346-354.
- (9) Windle, C. D.; Perutz, R. N., *Coord. Chem. Rev.* **2012**, *256*, 2562-2570.
- (10) Windle, C. D.; Campian, M. V.; Duhme-Klair, A. K.; Gibson, E. A.; Perutz, R. N.; Schneider, J., *Chem. Commun.* **2012**, *48*, 8189-8191.
- (11) Schneider, J.; Vuong, K. Q.; Calladine, J. A.; Sun, X. Z.; Whitwood, A. C.; George, M. W.; Perutz, R. N., *Inorg. Chem.* **2011**, *50*, 11877-11889.
- (12) Amoroso, A. J.; Banu, A.; Coogan, M. P.; Edwards, P. G.; Hossain, G.; Malik, K. M. A., *Dalton Trans.* **2010**, *39*, 6993-7003.

- (13) Perera, T.; Abhayawardhana, P.; Fronczek, F. R.; Marzilli, P. A.; Marzilli, L. G., *Eur. J. Inorg. Chem.* **2012**, 618-627.
- (14) Orth, S. D.; Barrera, J.; Sabat, M.; Harman, W. D., *Inorg. Chem.* **1993**, *32*, 594-601.
- (15) Wang, S. R.; Cheng, C. P., *J. Organomet. Chem.* **1995**, *490*, 111-116.
- (16) Horn, E.; Snow, M. R., *Aust. J. Chem.* **1980**, *33*, 2369-2376.

APPENDIX

- (1) <http://xray.princeton.edu/~phil/Facility/Guides/XrayDataCollection.html>.
- (2) <http://www.geo.arizona.edu/xtal/geos306/fall11-10.htm>.
- (3) Henry N.F.M., L. K., *Kynoch Press* **1952**, *Vol. 1*.
- (4) http://www.enotes.com/topic/Electromagnetic_radiation.
- (5) <http://en.wikipedia.org/wiki/Diffraction>.
- (6) <http://serc.carleton.edu/details/images/8400.html>.